DEPARTAMENTO DE FÍSICA MODERNA
UNIVERSIDAD DE CANTABRIA

INSTITUTO DE FÍSICA DE CANTABRIA
CSIC-UC

DETECCIÓN DE FUENTES EXTRAGALÁCTICAS EN MAPAS DE LA RADIACIÓN DEL FONDO CÓSMICO DE MICROONDAS MEDIANTE TÉCNICAS MULTIFRECUENCIALES

Memoria presentada para optar al título de Doctor otorgado por la Universidad de Cantabria

por

Luis Fernando Lanz Oca

Programa de Doctorado de Ciencias, Tecnología y Computación

Curso 2015/2016

Declaración de Autoría

Diego Herranz Muñoz, Doctor en Ciencias Físicas y profesor titular de la Universidad de Cantabria,

y

Marcos López-Caniego Alcarria, Doctor en Ciencias Físicas y científico en Aurora Technologies para la Agencia Espacial Europea,

CERTIFICAN que la presente memoria

Detección de fuentes extragalácticas en mapas de la radiación del fondo cósmico de microondas mediante técnicas multifrecuenciales

ha sido realizada por Luis Fernando Lanz Oca bajo nuestra dirección en el Instituto de Física de Cantabria, para optar al título de Doctor por la Universidad de Cantabria. Consideramos que esta memoria contiene aportaciones científicas suficientemente relevantes como para constituir la Tesis Doctoral del interesado.

En Santander, a 25 de enero de 2016,

Diego Herranz Muñoz

Marcos López-Caniego Alcarria

A Vega.

¿Anudas tú los lazos de las Pléyades o desatas las cuerdas del Orión?

¿Haces salir las Híadas a su tiempo y guías a la Osa y sus cachorros?

¿Conoces las leyes de los cielos? ¿Regulas su dominio sobre la tierra?

Job 38,31-33

Agradecimientos

La tesis que tienes entre las manos ha sido el fruto de muchos (más de los esperados) años, y no hubiera sido posible sin la inestimable ayuda de muchas personas. Pero para ser justos, el primer ≪gracias≫ se lo he de dar a José Luis Sanz, que me ofreció al entrar en una de sus clases de Relatividad General y Cosmología hacer la tesis en su grupo con el entonces profesor de las prácticas (y futuro director de esta tesis) Diego Herranz. Podría decirse que ese momento fue la superficie de *last scattering* de mi doctorado. Por supuesto, mil gracias a mis directores, el ya nombrado Diego y Marcos López-Caniego (el *root*), especialmente por estas últimas semanas y meses donde les he bombardeado con las sucesivas versiones de la tesis y los plazos de entrega. Sin sus consejos y sus directrices esta tesis no hubiera sido posible.

Por supuesto, también tengo que agradecer al resto del grupo su cercanía y disponibilidad siempre que ha sido necesario: Kike, Belén B., Chema, Patri, Patxi, Pier Paolo, Marina, Diego M., Franceso, etc. Y muy en particular a mis sucesivos compañeros de despacho, cuyo aporte, seguramente más vital que laboral, ha sido más importante que cualquier *paper* que hubiera podido publicar. Desde los primeros, como Jacobo y Andrés y su ≪sutil≫ diplomacia, hasta las maquinaciones de Marcos (no te perdonaré jamás lo del Diplomacy, Marcos, JAMÁS). También a Raquel, la gallega más americana (o al revés, no recuerdo) y su ayuda con mi inglés; a Biuse, cuyo buen humor es contagioso; a Raúl, por ser buen compañero de viaje y de conversaciones (y solo he pasado lo más fácil, chorbo); a Airam, prolongación de las ecuaciones en el mundo real y hacerme descubrir, junto a Raúl y Biuse, las maravillas culinarias del Emilio's. Y a David, nuestro *ironman* particular, por no ponerse límites (el Soplao te espera, chaval).

También es justo mencionar a otras personas con las que he compartido otros momentos extra-IFCA, como el fútbol junto a Gervasio, Esteban, Jordi, Núria, Richard, Federico, Diego T., Carlos, Dani, etc; el rol junto a Anuar, Nacho, Judit, Rosa, Belén H., Ángel, etc; el póker junto a Diego P. o Iñaki entre otros; y alguno más que seguramente se me escape (Lander, Joserra, etc). He tenido la oportunidad de descubrir a gente muy buena que no solo trabaja bien, sino con la que pasárselo bien.

A Joaquín, Laura, Gianfranco y Marcella por su hospitalidad en mis estancias en Trieste y Padua.

Y para terminar (tienes toda una tesis que leer), reconocer aquí a las personas que no me han pasado ni un código pero que han sido los pilares de todo este trabajo. Para empezar, mis padres, a los que no solo tengo que (*debo*) agradecer todo lo que me han dado, sino reconocérselo. A mis hermanos, por su apoyo. A mi tocayo, por estar ahí aunque no nos veamos mucho; la gente de Vista Alegre, por llevar un

mundo nuevo en sus corazones. A mis *cuñaos*, en particular a Cova y Jorge, y las *laurisilvas*. A Yoli, por la paciencia de estos últimos tiempos (no habrá una segunda tesis, jeje) y por su comprensión. Y a la enana, por hacerme olvidar todos los malos momentos con su sonrisa. Aunque no pueda leer aún estas palabras, espero que cuando pueda hacerlo sea tan feliz como lo soy yo con ella.

DEPARTAMENTO DE FÍSICA MODERNA
UNIVERSIDAD DE CANTABRIA

INSTITUTO DE FÍSICA DE CANTABRIA
CSIC-UC

DETECTION OF EXTRAGALACTIC SOURCES IN COSMIC MICROWAVE BACKGROUND MAPS WITH MULTIFREQUENCY TECHNIQUES

A dissertation submitted in partial fulfillment of the requirements for the degree of Doctor of Philosophy in Physics

by

Luis Fernando Lanz

Prologue

The observation and the analysis of the Cosmic Microwave Background (CMB) radiation is a crucial task to understand the early Universe and its properties. The last observations of this radiation (and its subsequent analysis) have allowed to know with more accuracy the age of the Universe (about 13.8 billion of years), the percentages of the composition of the Universe ($\sim 4.9\%$ of baryonic matter, $\sim 26.8\%$ of dark matter and the remaining $\sim 68.3\%$ of dark energy) and other cosmological parameters (Planck Collaboration et al., 2015e).

When observing the sky at the microwave frequency range, we can see a combination of different components, e.g., Galactic and extragalactic diffuse and compact emission, and instrumental noise, besides the CMB itself. In order to study and characterise, any, or all, of these component, it is important to develop techniques that separate them from the observational mixture we detect with our instruments. In the case of the extragalactic objects, that appear most of times like point sources due to their distance from us and the relatively poor angular resolution of the experiments, linear filters are suitable devices to detect them. Besides, their detection is not only interesting to remove them from the CMB data, but also to study the point sources themselves. In the literature there are many examples where filters have been successfully used to detect point sources.

Until the advent of experiments like WMAP and Planck, there was a lack of information about extragalactic compact sources in the frequency range 20-1000 GHz, gap that has been recently started to be covered with those experiments. Linear filters have been widely applied in these experiments, showing their efficiency. The literature also shows that most of times the techniques used has been single-frequency, i.e., filters deal with only one frequency each time. These single-frequency techniques, according to the latter results, have shown to be near the limit of their performance and capacity. While we wait for future higher resolution experiments we can develop new tools that improve the detection of fainter sources, tools that can be used in the future with the higher resolution experiments as well.

To achieve this goal, in this Thesis I will introduce a multifrequency linear filtering method. The use of two or more channels in a simultaneous way allow us to take into account more available information that is ignored in the single-frequency methods. In the case of this Thesis, the additional information used will be the cross-power spectrum of the noise, spatial information of the point sources (like the fact that one source is located in the same point in the sky at two different frequencies) and the parametrisation of the spectral behaviour of the point sources like a power law. The multifrequency

linear filter to be presented in this Thesis uses all this information in a natural way. Its performance is compared with the matched filter applying both techniques (the single- and the multi-frequency) in a set of realistic simulations of the Planck sky, showing the results in the Chapter 3. Accuracy in the recovered flux density and spectral index, percentages of spurious and real detections, etc, are better in general with the multifrequency method than with the matched filter.

Once the efficiency and power of the multifrequency method has been tested, it will be applied to real data, in particular the channels V and W (61 and 94 GHz, respectively) in the WMAP 7-year data. After some considerations (in particular the antenna beams) that must be taken into account respect to the Planck case mentioned in the previous paragraph, and explained more in detail in the Chapter 4, the multifilter tool obtains, in a totally blind search, a number of 119 5σ extragalactic objects at both channels simultaneously, to be compared with the 22 detections at 94 GHz in a *non*-blind search with the WMAP 3-year data (López-Caniego et al., 2007).

Contents

List of Figures

List of Tables

Chapter 1

INTRODUCTION

In the last years, several experiments have produced important advances in cosmology. The 'Concordance Model', the currently most accepted model in cosmology that is based on the inflation and on the ΛCDM model (where they are included the cold dark matter and a cosmological constant), is widely supported by different observations of the Cosmic Microwave Background (CMB), the accelerating expansion of the Universe measured with distant supernovae and the large scale structure of the Universe. According to the most recent results (Planck Collaboration et al., 2015e), the baryonic matter constitutes the 4.9% of the energy density of the Universe; the dark matter (non-baryonic weakly interacting matter) constitutes 26.8% of the energy density of the Universe; and the remaining 68.3% is the 'dark energy', with an equation of state close to a cosmological constant, and responsible of the current accelerating expansion of the Universe. Very little is known about the dark matter and energy and investigating the properties of these components is one of the challenges of cosmology in the next years. Dark matter must be 'cold', in the sense of low energetic or non relativistic particles (at least in its majority), because these kind of particles were necessary to form the structures that have collapsed into the form we observe nowadays. If the dark matter was 'hot' (or even 'warm'), the particles of dark matter could collapse and form structures but with less accumulation that observed.

1.1 The ΛCDM Model and the Cosmic Microwave Background

About 13,800 million years ago (Planck Collaboration et al., 2015e), the Universe was born in a 'big explosion' called the Big Bang, origin of the space-time as we know it.

Let us imagine the evolution of the Universe in a temporal line where we can draw the different epochs of its history (see Figure 1.1). Immediately after the Big Bang, we see the Planck Era ($0 < t <$

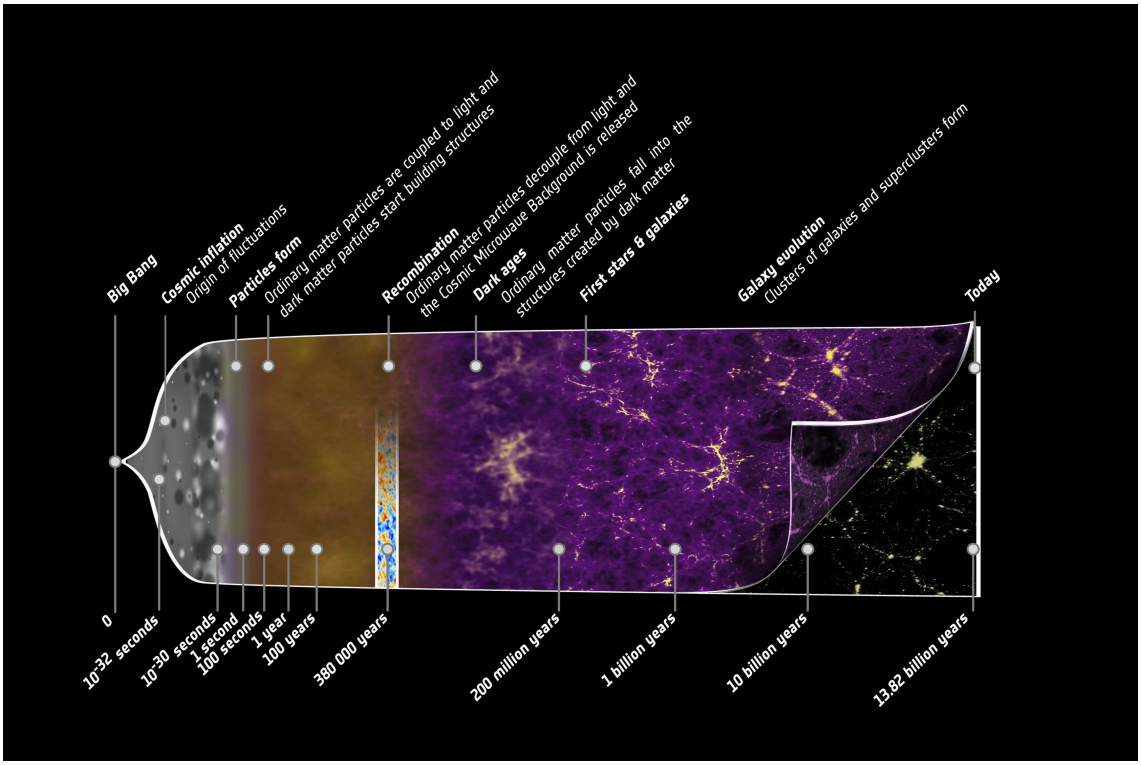

Figure 1.1 - This illustration summarises the almost 14-billion-year long history of our Universe. It shows the main events that occurred between the initial phase of the cosmos, where its properties were almost uniform and punctuated only by tiny fluctuations, to the rich variety of cosmic structure that we observe today, from stars and planets to galaxies and galaxy clusters. Copyright: ESA. Taken from `http://www.esa.int/spaceinimages/Images/2013/03/Planck_history_of_Universe_zoom`.

$10^{-43}s$). In this epoch, it is commonly accepted that the four fundamental interactions were unified and, for this reason, it is out from our knowledge since we do not have a theory that reconciles the quantum mechanics and the general relativity.

When $t \sim 10^{-36}$ s, the early Universe underwent, for a brief period of time ($\sim 10^{-32}$ s), an exponential expansion that increased the linear dimensions of the Universe by a factor of at least 10^{26} (Guth, 1981). This period is, for this reason, called the *inflation* and it was inserted *ad hoc* in the Big Bang model to solve some open questions in that moment, such as the horizon and the flatness problems. The first one talks about how it is possible that the Universe is statistically homogeneous and isotropic according to the cosmological principle. Without inflation, it is not possible to explain how two points located at opposite directions in the sky can be causally connected. However, we know from observations that all the regions on the horizon sphere show the same statistical properties. The inflation solved this problem, connecting them in the epoch previous to the accelerated expansion caused by it. With respect to the flatness problem, the question is why the total density is so close to the one that is necessary to have a flat Universe (flatness confirmed for the successive experiments for the observable universe). According to Friedmann equation (Friedman, 1922):

$$(\Omega^{-1} - 1)\rho a^2 = \frac{-3kc^2}{8\pi G}. \tag{1.1}$$

The right side of the equation is constant (c is the speed of light, G is the gravitational constant and k is the curvature parameter). In a Universe with inflation, the scale factor a behaves like $e^{\lambda t}$ and the factor ρa^2 (with ρ the total density of the Universe) grows quickly, allowing an arbitrary initial value for Ω (the ratio between the current density and the critical density), since the inflation can reduce it until almost zero.

The inflation is generated by a hypothetical scalar field whose associated particle would be the inflaton. According to this postulate, and before the inflation, the inflaton field would be at a high energy state. Then, and due to quantum fluctuations, a phase transition occured and the inflaton descended to the lowest energy state. This action produced the exponential grow of the scale factor, the so-called inflation. Moreover, this inflationary process had to produce perturbations in the metric, that have propagated until the present time in the form of gravitational waves. The study of these waves is one of the most challenging goals of modern observational cosmology, and the detection of primordial B-modes is nowadays a very active field of research (see section 1.2.3).

If we continue this journey through the history of the Universe, when $t = 3$ minutes the light nuclei were formed (the so-called *primordial nucleosynthesis*), basically hydrogen ($\sim 75\%$) and helium ($\sim 25\%$) (Alpher et al., 1948a). There are small quantities of another light nuclei such as lithium. Also we

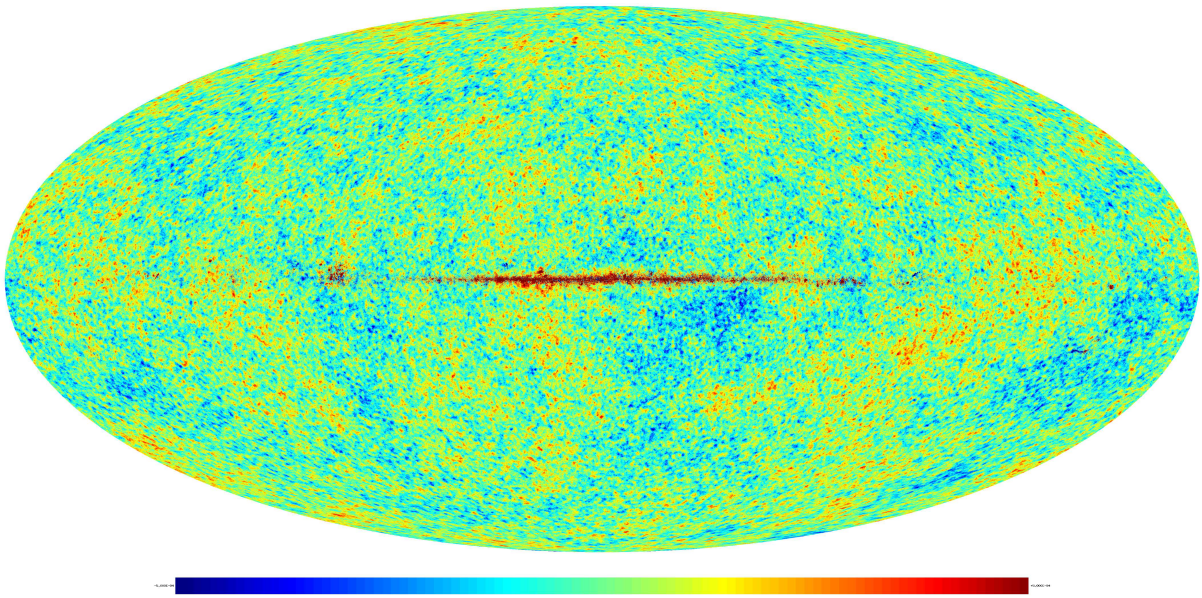

Figure 1.2 - CMB anisotropies measured by Planck by means of the Spectral estimation via Expectation-Maximization method. Copyright: ESA. Taken from Planck Collaboration et al. (2015b).

have the leptons and the radiation. At this point, the four fundamental forces separated and the Universe continued as a hot plasma composed by very energetic photons that were continuously interacting with electrons and baryons. In this way, at those temperatures, it was impossible to form stable atoms because the most energetic photons ionised any atom that would form at that epoch. The Universe continued its expansion and ∼380,000 years after the Big Bang it had cooled down to a temperature of $\sim 3000\,^{\circ}\mathrm{C}$. At that moment, protons and electrons could form atoms (recombination), the Universe became transparent (decoupling) and the photons travelled freely until the present time. The relative differences in the temperature of these photos with respect to the mean temperature of the CMB as measure today, ∼2.73 K, are the so-called anisotropies of the Cosmic Microwave Background (e.g., Figure1.2) . Nowadays, one can measure the photons coming from any direction of the sky to have a mean temperature of 2.7255 ± 0.0006 K (Fixsen, 2009).

After decoupling, we have atoms, other elementary particles and photons travelling free through the space. These are the so-called *dark ages*, because at this epoch the first stars had not yet formed. At a redshift between $6 < z < 20$ (between 150 millions and one billion of years after the Big Bang), matter started to form the first stars. These first stars ionised the hydrogen and the Universe reverted from a neutral state to an ionised plasma again. This epoch is known as the *reionisation*.

The detection of the CMB in 1964 by Arno Penzias and Robert Wilson of AT&T Laboratories Penzias and Wilson (1965) was a crucial support of the Big Bang Theory. By that time two different models coexisted and tried to explain the Universe and its origins: the theory of the Big Bang Alpher et al. (1948a) and the theory of the Steady-State Bondi and Gold (1948); Hoyle (1948). The theory of the Big Bang, as it was shown, tried to explain the Universe from a primordial 'big explosion' and how the atoms formed in a hot expanding Universe. George Gamow, Ralph Alpher and Robert Herman studied the thermal evolution of the Universe and predicted the current temperature of the Universe and the photons of the relic radiation after thousands of millions of years to be $T \sim 5$ K (Alpher et al., 1948b, 1949).

However, the Steady-State Theory, in its stricter version, proposes that the Universe remains stationary in its dynamical magnitudes (density, geometry, etc) and in its statistical properties, like the galactic counts. Therefore, as a consequence the Universe should look the same in the past and the present in every region of the space. The expansion of the Universe is a clear fact since Hubble discovered the recession of all the other galaxies ('nebulae' in that epoch) (Hubble, 1929). Therefore, the Steady-State Theory had to introduce a certain mass creation rate to maintain the same appearance through the time. This theory suffered a serious blow with the discovery of the CMB mentioned previously.

Fifteen years after Gamow and his team formulated the basics of CMB cosmology, Dicke and Zel'dovich rediscovered independently the theory of the primordial explosion. Dicke, Peebles, Roll and Wilkinson realised the importance of this relic radiation and decided to build an antenna to search for it. At that time, after an informal meeting with Penzias and Wilson that told them about their discovery, they determined that the excess of signal detected was due to the microwave background radiation (Penzias and Wilson, 1965; Dicke et al., 1965).

In the last decades, an increasing number of experiments have studied the CMB radiation and its properties. It has been found that this radiation is very uniform and isotropic all over the sky, roughly to 1 part in 100,000. The Big Bang Theory plus the inflation is the most natural and intuitive explanation to these facts, although several theoretical and observational issues remain to be explained. A notorious aspect of this primordial radiation is the fact that it is the most perfect black body known in the Universe (see Figure 1.3).

In the 1970s, several cosmologists such as Zel'dovich, Harrison, Peebles and Yu realised that the Universe should have small inhomogeneities in the matter distribution in order to explain the current structure of the Universe. Sunyaev declared that these inhomogeneities would have left an imprint in the CMB. These inhomogeneities were detected on the whole sky by the Differential Microwave Radiometer (DMR) instrument on the COBE satellite in the early 1990s Smoot et al. (1992).

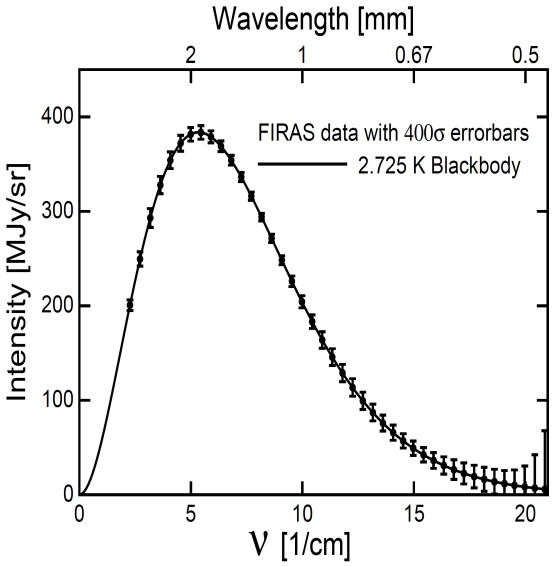

Figure 1.3 - CMB frequency spectrum obtained with the FIRAS instrument on COBE in 1996. As one can see, the experimental data fit perfectly to the theoretical model of the black body at T=2.725 K. The error bars were amplified 400 times in order to be seen. Taken from Fixsen et al. (1996). Copyright: The American Astronomical Society, reproduced with permission of the authors.

Later, BOOMERANG de Bernardis et al. (2000), MAXIMA Hanany et al. (2000) and Tenerife Gutiérrez et al. (2000) experiments determined in the late 1990s that the curvature of the Universe is close to zero, result confirmed by WMAP in 2003 Bennett et al. (2003).

The anisotropies of the CMB are the angular fluctuations in the temperature of this radiation field. In order to deal with these fluctuations in a statistical way, we may interpret them as a realisation of a random field on the sphere and use the spherical harmonics formulation to describe them:

$$\begin{aligned} \frac{\Delta T}{T}(\theta,\phi) = \frac{T(\theta,\phi)-T_0}{T_0} = \sum_{\ell=1}^{\infty}\sum_{m=-\ell}^{\ell} a_{\ell m} Y_{\ell m}(\theta,\phi), \\ a_{\ell m} = \int_0^{2\pi} d\phi \int_0^{\pi} \sin(\theta) d\theta \, Y^*_{\ell m}(\theta,\phi)\, \frac{\Delta T}{T}. \end{aligned} \tag{1.2}$$

If the temperature fluctuations are statistically isotropic, the variance of $a_{\ell m}$ does not depend on m:

$$< a_{\ell m} a^*_{\ell' m'} >= C_\ell \delta_{\ell\ell'} \delta_{mm'}, \tag{1.3}$$

where the averages must be taken over statistical ensembles. The quantities C_ℓ are the *angular power spectrum* of the temperature field.

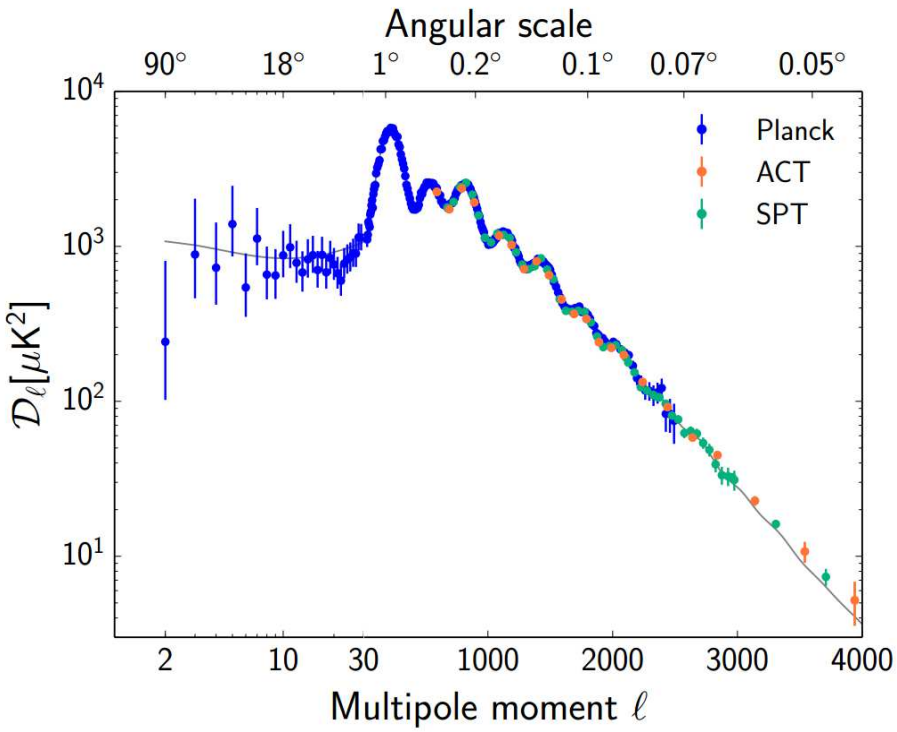

Figure 1.4 - Power spectrum of temperature fluctuations, $D_\ell = \ell(\ell+1)C_\ell^{TT}/2\pi$ estimated by three different experiments: the Atacama Cosmology Telescope (ACT), the South Pole Telescope (SPT), and Planck, where C_ℓ^{TT} are obtained from eq. 1.3. The dashed grey line corresponds to the Planck's best fit model. The horizontal axis is in logarithmic scale up to $\ell = 50$. The figure has been taken from Planck Collaboration et al. (2015h). Copyright: ESA.

If the fluctuations are Gaussian, it is sufficient to know the power spectrum (second order moment) and it can be accurately calculated for the inflationary models as a function of the cosmological parameters (Seljak and Zaldarriaga, 1996).

Checking the Figure 1.4, we can observe three regions:

- At large angular scales (or equivalently, small values of ℓ), we see a *plateau*. This is due to the fact that correspond to sizes on the last scattering surface larger than the horizon at the epoch of decoupling and therefore, not connected in a causal way. For this reason, no structure is expected at these scales. However, we can observe a deficit of low-ℓ power: the CMB power spectrum observed by Planck seems low at small values of ℓ, in particular in the range $2 \leq \ell \leq 30$ (Planck Collaboration et al., 2014c). It does not have any important impact on the cosmological parameter estimation, strongly determined by the high-multipole range.

- Intermediate regions ($30 \lesssim \ell \lesssim 1000$) correspond to regions with size less than the horizon.

Matter and radiation inside these regions are causally connected. Before the decoupling, acoustic oscillations occured in the baryon-photon fluid due to the competition between the gravitational force and the radiation pressure when the fluid collpased into the gravitational wells, resulting acoustic peaks in the Figure 1.4. The position of the peaks is determined by the geometry (Kamionkowski et al., 1994), the first in $\ell \sim 200$, the size of the horizon at the decoupling time.

- At smaller scales, temperature fluctuations are damped due to the fact the decoupling is not instantaneous (or what is the same, the last scattering surface has a width whose value is $\Delta z \sim 100$). Therefore, fluctuations with sizes smaller than this width will be reduced by other photons coming from different parts of the surface. Also, the 'Silk damping' (Silk, 1968), where photons coming from overdensed regions, dragging the baryons with them and smoothing the density fluctuations of photons and baryons, is other effect to be taken into account.

A crucial aspect to be considered when the power spectrum is measured is the *cosmic variance*, derived from the fact we only have one Universe and one sky to observe. This limitation is more notorious at small values of ℓ, introducing always a variance of $\frac{2}{2\ell+1}C_\ell^2$ in the calculations for Gaussian temperature fluctuations. A closely related aspect is the *sample variance*. Even if we imagine a full-sky experiment (like WMAP and Planck), we must discard some highly contaminated regions, like those close to the Galactic plane. This introduces a factor in the error equal to $f_{sky}^{-1/2}$, where f_{sky} is the fraction of the sky covered. These two error sources are always present and are independent of resolution and sensitivity of the experiment.

Additionally, there are several anomalies not entirely clarified and not observed in the CMB power spectrum. Let us show briefly:

- Low-multipole alignment was firstly detected by Tegmark et al. (2003). The CMB isotropic random field assumption results in a statistical independence of the preferred axes associated to the quadrupole ($\ell = 2$) and the octupole ($\ell = 3$). Planck Collaboration et al. (2014d) estimated an angular distance between both axes between 9° and 13°, depending on the component separation method used.

- Low variance. Monteserín et al. (2008) claimed a low value of the 3-year WMAP temperature data with respect to that expected from Gaussian simulations, result confirmed by Cruz et al. (2011) and Planck Collaboration et al. (2014d). The authors argued that, as the cosmological parameter estimation is not affected by low multipoles, simulations based on the best fit to ΛCDM model could differ from data at large angular scales.

- Cold Spot. A particular cold region in the Galactic southern hemisphere was detected by Vielva et al. (2004) in the first-year WMAP data. The authors observed an excess of kurtosis at scales $\sim 10^{\circ}$ with respect to the distribution expected from isotropic and Gaussian simulations. Many possible explanations have been suggested for the Cold Spot, from voids (Inoue and Silk, 2006) or underdensed regions (Finelli et al., 2014) to cosmic textures (Cruz et al., 2007).

- Hemispherical power asymmetry. Several estimators applied over the first-year data of WMAP revealed that the CMB temperature anisotropy pattern near the Galactic northern hemisphere has a lack of large scale features with respect to the southern hemisphere. Gordon et al. (2005) proposed a model in terms of a dipole modulated field. The preferred direction by using the 3-year WMAP data was, in Galactic coordinates, $(b = -27^{\circ}, l = 225^{\circ})$ (Eriksen et al., 2007) and $(b = -22^{\circ}, l = 224^{\circ}) \pm 24^{\circ}$ in the 5-year WMAP data (Hoftuft et al., 2009). The analysis carried out by the Planck Collaboration shows consistent results (Planck Collaboration et al., 2014d).

- Phase correlations. If the spatial distribution of the CMB anisotropies are well described by a random Gaussian field, the angular power spectrum contains all the statistical information. In this case, the harmonic coefficients (see eq. 1.2) can be written as a complex number with a real and an imaginary part, whose phase is the arc tan of the ratio between the imaginary and the real part. These phases (for $m \neq 0$ and $m \geq 1$) should be independent and identically distributed anf follow a uniform distribution in $[-\pi, \pi]$. The Planck Collaboration (Planck Collaboration et al., 2014d) found evidences that the low-ℓ phases are correlated. If true, this would indicate the existence of non-Gaussianity in the fluctuations of the CMB.

- Parity asymmetry. Two kind of parity transformations are usually considered: the point-parity reflections (between antipodal points in the sphere) and mirror reflections (through a plane and selecting a preferred direction in the sky). Land and Magueijo (2005) studied the CMB and found an evidence of odd point parity preference at low-ℓ values. This result has been confirmed by other works and Planck data. Planck Collaboration et al. (2014d) concluded that this asymmetry cannot be attributed to the low quadrupolar moment, because it increases up to values of $\ell \sim 22 - 25$. Their study of the mirror parity revealed and anti-symmetry close to the found for the dipole modulation.

1.2 CMB anisotropies

As it was previously commented, the CMB presents different types of inhomogeneities, that can be divided into two groups depending on their origin:

- **primary anisotropies**, which are due to effects that occurred at the moment of the last scattering surface or before.
- **secondary anisotropies**, which are due to the interactions of the CMB photons with hot gas or gravitational potentials, between the last scattering surface and the observer.

1.2.1 Primary anisotropies

The initial density fluctuations in the matter and radiation at the epoch of recombination are the origin of the CMB anisotropies. These fluctuations are also the origin of the large scale structures that we observe nowadays: overdensed regions are the seeds of areas where matter gravitationally collapses to form structures. We can distinguish between *adiabatic* and *isocurvature* fluctuations.

Adiabatic fluctuations are associated with a null variation of the specific entropy of each component at each point:

$$\delta\left(\frac{n_b}{n_\gamma}\right) = \delta\left(\frac{n_{DM}}{n_\gamma}\right) = 0, \tag{1.4}$$

where n_b, n_{DM}, n_γ denote the baryonic, dark mater and photon densities, respectively.

By contrast, isocurvature fluctuations are characterised by a null fluctuation of total energy at each point. According to the theory of General Relativity, is the energy, including the mass in this concept, that causes space-time to curve. This is the reason to call isocurvature to these kind of fluctuations. Mathematically, isocurvature fluctuations can be expressed as follows:

$$\delta(\rho_\gamma + \rho_b + \rho_{DM}) = 0. \tag{1.5}$$

Additionally, it is assumed the entropy per baryon is constant.

There are two main scenarios to explain these two initial seeds: inflation and topological defects. Inflation, as it was briefly explained, was a very short period of time in the early Universe where the scale factor grew exponentially. Inflationary models state the fluctuations were originated from the quantum oscillations boosted exponentially in the inflation (Hawking, 1982; Guth and Pi,

1982; Starobinsky, 1982; Bardeen et al., 1983). Inflationary models favour adiabatic fluctuations (Kolb and Turner, 1990) from a realisation of a homogeneous and isotropic Gaussian random field, fully characterised by their power spectrum $P(k) = Ak^n$. Standard inflation predicts $n = 1$ (Harrison, 1970; Zeldovich, 1972).

Topological defects scenarios consider cosmic strings, textures, etc, that might be formed during symmetry breaking phase transitions in the early Universe as seeds to initial perturbations (Vilenkin and Shellard, 1994). These fluctuations are non-Gaussian. There is also the possibility of obtaining hybrid scenarios combining inflation and topological defects.

Photon density fluctuations are not the only source of primary anisotropies. In the following paragraphs, some of them will be briefly explained.

- **Doppler effect**, produced by the motion of the observer with respect to the comoving coordinate system of the CMB. The 'blueshift' region will be observed in the direction of the motion, and the 'redshift' region in the opposite direction. As a result we obtain a dipole. This anisotropy was firstly detected in 1975 Corey and Wilkinson (1976), but it was not until 1996 that COBE measured its amplitude in a precise way: 3.372 ± 0.007 mK Fixsen et al. (1996). Strictly speaking, the Doppler effect is more an observational effect than a primary anisotropy.

- **Sachs-Wolfe effect** (SW), Sachs and Wolfe (1967), the most important physical process by which the primordial density fluctuations left their imprint on the CMB in the form of small variations in the temperature at scales larger than the horizon size at the last scattering ($\theta \sim 2^\circ$). Its origin is the gravitational potentials at the last scattering surface, when the photons enter and then leave the potential well at the epoch of recombination, gaining part of its energy and getting blueshifted and then loosing it and getting redshifted. The effect is not constant across the sky due to differences in the matter/energy density at the time of the last scattering.

At scales $0.1^\circ \lesssim \theta \lesssim 2^\circ$, the anisotropies are related to causal processes occurring in the matter-photon fluid until recombination. The coupling can be modelled through a harmonic oscillator that generates the already mentioned *acoustic peaks* (Hu and White (1996)). The combination of gravity and photon radiation pressure makes the perturbations to fluctuate.

Additionally, there are several physical processes that reduce the amplitude of the fluctuations, mainly at smaller angular scales. One of these mechanisms is the 'Silk damping' Silk (1968), where photons will travel from regions with a higher density to those with a lower density through diffusion, dragging the electrons, that are coupled to the protons, with them via Compton interaction. This diffusion has the effect of damping out the fluctuations.

1.2.2 Secondary anisotropies

As it was commented before, these anisotropies are produced due to the interactions of the CMB photons between the last scattering surface and us. The most important effects are:

Gravitational effects

If the photons cross a region with a potential well that is evolving they experiment a variation in their energy due to the variations in gravitational redshift/blueshift along their path. In the special case where the potential well is due to linear density perturbations in a Universe different from the Einstein-de Sitter one, this effect is known as the Integrated Sachs-Wolfe effect (ISW). In an Einstein-de Sitter Universe the ISW is equal to zero. Four different regimes can be distinguished for this mechanism: *early ISW*, when the potential decays between the decoupling time and the full matter domination; *late ISW*, when the potential decays due to the natural Universe expansion once matter no longer dominates the expansion (Λ or open models); *Rees-Sciama effect* (Rees and Sciama, 1968), which is due to non-linear evolution of collapsing structures; and finally all the other gravitational redshift effects, including gravitational lensing.

Scattering effects from reionisation

The reionisation is the epoch, after the recombination, where the first stars were formed and ionised the existing Universe at that time. During and after the reionisation, an increasing number of free electrons can interact and scatter with the CMB photons.

If we suppose that the Universe becomes reionised at a given redshift, a certain fraction of CMB photons will be scattered by free electrons. It means that one particular CMB photon observed from a given direction has not necessarily been originated from that direction.

Another effect that we have to take into account is the *Sunyaev-Zel'dovich effect (SZ)* Sunyaev and Zeldovich (1972). This effect is produced when CMB photons, during their passage through hot ionised gas (mainly in the inner regions of cluster of galaxies) are scattered by the hot electrons in the intra-cluster gas (inverse Compton effect). If we suppose that a certain fraction of the CMB photons that are travelling through the cluster are scattered to higher energies, the final result is an appreciable change in the CMB spectrum. This effect has a characteristic frequency dependence

that makes it easier to detect galaxy clusters. Mathematically, the CMB intensity change is given by:

$$\Delta I_\nu = 2\frac{(kT_{CMB})^3}{(hc)^2} y_C g(x), \tag{1.6}$$

where k, h and c are the Boltzmann, Planck constants and the speed of light (in the medium), respectively, and $x = h\nu/kt_{CMB}$. The spectral form of this effect is described by:

$$g(x) = x^4 e^x [x \cdot \coth(x/2) - 4]/(e^x - 1)^2, \tag{1.7}$$

which is negative (positive) at values of x smaller (larger) than $x_0 = 3.83$, that corresponds to a frequency of $\nu_0 = 217$ GHz.

The Comptonisation parameter is

$$y_C = \int \frac{kT_e}{mc^2} n_e \sigma_T dl, \tag{1.8}$$

where n_e and T_e are the electron density and temperature, respectively, σ_T is the Thomson cross section, and the integral is over a line of sight through the plasma.

1.2.3 Polarisation of the CMB

Another aspect to be considered in the analysis of the CMB is its polarisation: as an electromagnetic radiation, the CMB can be polarised and the study and analysis of this polarisation will allow us to better understand the CMB and the mechanisms that originated it. By contrast with the intensity, the polarisation is only generated by scattering (excluding the lensing effects), being the most direct probe of the last scattering surface (also of the reionisation).

Through the Thomson scattering, let us suppose incident unpolarised light that hits the electron, being the outgoing light polarised perpendicular to the plane of the scattering. Taking into account two incoming light directions, it is necessary to have some differences in the intensity of the incident light in order to have some degree of polarisation in the outcoming light, or in other words, the electron must see a quadrupole. This situation is only possible near the end of the recombination, when a quadrupole moment can be formed by the diffusion of photons into and out of the originally hot and cold regions. Recall that as photons from different temperature regions meet a temperature inhomogeneity is converted into an anisotropy. Nowadays, we observe the linear polarisation pattern that is the projection of the quadrupole anisotropies at recombination epoch, like figure 1.5 shows.

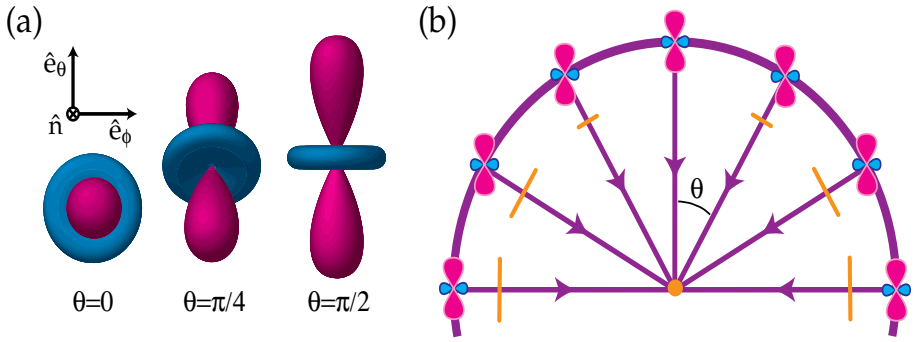

Figure 1.5 - In this figure it is shown how the quadrupole anisotropies are transformed into linear polarisation. In the figure (a) we see how the orientation of the quadrupole with respect to scattering direction $\hat{n}$ determines the sense and the magnitude of the polarisation. It is aligned with cold (red) lobes. In the figure (b) we see the same but represented as a function of θ. Taken from Hu and White (1997). Copyright: Elsevier B.V., reproduced with permission of the authors.

In general there are only three sources of quadrupole anisotropies: scalar (density perturbations), vectorial (vorticity in the plasma) and tensorial, directly related to gravitational waves. The vectorial perturbations are discarded in our scenario, remaining only the scalar and tensorial perturbations. And only the tensorial perturbations are able to produce the so-called *B-mode*, whose detection (at a certain level) would be an evidence of the gravitational waves produced during the inflation excluding the lensing effects.

But what is a B-mode? As it was said, the CMB, as electromagnetic radiation, can be polarised. The Stokes' parameters have been intensively used to describe the polarisation of the light. These parameters are four:

$$\begin{aligned} I &= |E_x|^2 + |E_y|^2, \\ Q &= \tfrac{1}{4}(|E_x|^2 - |E_y|^2), \\ U &= \tfrac{1}{2} Re(E_x E_y^*), \\ V &= \tfrac{1}{2} Im(E_x E_y^*), \end{aligned} \tag{1.9}$$

where E_x and E_y are the Cartesian coordinates of the field **E**. If $U = V = 0$ and $Q \neq 0$, light is linearly polarised in one of the Cartesian axis. If $Q = V = 0$ and $U \neq 0$, then the linear polarisation forms an angle of $45°$ with respect to the Cartesian axis. If $Q = U = 0$ and $V \neq 0$, the light is circularly polarised.

According to the Helmholtz's theorem, any vector field that satisfies some not very strong conditions can be decomposed into the sum of an irrotational and a nule-divergence fields. By analogy with the electric and magnetic fields, these fields are so-called the *E* and *B* modes, respectively. For a

didactic an intuitive introduction to CMB polarisation, see Hu and White (1997) and this website [1].

1.3 Galactic contamination

When the sky is observed at microwave and submillimetre frequencies, we do not only collect photons from the CMB. There are many sources of contamination at these frequencies that must be taken into account in order to make a proper study of the CMB and its anisotropies. The origin of a considerable percentage of this contamination comes from our own Galaxy in the form of diffuse emission. In addition, there are extragalactic sources (galaxies or clusters of galaxies) that are an important source of contamination at small angular scales and emit as well at these frequencies.

Finally, if our detection device is on the surface of the Earth or in our atmosphere, we have more sources of contamination whose origin is the atmosphere itself. In the following paragraphs we will review the main sources of Galactic contamination (see Figure 1.7).

1.3.1 Synchrotron emission

Any charged particle accelerated in a magnetic field emits radiation. In the case of non-relativistic electrons we observe the well-known cyclotron radiation whose frequency (the frequency of gyration in the magnetic field) is obtained to equal the centripetal and the magnetic Lorentz's forces:

$$\omega_B = \frac{qB}{\gamma mc}, \tag{1.10}$$

where q and m are the particle's charge and mass, respectively, B the intensity of the magnetic field, c is the light speed and γ the relativistic factor. In the relativistic case the emission is beamed into a narrow cone of $\Delta\theta = 2/\gamma$ of width, being more complex the spectrum and the pulse of radiation will be observed in a time period much shorter due to, precisely, this beaming effect. The spectrum will spread over a broader region with a cut off at the 'critical frequency':

$$\omega_c = \frac{3}{2}\gamma^2\omega_B \mathrm{sin}\alpha, \tag{1.11}$$

where $\mathrm{sin}\alpha$ represents the projection of the electron trajectory into a plane perpendicular to the magnetic field B. If γ increases, the pulses are shorter in time and more harmonics of the fundamental ω_B contribute. If $\gamma \to \infty$, we need a large number of harmonics to describe the emission and the envelope

[1] `http://background.uchicago.edu/~whu/intermediate/Polarization/polar0.html`

of this emission approaches the form of a certain function $F(x)$. The power per unit frequency emitted by each electron is:

$$P(\omega) = \frac{\sqrt{3}}{2\pi} \frac{q^3 B \sin\alpha}{mc^2} f\left(\frac{\omega}{\omega_c}\right), \tag{1.12}$$

where $F(x) = x \int_x^\infty K_{5/3}(y)dy$, being $K_{5/3}$ the modified Bessel function of 5/3 order.

Taking into account the Galaxy, the situation is more complicated: particle with different velocities are present and the magnetic field changes from a point to another. It can be demonstrated that, assuming a random direction for the motion of the electrons with respect to the magnetic field and a power law describes the electron energy spectrum the synchrotron luminosity is:

$$I(\nu) = \frac{\sqrt{3}q^3}{8\pi mc^2} \left(\frac{3q}{4\pi^3 c^5}\right)^{(p-1)/2} L N_0 B_{eff}^{(p+1)/2} \nu^{-(p-1)/2} a(p), \tag{1.13}$$

where L is the length along the line of sight through the considered emitting volume, B_{eff} is the effective magnetic field strength along the line of sight and $a(p)$ is a weak function of the electron energy spectrum:

$$a(p) = \Gamma\left(\frac{p}{4} + \frac{19}{12}\right) \Gamma\left(\frac{p}{4} + \frac{1}{12}\right) \frac{1}{p+1}, \tag{1.14}$$

where Γ is the Gamma function. Translating this luminosity in terms of brightness temperature, we obtain:

$$T(\nu) \propto \nu^{-(p+3)/2} = \nu^{-\beta}. \tag{1.15}$$

As it can be seen in the Figure 1.7, the synchrotron is the dominating foreground below 20 GHz. For more details of this radiation, see Rybicki and Lightman (1979) and Smoot (1999).

In addition, the radiation emitted by those relativistic electrons spiraling in a magnetic field is intrinsically highly polarised. Most of the energy is emitted in the plane of the electron's motion: about seven times more than in the orthogonal plane. In the case of a perfectly regular magnetic field, the synchrotron polarisation fraction may exceed 70%, although for realistic cases is significantly less. WMAP found a polarisation fraction of $\sim 3\%$ in the Galactic plane and $\sim 20\%$ at high Galactic latitudes (see cite Page et al. (2007)). There are other analysis that report polarisation fractions as high as 50% on large angular scales (see Kogut et al. (2007), Vidal et al. (2015)).

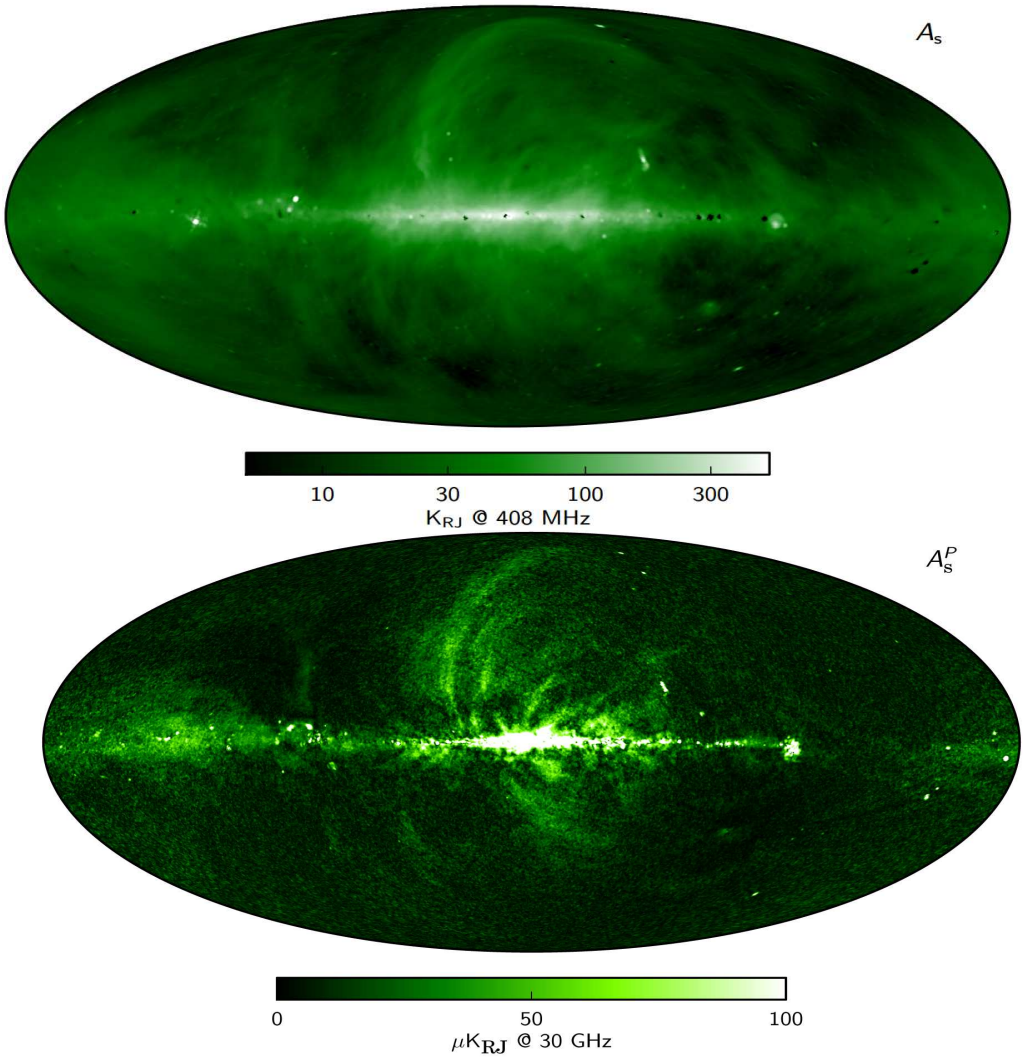

Figure 1.6 - Maximum a posteriori synchrotron map in intensity derived from the joint baseline analysis of *Planck*, WMAP and 408 MHz observations (top) and *Planck* polarisation amplitude map at 30 GHz, smoothed to an angular resolution of $40'$ (bottom). Taken from Planck Collaboration et al. (2015a). Copyright: ESA.

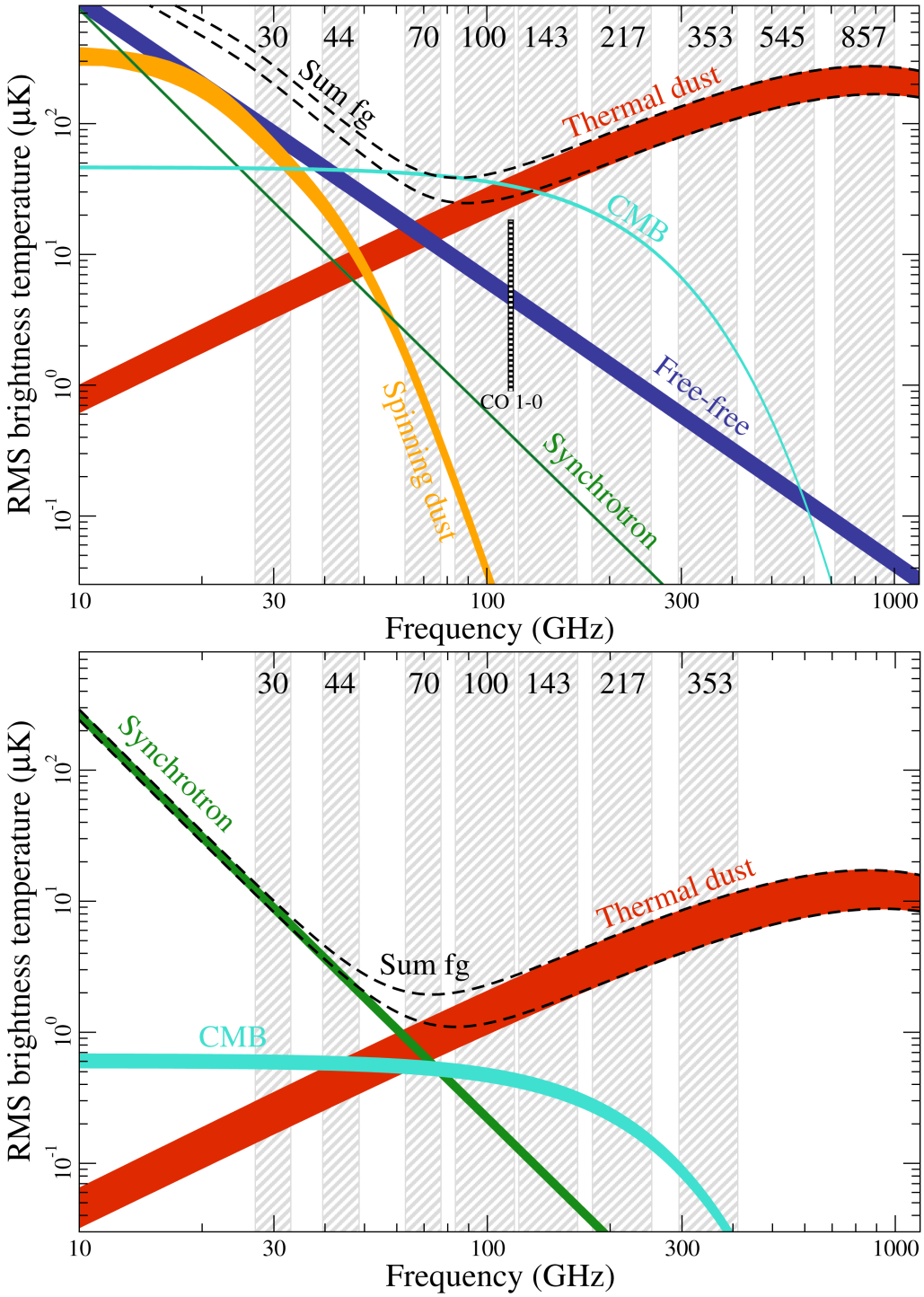

Figure 1.7 - Frequency dependence of the main Galactic contaminants of the CMB, both in intensity and polarisation. As one can see, between $\sim$ 60-90 GHz there is a window where the CMB dominates over the other contaminants. The shadowed regions correspond to the frequencies observed by Planck. Taken from `http://www.cosmos.esa.int/web/planck/picture-gallery`. Copyright: ESA.

1.3.2 Free-free emission

The *Bremsstrahlung* or free-free emission is an electromagnetic radiation produced when a charged particle is decelerated in the Coulomb field of another charged particle. In our case, these particles are free high energetic electrons ($T \sim 10^4$ K) interacting with ions of the interstellar medium. This radiation is poorly known, it is difficult to measure and dominates in a small range of frequencies (around ~ 50 GHz), where the other Galactic contaminants are minimum. As this radiation is intrinsically independent of the direction, it is unpolarised. For more details of this component, see Rybicki and Lightman (1979) and Smoot (1998).

1.3.3 Thermal dust

The radiation that dominates the Galactic emission above ~ 90 GHz is the emission produced by small grains of dust (just a few μm in size) in thermal equilibrium with the local radiation field, that absorb the UV light from the interstellar medium and re-emit it in the far infrared. These grains are basically silicon and carbonate grains of different sizes and shapes (in fact, the partial polarisation of this emission comes from their non-spherical shape and their alignment with existing magnetic fields) and can cluster forming dust clouds. The thermal dust emission can be modelled by a modified black-body radiation, the so called grey-body, because the dust thermal emission is optically thin in the submillimetre range:

$$S_\nu = \tau_\nu B_\nu \Omega_{cl}, \tag{1.16}$$

where S_ν is the flux density integrated over the clump solid angle Ω_{cl} (common to all frequencies), $\tau_\nu = N_{H_2} \mu m_H \kappa_{\nu_0} (\nu/\nu_0)^\beta$ is the dust optical lenght and B_ν is the well known Planck function at the dust colour temperature T_c ($T_c \sim 20K$):

$$B(\nu, T) = \frac{2h\nu^3}{c^2} \frac{1}{e^{\frac{h\nu}{kT}} - 1}, \tag{1.17}$$

where h, c and k are the Planck constant, the speed of light in the medium and the Boltzmann constant, respectively.

In the optical length expression, N_{H_2} is the H_2 gas column density, $\mu = 2.33$ is the mean mass per particle, m_H the mass of the proton, κ_{ν_0} the mass absorption coefficient at frequency ν_0 and β the dust emissivity spectral index (typical values between $1 \lesssim \beta \lesssim 2$), dependent on the nature of the dust grains (for more details see Désert et al. (1990)). We can rewrite the equation 1.16 in the following

way:

$$S_\nu = AB_\nu(T_c)\nu^\beta. \tag{1.18}$$

This expression allows us to see more clearly the three quantities that are not determined: the amplitude A, an effective temperature T_c and the spectral index β.

Finkbeiner et al. (1999) obtained a multi-component model capable of describing the dust emission between 100 and 3000 GHz. In this model they combine two grey bodies with different values of the dust spectral index (1.67 and 2.70) and temperatures (9.4 and 16.2 K, respectively).

This radiation is partially polarised due to the fact the dust particles are not spherical and they tend to align their major axes with the local magnetic field lines. Therefore, its contribution has to be taken into account in the CMB polarisation data at high frequencies. Until the arrival of *Planck*, the knowledge about this component was very poor. Nevertheless, the *Planck* collaboration has found that the dust contamination in polarisation is greater than the expected contribution: in fact, (Planck Collaboration et al., 2015c) observed a maximum dust polarisation fraction of 18% in their first analysis of the polarised dust emission based on the 353 GHz channel.

For more detail of this emission see Désert et al. (1990).

1.3.4 Spinning dust

In the last years, an anomalous Galactic emission at low frequencies has been detected. This emission cannot be accounted as thermal dust or free-free emission. Moreover, several studies have shown a correlation with thermal dust Kogut (1999); Leitch et al. (1997); de Oliveira-Costa et al. (1997); Watson et al. (2005). Draine and Lazarian Draine and Lazarian (1998a,b) proposed a process that could explain this peculiar radiation. This process has a frequency dependence similar to that of the free-free emission in a certain range of frequencies, but with a larger intensity, and is produced by rotational electric dipole emission and, thus, has been named *spinning dust*. Génova-Santos et al. (2015) reported upper limits for the polarisation fraction of this emission of $< 6.3\%$ and $< 2.8\%$ at 12 and 18 GHz, respectively.

1.3.5 CO emission

Some transitions between different energetic levels of the carbon monoxide are observed in the CMB temperature data. The first seven CO rotational transitions are in the frequency range observed by the High-Frequency Instrument of *Planck*, which cover the range between 100 and 857 GHz. In particular,

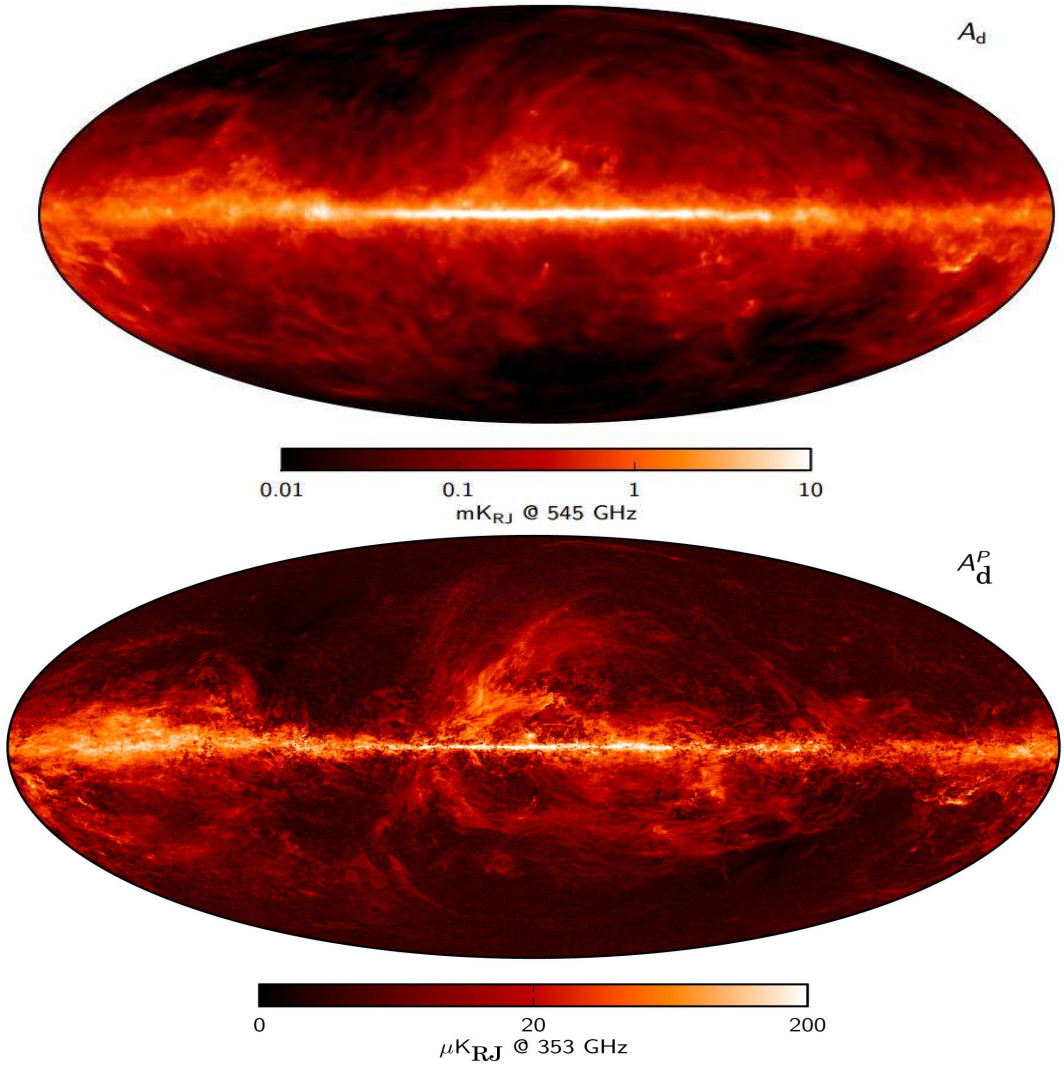

Figure 1.8 - Maximum a posteriori dust intensity map derived from the joint baseline analysis of *Planck*, WMAP and 408 MHz observations (top) and *Planck* polarisation amplitude map at 353 GHz, smoothed to an angular resolution of $40'$ (bottom). Taken from Planck Collaboration et al. (2015a). Copyright: ESA.

the first three of them ($J = 1 \rightarrow 0$; $J = 2 \rightarrow 1$; $J = 3 \rightarrow 2$), presented at 115, 230 and 345 GHz, respectively. This kind of emission is considered a good tracer of the molecular component of the interstellar medium since it is excited by collisions with H_2 and observable from the ground. See Planck Collaboration et al. (2015a) for more details.

1.4 Extragalactic components

Over the last few years, a big effort has been devoted to the problem of detecting point sources in CMB experiments. The main reason is that modern CMB experiments have reached resolution and sensitivity levels such that their capability to estimate the statistics of CMB fluctuations at high multipoles is no longer limited by instrumental noise but by Galactic and extragalactic foreground contamination. Among extragalactic contaminants, point sources are the most relevant at smaller angular scales, both in temperature Toffolatti et al. (1998); De Zotti et al. (1999); Hobson et al. (1999); De Zotti et al. (2005) and in polarisation Tucci et al. (2004, 2005); López-Caniego et al. (2009). Although the point sources are fainter in polarisation and not all of them are polarised, a better knowledge about them help us to remove the lensing effect that, as it was mentioned, transforms the E-mode into B-mode, contaminating the primordial B-mode. Moreover, the point sources are one of the most difficult contaminants to deal with and, at least in the frequency range spanned by CMB experiments, one of the most poorly known (but less with the arrival of Planck). Since the point sources contaminate the CMB radiation, hamper the efforts of cleaning the CMB from Galactic foregrounds and alter dramatically the statistics of the CMB fluctuations (e.g., the Gaussianity), it is therefore mandatory to detect the maximum possible number of extragalactic point sources (EPS) and to estimate their flux with the lowest possible error before any serious attempt to study the CMB anisotropies.

Until here, the point of view of scientists that study the CMB and see the point sources as a disturbing noise. But EPS are not only a contaminant to get rid of. The extragalactic sources were, for many years, the most powerful tool to study the distant Universe. In particular, from a cosmological point of view, early surveys generated an important debate previously mentioned, the Big Bang model versus the Steady-State through the (integral/differential) source counts, the number of objects per unit sky area (above/in an interval) of flux density. In the Figure 1.9, we can observe the historical importance of this discussion. The large plot it is taken from Longair (1966) and we see a set of observational points and two curves where at least one kind of sources show some kind of evolution. The E-deS curve is the one for an Einstein-de Sitter universe. As one can deduce, the observational points tell us something about some kind of evolution in the sources. This is precisely what we see in the right-top panel. Different curves that represent the source counts for different models are plotted. In particular,

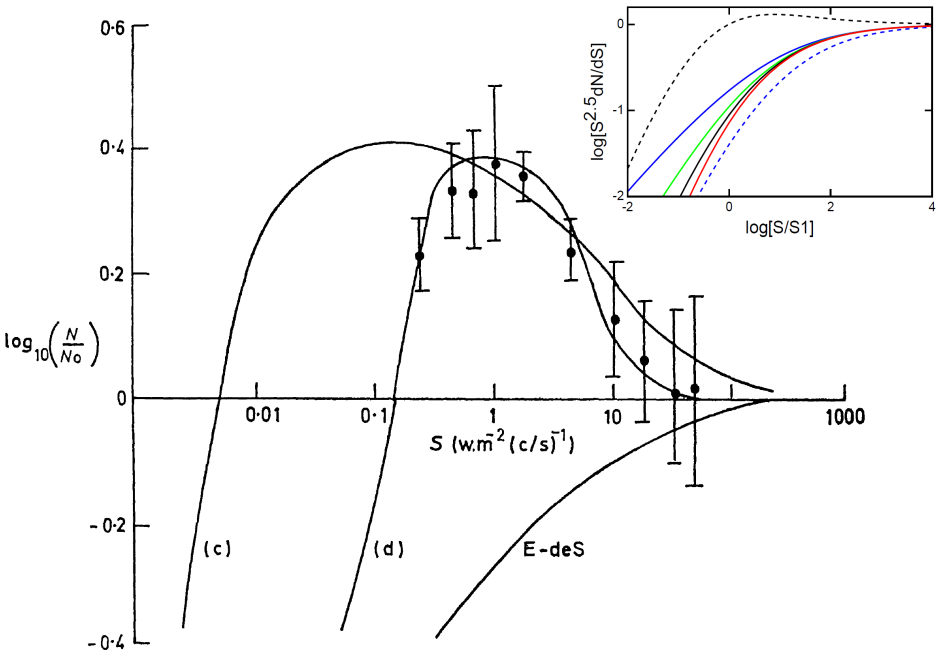

Figure 1.9 - In the large figure we show the source counts predicted by models with evolution in the sources (curves c and d) and in an Eisntein-de Sitter universe (E-deS curve). The points represent the observations as explained in Longair (1966), where this figure is taken. The right-top panel shows the source counts for different models: the Steady-State universe is the blue-dashed line; the dark energy-dominated universe is the blue solid line; the green, black and red solid lines represent universes with different values of Ω; and the black-dashed line is the real universe. The large figure was taken from Longair (1966) (Copyright: Royal Astronomical Society, reproduced with permission of the author) and the right-hand panel from `http://www.astro.ucla.edu/~wright/A275.pdf`, reproduced with permission of the author.

the Euclidean case has a slope of 1.5 and it is the point where all the curves converge. The Steady-State one is the blue-dashed line, the dark energy-dominated universe is the blue solid line and the curves between these two represent universes with different values of Ω. The black-dashed line is the real curve of source counts. As it is pretty clear from the plot, the real curve has a maximum that is not present in the other curves and tells us that counts (extragalactic objects as it will be see) underwent some kind of evolution in the past, rejecting the Steady-State model. However, as it was said before, this debate became obsolete when CMB radiation was discovered in 1965 (Penzias and Wilson, 1965).

The study of EPS at microwave frequencies is also very interesting from the standpoint of extragalactic astronomy. The current generation of CMB experiments is allowing one to obtain all-sky EPS catalogues that is starting to fill in the existing observational gap in our knowledge of the Universe in the frequency range from 20 to roughly 1000 GHz, gap that has only recently started to be covered by the Planck experiment, during the years of elaboration of this Thesis. We expect to derive source number counts and spectral indices, to study source variability and, therefore, to put constraints on the models of galaxy formation and evolution. For all these reasons, it is very important to develop suitable tools to detect this kind of sources.

At this point, one could wonder the following: what is a point source? Really, this is a technical question: a point source is an object whose angular size is less than the angular size of the resolution element. What is really interesting is the fact that they look like point sources due to the distance from us and to the relatively poor angular resolution of the experiments. At the frequencies observed in this Thesis ($\sim 30 - 100$ GHz, coincident with WMAP), point sources are dominated down to milli-Jansky [2] (mJy) by the traditional radio sources, usually accepted be powered by supermassive black holes in AGNs. At fainter flux densities it is observed as a flattening in the slope of the normalised differential counts, interpreted as the appearance of a new population: the star-forming galaxies (see Figure 1.10).

For more details of the following discussion, see De Zotti et al. (2010); de Young (2002).

1.4.1 Radio sources

Radio sources are mostly active galactic nuclei (AGN), with a strong non-thermal emission originated in the centre of these galaxies. This emission is synchrotron radiation produced by relativistic electrons moving along magnetic fields. Observing the figure 1.10 we can observe, at 30 GHz, the large variety of objects that we can find.

Usually, radio sources spectra are described by a power law ($S_\nu \propto \nu^\gamma$), where γ is the spectral index. In general, sources with $\gamma < -0.5$ are classified as *steep-spectrum* sources and *flat-spectrum*

[2] 1 Jy= 10^{-26} W m^{-2} Hz^{-1} = 10^{-23} erg s^{-1} cm^{-2} Hz^{-1}.

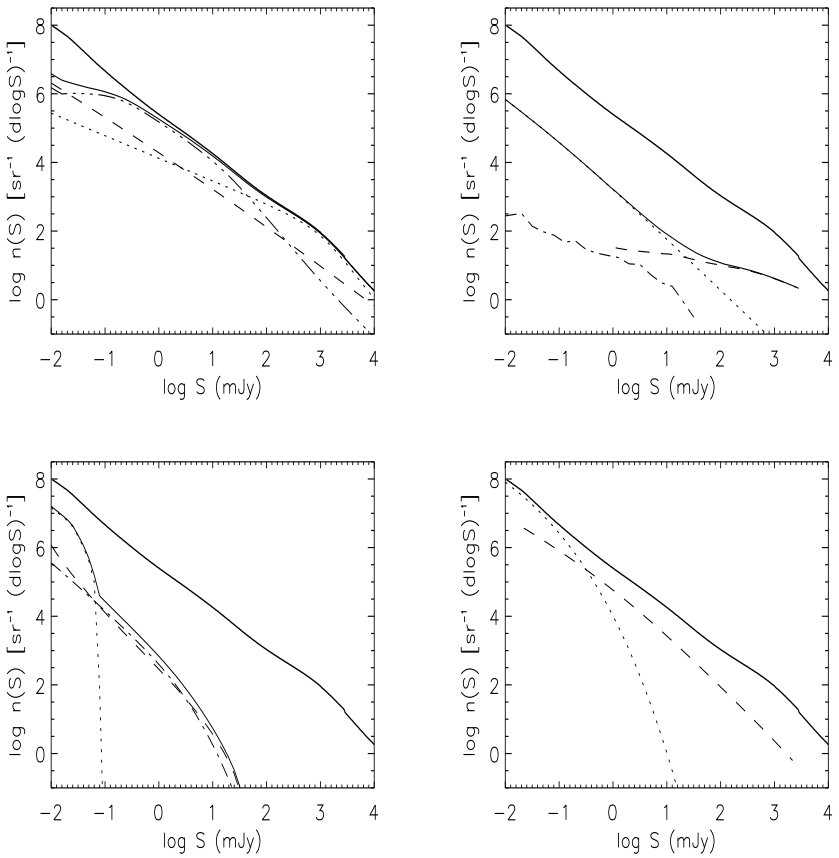

Figure 1.10 - Predicted differential counts at 30 GHz according to De Zotti et al. (2005). Upper left-hand panel (classical radio sources): flat spectrum radio quasars (dotted line); BL-Lacs (dashed line); steep-spectrum sources (triple dot-dashed line). Upper right-hand panel: ADAFs (dotted line); extreme GPS quasars and galaxies (dashed line); $\gamma-$ray bursts afterglows (dot-dashed line). Lower left-hand panel (star-forming galaxies): proto-spheroids (dotted line); spirals (dot-dashed line); starburst galaxies(dashed line). Lower right-hand panel: SZ effects on galactic scales (dotted line) and on cluster scales (dashed line). The sum of contributions of each panel is shown by a thin solid line. The overall total counts are indicated by a thick solid line. Copyright: ESO, reproduced with permission of the authors.

sources if $0 > \gamma > -0.5$ (if $\gamma > 0$ the source is *inverted*). Roughly speaking, steep-spectrum sources are associated to extended objects while flat-spectrum ones with compact sources. From a physical point of view, it is appropriate to consider the integrated spectra as the result of the combination of different components of the radio source: therefore, a flat spectrum is the superposition of emitting regions peaking over a broad frequency range (Kellermann et al., 1969). Broadly speaking, to radio telescopes the steep-spectrum objects showed extended double-lobed structures, while the flat-spectrum objects were point sources, unresolved until the Very-Long-Baseline Interferometry (VLBI) technique provided sub-arc-second mapping. The compact nature of flat-spectrum sources led to the conventional interpretation of synchrotron self-absorption at frequencies below the bump(s). In general, each source has a flat-spectrum core and extended steep-spectrum lobes and this implies that a power law is only applicable in a limited frequency range. Obviously, the reality is usually more complex: we can observe external absorption, self-absorption (producing spectra rising with the frequency) and energy losses of relativistic electrons. In this context, when we talk about extended or compact objects, it refers to the relative sizes of the emitting regions, but are viewed like point sources by WMAP or Planck due to the distance that separate them from us and to the relatively poor angular resolution of these experiments. Only some of the closer objects are observed like extended objects by these experiments.

Keeping in mind the separation between flat and steep-spectrum sources, a particular kind of sources that can be observed at those frequencies are the *blazars*. These sources are characterised by their high variability, their extremely compact size (therefore, their flat spectra across a wide range of frequencies) and the relativistic jet that we observe, characteristics observed both in intensity and in polarisation. If we observe the Figure1.10, we can notice in the upper left-hand panel the theoretical contribution of the steep and the flat (FSRQs and BL Lacs) spectrum sources to the differential counts at 30 GHz. Blazars are the main contributions at higher flux densities.

In addition to the steep spectrum objects, two classes of ultra steep-spectrum sources ($\gamma < -1.3$) have been discovered. The first one is related to galaxy clusters. The second class is very radio-luminous and are mostly identified with very high redshift radio galaxies Klamer et al. (2006). Therefore, the selection of these class of sources is a very effective way to find high redshift radio galaxies Miley and De Breuck (2008).

In very compact regions, synchrotron self-absorption can occur up to very high radio frequencies, giving rise to sources with spectral peaks in the GHz range. At high radio luminosities, these source are called *GHz Peaked Spectrum* (GPS) sources. These powerful and compact radio sources with a spectrum peaking at GHz frequencies are identified with both galaxies and quasars. It is widely accepted that GPS sources correspond to the early stages of the evolution of powerful radio sources, when the radio emitting region grows and expands within the interstellar medium of the host galaxy,

before plunging out into the intergalactic medium and becoming an extended radio source. An evidence that these sources are young came from VLBI measurements of propagation velocities. Speeds of up to $\sim 0.4c$ were measured, implying dynamical ages $\sim 10^3$ years. There is a clear anti-correlation between the peak (turnover) frequency and the projected linear size of GPS sources, suggesting that the process (probably synchrotron self-absorption) responsible for the turnover depends simply on the source size.

At these high frequencies, the presence of spectral peaks at low luminosities due to strong synchrotron self-absorption may be indicative of radiatively inefficient accretion, thought to correspond, as it will be shown, to late phases of the AGN evolution (ADAF/ADIOS objects, briefly explained below). Both the GPSs and the latter objects, with the $\gamma-$ray bursts (mentioned below) are shown in the upper right-hand panel of the Figure 1.10. As one can see, their contribution to the differential counts is below to the traditional radio sources at 30 GHz.

1.4.2 Sunyaev Zel'dovich effects and $\gamma-$ray bursts

Focusing in the Figure 1.10, one can notice that there are two additional contributions that, in principle, are not related to the traditional radio sources. The first one corresponds to the Sunyaev-Zel'dovich effect already explained in (see section 1.2.2). There are some recent evidences of statistically significant detections at 30 GHz of arcminute scale well in excess of predictions for primordial anisotropies of the CMB (by observations of the Cosmic Background Imager, CBI, (Mason et al., 2003) and the Berkeley-Illinois-Maryland Association Array, BIMA, (Dawson et al., 2002)). Although extragalactic sources are the main contributions to the fluctuations to that angular scales, it remains a substantial residual contribution to the CBI signal (De Zotti et al., 2004; Holder, 2002). Therefore, the most probable contribution is the thermal SZ effect (Gnedin and Jaffe, 2001). On the other hand, an important SZ signal is associated to the formation of the proto-spheroidal galaxies (see section 1.4.4), since the gas inside these objects is expected to have a large thermal energy, leading to a detectable SZ signal.

The second contribution comes from the afterglow emission of the γ- ray bursts (GRB). These GRBs are flashes of gamma rays coming from very energetic explosions that were observed in distant galaxies. These phenomena are the most brightest known events in the Universe. Their duration can oscillate between fraction of seconds until several hours. Usually, this initial burst is followed by less energetic 'afterglow' emitted at longer wavelengths.

Most observed GRBs are believed to consist of a narrow beam of intense radiation released during a supernova or hypernova. A subclass of GRBs, the 'short' bursts, appear to originate from a different process, may be due to the merger of binary neutron stars.

The sources of these GRBs are usually billions of light-years away from us, implying, as was said before, that they are extremely energetic. These events are also very rare, only a few per galaxy per million of years. The low time frequency of these events and their extremely high associated energy have been proposed as the origin of some massive extinction events in the past.

GRBs were firstly detected by the American Vela satellites. These satellites were designed to detect covert nuclear weapons tests, in particular from the USSR. In the late 1960s, they detected a flash of gamma radiation different from any known weapon signature. After discarding any terrestrial origin, the results were published in 1973 (Klebesadel et al., 1973).

The afterglows of the GRBs can me modelled as synchrotron emission from a decelerating blast wave in an ambient medium, maybe the interstellar medium of the host galaxy (Waxman, 1997; Wijers and Galama, 1999; Mészáros, 1999). The radio flux above the self-absorption break at $\lesssim 5$ GHz, is proportional to $\nu^{1/3}$ up to a peak frequency that decreases with time. This implies that surveys at different frequencies probe different phases of the expansion of the blast wave. Due to their high brightnesses, GRB afterglows may be detected at high redshifts and are therefore important tracers of the early star formation in the Universe, and of the absorption properties of the intergalactic medium across the reionisation phase.

The models that describe the different populations of radio and IR/sub-mm galaxies use the so-called *source number counts* (number of sources per stereo-radian and per flux interval) that take into account the number of objects from a certain population and their corresponding flux. Regarding the radio sources, number counts have been obtained from VLA observations for very low flux limits ($\sim \mu$Jy) at 1.41, 4.86 and 8.44 GHz Muxlow et al. (2005) and the models behave very well at this range of frequencies. In the last years, several groups have studied the observations at frequencies below 8 GHz and proposed models that explain these observations and, to a certain degree, extrapolate the number counts to higher frequencies. De Zotti et al. (2005); Tucci et al. (2011) improves the existing models. In De Zotti et al. (2005), the authors studied the contributions to the counts by different source populations in the range 20-30 GHz. This work is based on new evolutionary models for the flat-spectrum radio quasars (FSRQ), BL Lac objects and steep-spectrum sources. Advection-Dominated Accretion Flows/Adiabatic Inflow-Outflow Solutions sources (ADAF/ADIOS) and early phases of γ-ray burst afterglows were also considered in that study. The authors also took into account the synchrotron and free-free emission when estimating the counts of different populations of star-forming galaxies.

In Tucci et al. (2011) the authors focussed on blazars spectra, that dominate the mm-wavelenght number counts at brightest fluxes (see figure 1.10). In the most recent results (Massardi et al. (2011);

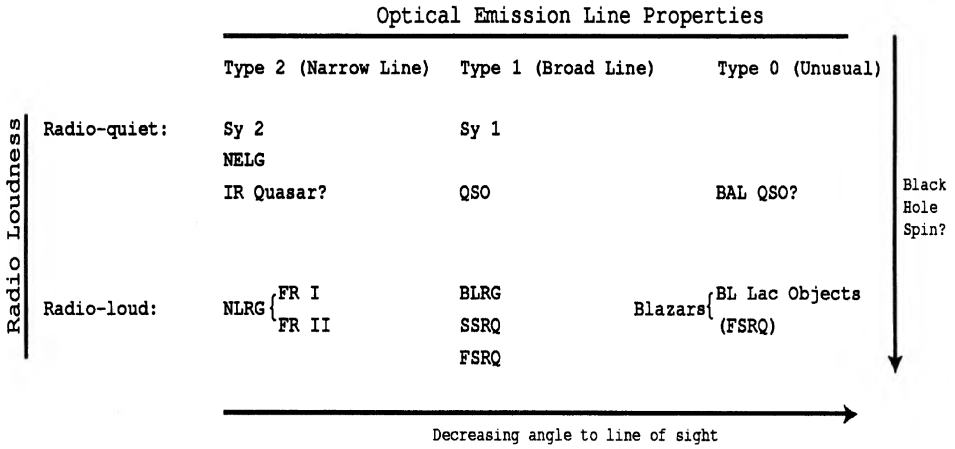

Table 1.1 - AGN taxonomy. Table where it is shown the dependence of the object that we observe respect to the viewing angle with the line of sight. Taken from Urry and Padovani (1995). Copyright: Astronomical Society of the Pacific, reproduced with permission of the authors.

Planck Collaboration et al. (2011b,a) and the results shown in the Chapter 4) there is a clear steepening in blazar spectra with emerging spectral indices between -0.5 and -1.2. The authors interpreted this spectral behaviour as the consequence, at least partially, by the transition from the optically-thick to optically-thin regime in the observed synchrotron emission of AGN jets (Marscher, 1996). A 'break' in the synchrotron spectrum of blazars above which the spectrum becomes steep is predicted by models of synchrotron emission from inhomogeneous and unresolved relativistic jets (Blandford and Königl, 1979; Königl, 1981; Marscher and Gear, 1985). In this context, the most relevant parameter is the dimension of the (approximated homogeneous and spherical) region responsible of the emission at the break frequency, being related to the distance of the emitting region to the AGN core in a conical jet. This distance should be parsec-scales at least for FSRQs, and $<<$ 1 pc for BL Lac objects. This model is able to predict the number counts and the spectral index distribution in the interval from 5 to 220 GHz.

In the previous subsections we have seen the large variety of objects observed at GHz range, and briefly commented some of their characteristic properties. At this point we can make a deliberation and wonder if they are a reflect of different objects or, in some way, the number of 'different' objects is more reduced and we see different physical aspects of the same object. Through several years, different efforts have been made in this direction until the model unification of AGNs (see Urry and Padovani (1995)). The Active Galactic Nuclei are galaxies whose very compact nuclei have an extremely high activity and are brighter than the rest of the galaxy. At the centre of this region there is a supermassive

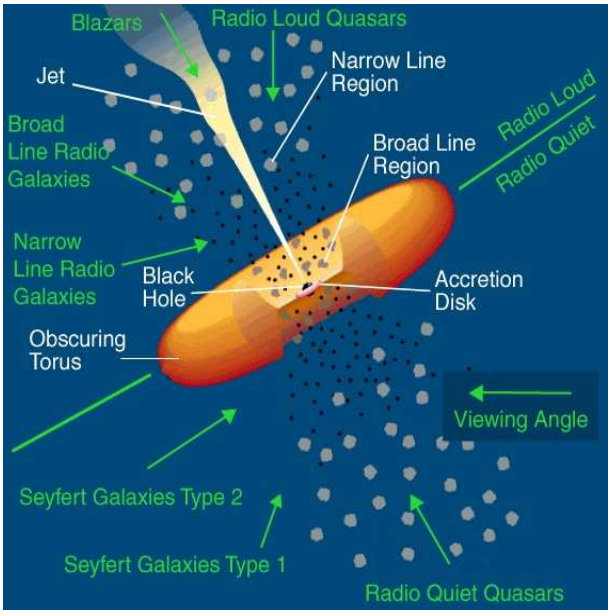

Figure 1.11 - Scheme (not to scale) where it is shown the unification model of AGNs. As it can be seen, the great variety is due to the viewing angle respect to line of sight. From Urry and Padovani (1995). Copyright: Astronomical Society of the Pacific, reproduced with permission of the authors.

black hole whose gravitational potential energy is the ultimate source of the AGN luminosity. Mater pulled toward the black hole looses angular momentum through viscous or turbulent processes in an accretion disk, which glows brightly at ultraviolet and perhaps soft X-ray wavelengths. Hard X-ray emission is also produced very near the black hole, perhaps in connection with a pervasive sea of hot electrons above the disk. If the black hole is spinning, energy may be extracted electromagnetically from the black hole itself. Strong optical and ultraviolet emission lines are produced in clouds of gas moving rapidly in the potential of the black hole, the so-called *broad-line clouds*. The optical and ultraviolet radiation is obscured along some lines of sight by a torus of gas and dust well outside the accretion disk and broad-line region. Beyond the torus, slower moving clouds of gas produce emission lines with narrower widths. Outflows of energetic particles occur along the poles of the disk or torus, escaping and forming collimated radio-emitting jets and sometimes giant radio sources when the host galaxy is an elliptical, but forming only very weak radio sources when the host galaxy is a gas-rich spiral. For more details, see Urry and Padovani (1995); de Young (2002).

According to this model, we observe the different objects depending on the viewing angles, as it can be seen in Figure 1.11. Table 1.1 gives a brief summary of the different objects that we observe as a function of the line of sight in the unification model. Depending of this fact, we have one of the different classes of AGNs shown in the Table 1.1. If the angle between the line of sight and the jet is

$\approx 0°$, we observe a very compact and variable object with flat spectra that we classify as *blazar*, where are included the BL Lac objects and the flat-spectra radio quasars (FSRQs). Therefore, according to the unification model (Figure 1.11 and Table 1.1), the blazars are AGNs whose orientation in the sky is almost perpendicular to the line of sight. When increasing the angle of sight with respect to the jet, we firstly observe the region called *broad line region* (BLR), where due to the proximity to the black hole, the rotational velocities are responsible of broad emission lines in the spectra. If the angle between the line of sight and the jet increases, the torus obscures the BLR and we only observe the *narrow line region* (NLR). Here, the rotational velocities are lower and therefore the emission lines are narrower.

Regarding the GPS sources, the identification of these sources is a key aspect in the study of the early evolution of radio-loud AGNs. Also, ADAF (see Rees et al. (1982))/ADIOS (see Blandford and Begelman (1999)) objects, as already mentioned, are thought to correspond to late phases of the AGN evolution, with luminosities below a few per cent of the Eddington limit. Observations at this range of radio frequencies are crucial to study the last stages of the AGN evolution, where the radiation/accretion efficiency is small.

1.4.3 Star-forming galaxies

The radio emission of star-forming galaxies is mostly synchrotron from relativistic electrons interacting with the galactic magnetic field, but with significant free-free contributions from the ionised interstellar medium. The radio emission of star-forming galaxies correlates with their star formation rate (Helou et al., 1985; Condon, 1992; Garrett, 2002), and this is expected if we think young stars are responsible for dust heating and for the generation, via supernovae, of synchrotron emitting relativistic electrons. The cross-over between synchrotron plus free-free emission, prevailing at cm wavelengths, and thermal dust emission generally occurs at $\lambda \simeq 2-3$ mm, so at tens of GHz (frequencies observed by WMAP and Planck), there are contributions for both components: the former associated to normal late-type galaxies and starburst galaxies at low to moderate redshifts, the latter to the hight-redshift population detected by sub-mm surveys ('SCUBA' galaxies). The relation between radio emission and star-formation rate is linear (Yun et al., 2001) in the range $10^{30} \lesssim L_\nu(60\mu \text{ m}) \lesssim 10^{32.5}$ erg s^{-1} Hz^{-1}:

$$L_{1.4GHz} = 1.16 \times 10^{-2} L_\nu(60\mu m). \tag{1.19}$$

At $L_\nu(60\mu \text{ m}) < 10^{30}$ erg s^{-1} Hz^{-1}, it is found that fluxes are lower that corresponding with the equation above written, but can be fit with a little correction. At lower fluxes, the only way is replacing the linear relation by a more complex equation (see equation 15 of De Zotti et al. (2010)).

There are different contributions to the global far-IR luminosity. In Luminous and Ultra Luminous

Infrared galaxies, the emission is dominated by warmed dust, associated with star formation. However, infrared 'cirrus' emission, heated by older stars, is more important in galaxies with lower star formation rates (see next section).

As one can see in the lower left-hand panel of the Figure1.10, their contribution at 30 GHz is important at low flux densities, being the number of differential counts above the traditional radio sources.

1.4.4 Dust-emission galaxies

The IR/sub-mm emission is produced by the dust, that absorbs UV and optical radiation, re-emitting it in the far-infrared. In this range of frequencies, the models available a few years ago did not match the latest observations with SCUBA and MAMBO. Then, a new kind of sources appear at those frequencies. This implied that a new population of sources could have been discovered, associated to high-redshift one detected by sub-mm surveys ('SCUBA galaxies'). Following Granato et al. (2001), and Granato et al. (2004), the 'SCUBA galaxies' are interpreted as proto-spheroidal galaxies (the progenitors of present day early-type galaxies and of massive bulges of disc galaxies) in the process of forming most of their stars. The model proposed by the authors for the galaxy formation takes into account the hierarchical clustering. In this hierarchical clustering context, dark matter halos, located in the places where the quantum perturbations were magnified during the inflation (and will provide the gravitational well to attract baryonic matter), build up through merging from smaller objects. Diffuse gas within the dark matter halo falls down into the star-forming regions at a rate that depends on the dynamic and cooling times. Part of this gas condenses into stars, at a rate again controlled by the local dynamic and cooling times. Due to supernovae and the active nuclei, gas also feels their feedback, heating it and possibly expelling it from the potential well: this supernova heating is more effective in shallower potential wells, being, obviously, the star formation faster in larger halos. In addition, the radiation drag on the cold gas decreases its angular momentum, entering into a reservoir around the central black hole, increasing its mass and the nuclear activity. The higher the star formation rate is, the higher the radiation drag and, consequently, the faster is the loss of angular momentum of the gas and the inflow to the central black hole. In turn, the kinetic energy carried by outflows driven by active nuclei through line acceleration can inject in the interstellar medium a sufficient amount of energy to unbind it and stop the star formation (the same mechanism injects in the inter galactic medium a substantial fraction of metals). Therefore, the larger is the halo, the more brief is the star-formation epoch. This implies that star-formation activity of the most massive galaxies quickly declines for $z \lesssim 3$. A 'quasar phase' follows (lasting $10^7 - 10^8$ years), and a long phase of passive evolution of galaxies ensues, becoming rapidly very red objects (Extremely Red Object). Intermediate and low mass spheroids

have lower star formations rates and less extreme optical depths, but more extensive in time (we could talk about an anti-hierarchical baryonic collapse). They show up as Lyman-Break Galaxies.

The authors in Cai et al. (2013) proposed a hybrid model for the evolution of galaxies and AGNs in the IR. For $z \geq 1.5$, the proto-spheroidal galaxies in the process of forming most of their stellar mass are the dominant population and we already have a physical model (Granato et al., 2004). At lower redshifts, the contribution of this population fades and almost disappears at $z \simeq 1$. At these redshifts, the late-type galaxies are the dominant. The epoch-dependent luminosity function of these galaxies has been modelled in terms of two populations: the 'warm' (starburst) and 'cold' (normal) galaxies, with different spectral energy distributions and evolutions. Simple truncated power law models have been adopted for these galaxies. 'Cold' galaxies evolve weakly only in luminosity, while 'warm' galaxies evolve both in luminosity and in density. For the proto-spheroidal galaxies, it is worked out, for the first time, the evolving luminosity functions of these objects as a whole (stellar plus AGN component).

Below $z = 1.5$, the far-IR emission of the proto-spheroidal galaxies and the associated AGNs fade out quickly. However, AGNs can be reactivated (by interactions, for example). This last phase of the AGNs have been phenomenologically described in an analogous way to the late-type galaxies.

Therefore, we can observe that above 350 μm, the main contributors to the CIB (Cosmic Infrared Background) are the proto-spheroidal galaxies. In this wavelength range, the late-type galaxies only dominate the counts at the brightest ('cold' galaxies) and the faintest ('warm' galaxies) flux densities. But these galaxies become important when wavelength decreases, being dominant below 250 μm. This strong variation with wavelength in the composition of IR sources implies specific predictions for auto- and cross-power spectra of the source distribution. This model predicts a high cross-correlation only at high wavelengths ($\geq$500 μm). Below this wavelength, the correlation weakens and it is expected small values for CIB fluctuations at 100 and 500 μm. In the Herschel[3]/SPIRE wavelength range, cross-correlation has been measured and the results are in good agreement with the model.

According to this model, the AGN contribution to the CIB is always sub-dominant. It is maximal in the mid-IR where it reaches 8.6% at 16 μm and 8.1% at 24 μm. The AGN contribution to the counts is also always subdominant. The CIB is estimated by Béthermin et al. (2011), obtaining a total value equal to 23.7$\pm$ 0.9 nW m^{-2} sr^{-1}. The fraction of lensed sources is below 10$\%$ at 500 μm and about 50$\%$ in the mm domain. It is important to say that the contribution of the CIB (firstly detected by Puget et al. (1996)) is the 50% over the extragalactic background light (EBL), the relic emission due to galaxy formation and accretion processes since the recombination to nowadays. The EBL is the second background radiation in importance after the CMB.

[3] `http://sci.esa.int/herschel/`

As it was said previously, star formation takes place in an early epoch ($z \gtrsim 2$) and for a brief period of time, in particular for the proto-spheroidal galaxies. Due to their high redshifts, there is a significant probability that these sources to be gravitationally lensed. The detection of a large number of these sources is important in order to study a relevant cosmological aspect such as the matter distribution in the high$-z$ Universe. The authors in Mancuso et al. (2015) predict the radio counts of star forming galaxies down to nJy levels along with redshift distributions down to the detection limits of the phase 1 Square Kilometre Array-mid telescope (SKA1-mid) and of its precursors. Such predictions were obtained by coupling epoch dependent star formation rate (SFR) functions with relations between SFR and radio (synchrotron and free-free) emission. The SFR functions were derived taking into account both the dust obscured and the unobscured star-formation, by combining far-infrared (FIR), ultra-violet (UV) and Hα luminosity functions up to high redshifts. The South Pole Telescope (SPT) counts of dusty galaxies at 95 GHz were revisited to perform a detailed analysis of the spectral energy distributions. The results obtained by the authors show that the deepest SKA1-MID surveys will detect high-z galaxies with SFRs two orders of magnitude lower compared to Herschel surveys. The highest redshift tails of the distributions at the detection limits of planned SKA1-MID surveys comprise a substantial fraction of strongly lensed galaxies, in particular the prediction is that in a survey down to 0.25 μJy at 1.4 GHz will detect $\sim$1200 strongly lensed galaxies per square degree, at redshifts up to 10. The SKA1-MID will thus provide a comprehensive view of the star formation history throughout the re-ionisation epoch, unaffected by dust extinction.

In addition, with the upcoming James Webb Space Telescope, we will be able to combine data from the far infrared with the optical and the near infrared, expanding our knowledge in this field.

One aspect for which Herschel is particularly well suited is the study of the evolution of galaxies at high redshifts. Taking spectroscopic observations with Keck I Low Resolution Imaging Spectrometer and the Keck II DEep Imaging Multi-Object Spectrograph at 24 μm from 36 Herschel-SPIRE 250-500 micron selected galaxies (HSGs) at $2 < z < 5$, Casey et al. (2012b) obtain individual source luminosities range from log($L_{IR}/L_{\odot}$)=12.5-13.6 (corresponding to star formation rates 500-9000 $M_{\odot}$/yr). Therefore, lower limits on the contribution of HSGs to the cosmic star formation rate density can placed at (7$\pm$ 2)$\times$ 10^{-3} $M_{\odot}$/yr h^3 Mpc^{-3} at $z \sim 2.5$, which is $> 10\%$ of the estimated total star formation rate density (SFRD) of the Universe from optical surveys. The contribution at $z \sim 4$ has a lower limit of 3$\times$ 10^{-3} $M_{\odot}$/yr h^3 Mpc^{-3}, $\gtrsim 20\%$ of the estimated total SFRD. In Casey et al. (2012a), for a sample of 767 Herschel-SPIRE selected galaxies (HSGs) at 250, 350, and 500 micron spectroscopically observed by Keck, the luminosity function and implied star-formation rate density contribution of HSGs at $z < 1.6$ are estimated and found overall agreement with work based on 24 μm extrapolations of the LIRG (Luminous IR Galaxies), ULIRG (Ultra-Luminous IR Galaxies) and total

infrared contributions (Casey et al., 2012b).The authors in Casey et al. (2012a) significantly increased the number of spectroscopically confirmed infrared-luminous galaxies at $z >> 0$ and demonstrates the growing importance of dusty starbursts for galaxy evolution studies and the build-up of stellar mass throughout cosmic time.

As it was mentioned before, theoretical models like Granato et al. (2004) predict that the star formation age is stopped due to the outflows from the active nuclei that eject the interstellar medium. However, in Harrison et al. (2012) the authors do not find strong evidence for suppressed star formation in $L_x > 10^{44}$ erg s^{-1} AGNs at $z \sim 1-3$, although Barthel et al. (2012) show symbiotic occurrence of star formation and black hole driven activity for three archetypal radio galaxies at redshifts 1.132, 1.575, and 2.474 with inferred star formation rates of hundreds of solar masses per year. The authors in Rodighiero et al. (2011) show the lesser importance of starburst in star formation at $z = 2$. Two main modes of star formation are known to control the growth of galaxies: a relatively steady one in disk-like galaxies, and a starburst mode in outliers from this steady sequence (see Elbaz et al. (2011) to know how to separate the starburst mode from a normal sequence). The authors show that starburst galaxies represent only 10% of the cosmic SFR density at $z \sim 2$. Only when limited to SFR > 1000 $M_\odot$/yr, these sources significantly contribute to the SFR density (46$\pm$ 20%).

The work Planck Collaboration et al. (2015f) is other example of a study of the early Universe. By using a novel method based on a component separation procedure using a combination of Planck and IRAS data, the authors try to select the most luminous cold submillimetre sources with spectral energy distributions peaking between 353 and 857 GHz at $5'$ resolution. A total number of 2151 Planck high-z source candidates (PHZ sources) were detected in the cleanest region of the sky, with flux density at 545 GHz above 500 mJy. Embedded in the CIB, their redshift is > 2. These objects can be divided in two populations: $\sim$3% of them were identified as strongly gravitationally lensed star-forming galaxies (prediction already done by Negrello et al. (2007)) and the rest appear as overdensities of dusty star-forming galaxies with $z > 2$ and may be considered as proto-cluster candidates. Therefore, this catalogue is complementary to the Planck Sunyaev-Zeldovich Catalogue (Planck Collaboration et al., 2014b) and may contain the progenitors of today's clusters. Hence the Planck List of High-redshift Source Candidates opens a new window on the study of the early ages of structure formation, and the understanding of the intensively star-forming phase at high-z.

The result shown in Planck Collaboration et al. (2015f) was confirmed by the *Herschel Space Observatory* of the ESA. In Planck Collaboration et al. (2015g), taken 234 sources distinguished by extreme brightness in the Planck all-sky submillimetre and millimetre maps (Planck Collaboration et al., 2014a) in the redshift range $z = 2 - 4$, about 97% are consistent with being overdensities of galaxies peaking at 350 μm or 500 μm whose photometric redshifts peak at $z \simeq 2$. The corresponding total star

formation rates could be $7 \times 10^3 M_{\odot}$ yr^{-1} per overdensity at $z > 2$. The remaining 3% are candidate lensed systems at redshifts $z > 2.2$.

As one can deduce, a correct detection of the point sources is a crucial task: the counts provide important information that allows us to study the evolution of these sources. The development of sophisticated tools to detect the point objects is growing and applied to the data. The goal of this Thesis is to use a mulitifilter (see section 2.9.1) that, taking into account multifrequency information, reduces the detection limit at the flux density. Of course, as it was said previously, there are more components than CMB and point sources, and a correct separation is needed. This is briefly discussed in the next section.

1.5 Component separation methods

As it was pointed out in the previous pages, when the sky is observed at these frequencies, we have several components contributing to the measured signal. In fact, this is a common problem in any observation. We have to separate the desired signal from other components that are always present and we have to remove. Obviously, the term 'signal' or 'noise' depends on our scientific goals. Scientists interested on the statistical analysis of the CMB want to obtain a CMB signal as clean as possible, using tools and methods that remove any other contribution to the total signal. By contrast, in this Thesis the interest is focused on the extragalactic point sources, considering as 'noise' the rest of components, even the CMB itself. There are many other scientists that study the distribution of the dust in the Galaxy, etc. And the devices developed to separate one signal from another will be, naturally, different, because different are the components to be studied (or removed).

Some of the techniques used for the separation of diffuse components are the following:

- **ILC**: Internal Linear Combination consists in a weighted linear combination of different frequency maps (very suitable in CMB experiments). It is easy to implement and we do not need any assumption about the physical foreground behaviour. The weight for each channel is calculated minimising the variance of the final combination.
- **ICA**: Independent Component Analysis assumes the signal is composed of different non-Gaussian statistically independent components. It is quite usual in CMB experiments that both the CMB and the instrumental noise are Gaussian. Since the instrumental noise can be only statistically characterised, the estimation of the CMB power spectrum is bias-corrected by an average level.

In practice, it is quite difficult to find a representation where the components are independent. Therefore, many procedures try to find representations where the components are as independent as possible. One of the methods based on ICA is the Spectral Matching of ICA (SMICA), selected by the *Planck* Collaboration, and that offers mutual decorrelation instead of independence, between components.

- **Maximum Entropy Method**: As we will see in the section 2.1, if we have a reasonable prior knowledge about the data, we can insert this information in our analysis. The Bayes' theorem provides a suitable framework in this case (see eq. 2.6). In this case, the estimator of a particular component is obtained by maximising the posterior probability. Or equivalently, by maximising the product of the likelihood and the prior (the numerator in the equation of the Bayes' theorem), since the evidence (the denominator) is a normalisation factor without any significance in the calculations. One particular example of this procedure is the Maximum Entropy Method (MEM, see Hobson and Lasenby (1998)), where the prior has the entropic form: $Pr(\mathbf{s}) \propto exp[\alpha S(\mathbf{s}, \mathbf{m})]$, being $\mathbf{s}$ the signal vector, $\mathbf{m}$ a model vector to which $\mathbf{s}$ defaults if there is not data, α a constant that depends on the scaling of the problem and S the cross-entropy of $\mathbf{s}$ and $\mathbf{m}$. And again, the goal is to estimate the components that maximise the product of the likelihood and the entropic prior.

The structure of the Thesis is as follows: in the Chapter 2 there is a brief introduction of filtering and detection methods commonly used in the detection of point sources. After that, there is a justification of the introduction of multifrequency filters, in particular the matched multifilter (MMF), the method used in this Thesis. In the Chapter 3 (Lanz et al., 2010), the MMF is checked by applying this tool in *Planck* simulated maps with point sources at frequencies closed at WMAP. The matched filter is also used in the same simulated maps to check the efficiency and robustness of the MMF. In the Chapter 4 (Lanz et al., 2013), the MMF is used in real WMAP 7-year data (channels V and W in a simultaneous way), covering the whole sky, verifying if the MMF improves another tools previously used to detect point sources. Then, there are shown some conclusions of the work done, just like some future and interesting prospects to be done with the MMF. Finally, a brief summary written in Spanish will be in the last chapter of this Thesis.

Chapter 2

Filtering and detection methods

In this chapter it will be discussed the detection problem and the devices and tools that one can usually find in order to help the detection process. But first of all, it is convenient to introduce some aspects related to the hypothesis test. The first question that emerges is: what is a hypothesis test? A hypothesis test is a statistical procedure whereby the veracity (or not) of a working hypothesis is validated. The hypotheses are usually asseverations about the characteristic of a population or several populations. Obviously, if a hypothesis can be rejected, there must be (at least one) other complementary and disjoint hypotheses in the case of be rejected the first one. Usually, the first hypothesis is called the *null hypothesis,* H_0, being the second the *alternative hypotheses,* $H_1, H_2, \ldots$. As it has been raised here, the hypothesis test is, in an intuitive way, something that is done almost everyday, and not only in the scientific context: if we think in a detective that has a set of clues, he or she must decide between several hypotheses according to those clues; the jury trial must decide between the innocence (null hypothesis by legal imperative) and the guilt (alternative hypothesis) of an accused person based on clues, statements, etc. Of course, science is (and *must* be) more rigorous and it is compulsory a systematic procedure, with tested statistical tools that allow the researcher to decide between the hypotheses. Hereinafter, in order to simplify, it will be considered the binary case with only two hypotheses: the null and the alternative hypotheses. Focusing our attention in the case of this Thesis, when a region of the sky is analysed, two hypotheses can be confronted: there is *not* any source in the map (null hypothesis) or, by contrast, there is at least one source (alternative hypothesis).

Once clarified what is a hypothesis, the next challenge for the researcher is to avoid as much as possible to make errors in the election of the hypothesis. Precisely, a *detector* is a rule that allows us to decide between the two hypotheses stated above (that is, there is a point source at a given point of the sky or not). Keeping in mind the goal of this Thesis, two are the possible errors than can be made in the test hypothesis: one could say that there is a source in the map (we choose the alternative

hypothesis, H_1) when this source is due to spurious effects: this kind of error is called *error of type I* or 'false positive' and it only depends on the statistics of the background and the detector chosen. By contrast, one can say that there is not any source in the map (we choose the null hypothesis, H_0) when actually there is a source (or more) in the same map: this is called *error of type II* or 'false negative'. The error of type I is directly related to the *reliability*, as will be explained below. Reliability tells us the percentage of real sources over the total number of detections. The error of type II is related to the *completeness*, because it tells us the number of dismissals we have: in the case of this Thesis, the number of real sources that we are not able to detect (above a given flux density, as explained below) and does not appear in our catalogue. This error depends on the statistics of the background, the detector chosen and the properties of the signal we want to detect. The probability of rejecting H_0 when it is actually true (i.e., the probability of making the error of type I) is usually denoted by α and $1-\alpha$ is the significance level. On the other side, the probability of accepting the null hypothesis when it is actually wrong is usually denoted by β. Therefore, $1-\beta$ is the probability of rejecting the null hypothesis when it is wrong, or equivalently, the probability of accepting the alternative hypothesis when it is true, the testing power.

Once the null hypothesis is formulated, it is necessary to have strong evidences against it if finally is rejected. Therefore, first of all is necessary to establish an interval where it is normal to have variations due to random effects. This region is so-called the *acceptance region* and the null hypothesis is not rejected inside this region: at this point it must be clarified one aspect, *not to reject the null hypothesis is not equivalent to accept it*. If these variations are larger, they could fall outside this acceptance region and we must reject the null hypothesis, accepting the alternative one. This region is so-called the *rejection region*. How large are these regions will depend on the value of α we choose.

In the figure 2.1 we can see two different situations. In the first of both, we can see the rejection region is formed by two disjoint areas located in the tails. This occurs when the null hypothesis is type $\mu = k$ and the alternative hypothesis is, therefore, $\mu \neq k$. This kind of tests are called *bilateral* or *two-tailed*. The second one presents a rejection region that is only in one side (in this figure it is on the right, but the discussion of this paragraph is completely symmetric if the rejection region was on the left). This case corresponds when null hypothesis is type $\mu \geq (\leq) k$, and therefore, the alternative hypothesis is $\mu < (>) k$. This kind of tests are called *unilateral* or *one-tailed*.

It has been introduced the hypothesis test, the acceptance and rejection regions and the possible errors we can make. Obviously, it would be desirable to reduce as much as possible both types of errors. But it is difficult, or even impossible, to achieve this goal, as one can see in the figure 2.2. In this figure we observe two distributions: the one at the left with a mean value μ equal to zero and the second one in the right with different values for μ. The purple tails of the distribution on the left represents

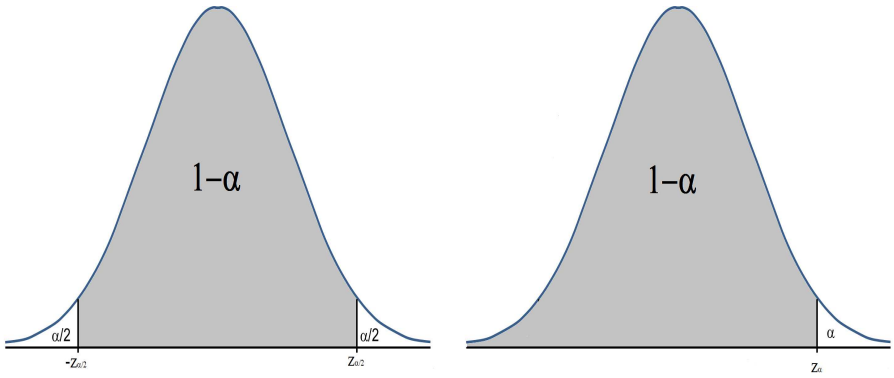

Figure 2.1 - Figure where they are shown the acceptance (grey areas) and rejection regions for an arbitrary value of α and for a bilateral test (left) and a right-sided unilateral test (right).

the intervals where the null hypothesis is rejected, being the rest of the area those values for which the null hypothesis is accepted. At the same time, we see the distribution on the right: this distribution has two different values for μ, and depending on these values and α, the area of β will increase or decrease (red areas), or in other words, the probability of choosing the null hypothesis when it is false will increase. As, in principle, we are not able to know the real value of μ, a crucial aspect is to develop some tools that allow us to decrease as much as possible the red areas. As we will see below, in the context of point source detection, filters are suitable tools that help us separating both distributions and therefore, reducing the red areas. Only to clarify this point, filters reduce the noise level or increase the signal, narrowing the distribution on the left. As will be seen below, this Thesis deals with this problem, developing and adapting a multifrequency tool that improves this characteristic.

Once seen that is impossible to eradicate the two types of errors at the same time, one can wonder which one is more tolerable in the sense that is less damaging for our scientific goals. Obviously, not all the scientists search the same goals, therefore some of them would desire eradicate the sources of one type of error and another scientists avoid the other type. Focusing again in the point source detection framework, one could think in the scientist that studies and analyses the statistical properties of the CMB. As was commented in the section 1.4, point sources are the most disturbing contaminants at low angular scales (or high values of ℓ). For this reason it is desirable to detect the higher number of point sources and discard the corresponding pixels from the statistical analysis. It is even better to allow the entrance of spurious objects in the catalogue and eliminate the corresponding pixels than to analyse the sky with real objects that have not been removed. There are many other regions in the sky that are masked or discarded from the analysis, like the Galactic plane, and subsequently it is not important to remove some pixels corresponding to spurious sources.

By contrast, we could find the scientist that wants to study the sources themselves and use a cata-

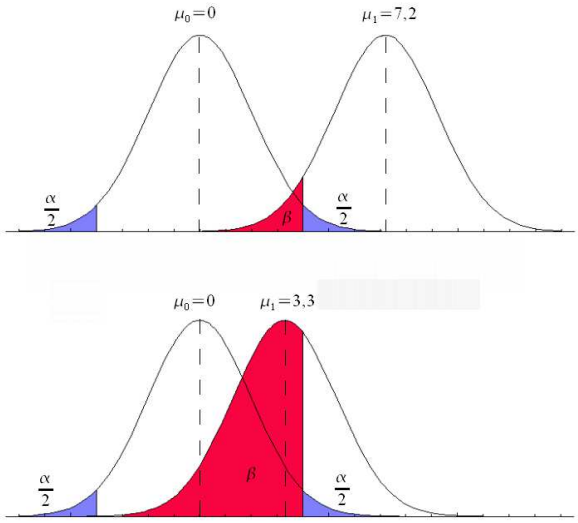

Figure 2.2 - Representation of the possible values to have an error of type II (red areas) for a given parameter μ. The closer is the distribution on the right to the supposed value under the null hypothesis, the higher is the probability to have this kind of error (false negative).

logue with a set of sources with their positions and flux densities as a reference. He needs a catalogue whose reliability is as high as possible because when he or she applies for observation time, he cannot waste the time observing regions in the sky where there is not any real object. In this case, reliability is much more important than completeness.

Until here, we have briefly seen what is a test hypothesis, the main types of errors we can make and the acceptance (and rejection) regions. The hypothesis tests can be divided in two groups: the **parametric** and the **non parametric** tests. The parametric tests validates a hypothesis that concerns a parameter of the distribution of a random variable, such as the mean value. As an example, we could say that the mean height of a population is 175 cm. Then, we could calculate the mean height of a sample of this population and say if the value of 175 cm is true or not (at a given significance level): this is a parametric test. The non-parametric tests, by contrast, does not tell anything about a particular parameter but a statistical characteristic of the distribution of a random variable.

Now, it would be time to make the test. Usually, we have a sample and we want to compare it with respect to a known population. The first step would be to establish the null and the alternative hypotheses, mutually exclusive. After that, it is necessary to know what type of test we have (unilateral or bilateral) and fix the acceptance and rejection regions from the significance level. Depending on the

chosen significance level, our acceptance region will increase or reduce. Finally, we choose a statistic (random variable with known probability distribution) whose values for the sample to be tested allow us to determine if the null hypothesis is accepted.

(Press et al., 1992a) shows in some of their chapters many hypotheses tests and their implementation in the corresponding programming language. Some of the most commons parametric tests are:

- Z-test: one of the most common between the parametric tests is the Z-test, test for which the distribution of the statistic can be approximated by a normal function under the null hypothesis. Because of the central limit theorem, many statistics are approximated by a normal distribution for large samples. The expression for this statistic and the rejection regions for bilateral and unilateral tests are the following:

$$\begin{gathered} z = \frac{\bar{x}-\mu_0}{\sigma/\sqrt{n}}; \\ z_{exp} \leq -z_{\alpha/2} \text{ or } z_{exp} \geq z_{\alpha/2} \text{ (bilateral test)}, \\ z_{exp} \leq -z_{\alpha} \text{ or } z_{exp} \geq z_{\alpha} \text{ (unilateral tests)}, \end{gathered} \tag{2.1}$$

  where $\bar{x}$ is the sample mean, μ_0 is the hypothesised population mean, σ is the (known) population standard deviation, n the sample size, z_{exp} the experimental value of the statistic and $z_{\alpha's}$ the theoretical values of the statistic that define the acceptance region. z is the distance to the mean in relation to the standard deviation.

- t-test: if the variance is unknown, the z-test is substituted by the *t-test*, where the *known* population standard deviation (see eq. 2.1), σ, is substituted by the *calculated* standard deviation of the sample. Here, the distribution that follows the statistic if the null hypothesis is true is the Student's t-distribution. The number of degrees of freedom is $n-1$. The rejection criteria are the same that before, taking into account the changes here commented.

- χ^2-test for the variance: in this case, the distribution of the statistic is the χ^2 distribution. The statistic and rejection criteria (for bilateral and unilateral tests) are the following:

$$\begin{gathered} \chi^2 = (n-1)\frac{s^2}{\sigma_0^2}; \\ \chi^2_{exp} \leq \chi^2_{1-\alpha/2;n-1} \text{ or } \chi^2_{exp} \geq \chi^2_{\alpha/2;n-1} \text{ (bilateral test)}, \\ \chi^2_{exp} \geq \chi^2_{\alpha;n-1} \text{ or } \chi^2_{exp} \leq \chi^2_{1-\alpha;n-1} \text{ (unilateral tests)}, \end{gathered} \tag{2.2}$$

  where n is the sample size, s^2 is the standard deviation of the sample and σ_0^2 is the known variance of the population. χ^2_{exp} is the experimental value of the statistic and $z_{\alpha's;n-1}$ the theoretical values of the statistic that define the acceptance region. As we can see in the expression

above written, the statistic gives us an idea about the ratio between both variances (the one of the sample and the population) times the degrees of freedom ($n-1$).

The tests above explained contrast a parameter of a sample with respect to a population. If we want to compare two samples it is possible to extrapolate them, as well as new tests appear. One of the most know is the *F-test*, used to contrast the variances of two samples. The statistic used in the text and the rejection criteria are:

$$\begin{gathered} F = \frac{s_1^2}{s_2^2}; \\ F_{exp}^2 \leq F_{1-\alpha/2;n_1+n_2-2}^2 \text{ or } F_{exp}^2 \geq F_{\alpha/2;n_1+n_2-2}^2 \text{ (bilateral test)}, \\ F_{exp}^2 \geq F_{\alpha;n_1+n_2-2}^2 \text{ or } F_{exp}^2 \leq F_{1-\alpha;n_1+n_2-2}^2 \text{ (unilateral tests)}, \end{gathered} \tag{2.3}$$

where n_i is the size of the sample i, s_i^2 is the standard deviation of the sample i. F_{exp}^2 is the experimental value of the statistic and $F_{\alpha's;n_1+n_2-2}$ the theoretical values of the statistic that define the acceptance region. As we can see in the expression above written, the statistic is the ratio between both variances and follows the F probability distribution.

Finally, in order to finish this brief (and incomplete) summary of hypothesis tests, it is introduced a non-parametric one: the *Mann-Whitney U-test*, applied over two independent samples. It is contrasted the equality of both samples. Let us suppose n_1 and n_2 the sizes of both samples. The observations are ordered in only one serie, specifying the original sample. From here, the quantities U_1 and U_2 can be easily obtained:

$$\begin{aligned} U_1 &= n_1 n_2 \frac{n_1(n_1+1)}{2} - r_1, \\ U_2 &= n_1 n_2 \frac{n_2(n_2+1)}{2} - r_2, \end{aligned} \tag{2.4}$$

where r_1 and r_2 are the sum of the ranks of both samples. The statistic $U = min(U_1, U_2)$ is compared to the value $U(n_1, n_2, \alpha)$, perfectly tabulated. Finally, the null hypothesis (both samples come from the same population) will not be rejected if $U < U(n_1, n_2, \alpha)$ and rejected otherwise.

Another non-parametric test that is widely known and used is the *Kolmogorov-Smirnov (K-S) test*. It contrasts if a sample of data come from a given distribution. The K-S statistic quantifies the distance between the empirical distribution function of the sample and the cumulative distributive function of the reference distribution. The null hypothesis is that our sample follows the reference distribution. The expression for the statistic is the following:

$$D_n = sup|F_n(x) - F(x)|, \tag{2.5}$$

where F_n and F are the empirical and the cumulative distributive functions, respectively. D_n is the supreme of the set of distances. The null hypothesis will be rejected if $D_n > D_\alpha$, where D_α depends on the significance level previously chosen. With some variations, the K-S test serves as a goodness of fit test.

In order to clarify all the concepts introduced until here in this chapter about the hypothesis test, let us imagine a simple example: in a given food for children it is specified that the average protein content is at least 42%. In order to verify this asseveration, 10 of these foods are analysed, obtaining a mean value equal to 40% with a standard deviation of 3.5%. Can we say that the specifications are correct taking into account the chosen sample at a significance level of 0.05 and supposing a normal distribution for the protein content? First of all, both hypotheses must be established:

- null hypothesis, H_0: the sample mean is equal to the specified for the food ($H_0 : \mu \geq 42\%$).
- Alternative hypothesis, H_1: the sample mean is different to the specified for the food ($H_1 : \mu < 42\%$).

In this example, mean values are checked and the variance of the normal distribution is unknown. Therefore, it is used the parametric t-test. $n = 10$, $\bar{x} = 40$ and $s = 3.5$. The statistic is: $t_{n-1} = (\bar{x} - \mu_0)/s/\sqrt{n}$. The experimental value of $t = -1.81$. Meanwhile, the corresponding value of t at the chosen significance level is $-t_{0.05;9} = -1.833$. Therefore, the null hypothesis is not rejected and the specifications for the protein content of the food are accepted.

Until here, some aspects about the hypothesis tests and the decision between hypotheses have been shown. Hereinafter, the discussion will be centred in the goal of this work: the detection of compact objects. In this context, we could establish the null hypothesis as follows: *There is not any source in the map*. The alternative hypothesis would say the opposite. But as commented before, in most of cases it is required a previous step that makes easier the final decision between hypotheses. Focusing in the case of point source detection, we usually observe in the same region of the sky several components that are mixed and where these sources are embedded in. And excepting the most bright sources, most of them are difficult or impossible to detect them directly from the data. Several tools have been developed in order to favour the posterior detection of point sources (many of them linear filters): the Mexican Hat Wavelet, the matched filter, the scale-adaptive filter, Bayesian approaches, etc. Some of them will be introduced in the next paragraphs. Our statistics will be the value of the filtered field at a given pixel and we have a right-sided tailed unilateral test. By analogy with the previously seen hypothesis tests, we establish our acceptance region for values of the filtered field below 5σ, being σ the standard deviation of the filtered field. As it will be see below, this kind of detector is a *thresholding* detector

because it separates the acceptance and rejection regions in function of the value of the intensity at each pixel.

Regarding the detection of compact objects, three statistical figures of merit are mainly considered: *reliability*, *accuracy* and *completeness*. Reliability and completeness have been already outlined before in this same chapter. Let us see briefly what are each one in a more rigorous way. Reliability (for a given detection criterion) can be defined as $R = 1 - n_e/(n_d + n_e)$, where n_e is the number of spurious detections and n_d is the number of true positives. According to this definition, if we do not have any spurious detection, $R = 1$, it means is completely reliable. By contrast, if all our detections are false (spurious), $R = 0$ and we do not have any real detection.

Completeness is the ratio, for a given detection criterion, between the true detected objects over the total number of real objects: $C = n_d/(n_d + n_m)$, where n_d, as before, is the number of true positives and n_m is the real objects NOT detected, missed by the catalogue. If we have a catalogue with a completeness of 0.99 over 0.5 Jy, it means 99% of the sources > 0.5 Jy are in our catalogue. Of course, this implies that one per cent of the real sources are not detected.

Accuracy refers to the goodness of the estimation of the intensity/flux (integrated intensity) of the sources that have been detected.

The ideal situation is to achieve good values for these three estimators. But as explained before, the real world is not as ideal as we would desire and we must find a compromise between them according to our goals.

At this point it is necessary to establish more clearly the difference, before outlined, between *filtering* and *detection* because they are intrinsically linked but are not the same. A filter is a device that selects in any way the frequencies which we are interested on. On the other hand, detection is a rule that we establish and that allows us to decide if there is a source or not. Strictly speaking, we can try to detect an object without any previous prefiltering step. However, filtering without the detection step has not so much sense. In many cases both are complementary and usually filtering is used to 'help' the detector to decide about the presence of sources, in particular when the sources are too faint to be detected directly from the data. In this case, it is necessary the previous filtering step to reduce the fluctuations of the noise and make easier the detection process. When there is a source with known profile and amplitude embedded in a Gaussian noise, it can be demonstrated that the optimal detector is a thresholding over a linear combination of the data that is the matched filter (see section 2.5). In general, even if the amplitude is unknown, the matched filter works as filter and detector.

Of course, the degree of difficulty of the detection is directly related to our statistical knowledge of the signal and the noise. If we know the pdf's (probability density functions) of both, we would

be able to develop a detector with better performance than if some of the pdf's are unknown, or very difficult to deal with them. Some assumptions about the signal and the noise have to be made, and if these assumptions were wrong (or not very close to reality), our results in terms of reliability, accuracy, etc, may be disastrous. By contrast, detectors with not very strong assumptions about the noise and the signal can be distant from the optimal detector, but are very robust against our poor knowledge of the pdf's. If we were in descending order from the methods that use more information about the noise and the signal to those that make less assumptions about the data, we will start with the Bayesian framework, optimal if we know perfectly the statistical behaviour of the noise and the signal. Posterior simplifications (it means loss of statistical information) will translate into loss of ideality but in practice gain of robustness against possible dangerous assumptions about the background and/or the signal. For example, the drop of the a priori knowledge of the n-PDF of the sources will lead to Neyman-Pearson detectors. Then the relax of the n-pdf of the background and trying to characterise it in terms of its second order statistics will lead to the well known matched filter. If we also drop any knowledge about the covariance matrix of the background, dealing with only the dispersion of the $1-$pdf of the background, this will lead to the use of band-pass filters with fixed waveform like the wavelets. For more details of this discussion see Herranz and Vielva (2010).

The next sections in this chapter will be distributed as follows: the starting point will be the Bayesian techniques, then the Neyma-Pearson rule will be introduced, and the filtering techniques will finish this chapter, remarking the necessity of introducing a new method: the *matched multifilter* (MMF). As one can see, the order goes from the optimal devices (optimal if we know perfectly the statistical behaviour of the noise and the signal) like the Bayesian tools, until the filtering methods, more distant from this optimality, but more robust in the sense of variations of changes in he statistical properties of the signal and/or the noise.

2.1 Bayesian approaches

Bayesian techniques provide a natural way to take into account the available information about the statistical distribution of both the sources and the noise. Until now, unfortunately, there are not so many works that deal with this problem into the Bayesian framework. Basically, two have been the reasons of this lack: the poor knowledge we had about the statistical properties of the extragalactic sources at sub-mm frequency range. On the other hand, mapping the posterior probability density of the sources (see eq. 2.6) is often a very expensive task from a computational point of view.

In the last years, with the advent of experiments that cover the whole sky in the sub-mm frequency range, our knowledge about the extragalactic sources is growing day by day. Respect

to the second point, (Argüeso et al., 2011a) propose a procedure, in contraposition to others like (Hobson and McLachlan, 2003; Carvalho et al., 2009, 2012), that is more simple. First of all, in order to introduce the Bayesian framework to the reader, let us write the Bayes' theorem that encourages this methodology:

$$P(\theta|D) \propto P(D|\theta)P(\theta), \tag{2.6}$$

where $P(\theta|D)$ is the *posterior*, $P(D|\theta)$ is the *likelihood* and $P(\theta)$ is the *prior*. In terms of probability, the posterior is the probability of getting the model, θ (in our case it could be the position, the amplitude, etc. of the point sources) given the data, D. The likelihood represents the probability of getting the data given the model. And the prior the probability of getting the model.

Different strategies are used in the Bayes' theorem framework in order to detect point sources. One could maximise the posterior distribution to locate the sources in the map and their flux densities. It is quite simple and for this reason reasonably easy to implement making some assumptions. But one could try to obtain the whole distribution of probability, allowing us to get more information like expected values, marginalise over variables, . . . This section will be subsequently divided in two parts: the first one will refer to Maximum a posteriori methods, taking as example Argüeso et al. (2011a). The second part will be dedicated to full samplers methods like the Powell Snakes (Carvalho et al., 2009, 2012).

2.1.1 Maximum a posteriori methods

If the data set is a discrete map of N_{pix} pixels, we can write the following expression:

$$\mathbf{y} = \tau\mathbf{a} + \mathbf{n}, \tag{2.7}$$

where τ is an $N_{pix} \times N$ matrix (being N the number of sources) whose columns are the lexicographically ordered versions of N replicas of the map of the beam pattern, (in vector form), each shifted on one of the source locations; $\mathbf{n}$ is the lexicographically ordered versions of the discrete maps of the generalised noise [1] (in vector form); $\mathbf{a}$ is the $N-$vector containing the fluxes of the sources. Therefore, $\mathbf{y}$ is the lexicographically ordered version of the discrete map (in vector form as well).

The unknowns are the source locations (included in the matrix τ), their fluxes (included in the vector $\mathbf{a}$) and the number of sources, N. At this point one can define $\mathbf{R}$ as the $N \times 2$ matrix containing

[1] In this Thesis, and if it does not say otherwise, the *generalised noise* is everything that is not the signal (point sources) like the foregrounds, the CMB, the instrumental noise, etc.

the locations of the sources.

By the Bayes' theorem (see eq. 2.6), the posterior distribution that is looked for can be expressed as follows:

$$p(N, \mathbf{R}, \mathbf{a}|\mathbf{y}) \propto p(\mathbf{y}|N, \mathbf{R}, \mathbf{a})p(N, \mathbf{R}, \mathbf{a}). \tag{2.8}$$

It is pretty clear that, known N, $\mathbf{R}$ and $\mathbf{a}$ are independent on it. Hence, the prior can be factorised in this way:

$$p(N, \mathbf{R}, \mathbf{a}) = p(\mathbf{R}, \mathbf{a}|N)p(N) = p(\mathbf{R}|N)p(\mathbf{a}|N)p(N). \tag{2.9}$$

Now, one can write explicitly the expressions for the different terms of the prior:

$$\begin{aligned} p(\mathbf{R}|N) &= \tfrac{N!(N_{pix}-N)!}{N_{pix}!}; \\ p(\mathbf{a}|N) &\propto \prod_{\alpha=1}^{N} \left[1 + \left(\frac{a_\alpha}{a_0}\right)^p\right]^{-\frac{\gamma}{p}}; \\ p(N) &= \tfrac{\lambda^N e^{-\lambda}}{N!}. \end{aligned} \tag{2.10}$$

The first equation takes into account the number of possible distinct lists of N locations in a discrete $N_{pix}-$pixel map. The second one shows (being p a positive number), in a phenomenological way, the power law behaviour of the strong sources with exponent γ and the uniform distribution of the weak sources, separated by a flux a_0 and a conditional prior with the form of the generalised Cauchy distribution (Rider, 1957). Finally, the third term is the Poisson distribution, with λ is the expected number of sources in the map.

Keeping in mind the expression 2.8, the likelihood function derives from the physics associated to the data model. In the mentioned paper of Argüeso et al. (2011a), the authors assumed that the generalised noise ($\mathbf{n}$ in eq. 2.7) is a Gaussian random field with mean equal to zero at a given covariance matrix, $\mathbf{C}$. This is only true if the only terms taken into account are the CMB and the instrumental noise, excluding other foregrounds because they have been removed by using component separation methods, for example (see section1.5). The likelihood can be expressed as:

$$p(\mathbf{y}|N, \mathbf{R}, \mathbf{a}) \propto exp[-\frac{(\mathbf{y} - \tau\mathbf{a})^t \mathbf{C}^{-1} (\mathbf{y} - \tau\mathbf{a})}{2}]. \tag{2.11}$$

With the prior and the likelihood characterised, there is only one step to make: to calculate the posterior by multiplying both the prior and the likelihood and find the values of $\mathbf{R}, \mathbf{a}$ and N that maximise the posterior. The eq. (12) of Argüeso et al. (2011a) is the negative log-posterior that results from

multiplying the three priors and the likelihood above mentioned. In the paper, the authors minimise this negative log-posterior with respect to the fluxes to estimate them. It is shown the detected sources must be in the peaks of the matched filtered maps, that appear naturally in the process. And finally, the authors choose the number of sources that minimise the negative log-posterior for the estimated fluxes previously obtained. The authors carry out simulations of Planck between 30 and 100 GHz, only with CMB and point sources and compare their method with the matched filter with a 5σ threshold (see section 2.2). In general, they obtain better levels of completeness with the Bayesian approach and no spurious sources from 0.7, 0.8, 0.55 and 0.3 Jy at 30, 44, 70 and 100 GHz respectively.

2.1.2 Full samplers: Powell Snakes as example

Carvalho et al. (2009) deals with the problem of extragalactic point source detection from a a Bayesian point of view as well. The starting point is obviously the Bayes' theorem (see eq. 2.6). The unknowns are again the position, the flux and the size of each source. The prior is factorised in four terms (one for each unknown), which is equivalent to say any of these quantities is independent of each other. The authors assume uniform distributions for all the priors, although the authors themselves say in the paper this assumption is not realistic for the flux and the size and was taken into account in a posterior work (Carvalho et al., 2012).

The authors assume the same statistical properties for the background that Argüeso et al. (2011a), therefore the likelihood is the same, but they re-write the log-likelihood in such a way that the computational cost is considerably reduced (see section 3.3 from Carvalho et al. (2009)).

The approach used in that work consists of launching a set of downhill minimisations in order to detect the local maxima (not the global maximum) in the posterior. The end-point of each minimisation will be a local maximum in the posterior, giving the optimal parameters for the detected object. A Gaussian approximation will be used around the peak and the detection is accepted or rejected according to an evidence criterion (see section 2.2):

$$\rho \equiv \frac{Pr(H_1|\mathbf{y})}{Pr(H_0|\mathbf{y})} > 1, \tag{2.12}$$

where the objects are randomly Poissonian distributed and assumed a criterion of 'symmetric loss': an undetected source is as bad as a spurious source.

If the detection is positive, the source is subtracted from the map before the next minimisation.

The first step is to pre-filter the map with a matched filter (that will be introduced in section 2.5). As the authors show, this filter appears as a result of maximising the posterior respect to the flux. Also,

as they remark, if the size of the sources is considered constant, in this scenario the matched filter is enough to locate the sources. Taking the size of the sources as an unknown, this pre-filtering (using a mean value for the size of the sources) is used in order to estimate the positions of the maxima, similarly to Argüeso et al. (2011a).

Once done this pre-filtering step, a 2-dimensional downhill minimisations using the Powell algorithm (Press et al., 1992b) are launched in the space of the positions. The starting points are the obtained in the previous step. The next step consists on searching in the full parameter space the maxima (performing a Gaussian approximation in each peak) by using as starting points the obtained in the previous step.

As the author themselves said in Carvalho et al. (2009), they kept in mind an upgrade of the Powell-Snakes method, improving the performance. The authors establish the following detection criterion $ln\left[\frac{Pr(H_1|\mathbf{y})}{Pr(H_0|\mathbf{y})}\right] \underset{H_0}{\overset{H_1}{\gtrless}} \xi$ (it can be demonstrated that is optimal in the binary case), with $\xi \equiv ln\frac{L_{10}}{L_{01}}$, being L_{ij} the loss associated to choose H_i when H_j is true (loss function simply maps the "mistakes" in our estimations/selections, thereby defining the penalty one incurs when making wrong elections). Then, more realistic priors are written (see section 3.3 from Carvalho et al. (2012)), using different ones in the source detection step that in the source estimation step. When it is necessary to calculate the equation above written, and in order to simplify the calculations, two assumptions are made: the sources are sufficiently separated and the variables of each source are mutually independent. In this case, we are allowed to make a single source approach and simplify the likelihood. Two additional considerations must be taken into account that move away the method from the optimality: the non-Gaussianity and the statistical inhomogeneity of the background. The solutions to these problems are the multi-frequency (to combine as much data as possible, i. e., doing a multi-channel analysis all the time) and the multi-model (more than one type of source), respectively. It is pertinent to say that, according to the authors themselves, the implementation of this method, as explained in their paper, is not yet completely finished.

It is worth remarking that the matched multifilter (see section 2.9.1) appears naturally in the process if the likelihood is maximised with respect to source amplitudes when they are enough separate from each other.

Summarising, Bayesian approaches search techniques that maximise or characterise in an effective and not very expensive (from a computational point of view) way the posterior distribution. Previously, we must do some assumptions about the statistical properties of the noise (likelihood) or the signal (prior). Depending on our prior knowledge of these two distributions, our Bayesian approach will be

suitable for the detection problem or not.

2.2 Neyman-Pearson and thresholding detectors

2.2.1 Thresholding

One of the most common detector used in Astronomy is the *thresholding*: taking into account all the possible values of the intensity, we divide them into two subspaces: those which are above an arbitrary value of the intensity and the rest. We say we have a detection in the first case, when a detection due to a statistical fluctuation of the background is very improbable. How improbable it is depends on the value of the threshold we choose. Usually, this threshold is expressed in terms of the standard deviation of the background, 5σ, maybe the most used threshold used, that has a pretty clear significance in Gaussian fields, since the probability of detecting an event due to a statistical fluctuation of the background is ~ 1 in 2 millions. Taking into account only linear filters, one could wonder which is the optimal filter. For the thresholding, the answer is the matched filter. As it was shown, this filter is the one that maximises the signal to noise ratio, reducing as much as possible the fluctuations of the noise and allowing an easier detection of the objects embedded in it. Thresholding will be the detector used in this Thesis.

2.2.2 Neyman-Pearson rule

Obviously, the thresholding is not the only possible detector. Thresholding only takes into account the possibility of having a source if the intensity in a point is above the pre-established threshold (as it was said, usually in terms of the σ of the noise), but there is much available information that could be used to increase the chance of detect sources in some particular situations. For example, information about the shape of the sources, their intensities and locations, possible clustering, etc, could be inserted in order to detect objects.

Implicitly, filtering usually introduces some *spatial* information (*spatial* means real space, by contrast with the Fourier space): as it will be seen in the next section, matched filter takes into account the shape of the sources; the Mexican Hat Wavelet uses the scale of the object, etc. Let us describe the Neyman-Pearson decision rule:

$$L(x_i) = \frac{p(x_i|H_1)}{p(x_i|H_0)} \geq L_*, \tag{2.13}$$

where $L(x_i)$ is the likelihood ratio, $p(x_i|H_0)$ pdf associated to the null hypothesis and $p(x_i|H_1)$ is

the pdf associated to the alternative hypothesis. x_i are a set of variables measured from the data (amplitude, curvature, etc). L_* is an arbitrary constant, defining the region of acceptance and fixed with some criterion. As it can be proved, given these likelihoods, the test statistics defined by this rule has the maximum power for a fixed value of the probability of false alarms. As a note added, a possible way to increase the power of the test is to add information by increasing the number of observable variables and to modify the likelihoods above expressed in the likelihood ratio, by means of some signal processing in order to make easier the discrimination between them.

Peak statistics

Returning to the discussion, let us assume, for simplicity, a 1D situation, with a Gaussian background [2] represented by a random field $\zeta(x)$ with mean equal to zero and power spectrum $P(q)$ ($\langle\zeta(\mathbf{q})\zeta^*(\mathbf{q}')\rangle = P(q)\delta_D(q-q')$). The distribution of maxima was studied by Rice (1954). The expected number of maxima per intervals $(x, x+dx)$, $(\nu, \nu+d\nu)$ and $(\kappa, \kappa+d\kappa)$ is:

$$n_b(\nu,\kappa) = \frac{n_b\kappa}{\sqrt{2\pi(1-\rho^2)}} e^{-\frac{\nu^2+\kappa^2-2\rho\nu\kappa}{2(1-\rho^2)}}, \tag{2.14}$$

where n_b is the expected total number density of maxima

$$n_b = \frac{1}{2\pi\theta_m}, \nu = \frac{\zeta}{\sigma_0}, \kappa = \frac{-\zeta''}{\sigma_2}, \theta_m = \frac{\sigma_1}{\sigma_2}, \rho = \frac{\sigma_1^2}{\sigma_0\sigma_2} = \frac{\theta_m}{\theta_c}, \theta_c = \frac{\sigma_0}{\sigma_1}, \tag{2.15}$$

where $\nu \in (-\infty, \infty)$ and $\kappa \in [0, \infty)$ are the normalised field and the curvature, respectively; σ_n^2 is the moment of order $2n$ associated to the field; θ_c, θ_m are the coherence scale of the field and maxima, respectively.

At this point, let us suppose a Gaussian source (this situation is very usual when the angular size of the object is smaller than the beam and the beam profile is Gaussian), whose profile is given by $\tau(x) = exp(-x^2/2R_0^2)$, being R_0 the beam width, and embedded in the previous background. In this case, the expected number density of maxima per intervals $(x, x+dx)$, $(\nu, \nu+d\nu)$ and $(\kappa, \kappa+d\kappa)$ (with a source of amplitude A) is given by Barreiro et al. (2003):

$$n(\nu,\kappa|\nu_s) = \frac{n_b\kappa}{\sqrt{2\pi(1-\rho^2)}} e^{-\frac{(\nu-\nu_s)^2+(\kappa-\kappa_s)^2-2\rho(\nu-\nu_s)(\kappa-\kappa_s)}{2(1-\rho^2)}}, \tag{2.16}$$

[2] In the rest of this Thesis, the noise is denoted by n. In this particular section, it is denoted by ζ because the number densities are denoted by n.

where $\nu \in (-\infty, \infty)$ and $\kappa \in [0, \infty)$, $\nu_s = A/\sigma_0$ is the normalised amplitude of the source; and $\kappa_s = -A\tau''_\phi/\sigma_2$ is the normalised curvature of the filtered source.

The detection problem

Now, let us consider a local peak in the $1D$ data set characterised by (ν_s, κ_s). $H_0 : n.d.f.n_b(\nu, \kappa)$ represents the null hypothesis, and $H_1 : n.d.f.n(\nu, \kappa)$ the alternative hypothesis, i.e. the local number density of maxima when there is a compact source:

$$n(\nu, \kappa) = \int_0^\infty d\nu_s \, p(\nu_s) n(\nu, \kappa | \nu_s). \tag{2.17}$$

A Bayesian approach has been assumed: at a concrete pixel we get the number of source detections weighting with the *a priori* probability, $p(\nu_s)$, if the sources are Poissonian spatially distributed.

Therefore, we can establish the following number densities to any rejection region $R_*(\nu, \kappa)$:

$$n_b^* = \int_{R_*} d\nu \, d\kappa \, n_b(\nu, \kappa), n^* = \int_{R_*} d\nu \, d\kappa \, n(\nu, \kappa), \tag{2.18}$$

where n_b^* is the number density of spurious sources (due to the fluctuations of the background) expected inside the region $R_*(\nu, \kappa)$, the rejection region (by contrast with R_-, the region where we do not find any source); whereas n^* is the number density of maxima expected in the same region of the (ν, κ) space in the presence of a local source.

At this point it is assumed a Bayesian Neyman-Pearson decision rule, using number densities instead of probabilities: the rejection region (it is rejected the null hypothesis that says there is not any source) R_* is given by the highest number density of detections n^* for a given number density of spurious detections n_b^*. Such a region is (criterion for detection):

$$L(\nu, \kappa) = \frac{n(\nu, \kappa)}{n_b(\nu, \kappa)} \geq L_*, \tag{2.19}$$

where L_* is a constant and $L(\nu, \kappa)$ defines the detector: if $L \geq L_*$ we decide a signal is present; if $L < L_*$ we decide there is not signal. It is remarkable to point out that the region of acceptance is completely equivalent to the usual given by the standard Neyman-Pearson test in terms of probabilities:

$$\frac{p(\nu, \kappa)}{p_b(\nu, \kappa)} \geq L'_*, \tag{2.20}$$

where $p_b(\nu,\kappa)$ and $p(\nu,\kappa)$ are the pdf's associated to the number densities to $n_b(\nu,\kappa)$ and $n(\nu,\kappa)$, respectively, and L'_* must be found, in order to compare different filters, by fixing the number density of spurious sources in the region of acceptance.

2.3 Filtering methods

From a colloquial point of view, 'filtering' means basically selection. When someone says that something has been previously filtered, it means that has been selected from a larger set, following some kind of criterion. Filters 'selects' in some way the desirable frequency in order to favour the detection. In the case of point source extraction, filtering is probably one the most used due to the fact that these sources have a characteristic angular size that makes suitable the use of filters to detect them because the size in the real space translates into a well known frequency (frequency as the opposite of the real space) that filter will use to select it. Therefore, if we consider a system with an input and an output, a filter is a device that selects in a proper way the signal that we want in the output. From a mathematical point of view a filter can be written as an operator:

$$L : f(x) \rightarrow g(x) = Lf(x), \tag{2.21}$$

where f is the input, g is the output, L represents the filter and x is the independent variable. Therefore, in our case, a filter is an operator that applied over the data (that contains not only our signal, the point sources in our case, but also another components like the CMB, another diffuse components, most of them are Galactic, and noise) maximises the signal to noise ratio (SNR, defined as the ratio between the maximum value of the signal and the variance of the field) of our point sources in the output. The filter is linear if the output is a linear functional of the inputs, and it is homogeneous if the output is delayed by υ when the input is delayed by the same value, $g(x-\upsilon) = L(f(x-\upsilon))$. The homogeneity is a suitable property of the filter. Let us consider the Dirac distribution δ. If f is continuous, its value at x is:

$$f(x) = \int f(u)\delta(x-u)du. \tag{2.22}$$

The continuity and linearity of L imply:

$$Lf(x) = \int f(u)L\delta(x-u)du. \tag{2.23}$$

If we say that $h(x) = L\delta(x)$, being h the impulse response of L, due to the homogeneity of the operator it can be said:

$$Lf(x) = \int f(u)h(x-u)du = \int h(u)f(x-u)du = h \otimes f(x), \tag{2.24}$$

where $\otimes$ denotes convolution. Therefore, this equation means that a homogeneous and linear filter is equivalent to a convolution with the impulse response h. This property is very useful because we can use the convolution theorem and obtain that:

$$Lf(x) = g(x) = h \otimes f(x) = \int (h(q)f(q)e^{-iqx}dq), \tag{2.25}$$

with $h(q)$ and $f(q)$ the corresponding Fourier transforms with the proper convention. $h(q)$ is known as the transfer function of the filter. Although all the dissertation has been made for continuous signals, it can be generalised to discreted data.

Looking at the previous expressions we observe that filtering an image with a homogeneous and linear filter is equivalent to multiply the Fourier transform of the image with a transfer function. This transfer function can be considered as a device that selects frequencies, frequency in the Fourier sense. This property is very useful because we will be able to reduce the contributions of the noise.

In the context of this work, we deal with compact sources whose profiles are well known. And from these profiles we can obtain the Fourier modes of the compact sources. Therefore, we can design transfer functions that preserve the frequencies of interest corresponding to the source while reducing as much as possible the remaining ones, the contribution of the non-desired background. This is the idea behind 'top-hat' band-pass filters, where the filter is set to zero outside the range of frequencies that one wants to preserve. However, under some circumstances band-pass filters can introduce ring-shape artifacts in the image in the real space. This is due to the discontinuity in the transfer function, that is translated in these artifacts that contaminate the image. This effect can produce some compact and spurious objects that after the filtering process can be wrongly considered as real objects.

For this reason, it is desirable to have a continuous filter in Fourier space in order to avoid those ring-shape artifacts. Ideally, we would like to have a filter that improves the detection of the compact sources embedded in a background. In other words, we would like to have an optimal filter. In this context optimal means that we want to maximise the signal to noise ratio (SNR) of the source.

In the literature there are several techniques that have shown their efficiency to detect compact sources. Most of them, at least until now, are single-frequency. It basically means that only one map is filtered and then, and if one wants to make any multi-frequency analysis, you must combine your

results obtained at different frequencies. A brief description about the most commonly used devices to detect compact objects is shown below.

As it was mentioned before, with a filter it is possible to select in any desired way the frequency components of a given signal. Therefore, one of the most suitable applications of filtering is the *denoising*: the noise usually manifests at high frequencies. In order to avoid this noise, we can apply a filter that excludes this high-frequency domain, without affecting the signal we want to observe and analyse. These *low-pass filters* (that remove the higher frequencies) are suitable to smooth the image, since the small scale details (equivalent to high frequencies in the Fourier domain) are removed from the signal. Depending on the range of frequencies we enhance after the filtering process, we can have a *high-pass filter* if we remove the low frequencies (large scales); a *band-pass filter* if we select a band of frequencies not to be removed; and a low-pass filter, as we specified before.

After this brief discussion, we can say that a filter is a device that preserves the signal we want, rather maximising the signal itself or removing the noise. In order to quantify this sentence, we can define what is meant by *optimal*. In order to emphasize this term, we are going to introduce two very well known filters: the matched filter (MF) and the Wiener filter, that lead to two different meanings of optimality. After that, other filtering devices such as the wavelets and the biparametric adaptive filter will be briefly explained.

2.4 Wiener filter

Let us consider that we have an underlying signal $u(x)$ that we want to measure. But what we observe is a corrupted signal $y(x)$. This imperfection may have two possible causes: the first one is the fact that the response of the measuring apparatus is not a Delta-δ. Therefore, the signal that we have has the following appearance:

$$s(x) = \int_{-\infty}^{+\infty} \tau(\iota) u(x - \iota) d\iota, \tag{2.26}$$

where τ is the response function. In addition, a second source of corruption is the noise n. At the end of the process of observation, we find something like this:

$$y(x) = s(x) + n(x) = \tau \otimes u(x) + n(x), \tag{2.27}$$

where the signal we want to measure, $u(x)$, is convolved with the response function of the apparatus, $\tau(x)$, and $n(x)$ is the noise.

Let $u(q)$, $\tau(q)$, and $y(q)$ be the Fourier transforms of $u(x)$, $\tau(x)$ and $y(x)$, respectively. We desire an estimator $\tilde{u}(x)$ as close as possible to $u(x)$. To obtain this, we need to find a filter $\psi(x)$ that satisfies the following:

$$\tilde{u}(q) = \frac{y(q)\psi(q)}{\tau(q)} \tag{2.28}$$

in the Fourier domain.

We can establish a closeness criterion between $u(q)$ and $\tilde{u}(q)$ based on a least-square sense, i.e.,

$$\int_{-\infty}^{+\infty} |\tilde{u}(x) - u(x)|^2 dx = \int_{-\infty}^{+\infty} |\tilde{u}(q) - u(q)|^2 dq \tag{2.29}$$

is minimum. The equality in this equation comes from Plancherel's formula. Taking into account equations (2.27, 2.28), and after some calculations, one can find that the expression of the filter that satisfies the condition (2.29) is the following:

$$\psi_{WF}(q) = \frac{|s(q)|^2}{|s(q)|^2 + |n(q)|^2}. \tag{2.30}$$

This is the expression for the Wiener filter and it is independent on u. As one can see, the implementation of this filter needs previous knowledge on $|s(q)|^2$ and $|n(q)|^2$ (or at least on $|s(q)|^2$). Theoretically, it is not possible such implementation having information only from the measured signal *y*. However, the extra information is easy to obtain and can give excellent results.

On the other hand, Wiener filter has some disadvantages: first of all, it is a biased estimator of the signal s, both in the real and Fourier spaces. The second limitation is the fact that Wiener filter is based on a minimal variance approach. It means that if we have a strong non-Gaussian signal (or equivalently, random fields whose statistical behaviour depends on higher second order moments), the application of Wiener filter is expected to be not optimal. Even in the case of a Gaussian random field, we need a good knowledge of the modelling of the data, the power spectrum of the underlying signal and the nature of the statistical uncertainties.

All of these limitations have not been an obstacle to apply this filter and the literature gives us several examples of this. Even now, when the field to be reconstructed is close to be a Gaussian field, Wiener filter is close to be optimal. In this case it is proven (Zaroubi et al., 1995) that Wiener estimator is equal to the Bayesian estimator that maximises the *a posteriori* probability. There are other methods that improve the performance of this filter, in particular in the field of image processing.

2.5 Matched filter

We have seen that the Wiener filter was optimal in the least-squares sense. But there are many other criteria that can be used to consider a filter as optimal. In this subsection we show a different one. Let us assume a single signal $s(x)$ with a maximum at $x_0 = 0$ (for simplicity) embedded in a noisy background $n(x)$. As it was said before, the *signal to noise ratio* (SNR) of the signal is the ratio between the maximum value of the signal and the standard deviation of the field (σ), and mathematically can be expressed as:

$$SNR = \frac{s(0)}{\sigma}. \tag{2.31}$$

Obviously, we are interested in making this number as large as possible in order to discriminate the signal from the unwanted background. By introducing a linear filter $\psi(x)$ we modify the data in a certain way and the new SNR is:

$$SNR_\psi = \frac{\psi \otimes s(0)}{\sigma_\psi}, \tag{2.32}$$

where σ_ψ is the standard deviation of the filtered field. To simplify the notation, $s_\psi \equiv \psi \otimes s$. Now we can define the *gain* of the filter as the ratio between equations 2.32 and 2.31. The way to optimise the detection of the signal s is to maximise the gain. One way to do that is to minimise σ_ψ and make $s_\psi = s(0)$. In the following lines it is shown how to obtain the expression of the MF.

First of all, let us assume a set of images corresponding to the same area of the sky observed simultaneously at N different frequencies:

$$y_\nu(\mathbf{x}) = f_\nu s_\nu(\mathbf{x}) + n_\nu(\mathbf{x}), \tag{2.33}$$

where $\nu = 1, \ldots, N$. At each frequency ν, y_ν is the total signal in the pixel $\mathbf{x}$ and s_ν represents the contribution of the point source to the total signal y_ν; for simplicity let us assume there is only one point source centred at the origin of the image; f_ν is the frequency dependence of the point source; and n_ν is the *background* or generalised noise (containing not only the instrumental noise, but also the contributions of the rest of components).

The intrinsic angular size of the point sources is smaller than the angular resolution of the detector. At each observing frequency, each source is convolved with the corresponding antenna beam. For simplicity we will assume the antenna beam can be well described by a symmetric 2D Gaussian function. Then we can write

$$s_\nu(x) = A\tau_\nu(x), \tag{2.34}$$

where $x = |\mathbf{x}|$ (since we are considering symmetric beams), A is the *amplitude* of the source and τ is the spatial template or *profile*. The background $n_\nu(\mathbf{x})$ is modelled as a homogeneous and isotropic random field with average value equal to zero and power spectrum P_ν defined by

$$\langle n_\nu(\mathbf{q}) n_\nu^*(\mathbf{q}')\rangle = P_\nu \delta_D^2(\mathbf{q}-\mathbf{q}'), \tag{2.35}$$

where $n_\nu(\mathbf{q})$ is the Fourier transform of $n_\nu(\mathbf{x})$ and δ_D^2 is the 2D Dirac distribution.

In the single frequency approach each channel is processed separately and independently from the other frequency channels. This approach is robust in the sense that it is not necessary to assume anything about the spectral behaviour of the sources. The main drawback of the single frequency approach, however, is that one misses the potential noise reduction that could be obtained with a wise use of the information present at the other frequencies.

The standard single frequency point source detection method in the literature is based on the *matched filter* Tegmark and de Oliveira-Costa (1998); Barreiro et al. (2003); López-Caniego et al. (2006). The matched filter is the optimal linear detector for a single map in the sense that it gives the maximum signal to noise amplification. The matched filter can be expressed in Fourier space in the following way:

$$\psi_{MF}(q) = \frac{\tau(q)}{aP(q)}, \;\; a = \int d\mathbf{q} \frac{\tau^2(q)}{P(q)}. \tag{2.36}$$

Here a is a normalisation factor that preserves the source amplitude after filtering.

We can consider the following example. Let us suppose that we have a Dirac-δ signal located (for simplicity) at $x = 0$. We observe this signal through a detector whose point spread function (psf) is a Gaussian with width equal to R_0, $G_{R_0}(x)$. Therefore, after passing the signal through the detector, we have a Gaussian centred at the position of the original one. Due to inherent imperfections of the measure procedure, we also have white noise that makes it more difficult to detect the signal. If the noise dominates the signal in such a way that power spectrum of the data is a good approximation of the power spectrum of the noise ($P(q) \simeq$ constant because it is white noise), the matched filter given by equation 2.36 is proportional to the Gaussian of the psf. This is a well known result: a Gaussian filter is the optimal one to denoise signals with a Gaussian profile embedded in white noise. What the Gaussian makes is to remove the scales $< R_0$, preserving features with larger scales. It can be seen as a correlation between the data and the impulse response of the filter. From this point of this view it is obvious that this correlation is maximum when that shape of the signal is close to $G_{R_0}(x)$ and close to zero elsewhere.

It is also remarkable that to produce a matched filter it is not necessary to know the signal power spectrum. The power spectrum that appears at equation 2.36 is calculated from the generalised noise.

If the signal we have is sparse, a good estimator of this power spectrum is the one obtained from the data (signal+noise). Therefore, the only previous knowledge is the profile of the signal. Point sources in CMB experiments are a perfect example where the application of the matched filter is ideal. We have point sources at different locations with the same profile (given by the beam of the antenna). Estimating the power spectrum from the data, we can build the matched filter without any other assumption (see Tegmark and de Oliveira-Costa (1998); Herranz et al. (2002a)). This filter is more robust than the Wiener filter because it makes less assumptions about the data. In addition, it can be normalised to be an unbiased estimator of the amplitude of the signal.

As a corollary, the matched filter (eq. 2.36) can be obtained directly from the already described Neyman-Pearson rule. It was already commented that the matched filter appears naturally in the Bayesian techniques (see section 2.1). Now, let us assume that we have to decide between the null and the alternative hypothesis on the basis of pixel intensities. For correlated Gaussian noise, the likelihoods of the eq. 2.13 are:

$$P(\mathbf{y}|\Theta,H_0) \propto exp[-\frac{1}{2}\mathbf{y}^T\mathbf{C}^{-1}\mathbf{y}], P(\mathbf{y}|\Theta,H_1) \propto exp[-\frac{1}{2}(\mathbf{y}-\mathbf{s})^T\mathbf{C}^{-1}(\mathbf{y}-\mathbf{s})], \tag{2.37}$$

where $\mathbf{C}$ is the correlation matrix of the noise and $\mathbf{s}$ is the source. It can be proven that H_1 (the alternative hypothesis) is chosen when the statistics $T(\mathbf{y}) \propto \mathbf{y}^T\mathbf{C}^{-1}\tau \geq \zeta_*$, where τ is the profile of the source (in the case of point sources, the profile of the beam). As we can see, the statistics T is the data $\mathbf{y}$ multiplied by an operator $\mathbf{C}^{-1}\tau$, the already known matched filter (see eq. 2.36).

2.6 Wavelets

Wavelets have been widely used for decades in signal processing, data compression, pattern recognition, denoising, etc. The property that makes them interesting is that they retain information about the scale and the position of features of the image. For this reason, wavelets have been used to detect point sources in astronomical images. Unlike the Fourier transform, wavelets allow us to have information about the importance of different scales at each position.

Let us consider the discrete wavelet transform. The wavelet basis is constructed from dilations and translations of the *mother* (or *analysing*) wavelet function ψ and a second related function $\phi(x)$ called the *father* (or *scaling*) function:

$$\begin{aligned} \psi_{j,l} &= 2^{j/2}\psi(2^j x - l), \\ \phi_{j,l} &= 2^{j/2}\phi(2^j x - l), \end{aligned} \tag{2.38}$$

where j and l are integer numbers that denote the dilation and translation indices, respectively. The functions ϕ and ψ have generally compact support and they usually are chosen to be orthogonal. They must together satisfy some mathematical relations, as shown by Daubechies (1988). In particular, two requirements are:

$$\begin{aligned} \int \psi(x)dx = 1, \\ \int \phi(x)dx = 0. \end{aligned} \tag{2.39}$$

The reconstruction of the signal $f(x)$ using the wavelet basis is given by

$$f(x) = a_{0,0}\phi_{0,0}(x) + \sum_j \sum_l w_{j,l}\psi_{j,l}(x), \tag{2.40}$$

being a, w the wavelet coefficients defined as:

$$\begin{aligned} a_{0,0} = \int f(x)\phi_{0,0}(x)dx, \\ w_{j,l} = \int f(x)\psi_{j,l}(x)dx. \end{aligned} \tag{2.41}$$

Equation 2.40 can be interpreted as the sum of a low resolution, smoothed function plus a series of consecutive refinements that carry information about the details of the function $f(x)$. The difference between the refinement level j and the next tells us about the structure of f at the scale j. Therefore, the scaling function ϕ carries information about structures of a certain scale inside a compact region. For this reason wavelets are very useful for the point-source detection problem, because they are able to separate structures from a given scale, those with the same scale as that of the wavelet, reducing the contribution of the other scales. In summary, wavelets can also be used as filters.

Now, let us consider the *continuous wavelet transform* (CWT). Instead of using an integer number of dilations and translations, we allow them to vary in a continuous way. For $R > 0$ and $b \in \mathbb{R}$,

$$\psi_{R,b}(x) = R^{-1/2}\psi\left(\frac{x-b}{R}\right). \tag{2.42}$$

CWT is thus defined as:

$$Wf(R,b) = \int_{-\infty}^{+\infty} f(x)\psi_{R,b}(x)dx = f \otimes \overline{\psi}_R(b), \tag{2.43}$$

where $\overline{\psi}_R(x) = R^{-1/2}\psi(-x/R)$. As an example, let us consider the well known *Mexican Hat wavelet* (MHW), a wavelet that has been widely used in the literature for the detection of point sources with Gaussian profiles (Cayón et al., 2000; López-Caniego et al., 2005; Vielva et al., 2001b;

López-Caniego et al., 2007; Planck Collaboration et al., 2014a). This wavelet can be obtained by applying the Laplacian operator to the Gaussian function of width R:

$$\psi(x) = \frac{1}{\sqrt{2\pi}} \left[2 - \left(\frac{x}{R} \right)^2 \right] e^{-\frac{x^2}{2R^2}}. \tag{2.44}$$

This wavelet is obtained from the second derivative (Laplacian operator) of a Gaussian. Due to this relation with the Gaussian (the exponential is an eigenvector of the derivation operator), the MHW gives a high correlation when it is used to filter a Gaussian signal. This is the reason to be used in order to detect Gaussian signals in many fields of Astronomy. For example, MHW has been successfully used to detect point sources from CMB data alone (Cayón et al., 2000; Vielva et al., 2001b) or in combination with other methods (Vielva et al., 2001a; López-Caniego et al., 2007; Planck Collaboration et al., 2011c, 2014a, 2015d).

It is pointed out that wavelets are compensated, i.e., integral below the curve is zero, and using them as filters helps to remove background contributions with scales of variation larger than the one of the wavelet.

In the case of the MHW, we can apply the Laplacian operator as many times as needed. By doing that, we obtain a family of wavelets. The first member of this family is the already cited MHW; the second one (after applying twice the Laplacian operator over the Gaussian) is the MHW2. This particular wavelet is the most suitable to detect point sources as was shown in González-Nuevo et al. (2006).

There is many literature devoted to wavelets, as Ogden (1997); Mallat (1998); Burrus et al. (1998).

2.7 Biparametric adaptive filter

Following the idea of the MHW family, in López-Caniego and Vielva (2012) the authors propose a filter with two free parameters that allows a better incorporation of the statistical properties of the background into the filtering process. One of these parameters is the scale R, as the wavelets, associated with a compression/expansion of the typical scale of the PSF. The second parameter is the index of the filter g, and can be seen as a generalisation of the order of the Laplacian operator used in the MHW family (González-Nuevo et al., 2006). It is related to the filter location in the Fourier space or, equivalently, with the filter oscillations in the real space and associated with the shape of the angular power spectrum of the background.

Taking into account the philosophy behind the wavelets, we can define that the filter is the scaling

version of a mother filter:

$$\Psi(\mathbf{x}, R, g, \mathbf{b}) = \frac{1}{R^2}\bar{\psi}_g\left(\frac{|\mathbf{x}-\mathbf{b}|}{R}\right). \tag{2.45}$$

This mother filter $\bar{\psi}_g$ is given in the Fourier space by:

$$\bar{\psi}_g(qR) = \frac{1}{\pi}\frac{1}{\Gamma(\frac{2+g}{2})}(qR)^g\tau(qR) \tag{2.46}$$

and therefore, the filter coefficients $\omega_g(r, \mathbf{b})$ after convolve a 2D image $f(\mathbf{x})$ with the filter, are given by:

$$\omega_g(R, \mathbf{b}) = \int d\mathbf{x} f(\mathbf{x})\Psi(\mathbf{x}, R, g, \mathbf{b}). \tag{2.47}$$

If we have a Gaussian PSF with beam disperssion equal to R_0, i. e., the case of point sources that are observed with an antenna whose beam is precisely Gaussian, we have the following expression:

$$\bar{\psi}_g(qR) = \frac{1}{\pi}\frac{1}{\Gamma(\frac{2+g}{2})}(qR)^g e^{-(qR)^2/2}, \tag{2.48}$$

and the filter coefficients at the positions of a source with amplitude A and profile $A\tau(qR)$ are:

$$\omega_g(R) = \frac{A2^{\frac{g+2}{2}}z^g}{(1+z^2)^{\frac{g+2}{2}}}, \tag{2.49}$$

being $z = R/R_0$. The filters parameters are determined by imposing a maximum amplification of the point source amplitude in the filter coefficients maps, similar in this case to the philosophy behind the matched filter.

This filter has shown a great versatility. As the authors showed in López-Caniego and Vielva (2012), they divided the sky in patches of 7.3×7.3 square degrees, checking the smooth and coherent change of the index g along the Galactic latitude, from the Galactic plane to the poles, in the presence of synchrotron radiation (30 GHz) and dust emission (> 217 GHz). In particular, the index can change from values close to 2 (highest Galactic latitudes) until ~ 12 (close to the Galactic plane) at several hundreds of GHz. It is particularly interesting the case at 70 GHz, where the CMB is the dominant diffuse component, and therefore the index g is close to be flat, $g \sim 4$, the index of the MHW2 (González-Nuevo et al., 2006). Comparing both methods, the authors show the BAF detects more objects (for $SNR > 5$) at all frequencies for Galactic latitudes $|b| > 30^\circ$.

The BAF proves to be a good tool because of the combination of the scale R and the index g that best fit to the profile of the sources and to the local properties of the background maximising the amplification of the detections.

2.8 Matrix Matched Multifilters

In Herranz and Sanz (2008), the authors introduced a method that is, as we will see, very close in its philosophy and mathematically, to the matched multifilter (MMF, section 2.9.1). In this case, and similarly to the MMF, we have N channels (or frequencies), and the data we observe can be modelled in the following way:

$$y_\nu(\mathbf{x}) = A_\nu \tau_\nu(\mathbf{x}) + n_\nu(\mathbf{x}), \tag{2.50}$$

where A_ν is the amplitude of the source at frequency ν, τ_ν is the spatial profile at the same frequency, n_ν is the noise (everything that is not the signal) at this frequency, and y_ν is what we observe at this channel. Let us assume, as it will be done with the MMF below, $N = 2$ without loss of generalisation and the noise is characterised by a mean value equals to zero and the following cross-power spectrum:

$$\langle n_{\nu_1}(\mathbf{q}) n^*_{\nu_2}(\mathbf{q}')\rangle = P_{\nu_1\nu_2}\delta^2_D(\mathbf{q}-\mathbf{q}'), \tag{2.51}$$

where $\mathbf{P} = P_{\nu_1\nu_2}$ is the cross-power spectrum.

Being a multifilter device, the authors wanted the N input channels to intervene in the elaboration of the any output maps. One possibility is the following:

$$\omega_{\nu_1}(\mathbf{x}) = \sum_{\nu_2} \int d\mathbf{q} e^{-i\mathbf{q}\cdot\mathbf{x}} \Psi_{\nu_1\nu_2}(\mathbf{q}) y_{\nu_2}(\mathbf{q}), \tag{2.52}$$

where $\mathbf{\Psi} = \Psi_{\nu_1\nu_2}$ is the matrix of multifilters (MTXF).

The desired requirements for these filters are:

- $\langle \omega_{\nu_i}(\mathbf{0})\rangle = A_{\nu_i}$, where ω_{ν_i} is the filtered map at frequency ν_i;
- the variances of the different ω are minimum, keeping constant the values of A_ν.

These two conditions, by applying the Lagrange's multipliers method, can be used to obtain the filters $\mathbf{\Psi}$ that satisfy them. After some calculations (see Appendix 2.10 to find a similar procedure),

one can find that the expression for the filters is given by:

$$\mathbf{\Psi}^* = \mathbf{F}\mathbf{P}^{-1}, \tag{2.53}$$

where $\mathbf{F} = (\lambda_{\nu_1\nu_2}\,\tau_{\nu_2})$, being $\lambda = \mathbf{H}^{-1}$ and $H_{\nu_1\nu_2} = \int d\mathbf{q}\,\tau_{\nu_1}(\mathbf{q})P^{-1}_{\nu_1\nu_2}\,\tau^*_{\nu_2}(\mathbf{q})$.

At this point it is interesting to consider a particular case: when the noise is completely uncorrelated among the different channels. In this case, the cross-power spectrum matrix is diagonal, being the elements of the diagonal the power spectrum of each channel. And therefore, the MTXF become in a diagonal matrix whose elements are the complex conjugate of the matched filters for each input map. For circularly symmetric source profiles, the whole process is equivalent to filter each image for the corresponding matched filter.

2.9 Motivations: why a new method?

It was mentioned that the detection and estimation of the flux of extragalactic point sources (EPS) are a difficult task. The main reason for this is that the many different types of EPS distributed in the sky form a very heterogeneous set of objects that do not have a common spectral behaviour. While other foreground contaminants follow a specific emission law that is more or less well known (or can be inferred from observations) and that varies relatively slowly and continuously across the sky, each EPS has an emission law that, in principle, can be totally different to any other and independent from them. From the point of view of statistical signal processing, the problem of detecting EPS is a case of sorely underdetermined component separation problem where the number M of components is much larger than the number N of frequency channels.

The most commonly used approach to this problem consists on working separately in each channel, introducing some of the most used tools in the previous sections, showing their characteristics and advantages (and disadvantages). The key idea is to take advantage of the fact that all the EPS have the same shape (basically, that of the beam) and filters are well suited to enhance this feature. In the field of CMB images, wavelet techniques Vielva et al. (2001a, 2003); González-Nuevo et al. (2006); Sanz et al. (2006); López-Caniego et al. (2007), matched filters (MF, Tegmark and de Oliveira-Costa (1998); Barreiro et al. (2003); López-Caniego et al. (2006); López-Caniego and Vielva (2012)) and other related linear filtering techniques Sanz et al. (2001); Chiang et al. (2002); Herranz et al. (2002a); López-Caniego et al. (2004, 2005); López-Caniego et al. (2005) have proved to be useful. All these techniques rely on the prior knowledge that the sources have a distinctive spatial behaviour and this fact is used to design some bandpass filter to enhance them with respect to the noise. In the sin-

gle frequency case (and analysing only linear filters), the matched filter is the optimal in the sense that it maximises the SNR. Detection can be further improved by including prior information about the sources, i.e. some knowledge about their flux distribution, in the frame of a Bayesian formalism Hobson and McLachlan (2003); Carvalho et al. (2009, 2012). As mentioned above, the Bayesian approach requires a good knowledge about the statistical properties of the signal and the background.

For now, multiwavelength detection of EPS in CMB images remains a largely unexplored field. In recent years, some attempts have been done in this direction Naselsky et al. (2002); Chen and Wright (2008); Wright et al. (2009). More recently, Herranz and Sanz (2008) have introduced the technique of *'matched matrix filters'* (MTXF) as the first fully multifrequency, non-parametric, linear filtering technique that is able to find EPS and to do unbiased estimations of their fluxes thanks to the distinctive spatial behaviour of the sources. This method incorporates at the same time some multiwavelength information, without assuming any specific spectral behaviour for the sources. Herranz et al. (2009) have applied the MTXF to realistic simulations of the *Planck* radio channels, showing that it is possible to practically double the number of detections, for a fixed reliability level, for some of the channels with respect to the single-frequency matched filter approach.

MTXF, as it was shown above, use multiwavelength information in such a way that it is not necessary to make any assumption about the spectral behaviour of the sources. In fact, in that formalism their spectral behaviour is entirely irrelevant. All the multiwavelength considerations concern only to the generalised noise and its correlations. In this sense, the MTXF method deals with only half of the problem. This has its advantages in terms of robustness and reliability, but one could wish to have a technique that uses multiwavelength information in the modelling of *both* the signal (EPS) and the noise. But, as it was mentioned before, the spectral behaviour of the EPS is not known.

In this Thesis, it will be shown that even if the spectral behaviour of the EPS is unknown a priori, it is still possible to determine it directly from the data by means of an adaptive filtering scheme that incorporates multifrequency information not only through the noise correlations among channels, but also about the sources themselves.

The problem is, in more than one sense, similar to the problem of detecting SZ clusters (that is the reason for which it was discussed that case a few sections above). In the SZ case, the spectral behaviour of the sources is known, but not their size. A way to deal with this problem is to introduce the scale of the source as a free parameter (for example, the cluster core radius r_c) in the design of a *'matched multifilter'* (MMF) and to optimise the value of this parameter for each source so that a maximum signal to noise ratio is obtained after filtering (see the details in Herranz et al. (2002c,b, 2005); Schäfer et al. (2006); Melin et al. (2006)). As the problem depends on the optimisation of one single parameter, the method is easy to implement in codes that are relatively fast.

In this Thesis it is presented a modification of the MMF technique (Herranz et al., 2002c) in which the mixing coefficients of the frequency dependence vector of the sources are considered as free parameters to be optimised, since the characteristic angular size is known (the one given by the antenna beam). As it will be shown, if the number of frequency channels is N and it is chosen wisely a fiducial frequency of reference, the number of free parameters to optimise is $N-1$. For simplicity, throughout this Thesis, it will be used as an example the case of two channels, $N=2$, but the method is valid for any number of channels $N>1$. Including this additional information it is expected to improve the results. Reminding the main statistical properties that characterises a catalogue, it is mainly desired to increase the completeness at low flux densities (around several hundreds of mJy in the case of WMAP), recovering the amplitudes (or the flux densities) as accurate as possible. At these flux density levels, we are observing distant objects, being important their detection and characterisation in order to make statistical and evolutionary model studies of these objects.

By summarising, the main goal is to reduce the detection limit level, achieving to increase the completeness of our catalogues at low flux densities. To reach this purpose, it is necessary to develop new tools. Until now, the main used techniques have been the filters, particularly well suited to the task of detecting point sources due to their capability to select frequencies. But the most recent results in experiments such as WMAP and Planck have shown that the single-frequency filters have reached their minimum flux density imposed by sensitivity levels of the instruments. At this moment, we can face the problem in two ways: waiting the appearance of new experiments with higher sensitivities or searching some way to increase our efficiency at detecting point sources at low flux densities: if most of methods are single frequency, a natural step is to develop a multifrequency one that uses more available information, unused in the single frequency ones. MTXF use the statistical information of the noise, reflected in the cross-power spectrum and the spatial information of the sources: the same source is located in the same place in different frequencies. MMF, the method used in this work, also parametrises the unknown spectral behaviour of the sources as a power law. The use of additional information will lead to an increase of the detection of point sources, reaching higher levels of completeness at low flux densities.

2.9.1 The Matched Multifilter

In the multi-frequency approach it is taken into account the statistical correlation of the noise between different frequency channels and the frequency dependence of the sources. Let us assume a set of images corresponding to the same area of the sky observed simultaneously at N different frequencies (see eq. 2.50) and a background modelled as a homogeneous and isotropic random field with average value equal to zero and cross-power spectrum equal to eq. 2.51.

Although it was said that the MTXF and the MMF share some formal aspects, here is when the main difference with respect to the MTXF becomes manifest: in this case (with the MMF), it is made *a priori* assumption about the spectral behaviour of the point sources because we assume a power law for that. Therefore, we only have one output map (and only one value of the A). And as a consequence, the MMF device is an $N \times 1$ vector of filters. By contrast, MXTMF does *not* make any a priori assumption about the spectral behaviour of the point sources. Therefore, it is necessary to have so many maps (one for each value of the A_ν) as channels we observe. And as a consequence, MTXF is an $N \times N$ matrix of filters.

Let us define a set of N linear filters ψ_ν that are applied to the data

$$w_\nu(\mathbf{b}) = \int d\mathbf{x}\; y_\nu(\mathbf{x})\psi_\nu(\mathbf{x};\mathbf{b}) = \int d\mathbf{q}\; e^{-i\mathbf{q}\cdot\mathbf{b}} y_\nu(\mathbf{q})\psi_\nu(q), \tag{2.54}$$

here $\mathbf{b}$ defines a translation. The right-hand part of equation (2.54) shows the filtering in Fourier space, where $y_\nu(\mathbf{q})$ and $\psi_\nu(q)$ are the Fourier transforms of $y_\nu(\mathbf{x})$ and $\psi_\nu(\mathbf{x})$, respectively. The quantity $w_\nu(\mathbf{b})$ is the filtered map ν at the position $\mathbf{b}$. The *total filtered map* is the sum

$$w(\mathbf{b}) = \sum_\nu w_\nu(\mathbf{b}). \tag{2.55}$$

Therefore, the total filtered field is the result of two steps: a) filtering and b) fusion. During the first step, each map y_ν is filtered with a linear filter ψ_ν, during the second step the resulting filtered maps w_ν are combined so that the signal s is boosted while the noise tends to cancel out. Note that the combination in eq. (2.55) is completely general, since any summation coefficients different than one can be absorbed in the definition of the filters ψ_ν. Then the problem consists of how to find the filters ψ_ν so that the total filtered field is *optimal* for the detection of point sources.

The total filtered field w is *optimal* (in the case of lineal filters) for the detection of the sources if:

1. $w(\mathbf{0})$ is an *unbiased* estimator of the amplitude of the source, so $\langle w(\mathbf{0})\rangle = A$;
2. the variance of $w(\mathbf{b})$ is minimum, that is, it is an *efficient* estimator of the amplitude of the source.

If the profiles τ_ν and the frequency dependence f_ν are known, and if the crosspower spectrum is known or can be estimated from the data, the solution to the problem is already known: the matched multifilter (MMF, Herranz et al. (2002c)):

$$\mathbf{\Psi}(q) = \alpha\, \mathbf{P}^{-1}\mathbf{F},\;\; \alpha^{-1} = \int d\mathbf{q}\; \mathbf{F}^t\mathbf{P}^{-1}\mathbf{F}, \tag{2.56}$$

where $\mathbf{\Psi}(q)$ is the column vector $\mathbf{\Psi}(q) = [\psi_\nu(q)]$, $\mathbf{F}$ is the column vector $\mathbf{F} = [f_\nu\tau_\nu]$ and $\mathbf{P}^{-1}$ is the inverse matrix of the cross-power spectrum $\mathbf{P}$. Finally, the variance of the total filtered field can be

obtained by the following expression:

$$\sigma_w^2 = \int d\mathbf{q} \boldsymbol{\Psi}^t \mathbf{P} \boldsymbol{\Psi} = \alpha. \tag{2.57}$$

In order to see how these expressions were obtained, see the Appendix 2.10.

An important aspect to remark in the MMF is the fact that the different maps (at different frequencies) must show a correlation in the noise. If not, the cross-power spectrum would be a diagonal matrix and as a result we would have N matched filters, one at each frequency. This is not our goal because we desire a multifilter since the beginning. For this reason, the maps that we take into account in our analysis have to be close in terms of frequency and therefore to show correlations between them.

MMF with unknown source frequency dependence

As it was previously discussed, the problem is that the frequency dependence f_ν of the sources is not known a priori. Then, the possibilities are either a) to admit defeat, returning to the single-frequency approach, b) to devise a filtering method that does not use the frequency dependence of the sources altogether or c) to model somehow the unknown frequency dependence in the framework of some optimisation scheme. The second approach was explored in Herranz and Sanz (2008); Herranz et al. (2009). In this Thesis, the third approach to the problem will be studied.

Before addressing this problem, it will be useful to rewrite eq. (2.56) in a slightly different way. Let us write the vector $\mathbf{F} = [f_\nu \tau_\nu]$ in matrix form as

$$\mathbf{F} = \mathbf{T}(q)\mathbf{f}(\nu), \tag{2.58}$$

with $\mathbf{T}$ a diagonal matrix $\mathbf{T}(q) = \mathrm{diag}[\tau_1(q), \ldots, \tau_N(q)]$ and $\mathbf{f} = [f_\nu]$ the vector of frequency dependence. Note that all the dependence in q is included in the matrix $\mathbf{T}$; this fact will be useful later on.

Now imagine that $\mathbf{f}$ describes the true (unknown) frequency dependence of the sources and that $\mathbf{g} = [g_\nu]$, $\nu = 1, \ldots, N$ is a new vector of equal size as $\mathbf{f}$, but whose elements can take any possible value. The MMF for vector $\mathbf{g}$ can be defined,

$$\begin{aligned} \boldsymbol{\Psi}_\mathbf{g}(q) &= \alpha_\mathbf{g}\, \mathbf{P}^{-1}\mathbf{T}\mathbf{g}, \\ \alpha_\mathbf{g}^{-1} &= \int d\mathbf{q}\, \mathbf{g}^t \mathbf{T}\mathbf{P}^{-1}\mathbf{T}\mathbf{g} = \mathbf{g}^t \mathbf{H}\mathbf{g}, \end{aligned} \tag{2.59}$$

where $\mathbf{H} = \int d\mathbf{q}\mathbf{T}\mathbf{P}^{-1}\mathbf{T}$ and the facts that $\mathbf{T}^t = \mathbf{T}$ and that vector $\mathbf{g}$ does not depend on $\mathbf{q}$ and can therefore go out of the integral have been used. When applied to a set of images where there is present

a point source with true amplitude A and true frequency dependence $\mathbf{f}$, the filters $\mathbf{\Psi_g}$ will lead to an estimation of the amplitude,

$$A_{\mathbf{g}} = w_{\mathbf{g}}(\mathbf{0}) = \alpha_{\mathbf{g}}\, A\, \mathbf{g}^t \mathbf{H} \mathbf{f}. \tag{2.60}$$

Note that if $\mathbf{g} \neq \mathbf{f}$, then $A_{\mathbf{g}} \neq A$. On the other hand, the variance of the filtered field would be, in analogy with eq. (2.57), $\sigma^2_{\mathbf{g}} = \alpha_{\mathbf{g}}$. Taking into account the SNR of the source in the total filtered map, one can ask what the vector $\mathbf{g}$ is that maximises the signal to noise ratio $SNR_{\mathbf{g}}$. Intuition alone indicates that $SNR_{\mathbf{g}}$ is maximum if and only if $\mathbf{g} = \mathbf{f}$. This can be formally proved with little effort by taking variations of $\mathbf{g}$ (see Appendix 2.11).

Then the problem can be solved via a maximisation algorithm. In the case of a non-blind search, where the position of a given point source is known, one can focus on that point source and iteratively try values of the elements of $\mathbf{g}$ until a maximum SNR is reached. In the case of a blind search, the situation is a little bit more difficult because in a given image there may be many different objects s_i with a different solution $\mathbf{g}_i$. A way to proceed is to filter many times the image, using each time a different set of values of the elements of $\mathbf{g}$ so that the appropriate range of frequency dependences is sufficiently well sampled, and then to proceed counting one by one all the possible detections and associating to each one the values of $\mathbf{g}$ that maximise the SNR of that source in particular.

It is relevant to remark that this situation is very similar to the case of the detection of galaxy clusters with unknown angular size described in Herranz et al. (2002c,b). In that case, the frequency dependence $\mathbf{f}$ was known but the size of the clusters (their source profile) was not. The cluster profile can be parametrised as a modified beta profile with a free scale parameter r_c (typically, the cluster core radius). In Herranz et al. (2002c,b), it was shown that the true scale of the clusters can be determined by maximising the SNR of the detected clusters as a function scale r_c of the filter.

In the case of this Thesis, factorisation (2.58) leads to equations (2.59) and (2.60); this is very convenient for implementation of the MMF when many filtering steps are necessary. The most time-consuming part of the filtering is the calculation of matrices $\mathbf{P}$ and $\mathbf{T}$ because they must be calculated for all values of $\mathbf{q}$. In the case of clusters with unknown size, $\mathbf{T}$ had to be calculated for every value of r_c. However, in the case that is being considered in this Thesis the only quantities that vary during the maximisation process are the elements of vector $\mathbf{g}$. This allows to compute the integrals of matrix $\mathbf{H}$ only once for each set of images. As a result, applying the MMF to large numbers of point sources with unknown frequency dependence is, in general, much faster than applying the MMF to the same number of clusters with unknown source profile.

The main difference is that while in the case of galaxy clusters it was necessary to maximise with respect to only one single parameter (the core radius), in the case of the unknown frequency dependence

it is necessary to maximise with respect to the N components of vector $\mathbf{g}$. This procedure can require a very large number of computations if N is big. Although it has been just seen that each free parameter of the frequency dependence can be mapped much faster than each free parameter of the source profile, it is still interesting to reduce the number of computations as much as possible.

Number of degrees of freedom of vector g

For N images, vector $\mathbf{g} = [g_1, \ldots, g_N]$ has N degrees of freedom. This makes the optimisation procedure more complex and computationally expensive. The situation can be lightened if one of the frequencies under consideration as our fiducial frequency of reference is chosen. Let us choose for example a concrete frequency $j \in \{1, \ldots, N\}$ to be our fiducial frequency of reference, then

$$\langle y_j(0) \rangle = A f_j \tau_j(0) = A \tag{2.61}$$

and therefore, since the profile τ_j is normalised to unity, f_j must be equal to one. Hence, one must look for vectors $\mathbf{g} = g_1, \ldots, g_{j-1}, 1, g_{j+1}, \ldots, N$ and the number of independent degrees of freedom is $N - 1$. If the number of channels is $N = 2$, there is only one degree of freedom for the optimisation problem. The case $N > 2$ does not introduce any modification in the strategy. As mentioned in section 2.9.1, the SNR of the sources has a global maximum if and only if $\mathbf{g} = \mathbf{f}$. This implies that the problem is not degenerated. The only complication is computational: as the number of free parameters to determine increases, more operations are needed in order to sample the parameter space. Fortunately, there aer many efficient maximisation algorithms available in the literature (amoeba, Matropolis algorithms, simulated annealing, etc.). Although the case of two channels will be considered for simplicity in this Thesis, the extension to $N > 2$ frequencies is straightforward.

Optional parametrisation of vector g

Another way to reduce the number of degrees of freedom of vector $\mathbf{g}$ is to find a suitable parametrisation for it. For example, the power law relationship

$$S(\nu) = S_0 \left(\frac{\nu}{\nu_0} \right)^{\gamma}, \tag{2.62}$$

where $S(\nu)$ is the flux at frequency ν, ν_0 is a frequency of reference, S_0 is the flux at that frequency of reference and γ is the *spectral index*. This equation is widely used in the literature. By using eq. (2.62), the reference flux S_0 can easily be related to the reference amplitude A of the sources and the number of degrees of freedom is just one, the spectral index γ.

However, the parametrisation of vector $\mathbf{g}$ has its own risks. For example, it is known that eq. (2.62) is valid only as an approximation for any given frequency interval and that its validity decreases as the size of the interval grows. If it is chosen to follow the parametric approach, it is known for sure that the results will be less and less accurate as the number N of channels grows, especially if the separation between frequency channels is large. On the other hand, eq. (2.62) is always exact if $N = 2$. Therefore, it can be safely used the parametrisation (2.62) for $N = 2$ channels, without loss of generality. Since the number of degrees of freedom is one either if (2.62) is used or not, the use of the parametrisation is irrelevant in this case. However, one may be interested in using it for historical, didactic and practical motivations. For example, eq. (2.62) is useful to express the physical properties of the sources in terms of their (steep, flat, inverted, etc.) spectral index.

It is relevant to remark that frequency dependence parametrisation, in the form of eq. (2.62) or any other way, may or may not be useful in some cases, but *it is not essential* at all for the method proposed in this Thesis.

2.10 Appendix A

In this appendix it is explained in more detail the obtention of the *Matched Multifilter*. Let us assume a set of images corresponding to the same area of the sky observed simultaneously at N different frequencies:

$$y_\nu(\mathbf{x}) = f_\nu s_\nu(\mathbf{x}) + n_\nu(\mathbf{x}), \tag{2.63}$$

where $\nu = 1, \cdots, N$. At each frequency ν, y_ν is the total signal in the pixel $\mathbf{x}$ and s_ν represents the contribution of the point source to the total signal y_ν; for simplicity let us assume there is only one point source centred at the origin of the image; f_ν is the frequency dependence of the point source; and n_ν is the background or generalised noise.

The intrinsic angular size of the point sources is smaller than the angular resolution of the detector. At each observing frequency, each source is convolved with the corresponding antenna beam (beam is the response of the antenna to a point source). For simplicity we will assume the antenna beam can be well described by a symmetric 2D Gaussian function. Then it can be written:

$$s_\nu(x) = A\tau_\nu(x), \tag{2.64}$$

where $x = |\mathbf{x}|$ (since we are considering symmetric beams), A is the amplitude of the source and τ

is the spatial template or *profile*. The background $n_\nu(\mathbf{x})$ is modelled as a homogeneous and isotropic random field with average value equal to zero and power spectrum P_ν defined by

$$\langle n_\nu(\mathbf{q}) n_\nu^*(\mathbf{q}')\rangle = P_\nu \delta_D^2(\mathbf{q}-\mathbf{q}'), \tag{2.65}$$

where $n_\nu(\mathbf{q})$ is the Fourier transform of $n_\nu(\mathbf{x})$ and δ_D^2 is the 2D Dirac distribution. In the single frequency approach each channel is processed separately and independently from the other frequency channels. This approach is robust in the sense that it is not necessary to assume anything about the spectral behaviour of the sources. The main drawback of the single frequency approach, however, is that one misses the potential noise reduction that could be obtained with a wise use of the information present at the other frequencies. The standard single frequency point source detection method in the literature is based on the matched filter (eq. 2.36).

In the multi-frequency approach it is taken into account the statistical correlation of the noise between different frequency channels and the frequency dependence of the sources. Now it is modelled the background $n_\nu(\mathbf{x})$ as a homogeneous and isotropic random field with average value equal to zero and crosspower spectrum $P_{\nu_1\nu_2}$ defined by:

$$\langle n_{\nu_1}(\mathbf{q}) n_{\nu_2}^*(\mathbf{q}')\rangle = P_{\nu_1\nu_2} \delta_D^2(\mathbf{q}-\mathbf{q}'), \tag{2.66}$$

where $n_\nu(\mathbf{q})$ is the Fourier transform of $n_\nu(\mathbf{x})$ and δ_D^2 is the 2D Dirac distribution. Now a set of N linear filters ψ_ν that are applied to the data can be defined:

$$\omega_\nu(\mathbf{b}) = \int d\mathbf{x} y_\nu(\mathbf{x})\psi_\nu(\mathbf{x};\mathbf{b}) = \int d\mathbf{q} e^{-i\mathbf{q}\cdot\mathbf{b}} y_\nu(\mathbf{q})\psi_\nu(q), \tag{2.67}$$

where $\mathbf{b}$ denotes a translation. It have been taken into account the following convention for the Fourier transform:

$$f(\mathbf{q}) = \frac{1}{2\pi}\int d\mathbf{x} f(\mathbf{x}) e^{i\mathbf{q}\cdot\mathbf{x}}, f(\mathbf{x}) = \frac{1}{2\pi}\int d\mathbf{q} f(\mathbf{q}) e^{-i\mathbf{q}\cdot\mathbf{x}}, \tag{2.68}$$

by which any convolution can be expressed as

$$\begin{array}{c} f\otimes g(\mathbf{b}) = \int d\mathbf{x} f(\mathbf{x}) g(\mathbf{b}-\mathbf{x}) = \frac{1}{(2\pi)^2}\iint d\mathbf{q} d\mathbf{q}' f(\mathbf{q}) g(\mathbf{q}') e^{-i\mathbf{q}'\cdot\mathbf{b}} \int d\mathbf{x} e^{-i\mathbf{x}\cdot(\mathbf{q}-\mathbf{q}')} = \\ = \int d\mathbf{q} f(\mathbf{q}) g(\mathbf{q}) e^{-i\mathbf{q}\cdot\mathbf{b}}. \end{array} \tag{2.69}$$

The right part of equation eq. 2.67 shows the filtering in Fourier space, where $y_\nu(\mathbf{q})$ and $\psi_\nu(q)$ are the Fourier transforms of $y_\nu(\mathbf{x})$ and $\psi_\nu(\mathbf{x})$, respectively. The total *filtered map* is the sum

$$\omega(\mathbf{b}) = \sum_\nu \omega_\nu(\mathbf{b}). \tag{2.70}$$

Therefore, the total filtered field is the result of two steps: a) filtering and b) fusion. During the first step each map y_ν is filtered with a linear filter ψ_ν ; during the second step the resulting filtered maps ω_ν are combined so that the signal s is boosted while the noise tends to cancel out. Note that the fusion in eq. 2.70 is completely general, since any summation coefficients different than one can be absorbed in the definition of the filters ψ_ν . Then the problem consists in how to find the filters ψ_ν so that the total filtered field is optimal for the detection of point sources. The total filtered field ω is optimal for the detection of the sources if it satisfies these two conditions:

- $\omega(\mathbf{0})$ is an *unbiased* estimator of the amplitude of the source, so $\omega(\mathbf{0}) = A$;
- the variance of $\omega(\mathbf{b})$ is *minimum*, that is, it is an *efficient* estimator of the amplitude of the source.

Going to the first condition, it can be expressed mathematically as:

$$2\pi \sum_\nu f_\nu \int dqq\tau_\nu\psi_\nu = 1. \tag{2.71}$$

Then, referring to the second condition, it can be easily proven the variance of ω, σ^2_ω is:

$$\sigma^2_\omega = \langle\omega(\mathbf{b})^2\rangle - \langle\omega(\mathbf{b})\rangle^2 = 2\pi \sum_{\nu_1\nu_2} \int dqq\psi_{\nu_1} P_{\nu_1\nu_2}\psi_{\nu_2}. \tag{2.72}$$

Now it is used the method of the *Lagrange's multipliers*. It consists on constructing a Lagrangian by using the conditions above referred. The Lagrangian is the following:

$$\begin{gathered} \mathscr{L} = \sigma^2_\omega(\psi_{\nu_1}, \psi_{\nu_2}) + \lambda[2\pi \textstyle\sum_\nu f_\nu \int dqq\tau_\nu(q)\psi_\nu(q) - 1] = \\ = 2\pi \textstyle\sum_{\nu_1\nu_2} \int dqq\psi_{\nu_1}(q)P_{\nu_1\nu_2}(q)\psi_{\nu_2}(q) + \lambda[2\pi \textstyle\sum_\nu f_\nu \int dqq\tau_\nu(q)\psi_\nu(q) - 1]. \end{gathered} \tag{2.73}$$

The following step is to derive the Lagrangian respect to the filter ψ and equals to zero. One aspect has to be considered here. In the previous development, there were two subindices, ν_1 and ν_2, that are mute ones. In order to derive the Lagrangian with respect to the filter, we take into account the two different frequencies instead of the mute subindices. For this reason, hereinafter the mute subindices

ν_1 and ν_2 will be changed by the subindices 1 and 2, to denote the two frequencies considered. Also, the dependences on q of the different expressions will be deleted to make more clear the expressions. In this case, it is obtained the following:

$$\begin{array}{c} \frac{\partial \mathscr{L}}{\partial \psi_1} = 4\pi \int dqqP_{11}\psi_1 + 4\pi \int dqqP_{12}\psi_2 + \lambda 2\pi f_1 \int dqq\tau_1 = \\ = 4\pi \sum_i \int dqqP_{1i}\psi_i + \lambda f_1 \int dqq\tau_1 = 0, \end{array} \tag{2.74}$$

where i goes from 1 to 2. The process is repeated for ψ_2, obtaining:

$$\frac{\partial \mathscr{L}}{\partial \psi_2} = 4\pi \sum_j \int dqqP_{2j}\psi_j + \lambda f_2 \int dqq\tau_2 = 0. \tag{2.75}$$

We can rewrite these two expressions in the form of a system of two equations as follows, taking into account that both are equal to zero:

$$\left.\begin{array}{l} 2\sum_i P_{1i}\psi_i + \lambda f_1\tau_1 = 0 \\ 2\sum_i P_{2i}\psi_i + \lambda f_2\tau_2 = 0 \end{array}\right\} \tag{2.76}$$

that can be expressed as a matricial equation:

$$2\mathbf{P}\mathbf{\Psi} = -\lambda\mathbf{F}, \tag{2.77}$$

where F is the column vector $\mathbf{F} = [f_i\tau_i]$, where i goes from 1 to 2. The only thing to make is to get Ψ from the expression:

$$\mathbf{\Psi} = \alpha\mathbf{P}^{-1}\mathbf{F}, \tag{2.78}$$

where $\alpha = -\lambda/2$. This is the expression for the *matched multifilter*. One can see that formally, is similar to the matched filter (see eq. 2.36): it is directly proportional to the profile of the beam τ, included in the vector $\mathbf{F}$, and inversely proportional to the power spectrum. For the matched multifilter, the constant of proportionality can be obtained from the first condition written before, where it is said the matched multifilter is an unbiased estimator of the amplitude of the source:

$$\begin{array}{c} 2\pi \sum_\nu \int dqqf_\nu\tau_\nu\psi_\nu = 1; \\ 2\pi \int dqq\mathbf{F}^t\alpha\mathbf{P}^{-1}\mathbf{F} = 1; \\ \frac{1}{2\pi} = \alpha \int dqq\mathbf{F}^t\mathbf{P}^{-1}\mathbf{F}; \\ \alpha^{-1} = \int d\mathbf{q}\mathbf{F}^t\mathbf{P}^{-1}\mathbf{F}. \end{array} \tag{2.79}$$

Finally, the expression from the variance of the filtered map can be obtained from 2.72:

$$\sigma_\omega^2 = \langle\omega(\mathbf{b})^2\rangle - \langle\omega(\mathbf{b})\rangle^2 = 2\pi \sum_{\nu_1\nu_2} \int dqq\psi_{\nu_1} P_{\nu_1\nu_2}\psi_{\nu_2} = \\ = \sum_{\nu_1\nu_2} \int d\mathbf{q}\psi_{\nu_1} P_{\nu_1\nu_2}\psi_{\nu_2} = \int d\mathbf{q}\mathbf{\Psi}^t\mathbf{P}\mathbf{\Psi}. \tag{2.80}$$

2.11 Appendix B

In this Appendix it will be demonstrated that $\mathbf{g} = \mathbf{f}$ in order to maximise the SNR of the MMF.

First of all, some expressions will be rewriten to make easier the posterior calculations. In general, sources have a frequency dependence equal to $\mathbf{F}$ ($\mathbf{F} = (f_\nu\tau_\nu)$). However, filters are allowed to have a general and different frequency dependence, $\mathbf{G}$.

$$\alpha^{-1} = \int d\mathbf{q}\mathbf{G}^t\mathbf{P}^{-1}\mathbf{G} = \gamma, \delta\gamma = 2\int d\mathbf{q}\delta\mathbf{G}^t\mathbf{P}^{-1}\mathbf{G}. \tag{2.81}$$

Also, the variance σ^2 can be redefined as follows:

$$\sigma^2 = \int d\mathbf{q}\mathbf{\Psi}^t\mathbf{P}\mathbf{\Psi} = \alpha^2 \int d\mathbf{q}\mathbf{G}^t(\mathbf{P}^{-1})^t\mathbf{P}\mathbf{P}^{-1}\mathbf{G} = \alpha^2 \int d\mathbf{q}\mathbf{G}^t\mathbf{P}^{-1}\mathbf{G} = \alpha. \tag{2.82}$$

Now it is defined the SNR for a source of amplitude A: $SNR = A/\sqrt{\sigma^2} = A/\sqrt{\alpha}$. The amplitude of the source is defined according eq. 2.60, remembering that frequency dependence of the source is $\mathbf{F}$ and for the multifilter is $\mathbf{G}$:

$$A = \alpha \int d\mathbf{q}\mathbf{G}^t\mathbf{P}^{-1}\mathbf{F} = \alpha\beta, \tag{2.83}$$

being β the integral. With all these ingredients, we can write the SNR as follows:

$$SNR = \frac{A}{\sqrt{\alpha}} = \sqrt{\alpha}\beta. \tag{2.84}$$

The following step is to maximise the SNR, taking variations with respect to G (denoted by the

symbol δ) of the previous expression:

$$\begin{aligned}
\delta(SNR) = \tfrac{1}{2}\tfrac{\delta\alpha\beta}{\sqrt{\alpha}} + \sqrt{\alpha}\delta\beta = 0; \\
\tfrac{\beta\delta\alpha}{2\alpha} + \delta\beta = 0; \\
\tfrac{\gamma\beta\delta\alpha}{2} + \delta\beta = 0; \\
-\tfrac{\gamma\beta\delta\gamma}{2\gamma^2} + \delta\beta = 0; \\
-\tfrac{1}{2}\beta\delta\gamma + \gamma\delta\beta = 0.
\end{aligned} \tag{2.85}$$

The last step consists on rewriting the last line of equations according to the corresponding integrals. That results on:

$$-\int d\mathbf{q}\,\mathbf{G}^t\mathbf{P}^{-1}\mathbf{F}\int d\mathbf{q}\,\delta\mathbf{G}^t\mathbf{P}^{-1}\mathbf{G} + \int d\mathbf{q}\,\mathbf{G}^t\mathbf{P}^{-1}\mathbf{G}\int d\mathbf{q}\,\delta\mathbf{G}^t\mathbf{P}^{-1}\mathbf{F} = 0. \tag{2.86}$$

If $\mathbf{G} = \kappa\mathbf{F}$ (being κ a scalar), in particular $\mathbf{G} = \mathbf{F}$, this expression is equal to zero.

Chapter 3

Application of the MMF over Planck simulated data

3.1 Introduction

In the last years, CMB experiments have improved their angular resolution and sensitivity, allowing us to study the CMB at higher multipoles with no longer limitation due to the instrument but the Galactic and extragalactic contamination.

As it was commented in previous chapters, a correct separation of the different components that constitute the map is essential if we want to study properly any of these components. Focusing only on the point sources, we discover that they are the most prominent contaminant at low angular scales (or high multipoles, $\ell > 500 - 1000$) both in temperature (Toffolatti et al., 1998; De Zotti et al., 1999; Hobson et al., 1999; De Zotti et al., 2005) and in polarisation (Tucci et al., 2004, 2005; López-Caniego et al., 2009; Argüeso et al., 2011b). Point sources have different frequency behaviour that cannot be known before the detection (by contrast, and without taking into account the relativistic effects, we know perfectly the spectral behaviour of the Sunyaev-Zel'dovich effect) because, in general, each source is an independent galaxy, different from any other that can observed in the sky. These particular characteristics make it necessary to develop methods capable to detect these sources, different from the ones developed to separate diffuse components. Filters, as were commented previously, are a suitable weapon to attack this problem: point sources are formally and mathematically characterised by their angular size, smaller than the beam of the experiment. Therefore, filters can select properly the objects we are interested on.

The detection and posterior removal of the point sources is very important in order to obtain CMB

maps as clean as possible. In this case, the goal is to obtain a catalogue as complete as possible, in particular at low flux densities, and a good accuracy of the fluxes, to be properly removed from the maps.

On the other hand, when the attention is focused on the extragalactic astrophysics, i. e. in the study of the source counts to analyse evolutionary models, it could be more important the obtention of a good reliable catalogue, closely followed by the accuracy. The reason is to have a catalogue with as fer spurious detections as possible.

The detection of extragalactic point sources with the introduction of a multifrequency method, the matched multifilter, is studied in this chapter. The used maps are a set of realistic simulations made with the *Planck Sky Model*, enough far away from the Galactic plane. The point sources are inserted *a posteriori*, convolved by their respective beams. In order to compare with the MMF, the maps are also filtered by the single frequency matched filter. As it was shown previously (see section 2.5), the matched filter is the optimal linear filter in the sense that maximises the signal to noise ratio (SNR). The procedure, as it will be explained more in detail, is to filter each map and find the spectral index (the only free parameter in the MMF) that maximises the SNR, and compare the number of detections, accuracy, spurious detections, etc, with respect to the matched filter. The detector, as it was already said, will be the 5σ thresholding and the detection is completely *blind*. It means we do not know before the detection if there is any source (or several) in the patch or not, by contrast with other works where the detection is not blind, like López-Caniego et al. (2007), based on the positions of known 5-GHz sources; and Massardi et al. (2009), combining a non-blind search by using the ATCA (Australia Telescope Compact Array) 20-GHz survey catalogue with a blind search. This information have been used in order to favour the detection, like placing the source that are going to be detected in the centre of the patch to remove as much as possible border effects after the filtering process, border effects that can modify the properties of the sources.

After saying that, some considerations must be taking into account to check the robustness and efficiency of the MMF:

- The multifilter has to be a suitable tool to make a blind detection, assuming a minimum number of assumptions about the data before the filtering process.
- It must be as robust as possible against possible systematics. As it was said, detection is done out the Galactic plane as defined below.
- The multifilter must not 'introduce' a high number of false detections, the so-called spurious detections. These detections, due to the statistical fluctuations of the background, satisfy the conditions of the detector. This condition is equivalent to say we have a *reliable* catalogue.

- And obviously, as commented before, the completeness and accuracy (flux density and position of the detected source in comparison with previous catalogues) will be taken into account in the analysis of he multifilter.

In order to avoid some systematic effects, the data will be previously passed through a window (the Hann window, (Jiang et al., 2002)) that removes to a large degree the aliasing effect, as explained below.

Of course, there are some tools that could not be considered in this analysis, because they require a more precise knowledge about the statistical properties of the background and the signal (the point sources themselves): there is not any assumption about the sources, like any spatial or flux distribution. In this Thesis, the only assumption is their characteristic angular size: the one given by the beam since they are smaller than the beam. Any other potential property that could be included in the analysis is discarded in order to gain in robustness in the multifilter.

Before continuing with the study of the MMF, let us consider some issues that arise when using linear filters related to the matched filter. As we can see in eq. 2.36, the expression of the matched filter in Fourier space is inversely proportional to the power spectrum of the noise (the same applies for the MMF, but in this case inversely proportional to the cross-power spectrum. Hereinafter in this section, in order to simplify the different considerations, the single-frequency case will be discussed). In principle, both the noise and the signal are mixed in the data, therefore we cannot calculate exactly the power spectrum of the noise before the extraction of the point sources from the noise. However, we can make a realistic assumption about the spatial and intensity distribution of the sources: they are sparsely distributed, that is: there are relatively few bright sources and the point source signal is sub-dominant over a vast majority of the pixels of the image or images considered. Under this assumption, the true, unknown power spectrum of the noise can be approximately estimated by the power spectrum directly measured from the observed data.

Once we have overcome this difficulty, the following step is to calculate the value of the power spectrum for all the Fourier modes. This case is very similar to the obtention of a histogram, when we have to build it from a set of data: if the number of bins is too small, we loose the underlying structure of the data. However, if the number of bins is too large (only a few data per bin), we only see noise. We find the same problem in the power spectrum of the images, in particular at low Fourier modes (large spatial structures). The main challenge at this moment is to bin properly the power spectrum, choosing the number of bins that avoid the two problems previously mentioned. Anyway, the problem subsists at low Fourier modes to some degree. This way to obtain the power spectrum is not general, there are other ones that are applied depending on the problem. These other methods incorporate some kind of

arbitrariness as well, like the number of bins in the case mentioned in this paragraph.

All the things mentioned in the previous paragraph makes a sensitive task the estimation of the power spectrum, being quite noisy at low Fourier modes in most of cases. As seen before, this is a problem when obtaining the matched filter since it is inversely proportional to the power spectrum. Therefore, if we have a noisy power spectrum, our matched filter will be equally noisy.

There are an additional problem that is when the image to be filtered is not complete (and therefore, some Fourier modes are not properly estimated) because some regions have been masked in order to avoid them because they are uncovered regions by the experiment, they are highly contaminated, etc. Sometimes, in order to build the matched filter, these regions are filled with pixels that show the same mean statistical properties that the map to be filtered. This situation is not present in this Thesis but must be taken into account when it happens.

As commented before, the theoretical superiority of the matched filter comes from the fact that is the linear filter that maximises the SNR for each source, it means it minimises the variance of the filtered noise. But we could find a situation where the noise is not Gaussian, and therefore the matched filter would not be necessarily the optimal linear filter anymore and hence it does not guarantees the number of spurious detections is minimum. This situation arises in the case of the CMB, due to the contribution of the Galactic foregrounds, highly non-Gaussian.

The question that emerges at this point is if the matched filter (or the MMF in the multifrequency method) is suitable, or better said, optimal taking into account all the previous considerations that could move away the matched filter from the optimality in real situations. López-Caniego et al. (2006) makes a comparison between the matched filter and two members of the Mexican Hat Wavelet, the MHW and the MHW2 (obtained by applying the Laplacian operator over the MHW). The authors used the most recent available templates of the epoch of the microwave sky by using the 'Planck Reference Sky Model', and for the extragalactic objects the up-to-date (in 2006) cosmological evolution models for sources. In order to have statistically significant results, the filtered area is equivalent to half of the sky at $30, 44, 70, 100, 143, 217, 353, 545$ and 857 GHz (the nine frequencies of Planck). Completeness, reliability and accuracy (both in amplitude like position), at the whole range of frequencies of Planck, are used to compare the three methods. The results are very similar for the matched filter and the MHW2, being worse for the MHW, in particular at low flux densities.

Therefore, once tested that the matched filter and the MHW2 show similar benefits, one could wonder which must be used. The obtaining of the power spectrum is relatively easy and in the cases of this Thesis is not computationally expensive: as said previously, the power spectrum is obtained directly from the observed data. Therefore, for a patch it is calculated once, despite the fact that one

single map is filtered several times for the MMF since the spectral index of the frequency dependence is a free parameter to be obtained by maximising the SNR for a given source. Precisely, this condition makes optimal the matched filter for linear filters and Gaussian noise.

By contrast, the MHW family members are obtained by applying successively the Laplacian operator over the Gaussian. This means the MHW family members are especially well suited to detect Gaussian-shaped sources (point sources that have been convolved by Gaussian beams). This is not the case for WMAP, in particular in the higher frequency channels (at 61 and 94 GHz). However, the matched filter, as its name indicates, can adapt its expression according to the profile of the source since it is directly proportional to it (see eq. 2.36).

Equally, we have seen another techniques in the previous chapter, like the Bayesian ones, where it is completely necessary to have good knowledge about the statistical properties of the noise and the signal. This makes the Bayesian model closer to the optimality but less robust against any unknown of the data.

With all these considerations taken into account, the matched filter is used as a starting point to expand the idea to a multifrequency framework, leading to the matched multifilter.

The structure of the chapter is as follows: after been introduced the MMF in the previous chapter (see eq. 2.78), a set of realistic simulations of the microwave sky at 44 and 100 GHz are made (section 3.2) by using the *Planck Sky Model* (see Delabrouille et al. (2013)). In this simulations, point sources are not included, therefore it is necessary to insert them a posteriori. According to previous works (see González-Nuevo et al. (2008)), the most probable values of the flux density and the spectral index for the sources are $[0.1, 1]$ Jy and $[-1.4, 1.0]$, respectively. Then, both methods, the single frequency and the matched multifilter are directly compared in the section 3.3 according to the completeness, accuracy in terms of spectral index and flux density and reliability. As it will be seen below, the matched multifilter improves the results obtained by the matched filter, in particular to low flux densities. Finally, a set of conclusion will be shown in the section 3.4.

3.2 Simulations

In order to illustrate the MMF method described above and to compare the MMF multi-frequency approach with the single frequency approach, a set of basic, yet realistic, simulations have been performed. The case of two frequency channels ($N = 2$) has been considered. Generalisation to more frequency channels is possible, as discussed in section 2.9.1, but it is maintained that number to keep things simple in this Thesis.

For this example, it is taken the case of the *Planck* mission (Tauber, 2005). The 44 GHz and 100 GHz *Planck* channels will be considered. The choice of the pair channels is not essential: any other pair of channels would have served the same for this exercise. This particular choice allows to study the case of radio sources in two, not adjoining, channels with different instrumental settings: the 44 GHz channel belongs to the Low Frequency Instrument of *Planck* and the 100 GHz channel belongs to the High Frequency Instrument.

For the simulations, the *Planck* Sky Model[1] (Delabrouille et al., 2013, PSM,) have been used, a flexible software package developed by *Planck* WG2 for making predictions, simulations and constrained realisations of the microwave sky. The simulated data used here are the same as in Leach et al. (2008), where the characteristics of the simulations are explained in more detail. Maps are expressed in $(\Delta T/T)$, thermodynamic units. Simulations include all the relevant astrophysical components: the CMB sky is based on a Gaussian realisation assuming the WMAP best-fitting C_ℓ at higher multipoles; Galactic emission is described by a three component model of the interstellar medium comprising free-free, synchrotron and dust emissions. Free-free emission is based on the model of Dickinson et al. (2003) assuming an electronic temperature of 7000 K. The spatial structure of the emission is estimated using a Hα template corrected for dust extinction. Synchrotron emission is based on an extrapolation of the 408 MHz map of Haslam et al. (1982) from which an estimate of the free-free emission was removed. A limitation of this approach is that this synchrotron model also contains any dust anomalous emission seen by WMAP at 23 GHz. The thermal emission from interstellar dust is estimated using model 7 of Finkbeiner et al. (1999).

For the purely descriptive purposes of this example, eight different regions of the sky located at intermediate Galactic latitudes are taken (four of them uniformly distributed across the 40° North Galactic latitude parallel and four of them distributed in the same way 40° South of the Galactic plane). For each region, a 512×512 pixel flat and square patch is selected (at 44 and 100 GHz). Pixel size is 1.72 arcmin for the two frequencies. Therefore, each patch covers an area of 14.656 deg^2 of the sky. Once the region havs been selected, simulated extragalactic point sources are added with a spectral behaviour described by eq. (2.62). It is taken as frequency of reference $\nu_0 = 44$ GHz. Note that eq. (2.62) is expressed in flux units and the maps are in $(\Delta T/T)_{th}$: the appropriate unit conversion before adding the sources is made. The antenna beam is also taken into account: the full width at half maximum (FWHM)=24 arcmin for the 44 GHz channel and FWHM=9.5 arcmin at 100 GHz. Finally, after doing that, it has been added to each patch uniform white noise with the nominal levels specified for *Planck* (The Planck Collaboration, 2006) and this pixel size.

The goal of this chapter is to compare the performance of the multi-frequency approach with that

[1] `http://www.apc.univ-paris7.fr/APC_CS/Recherche/Adamis/PSM/psky-en.php`

of the single-frequency matched filter. In particular, it is expected that the MMF is able to detect fainter sources than the matched filter. From recent works (López-Caniego et al., 2006; Leach et al., 2008), it is known that in this kind of *Planck* simulations, the matched filter can detect sources down to fluxes ~ 0.3 Jy (the particular value depends on the channel and the region of the sky). Here, sources in the interval $[0.1, 1.0]$ Jy will be simulated, plus a few cases, that will be described below, where even lower fluxes are necessary. Regarding the spectral index of the sources, according to González-Nuevo et al. (2008), most radio galaxies observed by WMAP at fluxes ~ 1 Jy show spectral indices that lie in the range $[-1.4, 1.0]$.

The interesting intervals of flux and spectral index are sampled by simulating sources with fluxes at 44 GHz $S_0 = \{0.1, 0.2, 0.3, 0.4, 0.5, 0.6, 0.7, 0.8, 0.9, 1.0\}$ Jy and values for the spectral index $\gamma = \{1.0, 0.7, 0.4, 0.1, -0.2, -0.5, -0.8, -1.1, -1.4\}$. For each pair of values (S_0, γ), 100 point sources have been simulated. The point sources are randomly distributed in the maps (the same source is placed in the same pixel in both frequencies), with only one constraint: it is forbidden to place a source closer than $FWHM_{44}/2$ pixels from any other. In this way, source overlapping is avoided. Image borders are also avoided. For each set of 100 sources, it is proceeded in the following way: one among the eight patches we have is randomly chosen we have and place 10 sources in it. Then, other patch (allowing repetition) is randomly chosen and place the next 10 sources, and so on. In total, 9000 sources have been simulated for this exercise (the additional simulations at fluxes below 0.1 Jy are not included).

Then, each image is filtered several times for different MMFs. As it was shown in the cited work (Lanz et al., 2010), the SNR of the detected source is maximal for the correct choice of this parameter, and by construction (we want an *efficient* estimator of the flux density of the source), the uncertainty assigned to the source is the square root of the variance expressed in eq. (2.57) for the correct value of γ. While the parametrisation of eq. (2.62) is perfectly adequate in our case, any other parametrisation, even a non-functional description of the vector $\mathbf{f}$ by means of its components, could be used in other cases, e.g. when more than two frequencies are considered simultaneously.

3.3 Results and discussion

In order to compare the matched filter (MF) and the matched multifilter (MMF), the same maps with both methods are used. It means that not only the maps but also the sources are identical for the two filters (their intrinsic fluxes and positions). Each simulation is filtered separately with the MF (2.36) and the MMF (2.56). In order to have a better estimation of the power spectra, avoiding as much as possible aliasing effects, a power spectrum estimator that uses the 2D Hann window (Jiang et al., 2002)

is implemented.

The performance of the two methods will be compared in terms of the following aspects: spectral index estimation, source detection and flux estimation.

3.3.1 Source detection

Direct comparison of source detection between the MF and the MMF is not an obvious task because for $N = 2$ input images the MF produces two filtered images, whereas the MMF produces only one combined filtered map. The meaning of 'detection' in the MMF case is straightforward (once a detection criterion is chosen, a source is detected or not), but in the MF case the situation is not so clear. Imagine it is decided to apply the same detection criterion to the two MF filtered images (which is not an obvious option), then for a given source three different outcomes of the detection are possible:

- The source may be detected in both maps.
- The source may be detected in only one of the maps.
- The source may be detected in none of the maps.

In the first two cases, point source catalogues can be obtained (with different number of objects, in principle, for the two frequencies), but only in the first case are we able to estimate the flux at the two frequencies and therefore the spectral index. In the case of the MMF, if the source is detected it is automatically known the spectral index and eq. (2.62) can be used to give the fluxes at the two frequencies.

Therefore, in the following lines two different cases will be distinguished when it is spoken about detections with the MF. On the one hand, the *intersection* of the detections in the two channels gives us the objects that can be used for studying the spectral index distribution; on the other hand, the *union* of the two sets gives us the total number of objects that can be detected in at least one of the channels. For the MMF, both sets are the same by definition.

Regarding the detection criterion, for simplicity it is applied the same criterion to all the filtered maps: the widespread 5σ threshold. Note that the 5σ threshold corresponds to different flux values for different filters. However, in this chapter, it will be followed the standard 5σ criterion for simplicity.

Figure 3.1 shows the real sources (in per cent) that are detected above a 5σ level detection whose intrinsic fluxes (values introduced in the simulations) in the reference frequency (S_0) are the corresponding values in the horizontal axis. Table 3.1 shows the flux at which it is able to detect at least the 95% of the sources. We can observe several interesting aspects. The first one is the fact that the

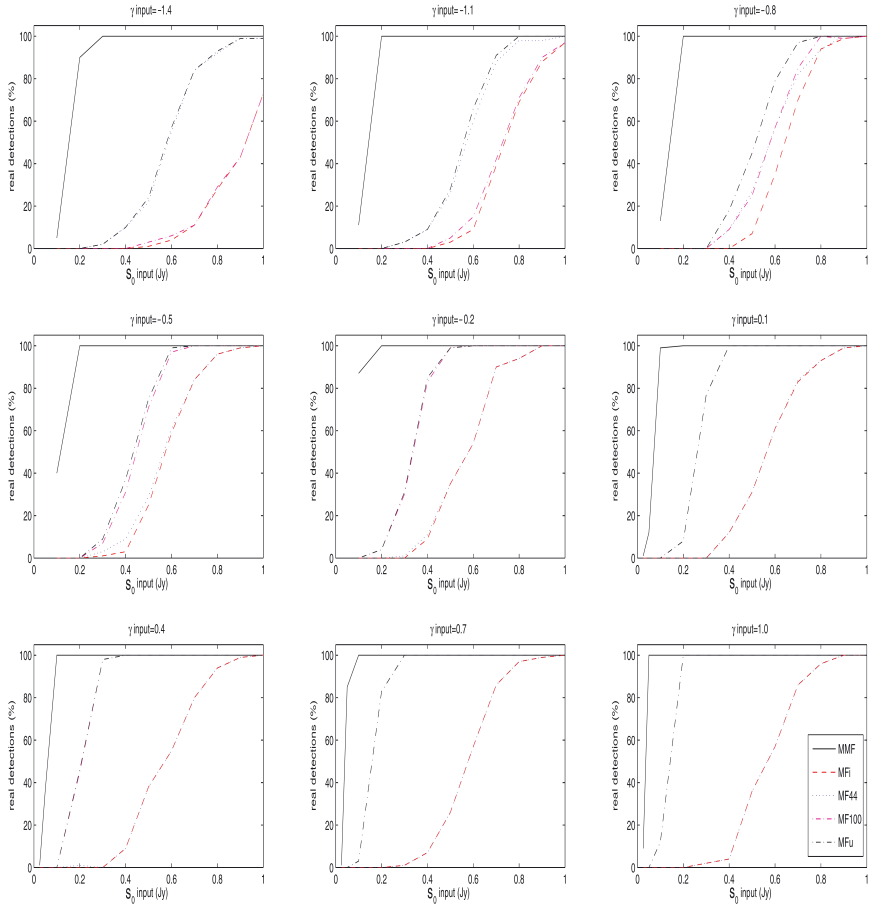

Figure 3.1 - Number of detections against the input value of S_0 for different values of the spectral index γ. MF44 represents the sources detected with the MF at 44 GHz. MF100 the same but at 100 GHz. MFi is the intersection of MF44 and MF100, and MFu is the union of MF44 and MF100.

MMF improves the level of detection with respect to the MF level for all the values of γ that have been inserted.

The second one is a natural selection effect. More flat/inverted sources ($\gamma \sim 0$/ positive values of γ) are detected at low fluxes than steep ones (negative values of γ). Figure 3.1 and Table 3.1 show us that the level of detections is higher for positive values of γ than for negative values. Keeping in mind that the reference frequency ν_0 is equal to 44 GHz, and according to eq. (2.62), it can be seen that for $\gamma < 0$, the simulated sources appear less bright at 100 GHz ($S_{100} < I_{44}$). In these conditions, it is quite difficult to detect sources at 100 GHz, and for this reason it is difficult to give the spectral indices for most of these point sources by means of the MF method when γ is strongly negative (for instance, $\gamma \lesssim -1$). On the other hand, for the opposite reason, two additional bins ($S_0 = 25$ and 50 mJy) are added for the cases $\gamma \geq 0.1$ because the MF (and the MMF too) seems to perform better at 100 GHz for high values of γ.

Another aspect to be remarked is the similar trend of the detection curve for the MF at 44 GHz for all the γ values (see Figure 3.1). The reason of this similarity is that the reference frequency is 44 GHz, and the maps simulated at this frequency are the same, independently of γ, with only one exception: the position of the sources. This means that statistically they are equivalent (with the inherent fluctuations due to the variation in the positions of the sources and the patches randomly selected). A similar number of detections is detected by means of the MF at 44 GHz, independently of γ. For this reason, it is difficult to characterise the spectral behaviour of the sources for $S_0 \lesssim 0.5$ Jy, because there is not a high percentage of detected sources at 44 GHz below that value of S_0.

Additionally, it is observed that the MMF is capable to detect sources with $S_0 < 0.1$ Jy for $\gamma \gtrsim 0.1$. It is interesting to compare this with the MF which does not detect sources below 0.1 Jy in the conditions of this chapter. The method presented her, allows us to detect point sources whose S_0 is too low to be detected with the traditional MF.

To summarise, it can be said that the MMF improves the detection level. Specially, remarkable are the cases where the sources are near to be *flat* (central row of Figure 3.1). At 100 GHz, the MF recovers the 100% of the sources for $S_0 \sim 0.4 - 0.6$ Jy. Meanwhile, the MMF reaches this level for $S_0 \sim 0.1$ Jy. This particular case is really interesting because high-frequency surveys show that most of the sources have this spectral behaviour.

3.3.2 Spectral index estimation

One interesting quantity commonly used to describe the different subpopulations of sources as a function of its frequency behaviour is the spectral index. Normally, in single-frequency detection methods,

γ	$S_{0(MMF)95\%}$ (Jy)	$S_{0(MF_{44})95\%}$ (Jy)	$S_{0(MF_{100})95\%}$ (Jy)	$S_{0(MFi)95\%}$ (Jy)	$S_{0(MFu)95\%}$ (Jy)
-1.4	0.3	0.9	>1.0	>1.0	0.9
-1.1	0.2	0.8	1.0	1.0	0.8
-0.8	0.2	0.9	1.0	0.9	0.7
-0.5	0.2	0.8	0.6	0.8	0.6
-0.2	0.2	0.9	0.5	0.9	0.5
0.1	0.1	0.9	0.4	0.9	0.4
0.4	0.1	0.9	0.3	0.9	0.3
0.7	0.1	0.8	0.3	0.8	0.3
1.0	0.05	0.8	0.2	0.8	0.2

Table 3.1 - Fluxes in the reference frequency (S_0) for which are detected at least the 95% of the sources for the different filtering methods. MMF, MF44, MF100, MFi, MFu as the Figure 3.1.

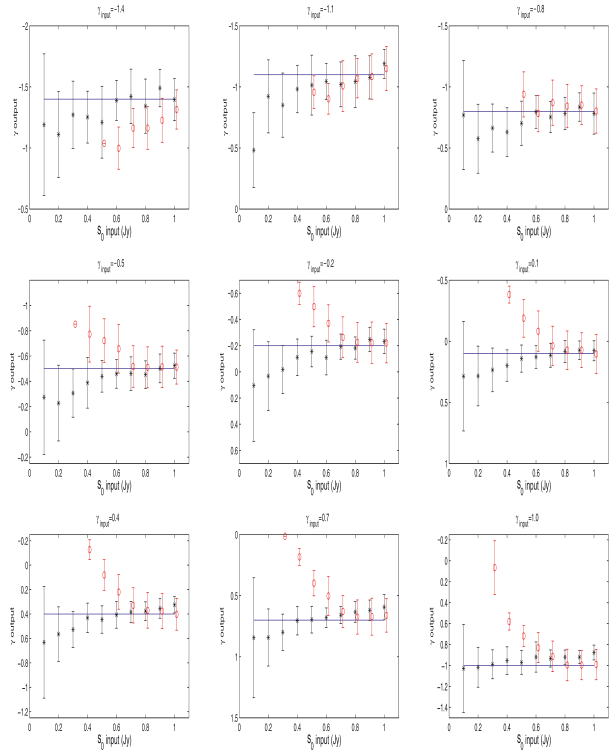

Figure 3.2 - Values of γ recovered by means of the MMF (asterisks) and the MF (circles). The line indicates the ideal recovering of the input. The circles corresponding to the MF are slightly displaced in the horizontal axis in order to distinguish the results.

the spectral indices are estimated using the detected fluxes in two different frequencies (equation 2.62). On the contrary, in the method proposed here, the spectral indices (the one that maximises the SNR) and the fluxes (only at the reference frequency) are simultaneously detected. Then, the fluxes at the other frequencies are estimated using the usual relation (equation 2.62). In Figure 3.2 one can see how the spectral indices are recovered by means of the MMF and by the MF. In general, we observe that the MMF is able to recover the value of γ with more accuracy and less uncertainty than the traditional MF.

Another aspect is that the error bars increases when S_0 is smaller. It seems logical because there are fainter sources and a smaller number of detections (see Figure 3.1). Then, at $S_0 = 0.1$ Jy, we can see that the estimation of γ is not as good as wished because it has a great uncertainty. The main reason is that the SNR is close to the threshold level imposed.

In the case of the MF, the spectral indices are correctly estimated for $S_0 \gtrsim 0.7$ Jy at $\gamma \geq -0.8$. At lower values of γ, it is found the same problem that it was mentioned before: there are a few detections at 100 GHz below 0.7 Jy (Figure 3.1). Since the detected sources are close to the noise level, the fluxes recovered present an overestimation with respect to the input value due to the Eddington bias (Eddington, 1913), an effect produced close to the noise level when a source is placed in a background peak. As it was said before, and seeing the Figure 3.1, more sources are detected at 100 GHz than at 44 GHz for values of the spectral index larger than -0.8.

Finally, we can observe an interesting aspect of the MF. When there are not sufficient detections in at least one channel (the sources detected are below the $\sim 40\%$ of the total number of sources), the estimation of the spectral index is not good. For $\gamma \leq -1.1$, the sources at 100 GHz are much fainter and the number of detections at this channel is really small. Then, because of the Eddington bias, the flux at this frequency is overestimated, and consequently, the value of γ is overestimated too. The Eddington bias explains as well the underestimation of γ in the other cases. The only difference is that now it is at 44 GHz where we have a smaller number of detections. If we also see the Figure 3.1, we observe that for values of $S_0 \lesssim 0.6$ Jy, we are pretty close to the noise level. It means that the noise fluctuations in the maps produce an overestimation in the flux at 44 GHz (S_0) and, as a consequence, an underestimation in γ. In summary, for $\gamma = -1.4$ and -1.1, the Eddington bias appears at 100 GHz (overestimation of the spectral index). For the rest of values of γ, this bias appears at 44 GHz (underestimation of the spectral index).

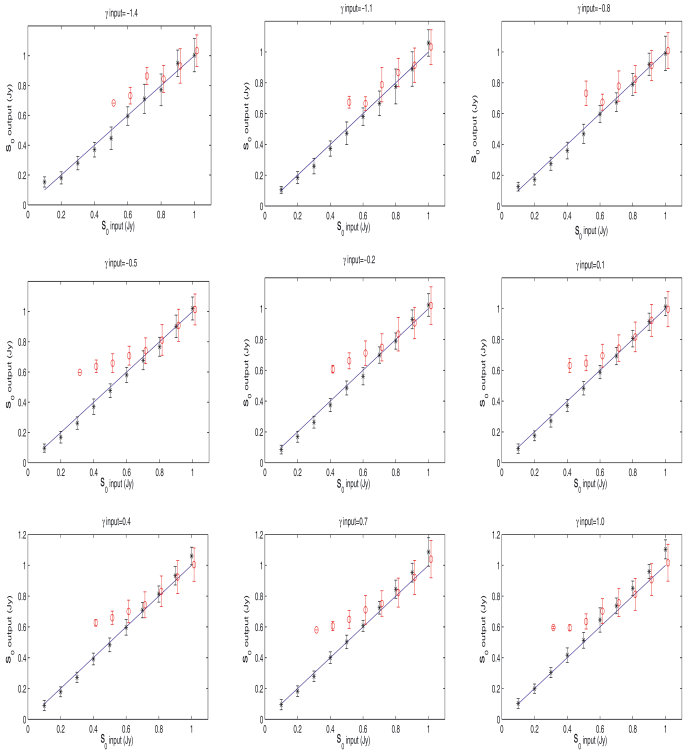

Figure 3.3 - Values of S_0 (flux at 44 GHz) recovered by means of the MMF (asterisks) and the MF (circles). The line indicates the ideal recovering of the input. The circles corresponding to the MF are slightly displaced in the horizontal axis in order to distinguish the results.

3.3.3 Flux estimation

Figure 3.3 shows the recovered flux at the reference frequency (44 GHz) for a given value of the spectral index. The error bars recovered with the MF are, in general, larger than the ones obtained with the MMF. It is particularly notorious at small values of S_0, where the recovered values of the flux have a good agreement with respect to the input values, with small error bars.

In general, for all the values of γ studied, the MMF is a suitable and effective tool to estimate the S_0 of the sources. For the MF, we observe a good determination of S_0 for input values above 0.7 Jy. For smaller values, S_0 has a higher value than its real one. That is due to the Eddington bias at 44 GHz. At this frequency, in Figure 3.1, we observe that for values smaller than 0.6 Jy, only a $\sim 40\%$ of the total sources are detected. That means that many of these sources are close to this noise level. For the correct estimation of S_0 and γ, it is necessary a good detection of the sources at the two channels. For low values of S_0 the number of detected objects is small and there are few statistics.

The same conclusions are applicable to the estimation of the fluxes at the second frequency (100 GHz in this chapter), even if in the MMF case these fluxes are estimated using equation 2.62 with the consequent propagation of the detection errors.

3.3.4 Reliability

For academic purposes, in the previous sections, we have seen simulations by introducing 100 sources for each of the pair values of flux at reference frequency and spectral index (see section 3.2), which simplifies the comparison between both filters for all the cases under study. However, it is well known that the number of sources per flux interval, the source number counts, is not constant (De Zotti et al., 2005; González-Nuevo et al., 2008) nor is the spectral index distribution (Sadler et al., 2008; González-Nuevo et al., 2008; Massardi et al., 2009). In order to study the performance of this multifrequency method under more realistic simulations, a new set of simulations (100) is produced with the following characteristics:

- It is used as a background the same eight regions described in the previous sections.
- The sources were simulated with an almost uniform Poissonian distribution (see González-Nuevo et al. (2005) for more details about the method) at 44 GHz, with fluxes that follow the source number counts model of De Zotti et al. (2005).
- The fluxes at 100 GHz were estimated assuming random spectral indices from the González-Nuevo et al. (2008) distribution.

- The point source maps were filtered with the same resolution as the background maps and randomly added to them.

There is also another interesting quantity commonly used in the study of the performance of a source detector: the number of spurious sources. Spurious sources are fluctuations of the background that satisfied the criteria of the detection method and therefore are considered as detected sources. It is clear that the best method will be the one that has the best detections versus spurious ratio. The maps are filtered using the MMF and the MF at both frequencies. The position and flux of the sources are estimated above 3σ level and, by comparing them with the input source simulations, one can count the number of real and spurious sources that are detected. It is necessary to change the detection level from 5σ to 3σ in order to increase the number of spurious sources to make the analysis.

In Figure 3.4, we observe the number of real sources that both methods are capable to detect, whose intrinsic fluxes are higher than the corresponding value in the horizontal axis. As we can observe at 44 GHz, MMF detects a higher number of real sources for fluxes below $\sim 0.4 - 0.5$ Jy, being this difference very important at lower fluxes. At 100 GHz, we observe a similar behaviour, but in this case the differences between the MF and the MMF start at ~ 0.2 Jy. If we observe the Figure 3.1, we note that the number of sources detected with the MF is higher at 100 GHz than at 44 GHz for values of the spectral index between 0 and -0.5. These values of γ, according to the model used to simulate the point sources in this section, are the most frequent for real sources. This gives us an idea about why the detection level of the MF is higher at 100 GHz.

In Figure 3.5, the *reliability* of both methods are compared at 44 and 100 GHz. Reliability above a certain recovered flux is defined as $r = N_d/(N_d + N_s)$, where N_d is the number of real sources above that flux, and N_s is the number of spurious sources above the same flux. At 44 GHz, a $\sim 100\%$ of reliability is reached at fluxes of ~ 0.3 Jy with the MMF. However, the MF at this frequency reaches this level of reliability only for ~ 1 Jy. On the other hand, at 100 GHz better levels of reliability are obtained. For instance, with the MMF we have at 0.1 Jy more than 95% of reliability, and the MF reaches these values for fluxes of ~ 0.3 Jy. Therefore, the MMF is more reliable than the Mf, specially at lower fluxes.

Additionally, and according to the expression of the reliability, it can established the flux for which we have the 5% of spurious sources. Using the MF, it is found $\sim 0.5 - 0.6$ Jy and 0.25 Jy at 4 and 100 GHz, respectively, to be compared with 0.15 Jy and < 0.1 Jy in the case of the MMF.

Moreover, it is made an additional plot where it is represent, for both frequencies, the number of real sources detected versus the number of the spurious sources (Figure 3.6). In this way, what it is represented is the number of sources that a method detects, given a number of spurious sources. If

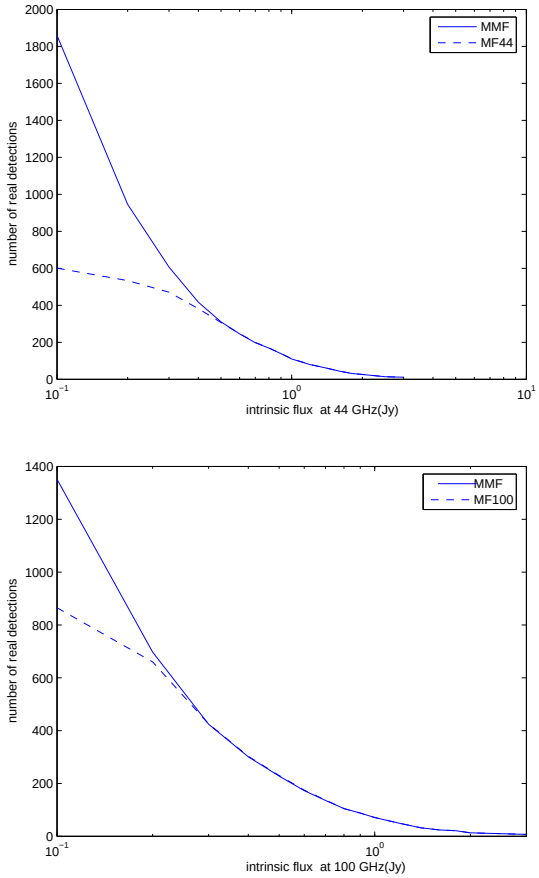

Figure 3.4 - Number of real sources recovered by the MMF (solid line) and the MF (dashed line) at 44 GHz (left-hand panel) and 100 GHz (right-hand panel) whose intrinsic fluxes are higher than the corresponding value in the $x-$axis.

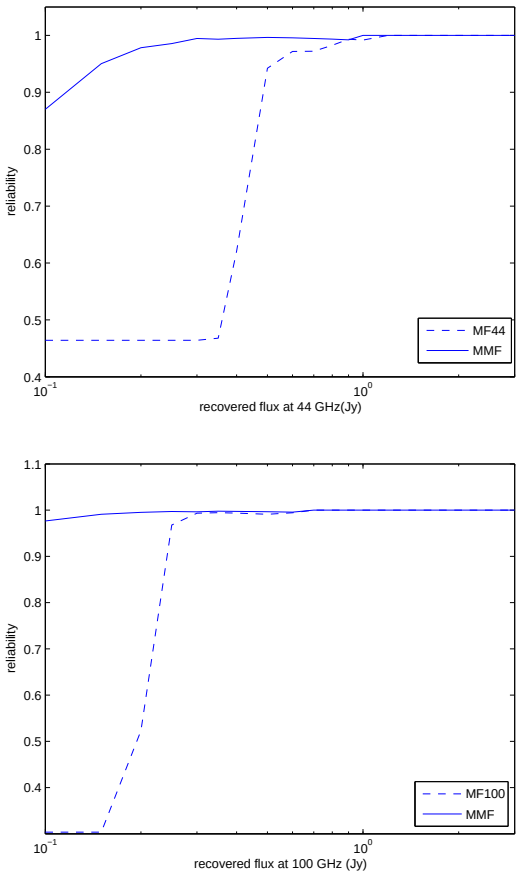

Figure 3.5 - Reliability versus recovered flux for the MMF (solid line) and the MF (dashed line) at 44 GHz (left-hand panel) and 100 GHz (right-hand panel).

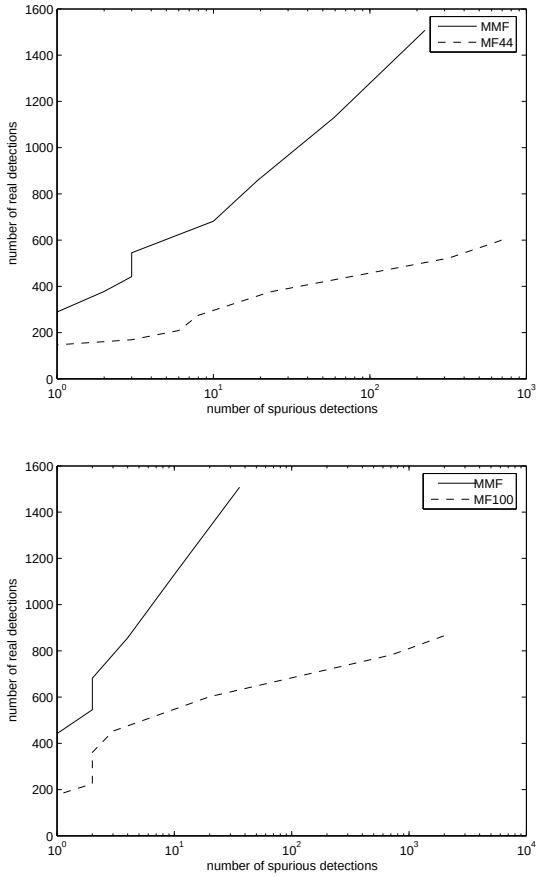

Figure 3.6 - Number of real sources recovered by the MMF (solid line) and the MF (dashed line) at 44 GHz (left-hand panel) and 100 GHz (right-hand panel) versus the number of spurious sources.

both plots are compared, we can see that the curve of the MMF is always above the MF. It means that, fixing a number of spurious detections, more real sources are detected with the MMF.

Finally, it is necessary to point out that the plots introduced here are not directly comparable to Figure 3.1, due to three basic and important differences:

- A different way to simulate the point sources.
- A different level of detection (in this case, a 3σ level).
- In Figure 3.1, it is represented the number of sources with the corresponding flux in the horizontal axis. In the plots of this section, what it is represented is the number of sources whose fluxes are higher than the corresponding value in the horizontal axis.

3.4 Conclusions

The detection of extragalactic point sources in CMB maps is a challenge. One has to remove them to do a proper study of the cosmic radiation. In addition, it is of great interest to study their properties, spatial and spectral distributions, etc. For this reason, it is necessary to have suitable tools to detect and extract these sources. There are many filtering techniques that have been used in this context. In this chapter, the MF have been used, one of the most studied techniques, and it have been compared with a new multifrequency one based on the MMF. The great difference is that the latter takes into account information from all the channels of the same sky region in a simultaneous way. In particular, an example for $N = 2$ is shown.

The different tests used have shown an improvement in the results obtained by the MMF with respect to the traditional MF. The number of detections is always higher when the MMF is used. In Figure 3.1 we see that there is a high number of detections with the MMF, even for small values of S_0. It should be studied in more detail, but it is easy to see that one could detect and characterise point sources with low fluxes for $\gamma > 0$. For this reason, this tool is a powerful technique to detect faint sources in CMB maps.

Another important aspect is to give a good estimation of the quantities chosen to determine the sources, basically the spectral index and the flux at the reference frequency. In both cases, we can see that the MMF improves the results obtained with the MF: the values are close to the input values with smaller error bars (with one exception, the determination of the spectral index for $S_0 \lesssim 0.5$ Jy at negative values of the input γ). This is a significant fact in order to be able to detect and study properly these kind of sources.

Additionally, a set of more realistic simulations have been made in order to study and compare both filters in the sense of the spurious sources. The threshold detection has also been changed from 5σ to 3σ to find more spurious sources and make a more complete statistical analysis. First of all, the number of real detections that we obtain with both techniques at 44 and 100 GHz is compared. By contrasting the plots of Figure 3.4, we appreciate that, at lower fluxes, more real sources with the MMF are detected than with the MF. This aspect is more notorious at 44 GHz.

One can also study the reliability of both methods. One can obtain a high number of real detections, and simultaneously find a large number of spurious sources. Precisely, the reliability is a quantity that gives the number of real detections over the total number of sources detected. Comparing the plots of the Figure 3.5, one can observe that the reliability of the MMF is much higher than the reliability of the MF for low fluxes. This difference is particularly important at 44 GHz, where the MF obtains similar values to the reliability of the MMF only for fluxes close to 1 Jy. At 100 GHz, the MF has the same reliability of the MMF only for fluxes greater then $\sim$0.3 Jy.

The last aspect used to compare both methods is to look at the number of real sources for a fixed number of spurious detections. The most efficient method is the one that has higher number of real detections for the same value of spurious detections. If we see the Figure 3.6, the best method is the MMF because its curves are always above the MF, i.e. if a number of spurious sources is taken, the MMF recovers a larger number of real objects.

Finally, it has been commented at the beginning of the subsection 2.9.1 the possibility of devising a filtering method (the MTXF) that does not use the frequency dependence of the sources altogether, totally independent of the frequency behaviour of the sources (flat, steep or inverted). This fact is significant in the sense that this filtering method is a robust technique for changes of f_ν. By contrast, it is necessary to impose the condition of orthonormalisation of the matrix of the filters (see Herranz and Sanz (2008) and Herranz et al. (2009) for more details). This condition minimises the power of the method. On the contrary, the MMF is optimal in the sense of the SNR (see section 2.9.1), but more complicated because another set of parameters (f_ν) has to be optimised. As one can see, the MTXF and the MMF are complementary.

Chapter 4

Application of the MMF over real WMAP 7-year data

4.1 Introduction

After checking the efficiency and robustness of the multifrequency method in simulated maps in the previous chapter, the next and natural step is to apply the MMF in *real* WMAP $7-$year maps at 61 and 94 GHz (channels V and W of WMAP). In order to compare the results obtained with the MMF, a comparison between the WMAP catalogues and the MMF one is done. It is necessary to remark at this point one aspect: the WMAP science team use two different methods to build their catalogue:

- The first one uses the matched filter in the harmonic space: $b_\ell/(b_\ell^2 C_\ell^{CMB} + C_\ell^{noise})$, where b_ℓ is the transfer function of the WMAP beam response (Jarosik et al., 2011) and C_ℓ's are the corresponding power spectra of the CMB and noise . Any $> 5\sigma$ peak in the filtered maps (threshold detector) in any channel is included in the catalogue and fitted in the real (and *unfiltered*) maps to a Gaussian profile plus a planar baseline. The Gaussian amplitude is converted to a flux density by using the conversion factors given by the Table 2 in Jarosik et al. (2011) and the uncertainty is calculated from the 1σ uncertainty in the fit amplitude. For the rest of channels, their flux densities are included if they exceed 2σ. Summarising, not all the sources included in this catalogue are 5σ in the frequency they appear: indeed, for a same object we could have only one 5σ detection in one channel and the rest could be 2σ.

- The second method is quite different from the used in this Thesis and is the CMB-free method that was originally applied to one-year and three-year V- and W-band maps by Chen and Wright

(2008), and to five-year V- and W- band maps by Wright et al. (2009). In the seven-year data is applied to Q, V and W bands by Chen and Wright (2009), being the V- and W- band maps smoothed to the resolution of Q band. A special ILC (see section 1.5) map is formed from the three maps using weights such that CMB fluctuations are removed, flat spectrum point sources are retained with flux densities normalised to the Q band and the variance of the ILC map is minimised. 5σ peaks in the filtered map are identified as point sources and their positions are obtained by the beam profile plus a baseline to the filtered map for each source. Their flux densities are estimated by integrating the Q, V and W temperature maps within $1^{\circ}.25$ of each source position, with a weighting function to enhance the contrast of the point source relative to background fluctuations, and applying a correction for Eddington bias due to noise.

Any source that appears in any of the two WMAP catalogues is included with a flag in the table 4.2. As one can see, the first method is the most similar to the used in this Thesis. The second is quite different, with a set of calculations and manipulations to the data that also make it very cumbersome the estimation of the error in the flux densities.

The structure of the chapter is as follows: first of all, a brief introduction about the application of the MMF over the WMAP data is done (section 4.2), explaining in detail some problems that appeared when maps were filtered, in particular the related to the antenna beams. In contrast with the previous chapter, where the beams were assumed to Gaussian profiles, the V and W channels of WMAP are distant from this analytical function. Fortunately, the WMAP science team provide the radial beam profiles that will be introduced in the code of the MMF. Once explained all these considerations about the data that must be taken into account, results are shown with the corresponding discussion (section 4.3). In particular, there are two tables with Galactic and extragalactic sources (see tables 4.1 and 4.2, respectively), showing their equatorial coordinates, their flux densities (and their errors), their spectral indices, their id. in other catalogues and the flags that indicate if they were detected by WMAP, NEWPS (see López-Caniego et al. (2007)) or the Early Release Compact Source Catalogue of Planck (see Planck Collaboration et al. (2011c)). A figure with their positions in the sky in Galactic coordinates is also shown (see figure 4.1) and a histogram with the spectral index distribution (see figure 4.2), confirming the steepening of the extragalactic sources. Then, two figures (see figure 4.3) of the Euclidean-normalised differential counts are shown, beside two theoretical models of the source counts and the Planck ones. In order to compare the accuracy in terms of flux density, the flux density recovered by the MMF is compared with the flux density recovered by Planck at 70 and 100 GHz (see figure 4.5) and the same sources that have been detected by ATCA (see figure4.4).

Finally, a set of conclusions are written (section 4.4), confirming that the matched multifilter is able to detect more than 100 compact objects at 94 GHz (at this point we have to remember the 22 detections

made by López-Caniego et al. (2007) in a *non-blind* search) and steepening of the extragalactic objects above ~ 70 GHz, according with other previous works, as it will be shown.

4.2 Application to WMAP data

The WMAP V and W bands are particularly interesting because only a small fraction of WMAP sources were detected with SNR $\geq 5\sigma$ in these bands. An adapted version of the code described in detail in the previous chapter as well as in López-Caniego et al. (2007), Massardi et al. (2009) and in López-Caniego et al. (2009) has been used in this chapter, modified in order to handle two frequencies simultaneously and to accommodate the MMF filtering. The code reads in an input parameter file containing the specific characteristics of the maps to be analysed as well as the patch size, the pixel size and overlap among the patches to effectively cover the 100% of the sky. Then, it reads in the two input maps in Flexible Image Transport System (FITS) format and extracts the patches to be analysed using the tangential plane approximation implemented in the CPACK library [1]. Each pair of V and W patches is analysed simultaneously using the MMF, and a first set of detections is produced. Next, as it was explained previously, the code iteratively explores different values of the spectral index for each source (the test values of the spectral index used in this work are $-3.5 \leq \gamma \leq 3.5$, with a step of 0.05), allowing for the appearance of new possible detections. At the end, the code gathers all the candidates and generates a list of detections above a given SNR, converting the positions of the detected objects in the plane to the sphere. Flat patches of $14^{\circ}.6 \times 14^{\circ}.6$ has been used, each containing 128×128 pixels. The pixel area is 6.871×6.871 arcmin^2, corresponding to the HEALPix resolution parameter $N_{side} = 512$ (see Górski et al. (2005), for more details). In total there are 371 patches, with significant overlaps among them in order to avoid as much as possible border effects. As described in Massardi et al. (2009), a two-step process is performed, first doing a blind search across the sky and then refining the analysis obtaining new patches centred at the positions of the sources identified in the blind step. In this way any projection and border effect that we could have is further reduced. The SNR of the detected source is maximal for the correct choice of this parameter, and again, by construction (it is desirable an *efficient* estimator of the flux density of the source), the uncertainty assigned to the source is the square root of the variance expressed in eq. (2.57) for the correct value of γ.

When dealing with the V and especially the W WMAP bands, it is necessary to carefully characterise the properties of the beams, both to build the optimal filters (eq. 2.56) and to obtain a good photometry of the sources. WMAP beams, particularly at 94 GHz, are highly non-Gaussian. It is also necessary to take into account that for the W band the pixel size (6.871 arcmin) is dangerously close

[1] `http://astro.ic.ac.uk/~mortlock/cpack/`

to the minimum sampling of the FWHM required to avoid aliasing and that real sources are not necessarily located at the geometrical centre of the pixels. These systematic effects are dealt with in the following way.

The beam transfer functions (circularly symmetric) provided by WMAP[2] are used to create high-resolution templates of the beams (equivalent to the HEALPix $N_{side} = 4096$) projected into the tangent plane. The maps used to perform the analysis have a pixel size corresponding to $N_{side} = 512$. However, as it was said before, it must be considered that sources are not necessarily located at the geometrical centre of these $N_{side} = 512$ pixels. Therefore, taking the beam transfer functions, each $N_{side} = 512$ pixel is divided into 8×8 subpixels ($N_{side} = 4096$) using the following formula:

$$b_\ell = 2\pi \int b^S(\theta) P_\ell(cos\theta) d(cos\theta)/\Omega_B. \tag{4.1}$$

We can see that any value of the beam template in any angular position (θ) can be obtained from the beam transfer function using the Legendre polynomials. Then, the high-resolution beams were averaged over all the 8×8 possible displacements of the source centre inside a $N_{side} = 512$ pixel. In order to obtain a well-estimated average of the beams, the process described in this paragraph is repeated 5000 times and averaged over the beam templates obtained. These effective beam templates were then degraded to the same resolution of the maps ($N_{side} = 512$). In this way, on average, the effects of pixelisation and the possible offsets of the sources with respect to the geometrical centre of the pixel are taken into account.

A careful correction for the non-circularity of the beams would require a detailed knowledge of the combination of beam orientations for all scans through every position in the sky. Since this information is not available, it is only applied to the flux densities an average correction factor that takes into account the effective beam areas for each channel. The correction factors were obtained using the self-calibration method based on SExtractor (Bertin and Arnouts, 1996) AUTO photometry, described in González-Nuevo et al. (2008). In that work, the NEWPS 3-year sources detected above the 5σ level by SExtractor and with flux densities $S \geq 1$ Jy were used for self-calibration. Only three W-band sources satisfied these requirements and therefore the correction factor for this band could not be reliably estimated. To overcome this problem SExtractor has been applied to the W map at the positions of 296 sources observed by the Australia Telescope Compact Array (ATCA) and the Very Large Array (VLA). 15 of them were detected at $\geq 3\sigma$ by SExtractor. Since all the ATCA/VLA sources have been detected at a very high significance level, it was sure that there were no spurious detections in this sample. These sources were used to recalculate the effective beam area at 94 GHz. It is obtained $(2.50 \pm 0.09) \times 10^{-5}$ sr, to be compared with the nominal value of 2.07×10^{-5} sr for the symmetrised beam. Note that all

[2] lambda.gsfc.nasa.gov/product/map/dr4/beam_xfer_get.cfm

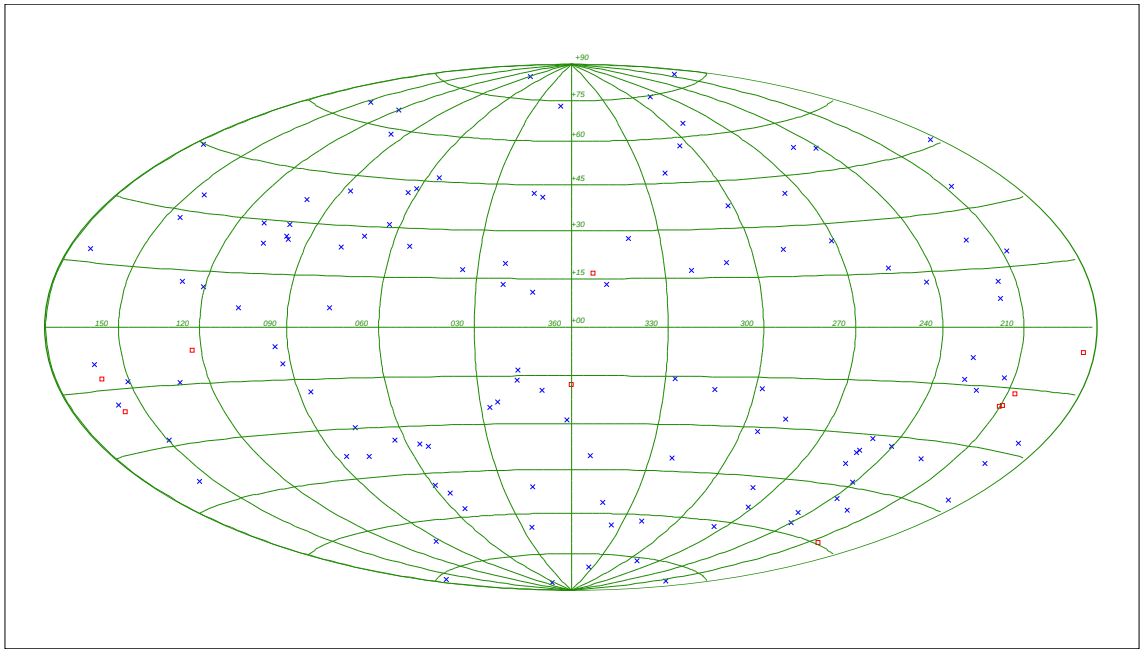

Figure 4.1 - Position on the sky, in Galactic coordinates, of the 129 sources detected by the MMF on the at 61- and 94-GHz WMAP 7-year maps. Blue crosses represent the position of the 119 sources with confirmed counterparts in other catalogues (see Table 4.2); red squares represent the positions of the 10 Galactic or unidentified detections (see Table 4.1).

the ingredients described in this section must be introduced in the code before the filtering process.

RA (°)	Declination (°)	$S_{94\mathrm{GHz}}$ (Jy beam^{-1})	*rms* (Jy)	Spectral index	Id in other catalogues
13.237	56.576	2.86	0.22	-1.25	NGC 281
44.622	-18.834	0.54	0.10	-2.40	...
52.264	31.338	4.81	0.57	4.50	NGC 1333
60.731	36.189	0.49	0.09	-3.35	NGC 1499
83.654	22.045	155	2	-1.15	Crab Neb
83.807	-5.419	216	3	-0.35	Orion region
84.018	-6.338	...	...	...	Orion region
85.396	-1.917	30	2	-0.2	Orion region
246.756	-24.633	...	...	...	Ophiucus region
285.398	-36.983	3.31	0.55	3.70	NGC 6729

Table 4.1 - Equatorial coordinates and identifications of the Galactic or unidentified detections. Sources without data are detections that, due to the multifrequency method, do not have a clear estimation of their flux density or the spectral index inside the studied range of γ.

Table 4.2 - Sources detected by the MMF on WMAP 7-year maps with counterparts in lower frequency catalogues. Presumably Galactic sources are listed in Table 4.1. The equatorial coordinates (first two columns) are in degrees. The flags in the last column indicate if the source is listed in any of the WMAP 7-year catalogues at any frequency (W) (Gold et al., 2011), in NEWPS 5-year at 61 GHz (N) (Massardi et al., 2009) or in the Planck catalogue at 70 or 100 GHz (P) (Planck Collaboration et al., 2011c). Sources without data are detections that, due to the multifrequency method, do not have a clear estimation of their flux density or the spectral index inside the studied range of γ. These sources with no flux density information are not taken into account in the subsequent analysis.

RA (°)	Declination (°)	$S_{94\mathrm{GHz}}$ (Jy beam^{-1})	*rms* (Jy)	spectral index	Id in other catalogues	Flags
1.483	-6.350	1.30	0.23	-0.80	PMN J0006-0623	WNP
5.033	73.493	1.41	0.26	-0.45	GB6 J0019+7327	P
6.514	-35.154	0.72	0.14	-1.65	PMN J0026-3512	WN
9.603	-24.892	1.65	0.33	0.30	PMN J0038-2459	WNP
16.715	-40.600	1.74	0.21	-0.55	PMN J0106-4034	WNP
23.160	-16.928	0.91	0.17	-1.20	PKS 0130-17	WNP
24.279	47.846	1.91	0.19	-1.20	GB6 J0136+4751	WNP
24.383	-24.518	1.56	0.30	0.20	PMN J0137-2430	WNP
32.749	-51.070	1.93	0.17	-1.00	PMN J0210-5101	WNP
34.293	73.803	0.73	0.13	-1.70	GB6 J0217+7349	NP
39.510	28.836	2.20	0.33	-0.20	GB6 J0237+2848	WNP
39.723	16.654	...	...	...	GB6 J0238+1637	WP
43.374	-54.666	1.56	0.20	-0.55	PMN J0253-5441	WNP
46.088	-62.233	1.31	0.25	0.05	PMN J0303-6211	WNP
49.957	41.450	2.67	0.16	-1.90	GB6 J0319+4130	WNP
50.377	-37.092	0.81	0.14	-1.55	Fornax A	NP
53.549	-40.203	1.47	0.25	-0.20	PMN J0334-4008	WNP
54.252	32.327	2.57	0.42	0.70	GB6 J0336+3218	P
54.862	-1.734	2.33	0.33	0.05	PMN J0339-0146	WNP
57.187	-27.832	1.36	0.26	0.00	PMN J0348-2749	WNP
61.062	-36.120	2.14	0.21	-0.65	PMN J0403-3605	WNP
64.548	38.025	1.96	0.16	-2.15	3C 111	NP
65.845	-1.374	3.39	0.25	-1.15	PMN J0423-0120	WNP
67.166	-37.869	1.66	0.29	0.05	PMN J0428-3756	WNP

Table 4.2 – continued

RA (°)	Declination (°)	$S_{94\mathrm{GHz}}$ (Jy beam^{-1})	*rms* (Jy)	spectral index	Id in other catalogues	Flags
68.301	5.418	3.51	0.41	0.50	GB6 J0433+0521	WNP
72.260	-81.053	1.61	0.28	0.25	PMN J0450-8100	WNP
73.914	-46.248	3.05	0.26	-0.50	PMN J0455-4616	WNP
74.270	-23.427	1.66	0.20	-0.75	PMN J0457-2324	WNP
78.849	-45.994	1.02	0.19	-1.40	PMN J0515-4556	WP
79.975	-45.795	2.30	0.21	-1.20	PMN J0519-4546	WNP
80.849	-36.456	2.57	0.19	-1.05	PMN J0522-3628	WNP
84.678	-44.028	3.15	0.21	-1.15	PMN J0538-4405	WNP
91.968	-6.396	7.99	0.49	0.40	PKS 0605-06	NP
92.460	-15.756	1.79	0.24	-0.50	PMN J0609-1542	WNP
97.363	-19.946	1.66	0.32	0.55	PMN J0629-1959	WNP
98.985	-75.242	2.03	0.19	-0.80	PMN J0635-7516	WNP
101.703	44.896	1.80	0.33	0.05	GB6 J0646+4451	WNP
102.564	-16.699	1.75	0.26	-0.35	PKS 0648-16	NP
110.556	71.313	2.15	0.26	-0.05	GB6 J0721+7120	WNP
111.493	-0.972	2.23	0.38	0.65	PMN J0725-0054	WP
114.856	1.724	0.96	0.18	-1.35	GB6 J0739+0136	WNP
117.689	12.478	2.04	0.23	-0.90	GB6 J0750+1231	WNP
126.524	3.272	1.27	0.22	-0.90	GB6 J0825+0309	WNP
129.076	-20.280	1.07	0.19	-1.10	PMN J0836-2017	WNP
130.356	70.885	0.91	0.15	-1.30	GB6 J0841+7053	WNP
133.730	20.128	2.48	0.29	-0.70	GB6 J0854+2006	WNP
140.233	44.738	0.89	0.14	-2.00	GB6 J0920+4441	WP
140.441	-26.324	1.07	0.21	-0.85	PMN J0921-2618	WP
141.810	38.974	2.63	0.21	-1.15	GB6 J0927+3902	WNP
159.372	-29.584	1.29	0.22	-0.75	PMN J1037-2934	WNP
159.659	5.136	0.80	0.16	-1.70	GB6 J1038+0512	W
164.323	-80.083	1.65	0.19	-0.85	PMN J1058-8003	WNP
164.615	1.562	2.86	0.22	-1.10	GB6 J1058+0133	WNP
171.870	-18.836	0.97	0.19	-1.20	PMN J1127-1857	WP
176.717	-38.190	0.92	0.15	-1.75	PMN J1147-3812	WNP

Table 4.2 – continued

RA (°)	Declination (°)	$S_{94\mathrm{GHz}}$ (Jy beam^{-1})	*rms* (Jy)	spectral index	Id in other catalogues	Flags
178.285	49.483	1.47	0.19	-0.70	GB6 J1153+4931	WNP
179.831	29.192	1.21	0.22	-0.60	GB6 J1159+2914	WNP
187.270	2.104	10.71	0.33	-1.20	GB6 J1229+0202	WNP
187.699	12.338	5.99	0.26	-1.05	GB6 J1230+1223	WNP
191.732	-25.848	...	...	...	PKS 1244-255	WNP
193.992	-5.821	8.59	0.32	-1.15	PMN J1256-0547	WNP
194.823	51.645	1.37	0.25	0.05	GB6 J1259+5141	W
197.630	32.472	0.82	0.13	-1.75	GB6 J1310+3220	WNP
201.390	-42.960	16.92	0.46	-1.20	Centaurus A	NP
204.426	-13.021	4.96	0.29	-0.60	PMN J1337-1257	WNP
209.267	19.351	1.39	0.21	-0.75	GB6 J1357+1919	WNP
214.876	54.421	1.05	0.20	-0.50	GB6 J1419+5423	WNP
216.967	-42.070	1.75	0.23	-0.75	PMN J1427-4206	WNP
229.382	-24.370	2.31	0.28	-0.40	PMN J1517-2422	WNP
237.415	2.563	1.54	0.27	-0.55	GB6 J1549+0237	WNP
237.763	5.461	1.77	0.26	-0.50	GB6 J1550+0527	WNP
243.420	34.145	2.58	0.25	-0.30	GB6 J1613+3412	WNP
244.386	-77.279	1.07	0.16	-1.20	PMN J1617-7717	WNP
246.561	-29.832	1.91	0.30	-0.40	PKS 1622-29	NP
248.816	38.155	3.25	0.25	-0.50	GB6 J1635+3808	WNP
249.747	57.392	1.98	0.29	0.55	GB6 J1638+5720	WNP
250.551	68.974	0.80	0.08	-2.45	GB6 J1642+6856	WNP
250.742	39.825	3.89	0.23	-0.75	GB6 J1642+3948	WNP
260.115	-1.025	2.18	0.27	-0.40	PKS 1717-00	NP
260.873	-65.025	1.32	0.25	-0.25	PMN J1723-6500	WP
263.303	-13.051	3.05	0.29	-0.30	PKS 1730-13	NP
263.593	38.888	1.08	0.20	-0.70	GB6 J1734+3857	WNP
265.933	-3.813	2.55	0.22	-0.90	PKS 1741-03	NP
267.966	9.655	4.05	0.26	-0.45	GB6 J1751+0938	WNP
268.340	28.738	1.65	0.21	-0.50	GB6 J1753+2847	WNP
270.301	78.459	1.05	0.17	-1.00	NVSS J180045+782804	WP

Table 4.2 – continued

RA (°)	Declination (°)	$S_{94\mathrm{GHz}}$ (Jy beam^{-1})	*rms* (Jy)	spectral index	Id in other catalogues	Flags
270.400	44.088	1.40	0.22	-0.45	GB6 J1801+4404	WNP
271.711	69.794	1.34	0.20	-0.25	GB6 J1806+6949	WNP
277.443	48.800	1.07	0.13	-1.60	GB6 J1829+4844	WNP
280.720	68.162	0.82	0.14	-0.90	GB6 J1842+6809	WP
282.241	67.063	0.84	0.13	-1.15	GB6 J1849+6705	WNP
287.737	-20.060	2.12	0.34	0.10	PMN J1911-2006	WNP
290.987	-21.081	1.50	0.25	-0.65	PMN J1923-2104	WNP
291.214	-29.282	7.01	0.28	-1.00	PMN J1924-2914	WNP
292.018	73.976	1.56	0.15	-1.20	GB6 J1927+7357	WNP
299.461	-38.755	2.04	0.26	-0.55	PMN J1957-3845	WNP
299.942	40.752	6.02	0.36	-2.25	Cygnus A	NP
300.337	-17.769	0.84	0.16	-1.60	PMN J2000-1748	WNP
302.849	-15.774	1.45	0.29	-0.25	PMN J2011-1546	WNP
314.018	-47.226	1.87	0.25	-0.45	PMN J2056-4714	WNP
323.562	-1.791	1.25	0.22	-1.00	PMN J2134-0153	WNP
324.128	0.682	1.67	0.28	-0.30	GB6 J2136+0041	WNP
327.069	6.999	3.98	0.23	-1.15	GB6 J2148+0657	WNP
327.945	-30.455	1.44	0.24	-0.55	PMN J2151-3028	WNP
328.366	47.275	1.93	0.26	-0.25	GB6 J2153+4716	NP
329.184	-69.703	1.81	0.22	-0.50	PMN J2157-6941	WNP
330.649	42.251	2.68	0.25	-0.30	GB6 J2202+4216	WNP
330.745	31.724	1.66	0.28	-0.05	GB6 J2203+3145	WNP
330.851	17.436	1.24	0.23	-0.70	GB6 J2203+1725	WNP
334.914	63.283	2.98	0.57	2.90	GB6 J2219+6317	NP
336.405	-5.002	3.43	0.26	-0.75	PMN J2225-0457	WNP
337.427	-8.582	2.69	0.30	-0.35	PMN J2229-0832	WNP
338.171	11.674	4.19	0.34	0.20	GB6 J2232+1143	WNP
338.909	-48.584	1.33	0.19	-0.85	PMN J2235-4835	WNP
341.600	-12.087	1.24	0.21	-1.05	PMN J2246-1206	WP
343.547	16.149	7.96	0.35	-0.35	GB6 J2253+1608	WNP
344.514	-28.003	3.58	0.28	-0.35	PMN J2258-2758	WNP

Table 4.2 – continued

RA (°)	Declination (°)	$S_{94\mathrm{GHz}}$ (Jy beam^{-1})	*rms* (Jy)	spectral index	Id in other catalogues	Flags
352.347	-47.438	1.18	0.22	-0.55	PMN J2329-4730	WP
359.607	-53.218	1.24	0.20	-0.60	PMN J2357-5311	WP

4.3 Results and discussion

The source detection was performed applying the MMF filter to the 7-year WMAP V and W maps, at 61 and 94 GHz, respectively. Only one (V1) of the 2 differencing assemblies has been used for the V band, because V1 and V2 are very similar. As for the W band, 2 (W2 and W3) out of the 4 differencing assemblies are used because their symmetrised beam profiles are geometrically very similar (same as for W1 and W4), and this makes the photometry easier. The W2 and W3 maps were combined pixel by pixel, weighting with the inverse of the variances of the pixels. To minimise the spurious detections due to the complex structure of the Galactic emissions near the equatorial plane and of the Large Magellanic Cloud (LMC) region, objects with $|b| \leq 5^\circ$ and within a radius of 5° around the LMC [$(80^\circ.894, -69^\circ.756)$ in equatorial coordinates] have been removed from the final catalogue. No sources are detected within the Small Magellanic Cloud.

4.3.1 Point source detection

The two-step filtering approach described in section 4.2 yields 129 5σ detections in the 61- and 94-GHz WMAP 7-year maps, outside the Galactic plane and LMC regions specified above. For each of them, the MMF gives the flux density at the reference frequency (94 GHz, ν_0 in eq. (2.62)) and the spectral index, the only free parameter of the method. The uncertainty on the spectral index can be estimated from intensive simulations made in Lanz et al. (2010). Table 4.1 lists the nine sources that are either well-known Galactic sources (like the Crab Nebula, the H_{II} regions NGC 281 and NGC 1499 or the star-formation regions NGC 1333 and NGC 6729) or located within Galactic molecular cloud complexes, like the Orion or the Ophiucus regions, or within regions of intense Galactic emissions, plus one unidentified source. Table 4.1 gives the flux densities within the WMAP 94-GHz beam. In most cases, these are lower limits to the total flux densities because the sources are resolved. Given the different beam sizes at the two frequencies, the spectral indices cannot be reliably estimated in the

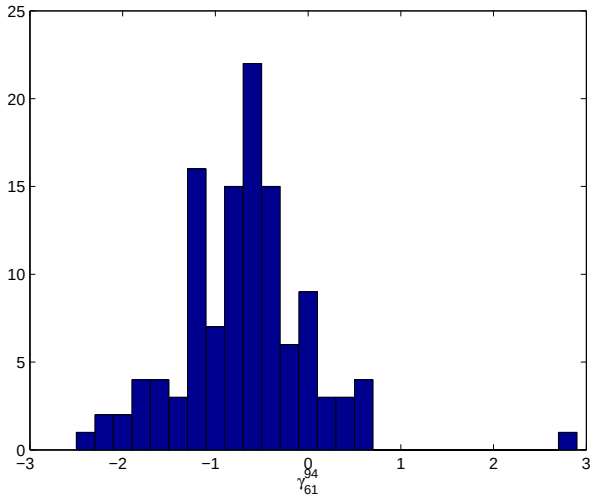

Figure 4.2 - Spectral index distribution of sources in Table 4.2.

case of resolved sources.

Excluding the 10 sources listed in Table 4.1, the MMF has detected 119 objects, listed in Table 4.2. All these objects have a counterpart in lower frequency radio catalogues, which cover the whole sky to much fainter flux density limits[3], (see Figure 4.1). The apparently ultrasteep ($\gamma_{61}^{94} = -2.25$) spectrum of Cygnus A is partly due to resolution effects (the 94-GHz beam encompasses a lower fraction of the total flux density than the 61-GHz beam).

In Tables 4.1 and 4.2, sources without an estimation of the flux density or the spectral index are objects that are only 'detected' at one frequency. Therefore, because the method used to filter the maps is multifrequency, the spectral indices of these sources fall outside the range studied in this work. These sources are not taken into account in the subsequent analysis.

The spectral index distribution of the sources in Table 4.2, shown in Figure 4.2, has a median value of -0.65 with a dispersion of 0.71. For comparison, Wright et al. (2009), mostly based on lower frequency WMAP data, found a mean spectral index $\langle\gamma\rangle = -0.09$, with a dispersion $\sigma = 0.28$. These results are therefore consistent with the steepening of source spectra above ~ 70 GHz found for different data sets (Sadler et al., 2008; González-Nuevo et al., 2008; Marriage et al., 2011; Massardi et al., 2010; Planck Collaboration et al., 2011b).

The Euclidean normalised source counts at 61 and 94 GHz are given in Table 4.3 and shown in Figure 4.3, where they are compared with the counts in the nearest *Planck* chan-

[3]Except for a few of the sources in Table 4.1, none of the objects detected by the MMF has an IRAS counterpart.

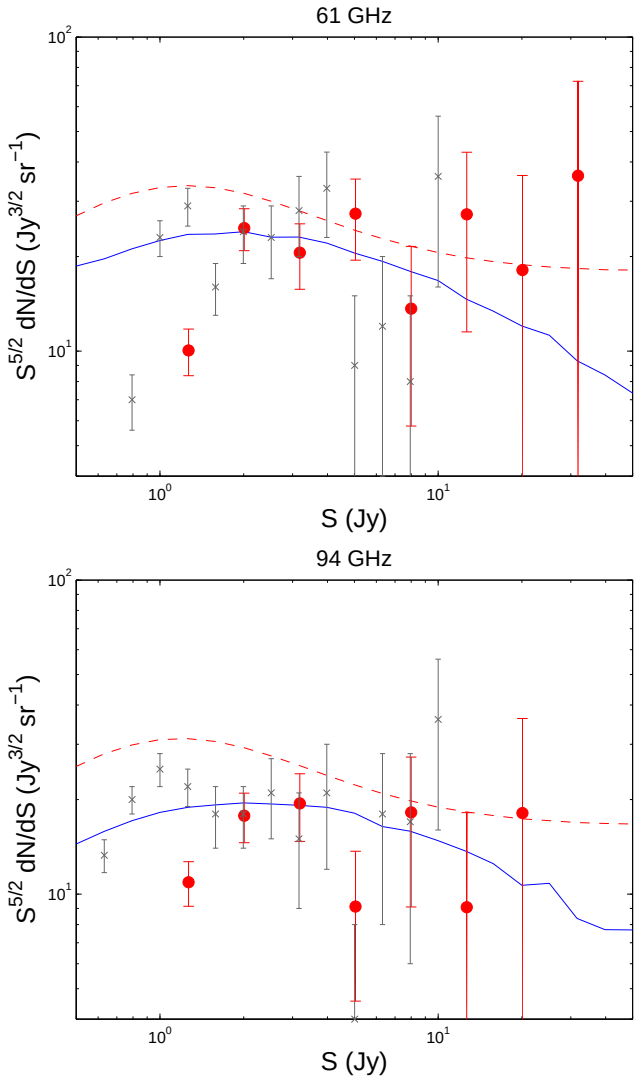

Figure 4.3 - 7-year WMAP Euclidean-normalised differential number counts at 61 and 94 GHz based on the MMF sample (red points) with Poissonian error bars and the Bayesian correction to the flux densities. The grey crosses are the *Planck* counts at 70 and 100 GHz (Planck Collaboration et al., 2011b). The solid lines are the prediction by the Tucci et al. (2011) model at 61 and 94 GHz, and the dashed lines are the prediction by the De Zotti et al. (2005) model at the same frequencies.

S (Jy)	$S^{5/2}$dN/dS (Jy$^{3/2}$ sr^{-1})	
	61 GHz	94 GHz
1.27	10.1±1.7	10.9±1.8
2.01	25±4	18±3
3.18	21±5	19±5
5.05	27±8	9±5
8.00	14±8	18±9
12.68	27±16	9±9
20.10	18±18	18±18
31.85	36±36	···

Table 4.3 - Euclidean-normalised differential number counts at 61 and 94 GHz, based on the MMF detections, in bins of $\Delta \log(S) = 0.2$ and taking into account the Bayesian correction to the flux densities.

nels (Planck Collaboration et al., 2011b) and with the predictions of the De Zotti et al. (2005) and Tucci et al. (2011) models.

In this figure, the flux densities obtained with the MMF were corrected with a Bayesian approach (Herranz et al., 2006) in order to remove as much as possible the Eddington bias (Eddington, 1913). This approach takes into account the distribution in flux density of the objects as a power law with unknown slope, and an additive Gaussian noise. It is important to point out that this correction is statistical, and therefore it has been taken into account only in the estimation of the source counts.

The comparison in Figure 4.3 shows that the completeness limit of the MMF is $\simeq 2$ Jy. Above this limit, the agreement with the *Planck* counts and with the Tucci et al. (2011) model is generally good. This confirms that the Tucci et al. (2011) model deals appropriately with the high-frequency behaviour of source spectra.

Although several data sets had suggested (Sadler et al., 2008; González-Nuevo et al., 2008) and then detected (Planck Collaboration et al., 2011b,a) a break in the bright extragalactic radio sources (at high-flux level) at ~ 70 GHz, this break is only well explained with the current data if the Tucci et al. (2011) model is considered.

4.3.2 Comparison with the WMAP catalogues

The WMAP Five-Band Point Source Catalog (Gold et al., 2011) lists all the sources that were detected at $\geq 5\sigma$ in at least one frequency channel, outside a mask excluding sources in the Galactic plane and

Magellanic Cloud regions. Flux densities in the other channels are reported if the signal is detected at a significance $> 2\sigma$. In this catalogue, 94-GHz flux densities are reported for 236 sources; 59 of them are detected at a $\geq 5\sigma$ level at 94 GHz. By contrast, the MMF guarantees that all the 119 (presumably) extragalactic sources, 104 of which are outside the WMAP Point Source Catalog mask, are detected at $\geq 5\sigma$ at 94 GHz. Most sources found by the MMF within the WMAP mask are close to the Galactic plane.

4.3.3 Comparison with NEWPS catalogues

López-Caniego et al. (2007) looked for sources in the WMAP 3-year maps at the positions of known 5-GHz sources (non-blind search) and reported 22 detections at 94 GHz (listed in the NEWPS 3-year catalogue). Massardi et al. (2009) combined a non-blind (based on the ATCA 20-GHz survey catalogue) and a blind search on WMAP 5-year maps, excluding the W (94 GHz) channel (NEWPS 5-year catalogue). At 61 GHz the authors detected 169 sources, 61 of which are not present in the catalogue of the MMF (if it is also taken into account Table 4.1); 45 of them, however, are detected at $\geq 3\sigma$ with the MMF in the blind step of the detection process previously explained. Seven of the other 18 sources are at $|b| < 15^\circ$ and may be contaminated by Galactic emission, and three lie in the LMC region, excluded from the search. The remaining eight sources have not been detected by the MMF. On the other hand, the MMF catalogue of extragalactic objects contains 16 sources not present in the NEWPS 5-year catalogue. It must be remarked that the MMF catalogue is completely based on a blind search, whereas the NEWPS catalogue was guided by a previous selection of sources detected at low frequency.

4.3.4 Comparison with ATCA and NRAO flux densities

The MMF sample of 94-GHz detections includes 85 sources with ground-based $\simeq 3$ mm observations either with ATCA[4] or with the NRAO 12-m telescope (Holdaway et al., 1994)[5]. The ATCA flux densities for these sources have been collected in the frequency range between 85 and 105 GHz with the 'old' ATCA digital correlator with up to 2×256 MHz bandwidth.

The MMF flux density estimates are compared with ATCA and NRAO measurements in Figure 4.4. There is evidence that the MMF somewhat overestimates the flux densities below $\simeq 2$ Jy, most likely due to the Eddington bias. Above 2 Jy the mean absolute fractional error $\langle |S_{\rm MMF} - S_{\rm ground}|/S_{\rm ground} \rangle \simeq 38\%$, somewhat higher than expected from the combination of nominal mea-

[4] http://www.narrabri.atnf.csiro.au/calibrators/index.html
[5] http://www.alma.nrao.edu/memos/html-memos/alma123/memo123.pdf

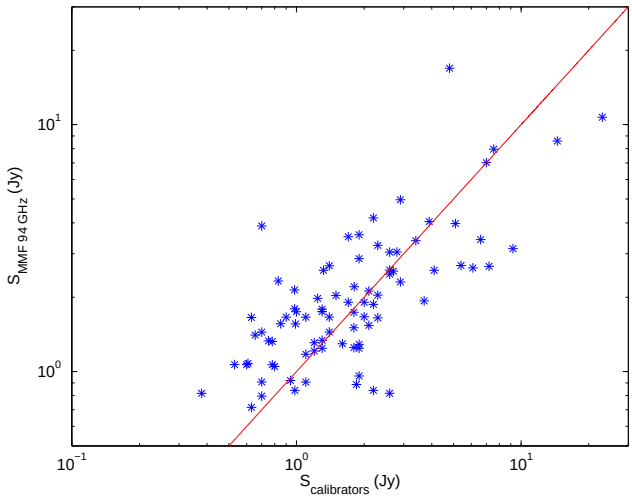

Figure 4.4 - Comparison between 94-GHz flux densities recovered by the MMF and the ATCA (3-mm) and NRAO (90-GHz) flux density measurements, for the 85 sources in common. No correction for the slightly different frequencies of the sets of measurements was made. The solid line is $x = y$.

surement errors and variability, suggesting that the true errors associated with the MMF flux density estimates are somewhat larger than the nominal values. In this respect, it must be noted that the WMAP 7-year maps are averages over 7 years of observations, while the ATCA and NRAO measurements refer to a single epoch.

4.3.5 Comparison with the *Planck* Early Release Compact Source Catalogue

Thanks to its higher sensitivity, *Planck* has detected far more sources than WMAP. The Early Release Compact Source Catalogue (ERCSC) lists 1381 sources detected at 100 GHz and 599 detected at 70 GHz; 308 and 788 of the ERCSC 70- and 100-GHz sources, respectively, are outside the WMAP Point Source Catalog mask. Three of the sources detected with the MMF in Table 4.2 are not present in the ERCSC, but are present in lower frequency catalogues with flux densities consistent with those inferred from WMAP data.

The ERCSC gives four different measures of flux density for each source. For the comparison with the results presented here, the estimate called FLUXDET has been chosen, which is calculated using an approach similar to the one referred here and appears to have higher reliability for low SNR values. Figure 4.5 compares the FLUXDET flux densities at 70 and 100 GHz with the MMF ones at the nearest WMAP frequencies (61 and 94 GHz, respectively). Again, there is evidence that the MMF flux densities are affected by the Eddington bias below $\simeq 2\,$Jy. The MMF flux densities of the five

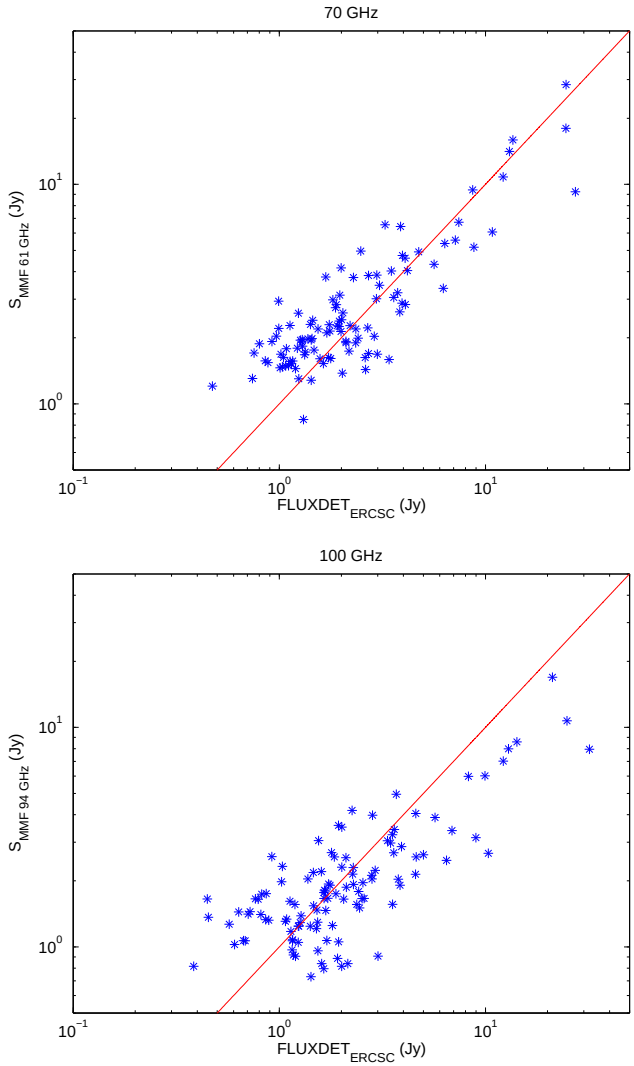

Figure 4.5 - Comparison of the flux densities recovered by the MMF on WMAP maps at 61 and 94 GHz with the FLUXDET values reported in the *Planck* ERCSC at 70 GHz (upper panel) and 100 GHz (lower panel), respectively. The solid line is $x = y$.

sources with $S_{\mathrm{MMF,94GHz}} \gtrsim 8\,\mathrm{Jy}$ are all lower than the ERCSC flux densities at 100 GHz. Two of these sources (the one at RA $= 91^{\circ}.968$, dec $= -6^{\circ}.396$ and Cen A) have a strong dust emission, seen in the IRAS survey, which enhances the 100-GHz flux density. The other three are well-known highly variable blazars (3C273, 3C279, 3C454.3), caught by Planck in a bright phase.

The spectral index distributions of the MMF sources are pretty close to that of the ERCSC sources: the median spectral index of the MMF sources is -0.65, with a standard deviation of 0.71; for ERCSC sources with $\gamma \leq 2$ (to avoid strong contamination by dust emission) and excluding the Galactic plane and the LMC region as defined previously in order to have a sample comparable with the MMF's, it is found a median value of -0.39 with a standard deviation of 0.52.

4.4 Conclusions

The detection of extragalactic point sources is a crucial task in the analysis of CMB maps because point sources are the main contaminant of the CMB power spectrum on small angular scales. From the same maps we can extract interesting astrophysical information about the point sources themselves. The development of efficient detection tools is therefore very important. The MMF holds the promise of achieving detections down to fainter flux densities than achievable by standard methods.

Applying this tool to 7-year WMAP maps at 61 and 94 GHz simultaneously, 129 5σ detections have been obtained at both frequencies, outside the Galactic plane (i.e. at $|b| > 5^{\circ}$) and the LMC regions. Nine of these sources, listed in Table 4.1, either are known Galactic sources or reside in regions of high Galactic emission. One additional source, also listed in Table 4.1, does not have a counterpart in low-frequency radio catalogues. All the other 119 sources, listed in Table 4.2, do have a low- frequency counterpart; 104 of them reside outside the WMAP Point Source Catalog mask. For comparison, the NEWPS 3-year catalogue contains 22 5σ detections at 94 GHz. Although the *Planck* ERCSC contains far more sources at the frequencies (70 and 100 GHz) nearest to those used in the present analysis, three sources not present in the ERCSC have been detected, yet with flux densities consistent with lower frequency measurements.

A comparison of the flux densities yielded by the MMF with those obtained at $\simeq 90\,\mathrm{GHz}$ with the ATCA or the NRAO 12-m telescope, and with the *Planck* ERCSC data at 70 and 100 GHz, shows a generally good agreement above $\simeq 2\,\mathrm{Jy}$, although the rms differences between MMF and ground-based or ERCSC values are larger than expected from variability and nominal measurement errors. This suggests that the errors associated with MMF flux density estimates are somewhat larger than the nominal values listed in Table 4.2. Below 2 Jy, the MMF flux densities tend to be somewhat overestimated, as the effect of the Eddington bias.

The distribution of 61–94 GHz spectral indices of sources in Table 4.2 has a median value equal to $\gamma_{61}^{94} = -0.65$ (with a dispersion of 0.71), while Wright et al. (2009), mostly based on lower frequency WMAP data, found a mean spectral index $\langle\gamma\rangle = -0.09$, with a dispersion $\sigma = 0.28$. The MMF results therefore confirm the steepening of extragalactic radio source spectra above ~ 70 GHz, suggested by various data sets (Sadler et al., 2008; González-Nuevo et al., 2008; Marriage et al., 2011; Massardi et al., 2010) and then confirmed by analyses of different samples (Planck Collaboration et al., 2011b,a; Giommi et al., 2012) of bright extragalactic sources extracted by the Planck ERCSC (Planck Collaboration et al., 2011c).

This average steepening observed in the spectra of bright extragalactic sources, which are mainly blazars in this frequency range (Angel and Stockman, 1980), has been recently interpreted by Tucci et al. (2011) in terms of the 'break' frequency, foreseen in the emission spectra of blazars by classic physical models for the synchrotron emission in the inner part of inhomogenous conical jets. Remarkably, this new model by Tucci et al. (2011) is able to give a good a fit not only to the source number counts presented here (see Figure 4.3; section 4.3.1), but also to almost all the published data on number counts and spectral index distributions of bright extragalactic radio sources up to, al least, 200-300 GHz.

Chapter 5

Conclusions and future work

5.1 Summary

In this Thesis I have introduced a novel technique for the multifrequency linear filtering and detection of point sources in astronomical images. This technique has been applied first to realistic simulations of CMB data and then to actual data from the WMAP satellite.

The framework of this Thesis has been summarised in the Introduction (see 1). The Cosmic Microwave Background (CMB) radiation was originated $\sim 380,000$ years after the Big Bang when the Universe cooled enough to form stable atoms due to the decoupling of the radiation (photons) and matter. After that moment, the radiation could travel through the space and we, after all this time since the decoupling, are able to observe it. This radiation, whose mean value is $T_0 = 2.7255 \pm 0.0006$ K (Fixsen, 2009), has some temperature anisotropies that were briefly commented in the Introduction. Between the last scattering surface and the observer, the path of CMB photons is affected by astrophysical scattering phenomena that can alter the energy distribution of CMB radiation and/or the trajectory of its photons. Moreover, Galactic and extragalactic foregrounds radiate at the same wavelenghts of the CMB. Thus the CMB radiation as observed from the Earth is combination of a number of contaminating signals that must be separated using the so-called *component separation* techniques before they can be studied. Some of the most relevant source separation methods were also briefly discussed in the Introduction (see section 1.5).

Point sources are the most prominent contaminant of the CMB radiation at small angular scales (multipoles $\ell > 500 - 1000$). As it was commented in Chapter 1, point sources are extragalactic objects that are unresolved by the relatively poor angular resolution of current microwave experiments. Point sources can be either Galactic or extragalactic. In this Thesis I have focused on extragalactic

sources, but the same methods described here can be applied to Galactic point sources as well. Regarding the nature of extragalactic point sources at microwave frequencies, it is believed that most sources below $\nu \sim 217$ GHz are traditional radio sources, while above that frequency the dominant population corresponds to dusty galaxies. However, the observational window between $\sim$20 and $\sim$1000 GHz has been closed until very recently and there is still a large uncertainty in our knowledge of the statistical and physical properties of extragalactic point sources at these frequencies. Therefore, it is necessary to detect these objects not only for the sake of CMB-based cosmology, but also in order to improve the models of galaxy formation and evolution. The goal of this Thesis is to introduce a detection/estimation method able to provide detection and unbiased flux density estimation of point sources down to unprecedented lower flux density limits.

In the literature one can find a large variety of tools that have developed over the years to detect compact sources, not only using linear filters, but also simple thresholding techniques and more complex Bayesian detectors. Some of these tools have been briefly explained in the Chapter 2. However, most of them operate at one single frequency (i.e. just one given image) and have reached (or they are very close) the optimal lower flux density limit given by instrumental and confusion noise in existing experiments. It is the general impression that single-frequency detection methods have reached some kind of efficiency 'plateau', with marginal improvements at the few percent level. This is the main reason to develop new methods that incorporate additional information of the data (the cross-power spectrum and the spatial information of the sources, beside the modelisation of the behaviour spectrum of the sources as a power law) in order to reduce the flux detection limit allowing to detect weaker sources. The multifrequency method used in this Thesis is an adaptation of the matched multifilter (MMF, Herranz et al. (2002c)) traditionally employed to detect SZ clusters in CMB data.

5.2 Conclusions

The MMF, as it was mentioned above, was previously used to detect galaxy clusters with the SZ effect (Herranz et al., 2002c). In this case, the frequency dependence of this effect is perfectly known, as it was shown in the section 1.2.2. In that work, one of the missing variables was the size of the clusters, therefore, this can be considered as a free parameter that we will use to estimate the radius of the cluster, assuming that the shape of the clusters can be described as a function of this variable. This idea has been used in this Thesis, but using a different observable as the free parameter. In this Thesis it is proposed to extend the same idea to a different parameter space, i.e., the electromagnetic frequency domain. In this work, the size is known a priori, since the sources to be detected are point-like objects, and therefore their sizes are given by the antenna beam of the experiment. What is unknown is the

frequency dependence (parametrised like a power law in this Thesis, although this election is optional). The free parameter is the spectral index of each source. In the case of the detection of point sources, we filter each set of maps (of the same region of the sky) as many times as different values of the spectral index we want to test. In other words, the same area of the sky is filtered by different MMFs.

After filtering the images with the different MMFs, the problem is reduced to find the value of the spectral index (for each source) that maximises the SNR (for that source). That value is the optimal estimate of the true value of γ (see Appendix 2.11). The SNR obtained by this way is the same for all the channels filtered simultaneously, in contrast with the single-frequency methods, where the SNR (worse than the obtained with the MMF) is in general different for the different channels. This is a desirable characteristic for two reasons: first, we are able to obtain catalogues where the same source has identical significance level across the different channels. Second, there are no 'holes' in such a catalogue: in the single-frequency methods, a same source can appear in a frequency and disappear in other one because it is below the detection threshold. This makes more difficult the posterior spectral study of the catalogue. By construction, this is impossible to happen in the MMF catalogue. All the sources have the same significance level for all the channels and therefore, they are present in all the frequencies analysed. This is a clear advantage with respect to the single-frequency methods. Regularly, catalogues with more than one frequency are constructed from other single-frequency catalogues. This usually results on, as it was said, in the appearance of holes in some columns due to the non-detection of a source in some of these frequencies. Sometimes one must turn to other experiments, make interpolations under some assumptions, etc, and it cannot be as easy to do as we would desire. The MMF removes this difficulty. By construction, if we have a detection, this is valid for all the channels. And therefore we have the flux densities for all the frequencies, allowing us to study the spectral behaviour of the object in all the frequency range studied.

The simplicity of the method, the ability to reduce the low limit of the flux density and the simultaneous detection of an object at different channels (with the same significance level) make the MMF a powerful and well suited tool to detect point sources at more than one frequency.

After obtaining mathematically the analytical expression of the MMF (see Appendix 2.10), it is necessary to test it in order to verify if it is more powerful than the single-frequency methods. In Chapter 3, a set of realistic simulations of the Planck sky are used (Delabrouille et al., 2013) (in particular, at 44 and 100 GHz), inserting a posteriori the point sources that must be detected. From these simulations we have extracted regions of the sky at intermediate Galactic latitude ($|b| = 40^\circ$) in order to avoid strong Galactic foreground contamination. For each pair of values of the flux density and the spectral

index, we have 100 sources in each of the different maps, and the only condition imposed is not to allow the overlapping between them. Once the sources are inserted in the maps, the matched filter and the MMF are applied in order to detect them, using a 5σ thresholding detector. The different tests used have shown an improvement in the results obtained by the MMF with respect to the traditional matched filter. The number of detections is always higher when the MMF is used (see Figure 3.1).

In order to study how many spurious detections are introduced by the MMF, a set of more realistic simulations were made, taking into account some aspects such as the fact that the sources present in a map do not necessarily have the same flux density or spectral index. The detection threshold is established in 3σ (by contrast to the usual 5σ) to allow a greater number of sources, both spurious and real, and therefore a better statistics of the results. Figure 3.6 is particularly interesting in this sense: it represents the number of real detections versus the number of spurious detections. Or in other words, if we fix the number of spurious objects that our filter introduces, the figure tells us the number of real objects that we have. If we turn this statement, (by changing the corresponding axis in the figure), we could talk about the number of spurious detections that each method introduces for a fixed number of real detections. This point is specially important because it tells us about which method introduces more spurious detections for a fixed number of true detections. We can see, by observing the figure 3.6, the MMF has a better behaviour in this aspect, with much less spurious detections.

After checking the good performance of the MMF in a set of realistic simulations of the Planck sky, it is tested in real data. This is done in the Chapter 4, where the 7-year data of the satellite WMAP of the NASA are used: in particular, the channels V and W (61 and 94 GHz, respectively).

The code used previously must be modified in order to take into account the different beams of WMAP respect to the Planck ones. As explained in section 4.2, WMAP beams are non Gaussian. With these considerations introduced in the code, the MMF is used to filter all the WMAP sky at 61 and 94 GHz simultaneously. The sky is divided in patches enough small such that the flat approximation is valid and therefore, we can use the Fourier space. In each region of the sky (two maps for each region) it is applied the MMF in the same way that in the Chapter 3, changing the spectral index and selecting the value of this parameter that maximises the SNR for each source.

Focusing only in the extragalactic objects (see Table 4.2), the MMF is able to detect, in a blind search, 119 5σ sources in the WMAP 7-year data at 61 and 94 GHz simultaneously. This number represents a considerable improvement with respect to the single-frequency methods. López-Caniego et al. (2007) detects, at 94 GHz, 22 5σ objects in a non-blind search in the WMAP 3-year data. These sources are completely identified in other surveys and, by comparing with calibrators of ATCA and

NRAO, the flux density recovered is good above $\sim$2 Jy at 94 GHz, below which the Eddington bias is present. Finally, we observe that the median value of the spectral index of the 119 detections is $\gamma_{61}^{94} = -0.65$ (with a dispersion of 0.71), confirming the steepening of extragalactic radio source spectra above $\sim$ 70 GHz, suggested by various data sets (Sadler et al., 2008; González-Nuevo et al., 2008; Marriage et al., 2011; Massardi et al., 2010) and then confirmed by analyses of different samples (Planck Collaboration et al., 2011b,a; Giommi et al., 2012) of bright extragalactic sources extracted by the Planck Early Release Compact Source Catalogue (Planck Collaboration et al., 2011c).

5.3 Future work

In this Thesis we have seen the power of the MMF when detecting point sources. The improvement with respect to other single-frequency methods is in the fact that two or more channels are used simultaneously. This implies that we are using more information in the analysis: cross-power spectrum of the noise, spatial information of the sources, and the parametrisation of the spectral behaviour of the sources like a spectral law (although this particular election is optional). This additional information is not used in the single-frequency methods by their construction itself. On the other hand, as it was explained in the Chapter 2, the Bayesian approaches represent the optimal way to detect sources whether the statistical properties of the signal and the noise are known (or can be well estimated). This is a more natural and elegant way to face the problem. The main difficulty is that we need to know perfectly (or well enough) the properties above referred. This is not always easy, and if we want to have a robust method that does not depend strongly on these assumptions, the MMF is a good election. Also, considering the Powell Snakes method (section 2.1.2), the authors themselves pointed out in Carvalho et al. (2012) that the MMF emerges naturally in their work as the estimator of the amplitude of the sources when maximised the likelihood ratio if the sources are sufficiently well-separated. This is one of the reasons for choosing the MMF approach in this Thesis.

An aspect to be considered in future works is to increase the number of channels to be filtered jointly. In this case, we have more information (in particular from the noise) that can be inserted in the analysis. This is something that has started to be used with Herschel at 250, 350 and 500 μm, by using the eq. 1.18 as the frequency dependence that will be inserted in the code. The preliminary results of theses analyses show a high number of detections as compared to what has been shown in this Thesis.

The extension to more channels can be also used with Planck, keeping in mind the fact that the MMF takes advantage from the cross-power spectrum of the noise and the position of a source across different frequencies. If the channels are very separated in frequency, those conditions could be no longer true, and the application of the MMF would not be longer advantageous.

One aspect that must be considered when using more frequencies is how to find the maximum of the SNR. In this Thesis, the number of values of the spectral index explored is not very large and it is easy to find the value of γ that maximises the SNR. If we have more than two frequencies, the SNR will be a function of more than one parameter. This is the case in Herschel, as explained above, where we have to determine two free parameters: an effective temperature and the spectral index. But this is even more complicated if the number of channels is much higher. In this case, it is necessary to develop a strategy to find the maximum of the SNR that determines the values of the free parameters. One can already use existing optimisation numerical algorithms, allowing us, in general, to find the maximum of a function within some limits given by a well established convergence criteria in a reasonable period of time.

Some of the iterative algorithms used to find extrema make use of the derivatives of the function. In the case considered here, where there is not an algebraic function, the finite differences must be used instead of the derivatives. For example, when the derivative is unavailable (or it is difficult to calculate), the quasi-Newton methods replace the derivatives of the function by the finite differences, being a generalisation of the secant method, that uses a succession of roots of secant lines to better approximate a root of a function.

Other examples are based on the gradient of the function to be maximised. One of the most prominent examples of this kind of algorithms is the gradient ascent method, that tries to find a local maximum of a function using gradient ascent, taking steps proportional to the positive of the gradient (or of the approximate gradient) of the function. If this method is used, one should take into account that the curvature of the function to be maximised varies smoothly. Obviously, the expression of the gradient must be replaced by the finite differences.

Other example that can be used to find the maximum of a function is the simulated annealing (whose name and inspiration come from the metallurgy). This technique involves heating and controlled cooling of a material to increase the size of its crystals and reduce defects. Both are attributes of the material that depend on its thermodynamic free energy. By analogy, the simulated annealing interprets the slow cooling as a slow decrease in the probability of accepting worse solutions as it explores the solution space. At each step, the simulated annealing considers some neighbouring state of the current state and probabilistically decides between both states. This probability depends on the energy of both states (and other global time-varying parameter called *temperature* by analogy with the metallurgy) and favours states with lower energy. One condition to be considered with this method is that, by analogy with the metallurgical case, the cooling rate is low enough for the probability distribution of the current state.

The amoeba method (also called Nelder-Mead or downhill simplex method) uses the simplices, a

special polytope of $n+1$ vertices in n dimensions. In 2D, the polytope is the triangle. From a set of points, $\mathbf{x}$, and ordering the corresponding $f(x_i)$ (being f the function to be minimised), it is calculated the centroid of the simplex from all points x_i, except x_{n+1} that gives the highest value for f. The amoeba method now takes a series of steps, most of them just moving the point of the simplex where the function is largest through the opposite face of the simplex to a lower point (*reflection*). When it can do so, the method expands the simplex in one or another direction to take larger steps. When it reaches a 'valley floor', the method contracts itself in the transverse direction and tries to go down the valley. If there is a situation where the simplex is trying to pass through 'the eye of a needle', it contracts itself in all directions, pulling itself in around its lowest (best) point. This method works well when the function varies smoothly and is unimodal.

There are other tools based on the sampling of the function that are useful when we want to maximise it. One recent example is the nested sampling. We can apply the Bayes' theorem (eq. 2.6) to compare two models/hypotheses (one can be true but not both at the same time). The knowledge of the different parts of this theorem entails the calculation of integrals that are usually difficult to carry out. In particular, the integral of the product of the likelihood and the prior over the parameters of the model. Starting with N points sampled from the prior, in each iteration from $1 < i < m$ (m is chosen by guesswork), L_i (that plays the role of the likelihood) is the minimum of the current values of the points and $w_i = X_{i-1} - X_i$ (it plays the role of the prior), being $X_i = exp(-i/N)$. The integral will be the product of L_i times w_i plus the value of the integral in the previous step. In the next iteration, another point will be sampled from the prior, maintaining the likelihood above L_i. The algorithm finishes when the difference in the integration between two consecutive steps is sufficiently small.

Many of the algorithms above referred are based on the Montecarlo methods. A Montecarlo method is a technique that relies on repeated random sampling to obtain numerical results. One of the most knowns applications is the obtention of the area under a curve (definite integral). By simulating a set of uniform random numbers, we obtain a new sample distributed according the function of interest, rejecting the ones that fall above the curve. This new sample can be used as a approximation of the original function, and estimate the area and other statistical values.

We can combine the Montecarlo method with the Markov chains. The Markov chain is a random process that undergoes transitions from a state to other one. This processes are characterised by their lack of memory, it means the distribution of the next state only depends on the current state and not on the sequence of events before it. The transition between one state and other will be determined by a matrix whose elements are the probabilities of one state given the current state. The typical example is the one that tells us the probabilities of getting a sunny or rainy day depending only of the current day (if sunny or rainy). The Markov chain Montecarlo methods (MCMC methods) generate samples

exploring the state space so that the chain spends more time in the most important regions.

Some of the methods are thought to find the minimum of a function and in this work it is necessary to find the maximum. We have two options: to change the algorithm to find the maximum or change the function f by $-f$ and find the minimum of the new one.

In the context of the future CMB experiments, the most important developments are being made to improve how knowledge of the CMB polarisation, in particular, as much information as could be obtained regarding the inflationary mechanism that is suppose to leave its imprint on the CMB polarisation B-modes. These instrumental initiatives account for ground-based and balloon-borne experiments, as well as satellites. Among the latter, it is worth mentioning the Japanese LiteBIRD mission[1], already considered in Phase A for JAXA, which consist in 15 frequencies (from 40 to 400 GHz), but with a poor angular resolution, which makes difficult to detect point sources on its maps. In addition, there have been several European proposals that, so far, have not been selected by ESA, among others, B-pol, COrE, PRISM and COrE+. At the time this Thesis is written, the CMB European community is working on the preparation of an updated version of the COrE+ proposal, to be submitted to the M5 call of ESA.

Just as an illustration of the instrumental capabilities of these missions, let us review briefly the last two European proposals. First, the Polarized Radiation Imaging and Spectroscopy Mission, PRISM (André et al., 2014), would have carried out a survey of the microwave to far-infrared full-sky in intensity and polarisation (and its absolute spectrum as well). Some of its scientific goals (in addition to study the physics of cosmic inflation) would have been to perform a galaxy cluster survey, understand the CIB, and to study the spectral distortions of the CMB. This experiment would have been composed of two instruments: a polarimetry imager measuring the intensity and the polarization between 30 and 6000 GHz with unprecedented sensitivity and angular resolution from 17 arcmin to 6 arcsec; and an lower angular resolution (1.4 degree) spectro-photometer. Due to its properties, PRISM would have been a perfect tool to study the early galaxy evolution and to extend the radio sources counts (both in intensity and in polarisation), in particular above 217 GHz. Second, Cosmic Origin Explorer+, COrE+[2] could map the polarisation of the microwave sky in 19 channels between 60 and 600 GHz with and angular resolution between 14 and 1.4 arcmin, respectively, with such as a precision ($\sim$10-30 times better than Planck) that the tensor modes produced by the inflation would be detected with a 3σ significance level, for values of $r > 0.001$. As in other full-sky experiments (like WMAP or Planck),

[1] http://indico.ipmu.jp/indico/getFile.py/access?contribId=3&sessionId=2&resId=0&materialId=slides&confId=72

[2] http://indico.ipmu.jp/indico/getFile.py/access?contribId=69&sessionId=2&resId=0&materialId=slides&confId=72

we would observe at the same time other components with Galactic and extragalactic origins. The most interesting for the purpose of this Thesis are the extragalactic ones. As in intensity, we can observe the SZ effect (see section 1.2.2), with different spectrum from the intensity, and point sources that correspond with the extragalactic objects described in the section 1.4. The use of the MMF in Planck and COrE+ could provide complementary catalogues in intensity and polarisation for the SZ effect and the extragalactic objects.

The dark Universe, and in particular the dark energy, are one of the most important challenges in Cosmology in the next years. Two observables that will be used are the clustering of galaxies to measure the baryon acoustic oscillations (BAO) and the weak lensing. BAOs are the regular and periodic fluctuations in the density of the visible baryonic matter as a consequence of the acoustic oscillations in the primordial plasma. The typical scale of this oscillations is (in comoving coordinates) $\sim$150 Mpc. The gravitational lensing is the effect that a gravitational field causes on the light, bending its trajectory: the most typical example in Cosmology is the light coming from a far object that undergoes this effect due to the gravitational field of a galaxy cluster. This effect distorts and magnifies the background image, being and important tool to study the early Universe. Missions like Euclid (Laureijs et al., 2011) and the Javalambre-Physics of the Accelerated Universe Astrophysical Survey, J-PAS (Benítez et al., 2014), will study, among other things, the dark Universe, in particular the dark energy.

The main instrument of J-PAS is a 2.5 m telescope with an effective field of view of 7 square degrees. J-PAS will cover at least 8000 square degrees using an unprecedented system of 56 narrow band filters in the optical. Euclid will be a 1.2m telescope with two instruments, the visual imager (VIS) at 550-900 nm, and the near-infrared spectrometer and photometer (NISP) at 920-2000 nm. Euclid will map at least an area of 15,000 square degrees in a wide survey and 40 additional ones in a deep survey. Both Euclid as J-PAS will be able to analyse both effects. The MMF could be applied in order to detect galaxy clusters, combining several frequencies and taking into account some parameters related to the shape of the object to be detected (included in τ in eq. 2.56). In addition, if there are a huge number of objects in the patch to be filtered, it is necessary to estimate the cross-power spectrum of the noise ($\mathbf{P}$ in eq. 2.56) in a different way to what was done previously in this Thesis: in a first step, we would need to remove the brightest sources in order to calculate the cross-power spectrum and then filter the image to detect the objects. After these considerations, the MMF will be a useful device that helps us to detect galaxy clusters and also individual galaxies in these maps and deepen in our knowledge of the early Universe.

To finish this brief review of future experiments, the Square Kilometre Array, SKA [3], will be a radio telescope with a collecting area of $\sim$1 km^2 and that will operating in a wide range of frequencies

[3] http://www.skatelescope.org/

(50 MHz-30 GHz when the third phase is finished). It will be 50 times more sensitive than any other radio instrument. This will be possible because SKA will be composed by thousands of small antennas spread over a distance of several thousands of kilometres, simulating a unique and giant radio telescope with high sensitivity and angular resolution. The SKA will provide continuous frequency coverage from 50 MHz to 14 GHz in the first two phases of its construction. A third phase will then extend the frequency range up to 30 GHz. The frequency range from 50 MHz to 14 GHz cannot be realised using one design of antenna and so the SKA will comprise separate sub-arrays of different types of antenna elements that will make up the SKA-low, SKA-mid and survey arrays. If there will be available maps of the same region of the sky at different frequencies, the MMF could be applied. The scientific goals of SKA will be wide due to its capacities, and the MMF will be again a useful device to detect a very large number of galaxies, helping to clear the dark areas of the science in the evolution of the galaxies.

But that's another story and shall be told another time.[4]

[4] *The Neverending Story*, M. Ende

Chapter 6

Resumen en castellano

En los últimos años se ha producido un avance significativo en la cosmología, pasando de ser meramente una disciplina especulativa a convertirse en una ciencia de precisión. Ello se debe a los más recientes experimentos que han hecho que las observaciones sean notablemente superiores en calidad y precisión a sus predecesoras. Todo ello se traduce en una mejor comprensión de nuestro universo y de sus observables, así como de su evolución, composición, dinámica, etc. El modelo que mejor explica el universo tal y como le vemos hoy en día es el conocido como Λ-CDM, caracterizado por la presencia dominante de energía oscura y materia oscura fría. Este modelo permite explicar, de un modo natural, la radiación del fondo cósmico de microondas (RFCM), la estructura a gran escala del universo y la expansión acelerada del mismo.

Según este modelo, el origen del universo tuvo lugar hace 13.800 millones de años (Planck Collaboration et al., 2015e) en una gran ≪explosión≫ llamada *Big Bang*, que dio lugar al espacio y el tiempo. Inmediatamente después del *Big Bang*, nos encontramos con la conocida como la *era de Planck*, un tiempo en el que se supone que las cuatro fuerzas elementales del universo (gravitatoria, interacciones fuerte y débil y electromagnética) estaban unificadas. Esto implicaría que las cuatro fuerzas elementales no serían más que cuatro aspectos de una misma interacción que se manifestarían de forma distinta dependiendo del rango energético en el que nos encontremos. Sobre esta época poco se puede decir al no contar con una teoría que nos describa lo que ocurre en ese rango de energías tan grandes.

Una pequeña fracción de segundo después del Big Bang tuvo lugar durante un tiempo muy breve una expansión como nunca sucedió antes ni después en el universo: denominada *inflación*, las dimensiones espaciales crecieron exponencialmente en este brevísimo periodo de tiempo. La inflación fue añadida *ad hoc* a la teoría existente para dar cuenta de ciertos problemas que no tenían fácil solución,

como el del horizonte; que pone de manifiesto la dificultad que supone para nuestro modelo el hecho de que las propiedades estadísticas en dos regiones del cielo diametralmente opuestas y no conectadas causalmente sean las mismas. O dicho de otro modo, por qué esas regiones, separadas una distancia tal que los fotones de una no han llegado hasta la otra (*no* están conectadas causalmente) presentan las mismas propiedades estadísticas. Si en los albores del universo se introduce un época inflacionaria, estas regiones estuvieron en el pasado interconectadas y de ahí sus idénticas propiedades.

Tres minutos después del *Big Bang*, los núcleos de los átomos más ligeros (como el H y el He) se habían formado en lo que se conoce como la *nucleosíntesis primordial*. Tras ello, el universo continuó su progresivo enfriamiento hasta que ~ 380.000 años después del *Big Bang* se produce la recombinación: hasta entonces el universo estaba compuesto, básicamente, de un plasma de fotones muy energéticos, núcleos ligeros y partículas elementales como los electrones. Estos fotones, altamente ionizantes, impedían la formación de átomos estables. Esto se mantuvo hasta que la temperatura fue lo suficientemente baja para permitir la formación de los primeros átomos estables. Fue en ese momento cuando los fotones pueden viajar libremente por el universo, dando lugar a la radiación del fondo cósmico de microondas que observamos hoy en día, conservando (en general) los fotones de la misma las diferencias relativas de temperatura de ese momento de la historia del universo. Actualmente, al medir esta radiación, muestra una temperatura media de $T_0 = 2,7255 \pm 0,0006$ K (Fixsen, 2009).

Después de este evento, tenemos un universo donde la materia aún no ha colapsado lo suficiente para formar las primeras estrellas y la radiación sigue viajando por el espacio. A esta época se le conoce como los *años oscuros* (*dark ages* en inglés), al no haber fuente alguna de luz. Sin embargo, entre 150 y 1.000 millones de años después del *Big Bang* tiene lugar la *reionización*, que es cuando la materia, al colapsar, da lugar a las primeras estrellas y galaxias y, como consecuencia de la radiación ultravioleta emitida por ellas, la materia volvió a estar casi en su totalidad ionizada.

En las últimas décadas se ha producido un incremento notable en el número de experimentos dedicados a estudiar la RFCM y sus propiedades tras su hallazgo en 1964 por Penzias y Wilson de los AT&T Laboratories (Penzias and Wilson, 1965), lo que les valió el premio Nobel. Por ejemplo, en los años 70 del pasado siglo, Zeldóvich, Harrison, Peebles y Yu se percataron de que el universo debería presentar pequeñas inhomogeneidades en su distribución de materia que dieran cuenta de la estructura a gran escala del mismo y que se traducirían en una impronta característica en la RFCM. Estas inhomogeneidades fueron por primera vez detectadas por el instrumento DMR (*Differential Microwave Radiometer*) de la misión COBE de la NASA a principios de los 90 del pasado siglo (ver Smoot et al. (1992)). Dichas inhomogeneidades resultaron ser de una parte en cien mil, aproximadamente.

Experimentos posteriores (MAXIMA (Hanany et al., 2000), BOOMERANG (de Bernardis et al., 2000) y Tenerife (Gutiérrez et al., 2000)) confirmaron que la curvatura del universo (observable) es muy cercana a cero.

El valor de la temperatura de la RFCM que observamos en todo el cielo puede ver como un campo aleatorio en la esfera y, por tanto, expresarse en función de los armónicos esféricos. (ec. 1.2). De aquí podemos obtener el espectro de potencias de la RFCM (ver ec. 1.3), que nos una idea de la aportación de cada escala a la intensidad total del campo de temperaturas. Si nos fijamos en la figura 1.4, podemos observar tres regiones claramente diferenciadas en el espectro:

- A escalas angulares grandes (o bajos multipolos, ℓ) observamos un *plateau*. Ello se debe a que se corresponde con tamaños en la superficie de última dispersión mayores que los del horizonte, por que lo no se aprecia ninguna estructura en el espectro.

- Regiones intermedias ($30 \lesssim \ell \lesssim 1000$) se corresponden con aquellas que tienen un tamaño angular menor que el del horizonte. Por tanto, materia y radiación en esta zona están causalmente conectadas. En el momento en el que materia y radiación estaban fuertemente acopladas (Hu and White, 1996), el fluido que componían podía ser modelizado como un oscilador armónico que genera los llamados *picos acústicos* al competir la presión de radiaicón y la fuerza gravitatoria cuando el fluido colapsa en los pozos de potencial. Estas oscilaciones acústicas en el fluido fotón-bariones se manifiestan en el espectro en forma de picos. La posición de los picos está directamente relacionada con la geometría, dándose el primero en $\ell \sim 200$, el tamaño del horizonte en el superficie de última dispersión.

- A escalas aún más pequeñas (valores altos de ℓ), las oscilaciones antes descritas se amortiguan debido al tamaño finito que tiene la superficie de última dispersión ($\Delta z \sim 100$): es decir, no se trata de un proceso que se dé instantáneamente. Por tanto, las fluctuaciones con un tamaño menor que el ancho de la superficie se verán reducidas por otros fotones que provienen de distintas partes de dicha superficie. También hay que tener en cuenta la *amortiguación de Silk* (Silk, 1968), donde los fotones procedentes de regiones con sobredensidad llevan consigo a los electrones a zonas menos densas, suavizando las fluctuaciones.

Por último, cuando se analiza el espectro de potencias de la RFCM hay que tener siempre presente dos aspectos. Primero, la *varianza cósmica*, que aparece por el simple hecho de tener un solo cielo que observar. Esto se hace más patente a grandes escalas angulares, ya que disponemos de pocas regiones con esos valores de ℓ. Observando la figura 1.4, vemos como para valores de ℓ bajos, las barras de error son mayores, y ello no se debe a defecto alguno del experimento sino a la varianza cósmica que

acabamos de describir.

Segundo, la *varianza de la muestra*. Este aparece cuando tenemos que eliminar regiones de nuestro análisis debido a que muestran una alta contaminación, como por ejemplo aquellas que se encuentran situadas cerca del plano galáctico.

Estos dos efectos siempre aparecen, en mayor o menor medida, en nuestros experimentos, y es algo que debemos tener en cuenta en los análisis de nuestros datos.

6.1 Anisotropías de la RFCM

Las anisotropías del fondo cósmico de microondas son fluctuaciones en la intensidad de la radiación del fondo cósmico (del orden de 1 entre 100.000). Podemos dividirlas en dos grandes grupos dependiendo de su origen: anisotropías primarias y secundarias.

- anisotropías primarias, debidas a los efectos que tuvieron lugar en la superficie de última dispersión o antes, en la época como conocida como recombinación, cuando la temperatura del universo es lo lo suficientemente baja para que se formen los primeros átomos estables y la radiación pueda viajar libremente, desacoplándose de la materia.

- anisotropías secundarias, que se deben a las interacciones de los fotones de la RFCM con materia o pozos de potencial gravitatorio que estos se encuentran en su trayectoria que les lleva desde la superficie de última dispersión hasta el observador.

6.1.1 Anisotropías primarias

Las anisotropías primarias son aquellas que se produjeron antes o durante la época de la recombinación.

Se pueden distinguir entre *adiabáticas* y de *isocurvatura*. Las primeras se caracterizan por una variación nula de la entropía específica de cada componente en todo punto. Formalmente se refleja por la expresión 1.4, donde n_b, n_{DM} y n_γ son las densidades bariónica, de materia oscura y de fotones, respectivamente.

Por el contrario, las fluctuaciones de isocurvatura se caracterizan por una variación nula de la energía total en cada punto. Matemáticamente se puede expresar con la ec. 1.5, donde las distintas ρ dan cuenta de las densidades de energía de cada componente.

Las densidades de fotones no son las únicas responsables de la existencia de anisotropías primarias. También puede haber otras que se muestran a continuación.

- Efecto Doppler: este se produce por el movimiento relativo del observador con respecto al sistema de coordenadas comóviles de la RFCM. Habrá un corrimiento al azul (hacia longitudes de onda menores en el espectro electromagnético) en la dirección hacia la cual se mueve el observador y al rojo (hacia longitudes de onda mayores en el espectro electromagnético) en la opuesta, tratándose, por tanto, de un efecto dipolar. Este efecto se aprecia en todo sistema en la que un observador se desplaza a través de un fluido. Este efecto fue observado por primera vez en 1975 (Corey and Wilkinson, 1976), pero no fue hasta 1996 que fue medido con precisión: $3,372 \pm 0,007$ mK (Fixsen et al., 1996). Más que una anisotropía es un efecto observacional.

- Efecto Sachs-Wolfe (SW): el más importante de los procesos físicos por medio del cual las fluctuaciones de densidad dejaron su huella en la RFCM (Sachs and Wolfe, 1967) a escalas angulares mayores que el tamaño del horizonte en la superficie de última dispersión ($\theta \sim 2^\circ$). Su origen son los potenciales gravitatorios en dicha superficie: un fotón cae en el pozo de potencial, dicho potencial evoluciona con el tiempo y luego el fotón lo abandona, ganando y perdiendo parte de su energía durante el proceso (desplazándose al azul o al rojo, respectivamente), habiendo un efecto neto al variar el pozo de potencial mientras el fotón lo atravesaba.

A escalas angulares $0,1^\circ \lesssim \theta \lesssim 2^\circ$, las anisotropías se relacionan con los procesos conectados causalmente en el fluido materia-radiación hasta la recombinación. El acoplamiento se puede modelar como un oscilador armónico que puede generar los así llamados *picos acústicos*: inhomogeneidades en el campo de materia indujeron fluctuaciones en el campo de temperatura de los fotones. Cuando la materia y la radiación se desacoplaron, los fotones conservaron la información sobre los campos de densidad en la superficie de última dispersión.

6.1.2 Anisotropías secundarias

Las anisotropías secundarias se producen, como se ha comentado, por las interacciones que sufren los fotones de la RFCM en su camino entre la superficie de última dispersión y el observador. Pasemos a describir brevemente solo los dos efectos más importantes que pueden causarlas.

Efectos gravitatorios

Los campos gravitatorios pueden ser la fuente de varias anisotropías secundarias en el campo de temperatura de la RFCM. Por ejemplo, si un fotón cae en un pozo de potencial para después salir, la variación de energía del mismo será nula siempre y cuando el pozo de potencial no varíe durante todo

el proceso. A este proceso se le llama *efecto Sachs-Wolfe integrado* (SWI), y se debe a perturbaciones en la densidad lineales. Solo en un universo Einstein-de Sitter, este efecto es igual a cero.

Podemos hablar de varios regímenes distintos para estre mismo mecanismo, como el SWI temprano, cuando el potencial decae entre la época del desacolplo y el momento en que la materia domina completamente el universo. El efecto SWI tardío, cuando el potencial decae debido a la expansión del universo una vez la materia no domina dicha expansión (modelos Λ o abiertos). El efecto *Rees-Sciama* (Rees and Sciama, 1968), que se debe a la evolución no lineal de estructuras colapsantes que modifican los pozos de potencial. Por último, las lentes gravitatorias, que sin modificar la energía de los fotones, sí que interfieren en su trayectoria, distorsionando la superficie de última dispersión.

Efectos de dispersión por la reionización

Como comentamos, la reionización es una época después de la recombinación en que, debido a la formación de las primeras estrellas y galaxias, la materia del universo vuelve a ionizarse. Como resultado de ello, se liberan gran cantidad de electrones que pueden dispersar de nuevo fotones de la RFCM. Esto hace que a las anisotropías primarias se sumen las secundarias, llegando las secundarias en algunos casos a dominar sobre las primarias. Otro efecto es que al observar un fotón de la RFCM en una determinada dirección, no quiere decir que provenga de dicha dirección, ya que ha podido ser dispersado y su trayectoria modificada.

Otro efecto que se produce en este contexto es el conocido como *efecto Sunyaev-Zeldóvich* (Sunyaev and Zeldovich, 1972). Este efecto tiene lugar cuando los fotones de la RFCM, al atravesar gas ionizado (principalmente en cúmulos galácticos) son dispersados por electrones energéticos del medio (efecto Compton inverso). Suponiendo que una cierta fracción de los fotones de la RFCM son movidos a más altas energías, se aprecia un cambio en el espectro de dicha radiación. Esta modificación tiene una dependencia frecuencial característica. La variación en la intensidad de la RFCM viene dada por la siguiente expresión:

$$\Delta I_\nu = 2\frac{(kT_{CMB})^3}{(hc)^2} y_C g(x), \tag{6.1}$$

siendo k, h y c las constantes de Boltzmann y Planck y la velocidad de la luz (en el medio), respectivamente, y $x = h\nu/kt_{CMB}$. La dependencia frecuencial del efecto viene dado por:

$$g(x) = x^4 e^x [x \cdot \coth(x/2) - 4]/(e^x - 1)^2, \tag{6.2}$$

resultando ser negativo (positivo) para valores de x menores (mayores) que $x_0 = 3.83$, que se corres-

ponde a una frecuencia de $\nu_0 = 217$ GHz.

El parámetro de comptonización es

$$y_C = \int \frac{kT_e}{mc^2} n_e \sigma_T dl, \tag{6.3}$$

donde n_e y T_e son la densidad de electrones y la temperatura respectivamente, σ_T es la sección eficaz de Thomson y la integral es sobre una línea de visión a través del plasma.

6.2 Polarización de la RFCM

Como toda radiación electromagnética, la RFCM también puede estar (y de hecho lo está) polarizada. La polarización únicamente se puede generar (si descartamos el efecto de lente gravitatoria) por fenómenos de dispersión. Por la dispersión de Thomson, un electrón que es golpeado por un fotón sin polarizar verá como el fotón dispersado estará linealmente polarizado, perpendicular al plano donde ha tenido lugar la dispersión. Como no hay nada de particular en tener este ejemplo, supongamos que hay otro fotón procedente de una dirección perpendicular al primero. La intensidad de los dos fotones ha de ser distinta para que el saliente tenga una polarización neta, es decir, el electrón ha de ≪ver≫ un cuadrupolo en la radiación entrante para que esta esté polarizada tras la dispersión. En el contexto de la RFCM, esto ocurre justo unos instantes antes de la recombinación, cuando los electrones del medio pueden ver un cuadrupolo en la radiación. El patrón de polarización que vemos en la actualidad no es más que una proyección de las anisotropías cuadrupolares en el momento de la recombinación (ver figura 1.5).

Las posibles fuentes de anisotropías cuadrupolares en el momento de la recombinación son tres: escalares, vectoriales y tensoriales. Las primeras se deben a perturbaciones en la densidad. Las vectoriales son debidas a fenómenos de vorticidad en el plasma por el desplazamiento Doppler. Este tipo de perturbaciones son despreciables en la recombinación. Por último, las tensoriales se dan cuando una onda gravitatoria pasa y deforma el espacio produciendo una anisotropía cuadruoplar. Entre las escalares y las tensoriales, solo estas últimas son capaces de producir el llamado *modo B* de polarización, que puede ser una evidencia de la presencia de ondas gravitatorias si somos capaces de aislar los efectos de lente gravitatoria.

Pero, ¿qué es el modo B? La RFCM puede ser descrita con los parámetros de Stokes (ver ec. 1.9), que nos dan idea de la polarización de la misma: Q nos dice el grado de polarización lineal a lo largo de uno de los ejes cartesianos y U y V a lo largo de ejes girados 45° con respecto a los cartesianos. Según el teorema de Helmholtz, y bajo ciertas condiciones no muy exigentes, todo campo vectorial puede

ser descrito como la suma de dos campos, uno con rotacional nulo y el otro con divergencia igual a cero. Debido a su semejanza con los campos electrostáticos y magnéticos, se denominan *modos E* y *B* respectivamente.

Ver Hu and White (1997) y la página web [1] para una introducción didáctica a la polarización de la RFCM.

6.3 Contaminantes de la RFCM

Al observar el cielo en las frecuencias en las que la RFCM es detectada, no todos los fotones que nos llegan provienen de dicha radiación. De hecho, solo una mínima parte procede de la RFCM debido a que hay otras fuentes que emiten fotones a esas frecuencias, siendo la más importante la propia Vía Láctea, nuestra galaxia. Esto en cuanto a fuentes de contaminación difusas, ya que si nos centramos en escalas angulares pequeñas ($\ell > 500 - 1000$) aparecen otras fuentes de emisión, en este caso extragalácticas (es decir, que están fuera de nuestra galaxia), como pueden ser otras galaxias o cúmulos de galaxias. Como se puede apreciar en la figura 1.7, en torno a los $90 - 100$ GHz hay una ventana donde la RFCM puede observarse mejor debido a que la intensidad de los otros contaminantes es menor. Por esto mismo es necesario conocer de la mejor manera posible el comportamiento de estos contaminantes para para poder separarlos y estudiar la RFCM y los propios contaminantes. Como veremos más adelante, la forma en que difieren las componentes difusas (mayormente galácticas) de las compactas (en su mayoría extragalácticas) nos obliga a desarrollar distintas herramientas para poder detectarlas y separarlas. Para experimentos en tierra o en la atmósfera, a todo esto hay que añadir los efectos que pueda introducir la propia atmósfera terrestre en los datos que vayan a ser analizados. Y por último, los errores que añade el propio instrumento.

El objetivo de esta tesis, como se expondrá más adelante, es el desarrollo y aplicación de una técnica multifrecuencial para la detección de fuentes compactas extragalácticas.

6.3.1 Contaminantes galácticos de la RFCM

En esta sección se expondrán brevemente algunas de las más importantes fuentes de contaminación de origen galáctico a las frecuencias de interés para el estudio de la RFCM.

[1] `http://background.uchicago.edu/~whu/intermediate/Polarization/polar0.html`

Sincrotrón

La emisión sincrotrón se produce cuando partículas cargadas son aceleradas por campos magnéticos. Mientras para velocidades no relativistas (radiación ciclotrón) la frecuencia de emisión es la frecuencia de giro de la partícula en el campo magnético, en el caso de velocidades relativistas el espectro es más complicado y se puede extender más allá de esa frecuencia de giro. Ver Rybicki and Lightman (1979) y Smoot (1999) para más detalles de esta radiación.

Emisión libre-libre o radiación de frenado

Esta radiación libre-libre o de frenado es la radiación electromagnética que se da cuando una partícula cargada es acelerada en el campo de Coulomb de otra partícula cargada. En nuestro caso se trata de electrones libres altamente energéticos que interaccionan con iones del medio interestelar y recibe el nombre de libre-libre porque los electrones permanecen libres después de la interacción. También se le conoce como radiación de frenado porque los electrones, aunque no son captados, sí suelen ser frenados.

Emisión térmica del polvo

Como se ve en la figura 1.7, los dos contaminantes galácticos antes mencionados dominan por debajo de los 90 GHz. Por encima de esa frecuencia vemos que la emisión galáctica dominante es la procedente del polvo. El polvo está compuesto por pequeños granos (con un tamaño típico de unas pocas micras) de silicio y carbonatos, que absorben la luz ultravioleta para reemitirla en el infrarrojo. Esta emisión puede modelarse como un cuerpo negro modificado, es decir, un cuerpo gris:

$$S_\nu = \tau_\nu B_\nu \Omega_{cl}, \tag{6.4}$$

donde se ve que la ley de Planck para el cuerpo negro (B_ν) es modificada por la longitud óptica del polvo, τ. Para lograr los objetivos de esta tesis, conviene reescribir la ecuación de arriba del siguiente modo:

$$S_\nu = A B_\nu(T_c) \nu^\beta, \tag{6.5}$$

donde tenemos, además de la amplitud, dos parámetros que ajustar: una temperatura efectiva T_c y el índice espectral β.

Para más detalles de esta emisión, ver Désert et al. (1990).

Conviene resaltar en este apartado la aparición en los últimos años de un nuevo tipo de emisión galáctica a bajas frecuencias que no tiene nada que ver con ningunas de las ya mencionadas. Draine and Lazarian (1998a,b) propusieron un nuevo mecanismo que explicaba esta nueva emisión, relacionándola con los granos del polvo en rotación.

6.3.2 Contaminates extragalácticos de la RFCM

Las fuentes extragalácticas, como se comentó anteriormente, son muy importantes a escalas angulares pequeñas. En principio, estas fuentes, a diferencia de las componentes difusas, tienen cada una de ellas un comportamiento espectral diferente. Además, su tamaño angular también resulta ser distinto, estando condicionado por la respuesta de la antena a una señal puntual (*beam* en inglés). Todo esto hace que la detección y extracción de estas fuentes sean necesarias para el correcto estudio de la RFCM a multipolos altos.

Sin embargo, como en el caso de las componentes galácticas, resulta interesante estudiar las fuentes extragalácticas por sí mismas, para entender su evolución y su encaje en la historia del universo. Dependiendo de cuál sea nuestro interés en estas fuentes, estaremos interesados en unos u otros aspectos de las mismas: por ejemplo, alguien que quiera simplemente detectarlas para eliminarlas de los mapas, estará muy interesado en una completitud alta a bajos flujos (definiendo completitud como la razón entre las detecciones reales y el número total de objetos que hay), para así eliminar el mayor número de ellas. Para los que estudian las fuentes teniendo que solicitar tiempo de observación en un telescopio, lo más importante es la fiabilidad (siendo la fiabilidad la razón entre las detecciones reales y las totales), seguido de la exactitud en la posición y la densidad de flujo de las fuentes (obviamente, una alta completitud es también deseable, pero contrloando el número de fuentes espurias). También puede darse el caso de querer incluir fuentes débiles que puedan resultar interesantes para el estudio que se haga, por lo que es más importante la completitud que la fiabilidad. Es por tanto habitual que se desarrollen distintas estrategias dependiendo de nuestras metas científicas.

Las poblaciones de fuentes extragalácticas se dividen, en el rango de frecuencias estudiadas en esta tesis, en dos poblaciones: radiofuentes y fuentes infrarrojas.

Radiofuentes

Las radiofuentes son, en gran parte, núcleos de galaxias activos con una fuerte emisión no térmica cuyo origen está en dicho centro galáctico. Dicha emisión, debida al efecto sincrotrón, tiene por origen la radiación que emiten electrones acelerados por campos magnéticos.

Si nos fijamos en la figura 1.10, vemos la gran variedad de radiofuentes que se observan. Cabe preguntarse si dicha variedad es una realidad o es solo algo aparente. Tras muchos años de estudio, Urry and Padovani (1995) llegaron a la conclusión de que la inmensa mayoría de las fuentes que se muestran en la figura arriba comentada responden a una apariencia impuesta a nuestras limitaciones como observadores: es decir, no estamos observando objetos que se podría clasificar como diferentes, sino que responden al mismo tipo de objeto con distinta apariencia al ser observado desde distintos ángulos. En este modelo unificado, los autores proponen que estos objetos son núcleos activos de galaxias más brillantes que las galaxias en que se hospedan. En el centro se halla un agujero negro supermasivo (ver figura 1.11), que es a su vez el motor de todo el sistema. Este agujero negro se alimenta de materia cercana que atrae y cae hacia él perdiendo momento angular. Según este modelo, se pueden distinguir dos zonas dependiendo de su distancia al agujero negro: la zona de emisión de *líneas anchas*, donde debido a su cercanía al agujero negro, sus velocidades de rotación son altas y por tanto las líneas de emisión se ensanchan. Rodeando todo este complejo encontramos una estructura opaca de gas y polvo de forma toroidal que absorbe la radiación óptica y ultravioleta. Y más allá de este toro encontramos la zona de emisión de *líneas estrechas*, donde su mayor distancia alagujero negro implica velocidades de rotación más bajas y, por tanto, líneas de emisión más estrechas. Por último, vemos el *chorro* (*jet* en inglés) de partículas altamente energéticas que salen de los polos y se internan en el medio intergaláctico. Según este modelo, la gran mayoría de los objetos de la figura 1.10 se explican porque la galaxia con núcleo activo se encuentra, con respecto al observador, orientada un determinado ángulo respecto a la línea de visión (ver tabla 1.1).

Para finalizar, tenemos dos clases de objetos más que emiten a estas frecuencias. Por un lado están las fases tempranas (fuentes con espectro picado en GHz) y tardías (objetos ADAF/ADIOS, por sus siglas en inglés) de los núcleos galácticos activos, interesantes para estudiar las correspondientes fases en la evolución de dichos núcleos galácticos. Y por otro lado se encuentran los estallidos de rayos gamma, cuyos *outflows* se pueden modelizar como radiación sincrotrón de una onda de choque que se decelera en el medio, posiblemente el medio interestelar de la galaxia en que se halla.

Galaxias con formación estelar

Como se puede ver en la figura 1.10, a flujos bajos destaca la contribución de la población constituida por galaxias con formación estelar. La emisión en radio de estas galaxias está relacionada con la formación estelar, ya que las estrellas jóvenes calientan el polvo y son las responsables, a través de las supernovas, de electrones relativistas emisores de radiación sincrotrón.

Fuentes infrarrojas

En el rango del infrarrojo/submilimétrico, la emisión se produce cuando el polvo absorbe radiación del óptico y el ultravioleta y lo reemite en el infrarrojo. Hasta hace no mucho, los modelos que se usaban para describir este tipo de fuentes no encajaban con las observaciones de SCUBA y MAMBO, por lo que se sugirió la presencia de una nueva población, las llamadas *galaxias SCUBA*, asociadas a una población a alto corrimiento al rojo detectadas en el rango de las submilimétricas y que, de acuerdo a Granato et al. (2001) y Granato et al. (2004), se interpretan como galaxias proto-esferoidales (las antecesoras de las actuales galaxias de tipo temprano y los bulbos masivos de galaxias de disco) en la fase en que están formando la mayor parte de sus estrellas. El modelo propuesto en ambos trabajos tiene en cuenta el agrupamiento jerárquico de la materia. En él, los halos de materia oscura se forman en los lugares favorecidos por las fluctuaciones cuánticas posteriormente acrecentadas en la inflación. Esos halos crearán pozos de potencial donde la materia bariónica caerá. El gas difuso que se halle dentro de los halos y condense será el germen de las futuras estrellas. A su vez, la acción de las supernovas y del propio centro galáctico hará que dicho gas se caliente y sea expulsado. Cuanto más grande sea el halo, más intenso y breve será el período de formación estelar (de hecho, la formación estelar decae rápidamente a $z \lesssim 3$ para las galaxias más masivas). A él le sigue una fase de cuásar (que durará entre $10^7 - 10^8$ años) y por último una etapa pasiva en la evolución galáctica, donde los objetos se enrojecen rápidamente.

En Cai et al. (2013), los autores presentan un modelo híbrido para la evolución de las galaxias y los AGN en el infrarrojo. Para $z \geq 1,5$, el modelo disponible es el de Granato et al. (2004). Para corrimientos al rojo menores, dominan las galaxias de tipo tardío, divididas en ≪frías≫ (normales) y ≪calientes≫ (o de estallido en la formación estelar, *starburst* en inglés). Las funciones de luminosidad (dependientes de época) de las dos poblaciones de las galaxias tardías no son más que simples leyes de potencia truncadas, mientras que para las de estallidos de formación estelar se trabaja por primera vez, y de forma conjunta, con la parte estelar y la nuclear de la galaxia. En este contexto, tenemos que las galaxias proto-esferoidales son los mayores contribuyentes al fondo cósmico infrarrojo por encima de las 350 micras, predominando las de tipo tardío a brillos altos (las normales) y bajos (las *starburst*). Por debajo de 250 micras, las galaxias proto-esferoidales son siempre subdominantes. Este hecho diferenciador nos puede ayudar a discriminar entre varios modelos, habiéndose corroborado el de Cai et al. (2013) con las observaciones de Herschel/SPIRE.

Como se ha visto, el estudio de estas fuentes nos proporciona información muy valiosa del universo temprano. Por ejemplo, Mancuso et al. (2015) predice el número de cuentas en radio de las galaxias con formación estelar hasta niveles de nJy para la fase 1 del telescopio Square Kilometre Array-mid. Las estimaciones de los autores dicen que detectarán galaxias con formación estelar dos órdenes de

magnitud por debajo de las detectadas por Herschel, así como un número considerable de galaxias que han sufrido el efecto lente gravitatoria.

En este contexto, Herschel se trata de un telescopio especialmente diseñado para el estudio de la evolución galáctica a altos corrimientos al rojo. Por ejemplo, Casey et al. (2012b) remarca la importancia de las galaxias infrarrojas con muy alta formación estelar en la tasa de formación estelar del universo, incluso en épocas muy tempranas. Así, su contribución a la densidad total de la tasa de formación estelar es del $> 10\%$ a $z \sim 2,5$, y del $\gtrsim 20\%$ a $z \sim 4$.

También permiten estudiar otros objetos a alto corrimiento al rojo. Así, en Planck Collaboration et al. (2015g) se toman 234 objetos muy brillantes detectados previamente por Planck y ubicados en el rango $z = 2 - 4$. El 97% de estos objetos se ha comprobado que son regiones con sobredensidad que se podrían corresponder con los antecesores de los actuales cúmulos galácticos, pudiéndose complementar con el catálogo Sunyaev-Zéldovich de Planck (Planck Collaboration et al., 2014b). El restante 3% son objetos que han sufrido el efecto lente gravitatoria.

Para estudiar bien el comportamiento de las diferentes poblaciones que observamos en radio e infrarrojo se usan las llamadas *cuentas de fuentes*, que no son otra cosa que el número de fuentes por estereo-radián y unidad de flujo. El modelo de De Zotti et al. (2005) mejoraba los preexistentes, estudiando las contribuciones a las cuentas entre 20 y 30 GHz de diferentes poblaciones. Ese trabajo estaba basado en nuevos modelos evolutivos para los radio cuásares de espectro plano, objetos BL-Lac y fuentes de espectro inclinado (ver tabla 1.1 para ver a qué se corresponden dichos objetos en relación al modelo unificado para núcleos galácticos activos). También son tenidos en cuenta los estallidos de rayos gamma y los objetos ADAF/ADIOS y las radiaciones sincrotrón y libre-libre al estimar las cuentas de diferentes poblaciones de galaxias con formación estelar.

En Tucci et al. (2011) los autores se centran en los espectros de los blazars, los objetos dominantes a flujos brillantes en las frecuencias aquí observadas (ver figura 1.10). En los resultados más recientes (Massardi et al. (2011); Planck Collaboration et al. (2011b,a) y los presentados en la sección 6.6) se ve una tendencia al empinamiento de los espectros de las fuentes. Este hecho se interpreta como, al menos parcialmente, la transición de un régimen ópticamente grueso a uno fino en la emisión sincrotrón de los chorros de los AGN (Marscher, 1996).

6.3.3 Separación de componentes difusas

Así pues, con toda esta variedad de componentes, tanto si se desea analizar la propia RFCM como cualquier otra señal presente en el mapa, se hace necesario el uso de herramienteas que nos permitan separar las distintas componentes. Entre los métodos que se usan para separar las componentes difusas se podrían citar las siguientes:

- *Combinación lineal interna* (ILC por sus siglas en inglés): que consiste en una combinación lineal de mapas a diferentes frecuencias, siendo el peso dado a cada mapa aquel que resulte de minimizar la varianza de la combinación resultante.

- *Análisis de componentes independientes* (ICA por sus siglas en inglés): asume que la señal está compuesta de distintas componentes no gaussianas estadísticamente independientes. Sin embargo, es bastante común en experimentos de la RFCM que la propia RFCM y el ruido instrumental sean gaussianos. Por tanto, en la práctica se trata de buscar representaciones donde la componentes sean independientes, o al menos tanto como sea posible.

- *Método de máxima entropía* (MEM por sus siglas en inglés): en este caso, la estimación de una componente en particular se obtiene maximizando la probabilidad *a posteriori* o, lo que es lo mismo, el producto de la verosimilitud y la probabilidad *a priori* (ver ec. 6.6). En este caso particular, la probabilidad *a priori* es del tipo entrópico: $Pr(\mathbf{s}) \propto exp[\alpha S(\mathbf{s}, \mathbf{m})]$, siendo $\mathbf{s}$ la señal, $\mathbf{m}$ un vector modelo en el que $\mathbf{s}$ se transforma en ausencia de datos, α una constante que depende de la escala del problema y S es la cross-entropía de $\mathbf{s}$ y $\mathbf{m}$.

Tras esta introducción se hará un breve repaso a la teoría de los test de hipótesis y los métodos que se usan para la detección de fuentes compactas en mapas de la RFCM (ver sección 6.4). Tras ello, se procederá a explicar y aplicar el método que se ha usado en esta tesis: el multifiltro adaptado (ver sección 6.4.4) sobre simulaciones realistas de Planck (ver sección 6.5 y Lanz et al. (2010)) y sobre datos de WMAP en los canales V y W (ver sección 6.6 y Lanz et al. (2013)). Por último, se expondrán un conjunto de conclusiones que resaltarán la potencia de esta herramienta.

6.4 Técnicas de filtrado y detección

Se ha visto previamente la importancia de una correcta detección de las fuentes compactas en los mapas de la RFCM. Vamos a exponer brevemente algunas de las herramientas más usadas para este caso. Pero antes de eso se hace necesario explicar, al menos brevemente, en qué consiste el problema

de la detección. Normalmente nos encontramos ante la disyuntiva de decidir, al menos, entre dos hipótesis complementarias. Así pues, debemos desarrollar algún tipo de procedimiento estadístico que nos permita decidir entre las diferentes hipótesis que se plantean. A este se le conoce como *test de hipótesis* y consiste en verificar la validez estadística de una hipótesis que se conoce como *nula* (H_0). En el caso binario, con solo dos hipótesis, de no ser aceptada dicha hipótesis, se dará por cierta la complementaria a la nula que se llamará *alternativa* (H_1).

En los tests de hipótesis se pueden dar, básicamente, dos tipos de errores, que son el de *tipo I*, consistente en elegir la hipótesis alternativa cuando es falsa y está muy relacionado, en el caso de detección de objetos, con el concepto de *fiabilidad* que veremos posteriormente; y el de *tipo II*, que es justamente el opuesto, elegir la hipótesis nula cuando es falsa, relacionado, a su vez, con la *completitud*. Nuestro objetivo será, en la medida de lo posible, minimizar nuestros errores, buscando un equilibrio entre ambos.

Por último, debemos definir un rango de validez para la hipótesis nula donde sea normal tener pequeñas variaciones que puedan ser atribuibles a fluctuaciones estadísticas y no a una posible detección. Este rango de validez viene dado por el valor de $1 - \alpha$, siendo α la probabilidad de rechazar la hipótesis nula cuando es cierta.

Centrándonos en el caso de esta tesis, donde se busca la detección de fuentes puntuales, la hipótesis nula es aquella que dice que no hay fuente alguna, siendo la contraria la alternativa. Lo siguiente es establecer un valor de α para fijar la región de aceptación de la hipótesis nula y un estadístico (que no es más que una variable aleatoria con una distribución de probabilidad dada) que nos permita elegir entre la hipótesis nula o la alternativa. En el caso de esta tesis, el estadístico es el valor del píxel y nuestra región de aceptación aquella cuyos valores sean menores a 5σ del mapa, siendo σ la desviación estándar del mismo. Tenemos, pues, un umbral de detección (ver sección 6.4.2). Es decir, si tenemos un píxel cuyo valor esté por debajo de 5σ, no rechazamos la hipótesis nula y diremos que no hay fuente. De lo contrario, tendremos una detección en los datos.

Pero como se dijo previamente, en los mapas no solo tenemos la señal que se desea obtener, también hay radiación de nuestra galaxia, la propia RFCM, ruido instrumental, etc. El cometido de esta tesis será la aplicación de una técnica de filtrado multifrecuencial que se adapta a las propiedades estadísticas del ruido definido local para ayudar en el proceso de detección. Cómo puede un filtro conseguir esto es algo que veremos a continuación.

Como se mencionó previamente, conviene evitar en la medida de lo posible cometer errores en nuestro proceso de detección: dependiendo de cuáles sean nuestros objetivos, priorizaremos unos sobre otros. En cuanto al catálogo que se obtenga, e íntimamente relacionado con lo anterior, conviene

resaltar tres características que medirán la bondad del mismo: la *completitud* y la *fiabilidad* anteriormente apuntadas y la *precisión* de nuestra detección. La primera nos dice el porcentaje de fuentes reales que detectamos para un cierto flujo. La fiabilidad nos da el porcentaje de fuentes reales detectadas sobre el total de detecciones (incluyendo las espurias). Es decir, la cantidad $100-$fiabilidad nos da el porcentaje de detecciones espurias. Y la precisión nos indica cuán precisa es nuestra detección en relación a flujo, posición, etc.

A continuación mostramos algunas de las herramientas más usadas para la detecciń de fuentes, como son las técnicas bayesianas, un par de detectores de los más comunes en el campo de la detección de objetos puntuales, como son el umbral de detección antes citado y el lema de Neyman-Pearson para el filtrado de los mapas, así como distintas técnicas de filtrado, para finalmente presentar el método usado en esta tesis, el multifiltro adaptado.

6.4.1 Técnicas bayesianas

Las técnicas bayesianas son los dispositivos óptimos para afrontar el proceso de detección si se tiene suficiente (y fiable) información estadística del ruido y la señal. El teorema de Bayes se enuncia de la siguiente manera:

$$P(\theta|D) \propto P(D|\theta)P(\theta), \tag{6.6}$$

siendo $P(\theta|D)$ la probabilidad *a posteriori* de un modelo dados unos datos, $P(D|\theta)$ es la verosimilitud o probabilidad de unos datos dado un modelo y $P(\theta)$ es la probabilidad *a priori* del modelo donde la θ representa el modelo y D los datos. La idea es maximizar la probabilidad *a posteriori*, es decir, buscar aquellos valores del modelo (posición de las fuentes, su amplitud, ...) que maximicen dicha probabilidad dados los datos. Este es un posible enfoque, pero también se podría caracterizar toda la distribución *a posteriori* y obtener así más información. Argüeso et al. (2011a) es un claro ejemplo del primer enfoque: las diferentes incógnitas (número de fuentes, sus posiciones y flujos) son independientes entre ellas y por tanto sus distribuciones *a priori* son independientes, siendo sus expresiones las dadas por las ecuaciones 2.9. Si se supone un ruido gaussiano, se conoce su verosimilitud y, por tanto, teniendo sus probabilidades *a priori*, también la *a posteriori*. Solo resta encontrar los valores de las incógnitas que la maximicen. Carvalho et al. (2009) es un claro ejemplo del segundo enfoque, donde se trata de caracterizar la distribución *a posteriori* al completo. Como hace Argüeso et al. (2011a), factoriza el la probabilidad *a priori* y asume las mismas propiedades estadísticas para el ruido, siendo

la verosimilitud la misma. A continuación filtran el mapa con el filtro adaptado (ec. 6.12) para localizar las fuentes y posteriormente, y mediante un método iterativo (Powell-Snakes), buscan los máximos en el espacio de parámetros, realizando una aproximación gaussiana en cada pico y siendo sometido cada uno a un criterio de detección basado en la regla de Neyman-Pearson que se introducirá en el siguiente apartado.

Los propios autores señalan algunas carencias de este método, y en un trabajo posterior (Carvalho et al., 2012) corrigen algunas como usar distribuciones *a priori* más realistas e introducen novedades como hacer extensivo el método a varias frecuencias. Sin embargo, como ellos mismos aclaran en su trabajo, tal implementación no se ha llevado a cabo del todo.

6.4.2 Detección

En esta secciń se comentarán dos procedimientos ampliamente usados para la detección de fuentes puntuales. Uno ya ha sido anteriormente apuntado, y se trata del umbral de detección. La idea es bastante sencilla: establecer un valor a partir del cual decimos que tenemos una detección. Así, en el caso de las fuentes puntuales, ese valor suele fijarse en términos de la desviación estándar del mapa, normalmente 3σ o 5σ (este último es el empleado en esta tesis): por tanto, si encontramos un píxel cuyo valor supere ese umbral, tenemos una detección.

Otro ejemplo de detector es el basado en la regla de Neyman-Pearson. El umbral de detección solo usa la probabilidad de tener una fuente si el flujo (o intensidad) está por encima de un cierto valor. Sin embargo, se puede usar información adicional para mejorar el proceso de detección. Esto es lo que se hace con la regla Neyman-Pearson. En este caso se usa la curvatura y el campo normalizado. Con esta información se pueden construir la densidad de picos tanto en ausencia (Rice, 1954) como en presencia de fuentes (Barreiro et al., 2003).

Aplicando una regla de Neyman-Pearson bayesiana, se puede ver que la región de rechazo de la hipótesis nula (es decir, se rechaza la hipótesis nula que dice que no hay fuentes aceptando la alternativa) es:

$$L(\nu,\kappa) = \frac{n(\nu,\kappa)}{n_b(\nu,\kappa)} \geq L_*, \tag{6.7}$$

donde L_* es una constante elegida con ciertos criterios y n y n_b son las densidades numéricas de detecciones y de detecciones espurias respectivamente.

6.4.3 Técnicas de filtrado

Al hablar de filtrado, nos viene a la cabeza la idea de selección, en el sentido de que si ≪filtramos≫ algo es porque dejamos pasar (o nos quedamos con) lo que nos interesa. Esta afirmación coloquial sin mucho rigor estadístico nos da una idea intuitiva de lo que es el proceso de filtrado. Matemáticamente hablando, un filtro puede ser definido como un operador tal que transforma de alguna forma los datos de entrada, dando lugar a unos de salida:

$$L : f(x) \rightarrow g(x) = Lf(x), \tag{6.8}$$

donde L representa el filtro, f los datos de entrada y g los de salida; x es la variable independiente. Es interesante que los filtros tengan las propiedades de linealidad y homogeneidad. Se puede ver que, en tal caso, se cumple lo siguiente:

$$Lf(x) = \int f(u)h(x-u)du = h \otimes f(x), \tag{6.9}$$

donde h es la respuesta al impulso δ, tal que $h = L\delta$. Como se ve, y gracias a estas dos propiedades, filtrar equivale a convolucionar. Y la convolución en el espacio de Fourier es simplemente un producto:

$$Lf(x) = g(x) = h \otimes f(x) = \int (h(q)f(q)exp^{-iqx}dq), \tag{6.10}$$

donde $h(q)$ y $f(q)$ son las transformadas de Fourier de h y f, respectivamente. En esta ecuación se puede apreciar que la función de transferencia $h(q)$ puede actuar como un dispositivo que seleccione las frecuencias, entendidas en el espacio de Fourier.

En esta tesis, como ya se ha dicho, el objetivo será la detección de fuentes compactas, es decir, aquellas que tienen un tamaño angular menor que el del *beam* del experimento. Por tanto, tienen una frecuencia bien determinada. Es por ello que los filtros resultan tan convenientes y han sido ampliamente usados en este campo.

A continuación se mostrarán algunos de los aplicados en la detección de fuentes puntuales:

- **Filtro de Wiener**: viene dado, en el espacio de Fourier, por la expresión

$$\psi_{WF}(q) = \frac{|s(q)|^2}{|s(q)|^2 + |n(q)|^2}, \tag{6.11}$$

donde $s(q)$ y $n(q)$ son las transformadas de la señal y el ruido respectivamente. La señal s es la

convolución de la señal subyacente y la respuesta del aparato (suponiendo que no sea una delta de Dirac). Este filtro es óptimo en el sentido de los mínimos cuadrados.

- **Filtro adaptado**: si deseamos tener un estimador insesgado y eficiente de la amplitud del objeto que deseamos detectar, como solución obtenemos el filtro adaptado cuya expresión es:

$$\psi_{MF}(q) = \frac{\tau(q)}{aP(q)}, \;\; a = \int d\mathbf{q} \frac{\tau^2(q)}{P(q)}. \tag{6.12}$$

  En esta ecuación, τ es el perfil que mejor describe la respuesta de la antena del experimento a un objeto puntual (*beam* en inglés), P el espectro de potencias del ruido y a una constante de normalización. El filtro adaptado es óptimo (dentro de los filtros lineales) en tanto en cuanto maximiza el cociente señal ruido.

- ***Ondículas*** o *wavelets* en inglés. Lo que hace interesante a esta herramienta es que conserva información espacial y de la escala de las estructuras de los mapas. Esto las convierte en sumamente adecuadas para la tarea de detectar fuentes puntuales. Un ejemplo de este tipo de funciones es la *ondícula de sombrero mexicano* (también conocida por MHW, las siglas en inglés de *Mexican Hat Wavelet*):

$$\psi(x) = \frac{1}{\sqrt{2\pi}} \left[2 - \left(\frac{x}{R} \right)^2 \right] e^{-\frac{x^2}{2R^2}}. \tag{6.13}$$

  La MHW se obtiene al aplicar el operador laplaciano sobre una gaussiana de anchura R y por eso es adecuada para la detección de fuentes con perfiles gaussianos (Cayón et al., 2000; López-Caniego et al., 2005; Vielva et al., 2001b). El laplaciano puede ser aplicado tantas veces como se desee sobre la gaussiana con el fin de obtener una familia completa de MHW. La MHW2 es particularmente interesante por sus prestaciones (González-Nuevo et al., 2006).

- **Filtro adaptativo biparamétrico**: mezclando la filosofía que hay detrás de las ondículas y del filtro adaptado, López-Caniego and Vielva (2012) desarrollan este filtro, cuya expresión es la siguiente:

$$\Psi(\mathbf{x}, R, g, \mathbf{b}) = \frac{1}{R^2} \bar{\psi}_g \left(\frac{|\mathbf{x} - \mathbf{b}|}{R} \right), \tag{6.14}$$

  dándonos R una idea de la escala y siendo g un índice que se podría decir que desempeña un rol similar al orden del laplaciano en las MHW. ψ_g es una función que, para el caso de fuentes gaussianas, toma la siguiente forma:

$$\bar{\psi}_g(qR) = \frac{1}{\pi} \frac{1}{\Gamma(\frac{2+g}{2})} (qR)^g e^{-(qR)^2/2}, \tag{6.15}$$

- **Matriz de multifiltros adaptados**: en Herranz and Sanz (2008), los autores desarrollan un herramienta que trabaja con varias frecuencias simultáneamente, teniendo como salida el mismo número de mapas que en la entrada. Se exige que estos multifitros cumplan dos requisitos, a saber, que el mapa filtrado combinado a una frecuencia dada sea un estimador insesgado de la amplitud de la fuente a dicha frecuencia; y que las varianzas de los distintos campos filtrados sean mínimas (estimador eficiente). Teniendo que cumplir estas dos condiciones, podemos comprobar (usndo el método de los multiplicadores de Lagrange) que la matriz de multifiltros han de ser de la siguiente manera:

$$\mathbf{\Psi}^* = \mathbf{F}\mathbf{P}^{-1}, \tag{6.16}$$

  donde $\mathbf{P}$ es el cross-espectro de potencias y $\mathbf{F}$ una matriz en donde está incluida el perfil del *beam* de la antena.

6.4.4 Multifiltro adaptado

Tras este breve paseo por distintos métodos de filtrado y detección, pasamos a explicar el filtro que se usará en esta tesis: el multifiltro adaptado (ver Herranz et al. (2002c)), y el porqué escogemos un método como este.

De entre todos los filtros que hemos visto (salvo la matriz de multifiltros adaptados), todos son mono-frecuenciales, es decir, filtran un único mapa a una frecuencia dada. Sin embargo, con esta estrategia no usamos toda la información disponible y los resultados más recientes de WMAP y Planck nos muestran que, aun funcionando correctamente, se aprecia que están al límite en su capacidad de detectar fuentes puntuales a flujos bajos. Así pues, se impone un cambio en nuestra estrategia de detección si queremos reducir el flujo límite de detección. Para ello, el uso de técnicas multifrecuenciales, como el multifiltro adaptado o las matrices de filtros adaptados (ec. 6.16), es una buena opción ya que utilizaremos información adicional, como puede ser la correlación que hay entre el ruido en dos frecuencias suficientemente cercanas y el hecho de poder usar cierta información espacial de las fuentes, como es el hecho de que la misma fuente aparece en la misma posición en dos frecuencias distintas. También se puede parametrizar la dependencia frecuencial de las fuentes (como una ley de potencias en esta tesis) aunque no pueda conocerse su comportamiento espectral antes de la detección. Esta es la principal diferencia con respecto a la matriz de multifiltros adaptados, como se verá a continuación, pues no parametrizar el comportamiento espectral de las fuentes hace que resulte necesario tener tantos mapas de salida como canales, y es lo que conlleva que la matriz de multifiltros sea una matriz $N \times N$, a diferencia del multifiltro adaptado, que es un vector N-dimensional de filtros.

Para conocer la expresión del multifiltro adaptado, necesitamos imponer unas condiciones. Estas serán dos: que el campo filtrado total sea un estimador insesgado de la amplitud de la fuente y que la varianza de dicho campo sea mínima, es decir, que sea un estimador eficiente de la amplitud de la fuente. Con estas condiciones, y haciendo uso de los multiplicadores de Lagrange, obtenemos la siguiente expresión para el multifiltro adaptado:

$$\mathbf{\Psi}(q) = \alpha\, \mathbf{P}^{-1}\mathbf{F},\;\; \alpha^{-1} = \int d\mathbf{q}\, \mathbf{F}^t\mathbf{P}^{-1}\mathbf{F}, \tag{6.17}$$

donde $\mathbf{\Psi}(q)$ es el vector columna $\mathbf{\Psi}(q) = [\psi_\nu(q)]$, $\mathbf{F}$ es el vector columna $\mathbf{F} = [f_\nu\tau_\nu]$ y $\mathbf{P}^{-1}$ es la inversa de la matriz del cross-espectro de potencias $\mathbf{P}$. Para conocer más detalles de cómo se obtiene la expresión del multifiltro adaptado, ver el desarrollo matemático del apéndice 2.10.

6.5 Aplicación del multifiltro adaptado en simulaciones de Planck

Una vez explicado el multifiltro adaptado, se procede a aplicar dicho multifiltro sobre simulaciones realistas del experimento Planck a 44 y 100 GHz. Para las simulaciones se ha usado el modelo la herramienta de simulación del cielo de microondas de Planck [2] (PSM por sus siglas en inglés, Delabrouille et al. (2013)). La emisión libre-libre está basada en el trabajo Dickinson et al. (2003), la sincrotrón en una extrapolación de Haslam et al. (1982) y la emisión térmica del polvo en el modelo 7 del trabajo Finkbeiner et al. (1999). Para simular las fuentes, escogemos ocho regiones situadas a latitudes galácticas $|b| = 40°$, tomando los flujos los valores $\{0,1,\ 0,2,\ 0,3,\ 0,4,\ 0,5,\ 0,6,\ 0,7,\ 0,8,\ 0,9,\ 1,0\}$ Jy y los índices espectrales $\{1,0,\ 0,7,\ 0,4,\ 0,1,\ -0,2,\ -0,5,\ -0,8,\ -1,1,\ -1,4\}$, respectivamente (para ver más detalles del porqué de estos valores, ver González-Nuevo et al. (2008)), simulando para cada par de valores 100 fuentes que serán distribuidas aleatoriamente en los mapas, evitando que se superpongan. Se procede de la siguiente manera: para cada conjunto de 100 fuentes se selecciona al azar uno de los ocho parches y colocamos en él 10 fuentes (aleatoriamente), y repetimos el proceso hasta tener todas las fuentes.

Para comprobar la potencia y eficacia del multifiltro adaptado, se usará el filtro adaptado (ec. 6.12) que intentará detectar las mismas fuentes. En la ecuación del multifiltro se ve un parámetro libre, que es el índice espectral: el estimador que usaremos del mismo es aquel que maximiza el cociente señal ruido para cada fuente después de haber filtrado la misma imagen con el multifiltro adaptado con diferentes valores del índice.

Las diferentes pruebas realizadas muestran una importante mejora con el multifiltro. Así, por

[2] `http://www.apc.univ-paris7.fr/APC_CS/Recherche/Adamis/PSM/psky-en.php`

ejemplo, el número de detecciones es siempre superior con el nuevo método. En la figura 3.1 se puede apreciar este efecto, en particular a flujos bajos, que son las regiones que revisten mayor interés.

También se aprecia que la precisión con la que estiman los parámetros con los que han sido definidas las fuentes, a saber, el flujo en la frecuencia de referencia, 44 GHz (ver ec. 2.62), y el índice espectral, se recuperan mejor con el multifiltro adaptado. Aspecto a tener en cuenta para posteriores estudios y análisis de dichas fuentes.

Para comprobar cuántas fuentes espurias introduce el multifiltro adaptado se realizan un nuevo conjunto de simulaciones más realistas, consistentes en simular fuentes que siguen una distribución de Poisson casi uniforme (González-Nuevo et al., 2005) a 44 GHz, y sus flujos el modelo de cuentas de De Zotti et al. (2005). Además, los flujos a 100 GHz se estiman asumiendo índices espectrales aleatorios de la distribución de González-Nuevo et al. (2008). Por último, y para dejar entrar más fuentes espurias en el proceso de detección, el umbral de detección se reduce de 5σ a 3σ. Se puede ver en la figura 3.4 que se detecta un mayor número de fuentes reales a flujos bajos (por debajo de $\sim 0.4 - 0.5$ Jy), especialmente a 44 GHz.

La fiabilidad es otro aspecto muy a tener en cuenta en la confección de catálogos: definida como la razón entre fuentes reales y fuentes detectadas, vemos que la fiabilidad del filtro adaptado solo se acerca a la del multifiltro para flujos próximos a 1 Jy a 44 GHz y a 0.3 Jy a 100 GHz.

Por último, se representan el número de fuentes reales frente a las espurias (ver figura 3.6). Como se ve, de nuevo el multifiltro mejora las prestaciones del filtro adaptado, estando la curva del multifiltro siempre por encima. Esto equivale a decir que, para un número de fuentes reales detectadas, el filtro adaptado mono-frecuencial introduce más espurias en el catálogo.

6.6 Aplicación del multifiltro adaptado a datos reales de WMAP tras siete años de misión

Tras ver el buen funcionamiento del multifiltro adaptado en simulaciones realistas de Planck, el siguiente paso natural es su aplicación sobre datos reales. Para ello se usarán los mapas de WMAP tras siete años de observaciones a 61 y 94 GHz (canales V y W), que resultan ser los más ruidosos y con un menor número de detecciones de fuentes puntuales. Obviamente, se tienen en cuenta las diferencias con respecto a las simulaciones de Planck. Una de las más notables es el relacionado con los *beams* de las antenas: a partir de las funciones de transferencia de los *beams*[3], y usando la ecuación 4.1, somos capaces de construir un perfil bidimensional de dicho *beam*. Se tendrá en cuenta,

[3] lambda.gsfc.nasa.gov/product/map/dr4/beam_xfer_get.cfm

además, que el centro de la fuente no tiene por qué estar en el centro del píxel y que los perfiles reales de WMAP no son simétricos rotacionalmente hablando (nuestro perfiles bidimensionales obtenidos a partir de las funciones de transferencia gracias a la ec. 4.1 hacen que, por construcción, sean simétricos rotacionalmente) de ahí que se tengan que tener en cuenta estos efectos en los cálculos.

Una vez tenemos los *beams*, procedemos a filtrar todo el cielo. Como nuestro multifiltro trabaja en el espacio de Fourier y no en el de los armónicos esféricos (ver ec. 6.12), dividimos el cielo en parches lo suficiente pequeños para que la aproximación plana sea válida. Una vez tenemos todo esto en cuenta, los pasos que se siguen en el filtrado son idénticos a los de la sección anterior. En este caso particular, la frecuencia de referencia será la de 94 GHz.

Vemos que el número de detecciones 5σ fuera del plano galáctico y de la Gran Nube de Magallanes es de 129. Nueve de estas fuentes se corresponden con zonas de nuestra galaxia (ver tabla 4.1) y otra no tiene homóloga en cualquier otro catálogo, resultando en un total de 119 fuentes de origen extragaláctico (ver tabla 4.2). Lo más reseñable es ver que en los datos de WMAP tras tres años de observaciones solo se detectan 22 fuentes 5σ a 94 GHz en una detección no ciega (López-Caniego et al., 2007) y que hay tres fuentes que el multifiltro es capaz de detectar sin que lo haya hecho el *Early Release Compact Source Catalog* de Planck.

Una comparación de los flujos hallados con el multifiltro para las fuentes detectadas muestra un buen acuerdo entre lo obtenido aquí y los calibradores y Planck (ver figuras 4.4 y 4.5) por encima de 2 Jy, con ciertas diferencias en los valores de la media cuadrática que podrían indicarnos errores para los flujos algo mayores de los indicados en la tabla 4.2.

La distribución del índice espectral para las fuentes extragalácticas detectadas muestra un valor medio igual a -0,65 con una dispersión de 0,71. Este resultado viene a señalar el empinamiento de las fuentes extragalácticas por encima de los $\sim$ 70 GHz, algo ya apuntado por Sadler et al. (2008); González-Nuevo et al. (2008); Marriage et al. (2011); Massardi et al. (2010), confirmado por los trabajos Planck Collaboration et al. (2011b,a); Giommi et al. (2012) y explicado por Tucci et al. (2011).

Como se ha visto en esta tesis, hemos modificado el multifiltro adaptado (Herranz et al., 2002c) para la detección de fuentes puntuales en mapa de la RFCM. El motivo es que los distintos métodos que se han venido aplicando hasta ahora, en su mayoría monofrecuenciales (ver capítulo 2), han mostrado (o están muy cerca de mostrar) una saturación en su efectividad al detectar estos objetos. Así, se hace necesario el desarrollo de nuevas herramientas que nos permitan detectar fuentes más débiles. Para ello, los métodos multifrecuenciales son muy adecuados, ya que hacen uso de una mayor cantidad de información (como puede ser el cross-espectro de potencias del ruido, información espacial de las

fuentes y parametrizar su comportamiento espectral como una ley de potencias) que nos permite, en los mapas filtrados, obtener un catálogo más completo.

Como se dijo en el párrafo anterior, el multifiltro adaptado ya se había utilizado para la detección de cúmulos de galaxias mediante el efecto Sunyaev-Zeldóvich (ver sección 1.2.2). En ese caso, el parámetro libre era el radio del cúmulo, ya que la dependencia frecuencial de dicho efecto es perfectamente conocida. Trasladando la idea a esta tesis, en este caso conocemos el tamaño de los objetos (fuentes puntuales, y por tanto con tamaño angular menor al del *beam* del experimento), desconociendo su comportamiento espectral. Modelizando dicho comportamiento como una ley de potencias (ver ec. 2.62), aunque dicha modelización es opcional, tenemos que el único parámetro libre es el índice espectral.

Con esto claro, el mapa en cuestión se filtra tantas veces como valores del índice espectral queramos probar, y el estimador óptimo de dicho índice será aquel que maximice el cociente señal ruido (SNR por sus siglas en inglés), como se ve en el Apéndice 2.11. Conviene resaltar que, en el caso del multifitro adaptado, la SNR es la misma para todos los mapas que se han filtrado simultáneamente. Esto difiere considerablemente de los métodos monofrecuencia, donde al filtrar un mapa cada vez, las SNR son por lo general distintas, pudiendo darse el caso de que haya fuentes que no son detectadas a ciertas frecuencias. Esto no puede pasar con el multifiltro adaptado: la fuente que es detectada lo es en todas las frecuencias y con la misma SNR, facilitando un posible análisis espectral de la misma al no tener que recurrir a catálogos externos, interpolaciones, etc.

La facilidad al implementar el multifiltro, su capacidad de reducir el límite inferior del flujo a partir del cual se detectan fuentes y lo explicado en el párrafo anterior, hacen del multifiltro adaptado una herramienta especialmente buena para la detección de objetos puntuales.

Exigiéndole que cumpla ciertos requisitos (ver Apéndice 2.10), obtenemos la expresión del multifiltro adaptado (ec. 6.17) y lo aplicamos primeramente a simulaciones realistas del cielo de Planck (comparando lo obtenido con el filtro adaptado) y luego a datos reales de la misión WMAP tras siete años de observaciones. Se puede apreciar que el multifiltro adaptado mejora el número de detecciones con respecto al filtro adaptado, en particular a flujos bajos, donde más interesa. Esto se puede apreciar si nos fijamos en la figura 3.6, donde para un número fijo de detecciones espurias, el número de reales siempre es superior para el multifitro.

Una vez probado con simulaciones, es la hora de probar su eficacia con datos reales, y de nuevo se aprecia que el multifiltro vuelve a demostrar ser un herramienta muy potente. Baste decir que el número de fuentes extragalácticas confirmadas a 61 y 94 GHz es de 119 (búsqueda ciega a 5σ). Compárese este número con las 22 obtenidas en los datos tras tres años de observaciones de la misma misión en

una detección NO ciega a 94 GHz (López-Caniego et al., 2007).

La potencia exhibida por el multifiltro adaptado hace plantearnos qué podría pasar si el número de canales usados es mayor. Creemos que la capacidad de detección se incrementaría, y para ello se ha empezado a utilizar en tres canales de Herschel, cuyos resultados preliminares muestran resultados esperanzadores. Dicha extensión a más frecuencias podría hacerse igualmente con Planck, haciendo hincapié que si las frecuencias escogidas están muy separadas, el método podría dejar de funcionar al dejar de tener las mismas fuentes o el mismo fondo en los mapas.

Otros aspectos entrarán en consideración cuando el método se extienda a más frecuencias. Uno será la dificultad que pueda entrañar hallar el máximo de la SNR en un espacio mayor que el unidimensional cuando son dos los mapas filtrados simultáneamente. Distintos métodos numéricos, disponibles en la literatura, podrían dar una solución rápida y eficaz al problema en cuestión.

Con todos estos ingredientes, se puede pensar en preparar el multifiltro de cara a futuras misiones. Dos campos serán muy importantes en los próximos años: la polarización de la RFCM (para la posible detección del modo B) y la comprensión de la materia y energía oscuras.

La misión COrE++ [4], aún no aprobada por la ESA, proporcionaría mapas del cielo de microondas en 15 canales entre 45 y 795 GHz con precisión y resolución mejores que Planck. La aplicación del multifiltro nos permitiría detectar fuentes extragalácticas que complementarían los catálogos de Planck.

El otro gran foco de interés de la cosmología en los próximos años será desentrañar los misterios de la parte oscura del universo: la materia y la energía oscuras. Para ello, en algunas misiones se utilizan dos fenómenos como son el efecto de lente gravitatoria y las oscilaciones acústicas bariónicas. El primero es debido a la distorsión en la trayectoria de la luz en presencia de un campo gravitatorio; el segundo por las fluctuaciones (periódicas) en la densidad de la materia bariónica como consecuencia de las oscilaciones acústicas en el plasma primordial, y que se manifiestan en una escala de 150 Mpc (en coordenadas comóviles). Misiones como Euclid (Laureijs et al., 2011) y J-PAS Benítez et al. (2014) llevarán a cabo el mapeo de grandes áreas del cielo, principalmente en el óptico, y en varias frecuencias. El multifiltro podrá, por tanto, ser aplicado, ayudando en la detección de cúmulos de galaxias para una mejor observación de las oscilaciones acústicas bariónicas.

[4] http://indico.ipmu.jp/indico/getFile.py/access?contribId=69&sessionId=2&resId=0&materialId=slides&confId=72

Bibliography

R. A. Alpher, H. Bethe, and G. Gamow. The Origin of Chemical Elements. *Physical Review*, 73(7): 803–804, April 1948a. doi: 10.1103/PhysRev.73.803.

R. A. Alpher, R. Herman, and G. A. Gamow. Thermonuclear Reactions in the Expanding Universe. *Physical Review*, 74:1198–1199, November 1948b. doi: 10.1103/PhysRev.74.1198.2.

R. A. Alpher, R. Herman, and G. A. Gamow. Erratum: Thermonuclear Reactions in the Expanding Universe. *Physical Review*, 75:701–701, February 1949. doi: 10.1103/PhysRev.75.701.

P. André, C. Baccigalupi, A. Banday, D. Barbosa, B. Barreiro, J. Bartlett, N. Bartolo, E. Battistelli, and et al. PRISM (Polarized Radiation Imaging and Spectroscopy Mission): an extended white paper. J. Cosmology Astropart. Phys., 2:006, February 2014. doi: 10.1088/1475-7516/2014/02/006.

J. R. P. Angel and H. S. Stockman. Optical and infrared polarization of active extragalactic objects. ARA&A, 18:321–361, 1980. doi: 10.1146/annurev.aa.18.090180.001541.

F. Argüeso, E. Salerno, D. Herranz, J. L. Sanz, E. E. Kuruoğlu, and K. Kayabol. A Bayesian technique for the detection of point sources in cosmic microwave background maps. MNRAS, 414:410–417, June 2011a. doi: 10.1111/j.1365-2966.2011.18398.x.

F. Argüeso, J. L. Sanz, and D. Herranz. Filter Design for the Detection/Estimation of the Modulus of a Vector. Application to Polarization Data. *arXiv:1101.0701v1, accepted for publication in Signal Processing*, January 2011b.

J. M. Bardeen, P. J. Steinhardt, and M. S. Turner. Spontaneous creation of almost scale-free density perturbations in an inflationary universe. Phys. Rev. D, 28:679–693, August 1983. doi: 10.1103/PhysRevD.28.679.

R. B. Barreiro, J. L. Sanz, D. Herranz, and E. Martínez-González. Comparing filters for the detection of point sources. MNRAS, 342:119–133, June 2003. doi: 10.1046/j.1365-8711.2003.06520.x.

P. Barthel, M. Haas, C. Leipski, and B. Wilkes. Extreme Host Galaxy Growth in Powerful Early-epoch Radio Galaxies. ApJ, 757:L26, October 2012. doi: 10.1088/2041-8205/757/2/L26.

N. Benítez, R. Dupke, M. Moles, L. Sodré, A. J. Cenarro, A. Marín-Franch, K. Taylor, D. Cristóbal, and et al. J-PAS: The Javalambre-Physics of the Accelerated Universe Astrophysical Survey. *arXiv:1403.5237v1*, March 2014.

C. L. Bennett, M. Halpern, G. Hinshaw, N. Jarosik, A. Kogut, M. Limon, S. S. Meyer, L. Page, D. N. Spergel, G. S. Tucker, E. Wollack, E. L. Wright, C. Barnes, M. R. Greason, R. S. Hill, E. Komatsu, M. R. Nolta, N. Odegard, H. V. Peiris, L. Verde, and J. L. Weiland. First-Year Wilkinson Microwave Anisotropy Probe (WMAP) Observations: Preliminary Maps and Basic Results. ApJS, 148:1–27, September 2003. doi: 10.1086/377253.

E. Bertin and S. Arnouts. SExtractor: Software for source extraction. A&AS, 117:393–404, June 1996.

M. Béthermin, H. Dole, G. Lagache, D. Le Borgne, and A. Penin. Modeling the evolution of infrared galaxies: a parametric backward evolution model. A&A, 529:A4, May 2011. doi: 10.1051/0004-6361/201015841.

R. D. Blandford and M. C. Begelman. On the fate of gas accreting at a low rate on to a black hole. MNRAS, 303:L1–L5, February 1999. doi: 10.1046/j.1365-8711.1999.02358.x.

R. D. Blandford and A. Königl. Relativistic jets as compact radio sources. ApJ, 232:34–48, August 1979. doi: 10.1086/157262.

H. Bondi and T. Gold. The Steady-State Theory of the Expanding Universe. MNRAS, 108:252, 1948.

C. S. Burrus, R. A. Gopinath, and H. Guo. *Introduction to wavelets and Wavelets Transforms: A Primer*. Prentice-Hall, Inc., 1998. ISBN 0-13-489600-9.

Z.-Y. Cai, A. Lapi, J.-Q. Xia, G. De Zotti, M. Negrello, C. Gruppioni, E. Rigby, G. Castex, J. Delabrouille, and L. Danese. A Hybrid Model for the Evolution of Galaxies and Active Galactic Nuclei in the Infrared. ApJ, 768:21, May 2013. doi: 10.1088/0004-637X/768/1/21.

P. Carvalho, G. Rocha, and M. P. Hobson. A fast Bayesian approach to discrete object detection in astronomical data sets - PowellSnakes I. MNRAS, 393:681–702, March 2009. doi: 10.1111/j.1365-2966.2008.14016.x.

P. Carvalho, G. Rocha, M. P. Hobson, and A. Lasenby. PowellSnakes II: a fast Bayesian approach to discrete object detection in multi-frequency astronomical data sets. MNRAS, 427:1384–1400, December 2012. doi: 10.1111/j.1365-2966.2012.22033.x.

C. M. Casey, S. Berta, M. Béthermin, J. Bock, C. Bridge, J. Budynkiewicz, D. Burgarella, E. Chapin, and et al. A Redshift Survey of Herschel Far-infrared Selected Starbursts and Implications for Obscured Star Formation. ApJ, 761:140, December 2012a. doi: 10.1088/0004-637X/761/2/140.

C. M. Casey, S. Berta, M. Béthermin, J. Bock, C. Bridge, D. Burgarella, E. Chapin, S. C. Chapman, and et al. A Population of z $>$ 2 Far-infrared Herschel-SPIRE-selected Starbursts. ApJ, 761:139, December 2012b. doi: 10.1088/0004-637X/761/2/139.

L. Cayón, J. L. Sanz, R. B. Barreiro, E. Martínez-González, P. Vielva, L. Toffolatti, J. Silk, J. M. Diego, and F. Argüeso. Isotropic wavelets: a powerful tool to extract point sources from cosmic microwave background maps. MNRAS, 315:757–761, July 2000. doi: 10.1046/j.1365-8711.2000.03462.x.

X. Chen and E. L. Wright. Extragalactic Point-Source Search in WMAP 61 and 94 GHz Data. ApJ, 681:747–755, July 2008. doi: 10.1086/588249.

X. Chen and E. L. Wright. Extragalactic Point Source Search in Five-Year WMAP 41, 61, and 94 GHz Maps. ApJ, 694:222–234, March 2009. doi: 10.1088/0004-637X/694/1/222.

L.-Y. Chiang, H. E. Jørgensen, I. P. Naselsky, P. D. Naselsky, I. D. Novikov, and P. R. Christensen. An adaptive filter for the construction of the Planck Compact Source Catalogue. MNRAS, 335: 1054–1060, October 2002. doi: 10.1046/j.1365-8711.2002.05692.x.

J. J. Condon. Radio emission from normal galaxies. ARA&A, 30:575–611, 1992. doi: 10.1146/annurev.aa.30.090192.003043.

B. E. Corey and D. T. Wilkinson. A Measurement of the Cosmic Microwave Background Anisotropy at 19 GHz. In *Bulletin of the American Astronomical Society*, volume 8 of *Bulletin of the American Astronomical Society*, page 351, March 1976.

M. Cruz, N. Turok, P. Vielva, E. Martínez-González, and M. Hobson. A Cosmic Microwave Background Feature Consistent with a Cosmic Texture. *Science*, 318:1612–, December 2007. doi: 10.1126/science.1148694.

M. Cruz, P. Vielva, E. Martínez-González, and R. B. Barreiro. Anomalous variance in the WMAP data and Galactic foreground residuals. MNRAS, 412:2383–2390, April 2011. doi: 10.1111/j.1365-2966.2010.18067.x.

I. Daubechies. Orthonormal bases of compactly supported wavelets. Comm. Pure Appl. Math., 41: 909–996, October 1988. doi: 10.1002/cpa.3160410705.

K. S. Dawson, W. L. Holzapfel, J. E. Carlstrom, M. Joy, S. J. LaRoque, A. D. Miller, and D. Nagai. Measurement of Arcminute-Scale Cosmic Microwave Background Anisotropy with the Berkeley-Illinois-Maryland Association Array. ApJ, 581:86–95, December 2002. doi: 10.1086/344226.

P. de Bernardis, P. A. R. Ade, J. J. Bock, J. R. Bond, J. Borrill, A. Boscaleri, K. Coble, B. P. Crill, and et al. A flat Universe from high-resolution maps of the cosmic microwave background radiation. Nature, 404:955–959, April 2000.

A. de Oliveira-Costa, A. Kogut, M. J. Devlin, C. B. Netterfield, L. A. Page, and E. J. Wollack. Galactic Microwave Emission at Degree Angular Scales. ApJ, 482:L17–L20, June 1997. doi: 10.1086/310684.

D. S. de Young. *The physics of extragalactic radio sources*. 2002.

G. De Zotti, L. Toffolatti, F. Argüeso, R. D. Davies, P. Mazzotta, R. B. Partridge, G. F. Smoot, and N. Vittorio. The Planck Surveyor Mission: Astrophysical Prospects. In L. Maiani, F. Melchiorri, and N. Vittorio, editors, *3K cosmology*, volume 476 of *American Institute of Physics Conference Series*, pages 204–+, 1999.

G. De Zotti, C. Burigana, A. Cavaliere, L. Danese, G. L. Granato, A. Lapi, P. Platania, and L. Silva. The Sunyaev-Zeldovich effect as a probe of the galaxy formation process. In G. Bertin, D. Farina, and R. Pozzoli, editors, *Plasmas in the Laboratory and in the Universe: New Insights and New Challenges*, volume 703 of *American Institute of Physics Conference Series*, pages 375–384, April 2004. doi: 10.1063/1.1718483.

G. De Zotti, R. Ricci, D. Mesa, L. Silva, P. Mazzotta, L. Toffolatti, and J. González-Nuevo. Predictions for high-frequency radio surveys of extragalactic sources. A&A, 431:893–903, March 2005. doi: 10.1051/0004-6361:20042108.

G. De Zotti, M. Massardi, M. Negrello, and J. Wall. Radio and millimeter continuum surveys and their astrophysical implications. A&A Rev., 18:1–65, February 2010. doi: 10.1007/s00159-009-0026-0.

J. Delabrouille, M. Betoule, J.-B. Melin, M.-A. Miville-Deschênes, J. Gonzalez-Nuevo, M. Le Jeune, G. Castex, G. de Zotti, and et al. The pre-launch Planck Sky Model: a model of sky emission at submillimetre to centimetre wavelengths. A&A, 553:A96, May 2013. doi: 10.1051/0004-6361/201220019.

F.-X. Désert, F. Boulanger, and J. L. Puget. Interstellar dust models for extinction and emission. A&A, 237:215–236, October 1990.

R. H. Dicke, P. J. E. Peebles, P. G. Roll, and D. T. Wilkinson. Cosmic Black-Body Radiation. ApJ, 142:414–419, July 1965. doi: 10.1086/148306.

C. Dickinson, R. D. Davies, and R. J. Davis. Towards a free-free template for CMB foregrounds. MNRAS, 341:369–384, May 2003. doi: 10.1046/j.1365-8711.2003.06439.x.

B. T. Draine and A. Lazarian. Electric Dipole Radiation from Spinning Dust Grains. ApJ, 508:157–179, November 1998a. doi: 10.1086/306387.

B. T. Draine and A. Lazarian. Diffuse Galactic Emission from Spinning Dust Grains. ApJ, 494: L19–L22, February 1998b. doi: 10.1086/311167.

A. S. Eddington. On a formula for correcting statistics for the effects of a known error of observation. MNRAS, 73:359–360, March 1913.

D. Elbaz, M. Dickinson, H. S. Hwang, T. Díaz-Santos, G. Magdis, B. Magnelli, D. Le Borgne, F. Galliano, and et al. GOODS-Herschel: an infrared main sequence for star-forming galaxies. A&A, 533: A119, September 2011. doi: 10.1051/0004-6361/201117239.

H. K. Eriksen, A. J. Banday, K. M. Górski, F. K. Hansen, and P. B. Lilje. Hemispherical Power Asymmetry in the Third-Year Wilkinson Microwave Anisotropy Probe Sky Maps. ApJ, 660:L81–L84, May 2007. doi: 10.1086/518091.

F. Finelli, J. García-Bellido, A. Kovács, F. Paci, and I. Szapudi. A Supervoid Explanation of the Cosmic Microwave Background Cold Spot. In *IAU Symposium*, volume 306 of *IAU Symposium*, pages 153–155, May 2014. doi: 10.1017/S1743921314013714.

D. P. Finkbeiner, M. Davis, and D. J. Schlegel. Extrapolation of Galactic Dust Emission at 100 Microns to Cosmic Microwave Background Radiation Frequencies Using FIRAS. ApJ, 524:867–886, October 1999. doi: 10.1086/307852.

D. J. Fixsen. The Temperature of the Cosmic Microwave Background. ApJ, 707:916–920, December 2009. doi: 10.1088/0004-637X/707/2/916.

D. J. Fixsen, E. S. Cheng, J. M. Gales, J. C. Mather, R. A. Shafer, and E. L. Wright. The Cosmic Microwave Background Spectrum from the Full COBE FIRAS Data Set. ApJ, 473:576, December 1996. doi: 10.1086/178173.

A. Friedman. Über die Krümmung des Raumes. Zeitschrift für Physik, 10:377–386, 1922. doi: 10.1007/BF01332580.

M. A. Garrett. The FIR/Radio correlation of high redshift galaxies in the region of the HDF-N. A&A, 384:L19–L22, March 2002. doi: 10.1051/0004-6361:20020169.

R. Génova-Santos, J. A. Rubiño-Martín, R. Rebolo, A. Peláez-Santos, C. H. López-Caraballo, S. Harper, R. A. Watson, M. Ashdown, and et al. QUIJOTE scientific results - I. Measurements of the intensity and polarisation of the anomalous microwave emission in the Perseus molecular complex. MNRAS, 452:4169–4182, October 2015. doi: 10.1093/mnras/stv1405.

P. Giommi, G. Polenta, A. Lähteenmäki, D. J. Thompson, M. Capalbi, S. Cutini, D. Gasparrini, J. González-Nuevo, and et al. Simultaneous Planck, Swift, and Fermi observations of X-ray and γ-ray selected blazars. A&A, 541:A160, May 2012. doi: 10.1051/0004-6361/201117825.

N. Y. Gnedin and A. H. Jaffe. Secondary Cosmic Microwave Background Anisotropies from Cosmological Reionization. ApJ, 551:3–14, April 2001. doi: 10.1086/320076.

B. Gold, N. Odegard, J. L. Weiland, R. S. Hill, A. Kogut, C. L. Bennett, G. Hinshaw, X. Chen, J. Dunkley, and M. Halpern. Seven-year Wilkinson Microwave Anisotropy Probe (WMAP) Observations: Galactic Foreground Emission. ApJS, 192:15–+, February 2011. doi: 10.1088/0067-0049/192/2/15.

J. González-Nuevo, L. Toffolatti, and F. Argüeso. Predictions of the Angular Power Spectrum of Clustered Extragalactic Point Sources at Cosmic Microwave Background Frequencies from Flat and All-Sky Two-dimensional Simulations. ApJ, 621:1–14, March 2005. doi: 10.1086/427425.

J. González-Nuevo, F. Argüeso, M. López-Caniego, L. Toffolatti, J. L. Sanz, P. Vielva, and D. Herranz. The Mexican hat wavelet family: application to point-source detection in cosmic microwave background maps. MNRAS, 369:1603–1610, July 2006. doi: 10.1111/j.1365-2966.2006.10442.x.

J. González-Nuevo, M. Massardi, F. Argüeso, D. Herranz, L. Toffolatti, J. L. Sanz, M. López-Caniego, and G. De Zotti. Statistical properties of extragalactic sources in the New Extragalactic WMAP Point Source (NEWPS) catalogue. MNRAS, 384:711–718, February 2008. doi: 10.1111/j.1365-2966.2007.12733.x.

C. Gordon, W. Hu, D. Huterer, and T. Crawford. Spontaneous isotropy breaking: A mechanism for CMB multipole alignments. Phys. Rev. D, 72(10):103002, November 2005. doi: 10.1103/PhysRevD.72.103002.

K. M. Górski, E. Hivon, A. J. Banday, B. D. Wandelt, F. K. Hansen, M. Reinecke, and M. Bartelmann. HEALPix: A Framework for High-Resolution Discretization and Fast Analysis of Data Distributed on the Sphere. ApJ, 622:759–771, April 2005. doi: 10.1086/427976.

G. L. Granato, L. Silva, P. Monaco, P. Panuzzo, P. Salucci, G. De Zotti, and L. Danese. Joint formation of QSOs and spheroids: QSOs as clocks of star formation in spheroids. MNRAS, 324:757–768, June 2001. doi: 10.1046/j.1365-8711.2001.04369.x.

G. L. Granato, G. De Zotti, L. Silva, A. Bressan, and L. Danese. A Physical Model for the Coevolution of QSOs and Their Spheroidal Hosts. ApJ, 600:580–594, January 2004. doi: 10.1086/379875.

A. H. Guth. Inflationary universe: A possible solution to the horizon and flatness problems. Phys. Rev. D, 23:347–356, January 1981. doi: 10.1103/PhysRevD.23.347.

A. H. Guth and S.-Y. Pi. Fluctuations in the new inflationary universe. *Physical Review Letters*, 49: 1110–1113, October 1982. doi: 10.1103/PhysRevLett.49.1110.

C. M. Gutiérrez, R. Rebolo, R. A. Watson, R. D. Davies, A. W. Jones, and A. N. Lasenby. The Tenerife Cosmic Microwave Background Maps: Observations and First Analysis. ApJ, 529:47–55, January 2000. doi: 10.1086/308246.

S. Hanany, P. Ade, A. Balbi, J. Bock, J. Borrill, A. Boscaleri, P. de Bernardis, P. G. Ferreira, V. V. Hristov, A. H. Jaffe, A. E. Lange, A. T. Lee, P. D. Mauskopf, C. B. Netterfield, S. Oh, E. Pascale, B. Rabii, P. L. Richards, G. F. Smoot, R. Stompor, C. D. Winant, and J. H. P. Wu. MAXIMA-1: A Measurement of the Cosmic Microwave Background Anisotropy on Angular Scales of 10'-5°. ApJ, 545:L5–L9, December 2000. doi: 10.1086/317322.

C. M. Harrison, D. M. Alexander, J. R. Mullaney, B. Altieri, D. Coia, V. Charmandaris, E. Daddi, H. Dannerbauer, K. Dasyra, A. Del Moro, M. Dickinson, R. C. Hickox, R. J. Ivison, J. Kartaltepe, E. Le Floc'h, R. Leiton, B. Magnelli, P. Popesso, E. Rovilos, D. Rosario, and A. M. Swinbank. No Clear Submillimeter Signature of Suppressed Star Formation among X-Ray Luminous Active Galactic Nuclei. ApJ, 760:L15, November 2012. doi: 10.1088/2041-8205/760/1/L15.

E. R. Harrison. Fluctuations at the Threshold of Classical Cosmology. Phys. Rev. D, 1:2726–2730, May 1970. doi: 10.1103/PhysRevD.1.2726.

C. G. T. Haslam, C. J. Salter, H. Stoffel, and W. E. Wilson. A 408 MHz all-sky continuum survey. II - The atlas of contour maps. A&AS, 47:1–+, January 1982.

S. W. Hawking. The development of irregularities in a single bubble inflationary universe. *Physics Letters B*, 115:295–297, September 1982. doi: 10.1016/0370-2693(82)90373-2.

G. Helou, B. T. Soifer, and M. Rowan-Robinson. Thermal infrared and nonthermal radio - Remarkable correlation in disks of galaxies. ApJ, 298:L7–L11, November 1985. doi: 10.1086/184556.

D. Herranz and J. L. Sanz. Matrix Filters for the Detection of Extragalactic Point Sources in Cosomic Microwave Background Images. *IEEE Journal of Selected Topics in Signal Processing*, 2:727–734, October 2008. doi: 10.1109/JSTSP.2008.2005339.

D. Herranz and P. Vielva. Cosmic microwave background images. *IEEE Signal Processing Magazine*, 27:67–75, January 2010. doi: 10.1109/MSP.2009.934716.

D. Herranz, J. Gallegos, J. L. Sanz, and E. Martínez-González. Point source detection and extraction from simulated Planck time-ordered data using optimal adaptive filters. MNRAS, 334:533–541, August 2002a. doi: 10.1046/j.1365-8711.2002.05517.x.

D. Herranz, J. L. Sanz, R. B. Barreiro, and E. Martínez-González. Scale-adaptive Filters for the Detection/Separation of Compact Sources. ApJ, 580:610–625, November 2002b. doi: 10.1086/342651.

D. Herranz, J. L. Sanz, M. P. Hobson, R. B. Barreiro, J. M. Diego, E. Martínez-González, and A. N. Lasenby. Filtering techniques for the detection of Sunyaev-Zel'dovich clusters in multifrequency maps. MNRAS, 336:1057–1068, November 2002c. doi: 10.1046/j.1365-8711.2002.05704.x.

D. Herranz, J. L. Sanz, R. B. Barreiro, and M. López-Caniego. The estimation of the Sunyaev-Zel'dovich effects with unbiased multifilters. MNRAS, 356:944–954, January 2005. doi: 10.1111/j.1365-2966.2004.08555.x.

D. Herranz, J. L. Sanz, M. López-Caniego, and J. González-Nuevo. A Bayesian Approach To Flux Correction In Extragalactic Detection. *IEEE International Symposium on Signal Processing and Information Technology*, 1:541–544, 2006. doi: http://doi.ieeecomputersociety.org/10.1109/ISSPIT.2006.270860.

D. Herranz, M. López-Caniego, J. L. Sanz, and J. González-Nuevo. A novel multifrequency technique for the detection of point sources in cosmic microwave background maps. MNRAS, 394:510–520, March 2009. doi: 10.1111/j.1365-2966.2008.14336.x.

M. P. Hobson and A. N. Lasenby. The entropic prior for distributions with positive and negative values. MNRAS, 298:905–908, August 1998. doi: 10.1046/j.1365-8711.1998.01707.x.

M. P. Hobson and C. McLachlan. A Bayesian approach to discrete object detection in astronomical data sets. MNRAS, 338:765–784, January 2003. doi: 10.1046/j.1365-8711.2003.06094.x.

M. P. Hobson, R. B. Barreiro, L. Toffolatti, A. N. Lasenby, J. L. Sanz, A. W. Jones, and F. R. Bouchet. The effect of point sources on satellite observations of the cosmic microwave background. MNRAS, 306:232–246, June 1999.

J. Hoftuft, H. K. Eriksen, A. J. Banday, K. M. Górski, F. K. Hansen, and P. B. Lilje. Increasing Evidence for Hemispherical Power Asymmetry in the Five-Year WMAP Data. ApJ, 699:985–989, July 2009. doi: 10.1088/0004-637X/699/2/985.

M.A. Holdaway, F.N. Owen, and M.P. Rupen. Source counts at 90 ghz. Alma memo #123, National Radio Astronomy Observatory, 1994. URL `http://www.alma.nrao.edu/memos/html-memos/alma123/memo123.pdf`.

G. P. Holder. Radio Point Sources and the Thermal Sunyaev-Zeldovich Power Spectrum. ApJ, 580: 36–41, November 2002. doi: 10.1086/343094.

F. Hoyle. A New Model for the Expanding Universe. MNRAS, 108:372, 1948.

W. Hu and M. White. Acoustic Signatures in the Cosmic Microwave Background. ApJ, 471:30, November 1996. doi: 10.1086/177951.

W. Hu and M. White. A CMB polarization primer. New A, 2:323–344, October 1997. doi: 10.1016/S1384-1076(97)00022-5.

E. Hubble. A Relation between Distance and Radial Velocity among Extra-Galactic Nebulae. *Proceedings of the National Academy of Science*, 15:168–173, March 1929. doi: 10.1073/pnas.15.3.168.

K. T. Inoue and J. Silk. Local Voids as the Origin of Large-Angle Cosmic Microwave Background Anomalies. I. ApJ, 648:23–30, September 2006. doi: 10.1086/505636.

N. Jarosik, C. L. Bennett, J. Dunkley, B. Gold, M. R. Greason, M. Halpern, R. S. Hill, G. Hinshaw, A. Kogut, E. Komatsu, D. Larson, M. Limon, S. S. Meyer, M. R. Nolta, N. Odegard, L. Page, K. M. Smith, D. N. Spergel, G. S. Tucker, J. L. Weiland, E. Wollack, and E. L. Wright. Seven-year Wilkinson Microwave Anisotropy Probe (WMAP) Observations: Sky Maps, Systematic Errors, and Basic Results. ApJS, 192:14, February 2011. doi: 10.1088/0067-0049/192/2/14.

H. Jiang, W. R. Chen, and H. Liu. Techniques to improve the accuracy and to reduce the variance in noise power spectrum measurement. *IEEE Transactions on Biomedical Engineering*, 11:1270–1278, November 2002. doi: 10.1109/TBME.2002.804595.

M. Kamionkowski, D. N. Spergel, and N. Sugiyama. Small-scale cosmic microwave background anisotropies as probe of the geometry of the universe. ApJ, 426:L57, May 1994. doi: 10.1086/187339.

K. I. Kellermann, I. I. K. Pauliny-Toth, and P. J. S. Williams. The Spectra of Radio Sources in the Revised 3C Catalogue. ApJ, 157:1, July 1969. doi: 10.1086/150046.

I. J. Klamer, R. D. Ekers, J. J. Bryant, R. W. Hunstead, E. M. Sadler, and C. De Breuck. A search for distant radio galaxies from SUMSS and NVSS - III. Radio spectral energy distributions and the z-α correlation. MNRAS, 371:852–866, September 2006. doi: 10.1111/j.1365-2966.2006.10714.x.

R. W. Klebesadel, I. B. Strong, and R. A. Olson. Observations of Gamma-Ray Bursts of Cosmic Origin. ApJ, 182:L85, June 1973. doi: 10.1086/181225.

A. Kogut. Anomalous Microwave Emission. In A. de Oliveira-Costa and M. Tegmark, editors, *Microwave Foregrounds*, volume 181 of *Astronomical Society of the Pacific Conference Series*, page 91, 1999.

A. Kogut, J. Dunkley, C. L. Bennett, O. Doré, B. Gold, M. Halpern, G. Hinshaw, N. Jarosik, E. Komatsu, M. R. Nolta, N. Odegard, L. Page, D. N. Spergel, G. S. Tucker, J. L. Weiland, E. Wollack, and E. L. Wright. Three-Year Wilkinson Microwave Anisotropy Probe (WMAP) Observations: Foreground Polarization. ApJ, 665:355–362, August 2007. doi: 10.1086/519754.

E. W. Kolb and M. S. Turner. *The early universe.* 1990.

A. Königl. Relativistic jets as X-ray and gamma-ray sources. ApJ, 243:700–709, February 1981. doi: 10.1086/158638.

K. Land and J. Magueijo. Is the Universe odd? Phys. Rev. D, 72(10):101302, November 2005. doi: 10.1103/PhysRevD.72.101302.

L. F. Lanz, D. Herranz, J. L. Sanz, J. González-Nuevo, and M. López-Caniego. A multifrequency method based on the matched multifilter for the detection of point sources in CMB maps. MNRAS, 403:2120–2130, April 2010. doi: 10.1111/j.1365-2966.2010.16260.x.

L. F. Lanz, D. Herranz, M. López-Caniego, J. González-Nuevo, G. de Zotti, M. Massardi, and J. L. Sanz. Extragalactic point source detection in Wilkinson Microwave Anisotropy Probe 7-year data at 61 and 94 GHz. MNRAS, 428:3048–3057, February 2013. doi: 10.1093/mnras/sts252.

R. Laureijs, J. Amiaux, S. Arduini, J.-L. Augueres, J. Brinchmann, R. Cole, M. Cropper, C. Dabin, L. Duvet, A. Ealet, and et al. Euclid Definition Study Report. *arXiv:1110.3193v1*, October 2011.

Leach et al. Component separation methods for the PLANCK mission. A&A, 491:597–615, November 2008. doi: 10.1051/0004-6361:200810116.

E. M. Leitch, A. C. S. Readhead, T. J. Pearson, and S. T. Myers. An Anomalous Component of Galactic Emission. ApJ, 486:L23–L26, September 1997. doi: 10.1086/310823.

M. S. Longair. On the interpretation of radio source counts. MNRAS, 133:421, 1966.

M. López-Caniego and P. Vielva. Biparametric adaptive filter: detection of compact sources in complex microwave backgrounds. MNRAS, 421:2139–2154, April 2012. doi: 10.1111/j.1365-2966.2012.20444.x.

M. López-Caniego, D. Herranz, R. B. Barreiro, and J. L. Sanz. A Bayesian approach to filter design: detection of compact sources. In C. A. Bouman and E. L. Miller, editors, *Computational Imaging II. Edited by Bouman, Charles A.; Miller, Eric L. Proceedings of the SPIE, Volume 5299, pp. 145-154 (2004).*, volume 5299 of *Presented at the Society of Photo-Optical Instrumentation Engineers (SPIE) Conference*, pages 145–154, May 2004. doi: 10.1117/12.541151.

M. López-Caniego, D. Herranz, R. B. Barreiro, and J. L. Sanz. Filter design for the detection of compact sources based on the Neyman-Pearson detector. MNRAS, 359:993–1006, May 2005. doi: 10.1111/j.1365-2966.2005.08961.x.

M. López-Caniego, D. Herranz, J. L.. Sanz, and R. B. Barreiro. Detection of Point Sources on Two-Dimensional Images Based on Peaks. *EURASIP Journal on Applied Signal Processing*, 15:2426–2436, July 2005.

M. López-Caniego, D. Herranz, J. González-Nuevo, J. L. Sanz, R. B. Barreiro, P. Vielva, F. Argüeso, and L. Toffolatti. Comparison of filters for the detection of point sources in Planck simulations. MNRAS, 370:2047–2063, August 2006. doi: 10.1111/j.1365-2966.2006.10639.x.

M. López-Caniego, J. González-Nuevo, D. Herranz, M. Massardi, J. L. Sanz, G. De Zotti, L. Toffolatti, and F. Argüeso. Nonblind Catalog of Extragalactic Point Sources from the Wilkinson Microwave Anisotropy Probe (WMAP) First 3 Year Survey Data. ApJS, 170:108–125, May 2007. doi: 10.1086/512678.

M. López-Caniego, M. Massardi, J. González-Nuevo, L. Lanz, D. Herranz, G. De Zotti, J. L. Sanz, and F. Argüeso. Polarization of the WMAP Point Sources. ApJ, 705:868–876, November 2009. doi: 10.1088/0004-637X/705/1/868.

S. Mallat. *A wavelet tour of signal processing*. Academic Press, 1998. ISBN 0-8176-3864-4.

C. Mancuso, A. Lapi, Z.-Y. Cai, M. Negrello, G. De Zotti, A. Bressan, M. Bonato, F. Perrotta, and L. Danese. Predictions for Ultra-deep Radio Counts of Star-forming Galaxies. ApJ, 810:72, September 2015. doi: 10.1088/0004-637X/810/1/72.

T. A. Marriage, J. B. Juin, Y.-T. Lin, D. Marsden, M. R. Nolta, B. Partridge, P. A. R. Ade, P. Aguirre, and et al. The Atacama Cosmology Telescope: Extragalactic Sources at 148 GHz in the 2008 Survey. ApJ, 731:100–+, April 2011. doi: 10.1088/0004-637X/731/2/100.

A. P. Marscher. The Inner Jets of Blazars. In P. E. Hardee, A. H. Bridle, and J. A. Zensus, editors, *Energy Transport in Radio Galaxies and Quasars*, volume 100 of *Astronomical Society of the Pacific Conference Series*, page 45, 1996.

A. P. Marscher and W. K. Gear. Models for high-frequency radio outbursts in extragalactic sources, with application to the early 1983 millimeter-to-infrared flare of 3C 273. ApJ, 298:114–127, November 1985. doi: 10.1086/163592.

B. S. Mason, T. J. Pearson, A. C. S. Readhead, M. C. Shepherd, J. Sievers, P. S. Udomprasert, J. K. Cartwright, A. J. Farmer, and et al. The Anisotropy of the Microwave Background to l = 3500: Deep Field Observations with the Cosmic Background Imager. ApJ, 591:540–555, July 2003. doi: 10.1086/375507.

M. Massardi, M. López-Caniego, J. González-Nuevo, D. Herranz, G. De Zotti, and J. L. Sanz. Blind and non-blind source detection in WMAP 5-yr maps. MNRAS, 392:733–742, January 2009. doi: 10.1111/j.1365-2966.2008.14084.x.

M. Massardi, A. Bonaldi, M. Negrello, S. Ricciardi, A. Raccanelli, and G. De Zotti. A model for the cosmological evolution of low-frequency radio sources. MNRAS, 404:532–544, May 2010. doi: 10.1111/j.1365-2966.2010.16305.x.

M. Massardi, A. Bonaldi, L. Bonavera, M. López-Caniego, G. de Zotti, and R. D. Ekers. The Planck-ATCA Co-eval Observations project: the bright sample. MNRAS, 415:1597–1610, August 2011. doi: 10.1111/j.1365-2966.2011.18802.x.

J.-B. Melin, J. G. Bartlett, and J. Delabrouille. Catalog extraction in SZ cluster surveys: a matched filter approach. A&A, 459:341–352, November 2006. doi: 10.1051/0004-6361:20065034.

P. Mészáros. Gamma-ray burst afterglows and their implications. A&AS, 138:533–536, September 1999. doi: 10.1051/aas:1999341.

G. Miley and C. De Breuck. Distant radio galaxies and their environments. A&A Rev., 15:67–144, February 2008. doi: 10.1007/s00159-007-0008-z.

C. Monteserín, R. B. Barreiro, P. Vielva, E. Martínez-González, M. P. Hobson, and A. N. Lasenby. A low cosmic microwave background variance in the Wilkinson Microwave Anisotropy Probe data. MNRAS, 387:209–219, June 2008. doi: 10.1111/j.1365-2966.2008.13149.x.

T. W. B. Muxlow, A. M. S. Richards, S. T. Garrington, P. N. Wilkinson, B. Anderson, E. A. Richards, D. J. Axon, E. B. Fomalont, K. I. Kellermann, R. B. Partridge, and R. A. Windhorst. High-resolution studies of radio sources in the Hubble Deep and Flanking Fields. MNRAS, 358:1159–1194, April 2005. doi: 10.1111/j.1365-2966.2005.08824.x.

P. Naselsky, D. Novikov, and J. Silk. A combined multifrequency map for point source subtraction. MNRAS, 335:550–554, September 2002. doi: 10.1046/j.1365-8711.2002.05525.x.

M. Negrello, F. Perrotta, J. González-Nuevo, L. Silva, G. De Zotti, G. L. Granato, C. Baccigalupi, and L. Danese. Astrophysical and cosmological information from large-scale submillimetre surveys of extragalactic sources. MNRAS, 377:1557–1568, June 2007. doi: 10.1111/j.1365-2966.2007.11708.x.

R. T. Ogden. *Essential Wavelets for Statistical Applications and Data Analysis* . Birkhäuser, 1997. ISBN 0-8176-3864-4.

L. Page, G. Hinshaw, E. Komatsu, M. R. Nolta, D. N. Spergel, C. L. Bennett, C. Barnes, R. Bean, O. Doré, J. Dunkley, M. Halpern, R. S. Hill, N. Jarosik, A. Kogut, M. Limon, S. S. Meyer, N. Odegard, H. V. Peiris, G. S. Tucker, L. Verde, J. L. Weiland, E. Wollack, and E. L. Wright. Three-Year Wilkinson Microwave Anisotropy Probe (WMAP) Observations: Polarization Analysis. ApJS, 170: 335–376, June 2007. doi: 10.1086/513699.

A. A. Penzias and R. W. Wilson. A Measurement of Excess Antenna Temperature at 4080 Mc/s. ApJ, 142:419–421, July 1965. doi: 10.1086/148307.

Planck Collaboration, J. Aatrokoski, P. A. R. Ade, N. Aghanim, H. D. Aller, M. F. Aller, E. Angelakis, M. Arnaud, M. Ashdown, J. Aumont, and et al. Planck early results. XV. Spectral energy distributions and radio continuum spectra of northern extragalactic radio sources. A&A, 536:A15, December 2011a. doi: 10.1051/0004-6361/201116466.

Planck Collaboration, P. A. R. Ade, N. Aghanim, F. Argüeso, M. Arnaud, M. Ashdown, J. Aumont, C. Baccigalupi, A. Balbi, A. J. Banday, and et al. Planck early results. XIII. Statistical properties of extragalactic radio sources in the Planck Early Release Compact Source Catalogue. A&A, 536: A13, December 2011b. doi: 10.1051/0004-6361/201116471.

Planck Collaboration, P. A. R. Ade, N. Aghanim, M. Arnaud, M. Ashdown, J. Aumont, C. Baccigalupi, A. Balbi, A. J. Banday, R. B. Barreiro, and et al. Planck early results. VII. The Early Release Compact Source Catalogue. A&A, 536:A7, December 2011c. doi: 10.1051/0004-6361/201116474.

Planck Collaboration, P. A. R. Ade, N. Aghanim, F. Argüeso, C. Armitage-Caplan, M. Arnaud, M. Ashdown, F. Atrio-Barandela, J. Aumont, C. Baccigalupi, and et al. Planck 2013 results. XXVIII. The Planck Catalogue of Compact Sources. A&A, 571:A28, November 2014a. doi: 10.1051/0004-6361/201321524.

Planck Collaboration, P. A. R. Ade, N. Aghanim, C. Armitage-Caplan, M. Arnaud, M. Ashdown, F. Atrio-Barandela, J. Aumont, H. Aussel, C. Baccigalupi, and et al. Planck 2013 results. XXIX. The Planck catalogue of Sunyaev-Zeldovich sources. A&A, 571:A29, November 2014b. doi: 10.1051/0004-6361/201321523.

Planck Collaboration, P. A. R. Ade, N. Aghanim, C. Armitage-Caplan, M. Arnaud, M. Ashdown, F. Atrio-Barandela, J. Aumont, C. Baccigalupi, A. J. Banday, and et al. Planck 2013 results. XV. CMB power spectra and likelihood. A&A, 571:A15, November 2014c. doi: 10.1051/0004-6361/201321573.

Planck Collaboration, P. A. R. Ade, N. Aghanim, C. Armitage-Caplan, M. Arnaud, M. Ashdown, F. Atrio-Barandela, J. Aumont, C. Baccigalupi, A. J. Banday, and et al. Planck 2013 results. XXIII. Isotropy and statistics of the CMB. A&A, 571:A23, November 2014d. doi: 10.1051/0004-6361/201321534.

Planck Collaboration, R. Adam, P. A. R. Ade, N. Aghanim, M. I. R. Alves, M. Arnaud, M. Ashdown, J. Aumont, C. Baccigalupi, A. J. Banday, and et al. Planck 2015 results. X. Diffuse component separation: Foreground maps. *arXiv:1502.01588v2*, February 2015a.

Planck Collaboration, R. Adam, P. A. R. Ade, N. Aghanim, M. Arnaud, M. Ashdown, J. Aumont, C. Baccigalupi, A. J. Banday, R. B. Barreiro, and et al. Planck 2015 results. IX. Diffuse component separation: CMB maps. *arXiv:1502.05956v1*, February 2015b.

Planck Collaboration, P. A. R. Ade, N. Aghanim, D. Alina, M. I. R. Alves, C. Armitage-Caplan, M. Arnaud, D. Arzoumanian, M. Ashdown, F. Atrio-Barandela, and et al. Planck intermediate results. XIX. An overview of the polarized thermal emission from Galactic dust. A&A, 576:A104, April 2015c. doi: 10.1051/0004-6361/201424082.

Planck Collaboration, P. A. R. Ade, N. Aghanim, F. Argüeso, M. Arnaud, M. Ashdown, J. Aumont, C. Baccigalupi, A. J. Banday, R. B. Barreiro, and et al. Planck 2015 results. XXVI. The Second Planck Catalogue of Compact Sources. *arXiv:1507.02058v1*, July 2015d.

Planck Collaboration, P. A. R. Ade, N. Aghanim, M. Arnaud, M. Ashdown, J. Aumont, C. Baccigalupi, A. J. Banday, R. B. Barreiro, J. G. Bartlett, and et al. Planck 2015 results. XIII. Cosmological parameters. *arXiv:1502.01589v2*, February 2015e.

Planck Collaboration, P. A. R. Ade, N. Aghanim, M. Arnaud, J. Aumont, C. Baccigalupi, A. J. Banday, R. B. Barreiro, N. Bartolo, E. Battaner, and et al. Planck intermediate results. XXXIX. The Planck list of high-redshift source candidates. *arXiv:1508.04171v2*, August 2015f.

Planck Collaboration, N. Aghanim, B. Altieri, M. Arnaud, M. Ashdown, J. Aumont, C. Baccigalupi, A. J. Banday, R. B. Barreiro, N. Bartolo, and et al. Planck intermediate results. XXVII. High-redshift infrared galaxy overdensity candidates and lensed sources discovered by Planck and confirmed by Herschel-SPIRE. A&A, 582:A30, October 2015g. doi: 10.1051/0004-6361/201424790.

Planck Collaboration, N. Aghanim, M. Arnaud, M. Ashdown, J. Aumont, C. Baccigalupi, A. J. Banday, R. B. Barreiro, J. G. Bartlett, N. Bartolo, and et al. Planck 2015 results. XI. CMB power spectra, likelihoods, and robustness of parameters. *arXiv:1507.02704v1*, July 2015h.

W. H. Press, S. A. Teukolsky, W. T. Vetterling, and B. P. Flannery. *Numerical recipes in FORTRAN. The art of scientific computing*. 1992a.

W. H. Press, S. A. Teukolsky, W. T. Vetterling, and B. P. Flannery. *Numerical recipes in C. The art of scientific computing*. 1992b.

J.-L. Puget, A. Abergel, J.-P. Bernard, F. Boulanger, W. B. Burton, F.-X. Désert, and D. Hartmann. Tentative detection of a cosmic far-infrared background with COBE. A&A, 308:L5, April 1996.

M. J. Rees and D. W. Sciama. Large-scale Density Inhomogeneities in the Universe. Nature, 217: 511–516, February 1968. doi: 10.1038/217511a0.

M. J. Rees, M. C. Begelman, R. D. Blandford, and E. S. Phinney. Ion-supported tori and the origin of radio jets. Nature, 295:17–21, January 1982. doi: 10.1038/295017a0.

S. O. Rice. Mathematical Analysis of Random Noise. 23-24:133, 1954.

P. R. Rider. Generalized Cauchy distributions . Ann. Inst. Stat. Math., 9:215–223, 1957.

G. Rodighiero, E. Daddi, I. Baronchelli, A. Cimatti, A. Renzini, H. Aussel, P. Popesso, D. Lutz, P. Andreani, S. Berta, A. Cava, D. Elbaz, A. Feltre, A. Fontana, N. M. Förster Schreiber, A. Franceschini, R. Genzel, A. Grazian, C. Gruppioni, O. Ilbert, E. Le Floch, G. Magdis, M. Magliocchetti, B. Magnelli, R. Maiolino, H. McCracken, R. Nordon, A. Poglitsch, P. Santini, F. Pozzi, L. Riguccini, L. J. Tacconi, S. Wuyts, and G. Zamorani. The Lesser Role of Starbursts in Star Formation at z = 2. ApJ, 739:L40, October 2011. doi: 10.1088/2041-8205/739/2/L40.

G. B. Rybicki and A. P. Lightman. *Radiative processes in astrophysics*. 1979.

R. K. Sachs and A. M. Wolfe. Perturbations of a Cosmological Model and Angular Variations of the Microwave Background. ApJ, 147:73, January 1967. doi: 10.1086/148982.

E. M. Sadler, R. Ricci, R. D. Ekers, R. J. Sault, C. A. Jackson, and G. De Zotti. The extragalactic radio-source population at 95 GHz. MNRAS, 385:1656–1672, April 2008. doi: 10.1111/j.1365-2966.2008.12955.x.

J. L. Sanz, D. Herranz, and E. Martínez-Gónzalez. Optimal Detection of Sources on a Homogeneous and Isotropic Background. ApJ, 552:484–492, May 2001. doi: 10.1086/320550.

J. L. Sanz, D. Herranz, M. López-Caniego, and F. Argüeso. Wavelets on the sphere. Application to the detection problem. In *Proceedings of the 14th European Signal Processing Conference (2006).*, EUSIPCO 2006 Conference, pages 1–5, September 2006.

B. M. Schäfer, C. Pfrommer, R. M. Hell, and M. Bartelmann. Detecting Sunyaev-Zel'dovich clusters with Planck - II. Foreground components and optimized filtering schemes. MNRAS, 370:1713–1736, August 2006. doi: 10.1111/j.1365-2966.2006.10622.x.

U. Seljak and M. Zaldarriaga. A Line-of-Sight Integration Approach to Cosmic Microwave Background Anisotropies. ApJ, 469:437, October 1996. doi: 10.1086/177793.

J. Silk. Cosmic Black-Body Radiation and Galaxy Formation. ApJ, 151:459, February 1968. doi: 10.1086/149449.

G. F. Smoot. Galactic Free-Free and Hα Emission. *arXiv:astro-ph/9801121v2*, January 1998.

G. F. Smoot. CMB Synchrotron Foreground. In A. de Oliveira-Costa and M. Tegmark, editors, *Microwave Foregrounds*, volume 181 of *Astronomical Society of the Pacific Conference Series*, page 61, 1999.

G. F. Smoot, C. L. Bennett, A. Kogut, E. L. Wright, J. Aymon, N. W. Boggess, E. S. Cheng, G. de Amici, S. Gulkis, M. G. Hauser, G. Hinshaw, P. D. Jackson, M. Janssen, E. Kaita, T. Kelsall, P. Keegstra, C. Lineweaver, K. Loewenstein, P. Lubin, J. Mather, S. S. Meyer, S. H. Moseley, T. Murdock, L. Rokke, R. F. Silverberg, L. Tenorio, R. Weiss, and D. T. Wilkinson. Structure in the COBE differential microwave radiometer first-year maps. ApJ, 396:L1–L5, September 1992. doi: 10.1086/186504.

A. A. Starobinsky. Dynamics of phase transition in the new inflationary universe scenario and generation of perturbations. *Physics Letters B*, 117:175–178, November 1982. doi: 10.1016/0370-2693(82)90541-X.

R. A. Sunyaev and Y. B. Zeldovich. The Observations of Relic Radiation as a Test of the Nature of X-Ray Radiation from the Clusters of Galaxies. *Comments on Astrophysics and Space Physics*, 4: 173–+, November 1972.

J. A. Tauber. The Planck Mission. In A. N. Lasenby and A. Wilkinson, editors, *New Cosmological Data and the Values of the Fundamental Parameters*, volume 201 of *IAU Symposium*, pages 86–+, 2005.

M. Tegmark and A. de Oliveira-Costa. Removing Point Sources from Cosmic Microwave Background Maps. ApJ, 500:L83+, June 1998. doi: 10.1086/311410.

M. Tegmark, A. de Oliveira-Costa, and A. J. S. Hamilton. High resolution foreground cleaned CMB map from WMAP. Phys. Rev. D, 68(12):123523, December 2003. doi: 10.1103/PhysRevD.68.123523.

The Planck Collaboration. The Scientific Programme of Planck. *arXiv:astro-ph/0604069v1*, April 2006.

L. Toffolatti, F. Argüeso Gómez, G. De Zotti, P. Mazzei, A. Franceschini, L. Danese, and C. Burigana. Extragalactic source counts and contributions to the anisotropies of the cosmic microwave background: predictions for the Planck Surveyor mission. MNRAS, 297:117–127, June 1998.

M. Tucci, E. Martínez-González, L. Toffolatti, J. González-Nuevo, and G. De Zotti. Predictions on the high-frequency polarization properties of extragalactic radio sources and implications for polarization measurements of the cosmic microwave background. MNRAS, 349:1267–1277, April 2004. doi: 10.1111/j.1365-2966.2004.07593.x.

M. Tucci, E. Martínez-González, P. Vielva, and J. Delabrouille. Limits on the detectability of the CMB B-mode polarization imposed by foregrounds. MNRAS, 360:935–949, July 2005. doi: 10.1111/j.1365-2966.2005.09123.x.

M. Tucci, L. Toffolatti, G. De Zotti, and E. Martínez-González. High-frequency predictions for number counts and spectral properties of extragalactic radio sources. New evidence of a break at mm wavelengths in spectra of bright blazar sources. A&A, 533:A57, September 2011. doi: 10.1051/0004-6361/201116972.

C. M. Urry and P. Padovani. Unified Schemes for Radio-Loud Active Galactic Nuclei. PASP, 107:803, September 1995. doi: 10.1086/133630.

M. Vidal, C. Dickinson, R. D. Davies, and J. P. Leahy. Polarized radio filaments outside the Galactic plane. MNRAS, 452:656–675, September 2015. doi: 10.1093/mnras/stv1328.

P. Vielva, R. B. Barreiro, M. P. Hobson, E. Martínez-González, A. N. Lasenby, J. L. Sanz, and L. Toffolatti. Combining maximum-entropy and the Mexican hat wavelet to reconstruct the microwave sky. MNRAS, 328:1–16, November 2001a. doi: 10.1046/j.1365-8711.2001.04693.x.

P. Vielva, E. Martínez-González, L. Cayón, J. M. Diego, J. L. Sanz, and L. Toffolatti. Predicted Planck extragalactic point-source catalogue. MNRAS, 326:181–191, September 2001b. doi: 10.1046/j.1365-8711.2001.04592.x.

P. Vielva, E. Martínez-González, J. E. Gallegos, L. Toffolatti, and J. L. Sanz. Point source detection using the Spherical Mexican Hat Wavelet on simulated all-sky Planck maps. MNRAS, 344:89–104, September 2003. doi: 10.1046/j.1365-8711.2003.06792.x.

P. Vielva, E. Martínez-González, R. B. Barreiro, J. L. Sanz, and L. Cayón. Detection of Non-Gaussianity in the Wilkinson Microwave Anisotropy Probe First-Year Data Using Spherical Wavelets. ApJ, 609:22–34, July 2004. doi: 10.1086/421007.

A. Vilenkin and E. P. S. Shellard. *Cosmic strings and other topological defects*. 1994.

R. A. Watson, R. Rebolo, J. A. Rubiño-Martín, S. Hildebrandt, C. M. Gutiérrez, S. Fernández-Cerezo, R. J. Hoyland, and E. S. Battistelli. Detection of Anomalous Microwave Emission in the Perseus Molecular Cloud with the COSMOSOMAS Experiment. ApJ, 624:L89–L92, May 2005. doi: 10.1086/430519.

E. Waxman. Gamma-Ray–Burst Afterglow: Supporting the Cosmological Fireball Model, Constraining Parameters, and Making Predictions. ApJ, 485:L5–L8, August 1997. doi: 10.1086/310809.

R. A. M. J. Wijers and T. J. Galama. Physical Parameters of GRB 970508 and GRB 971214 from Their Afterglow Synchrotron Emission. ApJ, 523:177–186, September 1999. doi: 10.1086/307705.

E. L. Wright, X. Chen, N. Odegard, C. L. Bennett, R. S. Hill, G. Hinshaw, N. Jarosik, E. Komatsu, M. R. Nolta, L. Page, D. N. Spergel, and et al. Five-Year Wilkinson Microwave Anisotropy Probe Observations: Source Catalog. ApJS, 180:283–295, February 2009. doi: 10.1088/0067-0049/180/2/283.

M. S. Yun, N. A. Reddy, and J. J. Condon. Radio Properties of Infrared-selected Galaxies in the IRAS 2 Jy Sample. ApJ, 554:803–822, June 2001. doi: 10.1086/323145.

S. Zaroubi, Y. Hoffman, K. B. Fisher, and O. Lahav. Wiener Reconstruction of the Large-Scale Structure. ApJ, 449:446, August 1995. doi: 10.1086/176070.

Ya. B. Zeldovich. A hypothesis, unifying the structure and the entropy of the Universe. MNRAS, 160: 1P, 1972.